

Modelling water partitioning in dryland regions: a multiscale analysis



Edisson Andrés Quichimbo Miguitama
School of Earth and Environmental Science
Cardiff University

A thesis submitted for the degree of
Doctor of Philosophy

Cardiff, September 2021

Abstract

Dryland regions, characterised by naturally limited water availability, cover around 40% of the global land surface and sustain a vast population of around 2.1 billion people. These environments pose many challenges for water resources allocation for humans and water availability to ecology, yet there are currently major limitations in our ability to assess the dryland water balance, especially under a changing climate. Therefore, understanding and quantifying the mechanisms that control the water balance in dryland regions is of key importance not only to improve the management of limited water resources, but also to understand the future impacts of climate change in their spatial and temporal variability.

Here, a series of numerical models at different temporal and spatial scales were developed to characterize and quantify the main mechanisms that control the water partitioning and flow pathways in dryland regions. First, by using physically-based numerical models which are able to describe the complexity of groundwater - surface water interactions, the analysis focused on the characterization of the infiltration of water through the streambed of ephemeral streams. Focused groundwater recharge, sourced from such transmission losses, is a mechanism that has received little attention in the literature due to the highly dynamic characteristics of this process and the scarcity of data required for a proper evaluation. Second, a novel, parsimonious, hydrologic model of DRYland water Partitioning (DRYP), has been developed to quantify the water partitioning in data scarce regions. The performance of DRYP was firstly evaluated by using synthetic experiments, and then it was tested in the data-rich Walnut Gulch Experimental Watershed, Arizona, US. It was finally applied in the semi-arid Upper Ewaso Ng'iro basin, Kenya, an area with limited data availability.

Results of this study show that groundwater - surface water interactions play an important role in water partitioning in drylands, and need to

be included in models in order to reduce the uncertainty of water balance quantification of these regions. The spatial and temporal variation in model process description as well as forcing variables also have a great impact on dryland water partitioning. A high spatial (≤ 1 km) and temporal (< 1 d) resolution is required to adequately represent the development and subsurface interactions of ephemeral streams. Although highly uncertain, global datasets of climatological data, as well as regional and global datasets of surface and subsurface parameters, used in the parsimonious model DRYP can provide useful spatially and temporally information to quantify water partitioning in data scarce-regions. This study also highlights the importance of recharge from ephemeral streams in the water balance of dryland regions, a recharge mechanism that can become dominant as the aridity increases.

Acknowledgements

I would like to express my deepest thanks to my supervisors, Dr Mark Cuthbert and Dr Michael Singer, for their enormous support, encouragement and superb advice. Dr Mark Cuthbert took me on as his student, and provided not only brilliant ideas and constructive criticism, but also personal support. Dr Michael Singer greatly supported my work and provided me with encouragement and excellent academic advice. I greatly admire their work and feel honoured and proud to work with great scientists. I am also thankful for their enormous patience during this four-year period.

My deep gratitude also goes to Dr Katerina Michaelides (University of Bristol) - for her kind words during difficult periods as well as her great academic and personal support. It has been a privilege meeting such a great scientist.

I would also like to thank many others who provided support to this work. Great thanks to Dr Daniel Hobley for his immense support and willingness to help with Landlab which provided immediate support to my research. Many thanks to Dr Steve Birkinshaw for his openness to provide help with SHETRAN, and also to Dr. Rafael Rosolem who provided very helpful suggestions and was always open to talk about my research.

Funding for this PhD came from a Vice-Chancellor's International Scholarship for Research Excellence from Cardiff University. Further funding support is gratefully acknowledged from the project 'Drought resilience in East African dryland Regions (DRIER)' (Royal Society).

Thanks to the USDA-ARS Southwest Watershed Research funded by the United States Department of Agriculture, Agricultural Research Service, for providing the WGEW groundwater dataset.

Thanks to the DRIER and DOWN2EARTH teams - their comments and suggestions were always welcome.

I am thankful to all my colleagues, friends, academics and staff members of Cardiff University, who have provided support, encouragement, friendship, and advice.

Last but not least, I would like to thank to my family, although quite far away, without their support it would have been very difficult to complete this dissertation.

To my parents, Ines and Gerardo...

to my sister and brothers...

to my nephews Mateo and Andrés...

Contents

1	Introduction	1
1.1	Background and Motivation	1
1.2	Scope and Objectives	4
1.3	Thesis outline	5
2	Overview of Dryland Hydrology and Modelling	7
2.1	Introduction	7
2.2	Definition of dryland regions	7
2.3	Main hydrological processes in dryland regions	8
2.4	Modelling water partitioning in dryland regions	14
2.5	Summary	15
3	Characterising groundwater - surface water interactions in dryland regions: A transect scale analysis	17
3.1	Introduction	17
3.2	An overview of groundwater - surface water interactions	18
3.3	A conceptual model of ephemeral stream-aquifer interactions	20
3.4	Methods	21
3.4.1	Numerical modelling	21
3.4.2	Model Geometry	22
3.4.3	Governing equations and numerical methods	22
3.4.4	Boundary conditions	23
3.4.5	Initial conditions	25
3.4.6	Base Case scenario and sensitivity analysis	25
3.5	Results	28
3.5.1	Conceptualising a single flow event in time and space	28
3.5.2	The influence of dry period duration between flow events and water table depth on streambed infiltration rates	32

3.5.3	The influence of streamflow duration	32
3.5.4	The influence of sediment properties	33
3.5.5	The influence of geometrical characteristics of the stream channel	35
3.5.6	Caveats and limitations of the analysis	37
3.6	Conclusion	38
4	Characterising groundwater - surface water interactions in dryland regions: A reach scale analysis	40
4.1	Introduction	40
4.2	A conceptual model of groundwater - surface water interactions in ephemeral streams	41
4.3	Methods	44
4.3.1	Numerical modelling	44
4.3.2	Distributed River Flow and Sediment Transport Modelling System, SHETRAN	44
4.3.3	Model Geometry	45
4.3.4	Boundary conditions	46
4.3.5	Model time step	47
4.3.6	Model parameters	47
4.3.7	Test case scenarios and sensitivity analysis	47
4.4	Results	50
4.4.1	Characterisation of groundwater - surface water interactions .	50
4.4.2	Assessing the sensitivity of transmission losses	57
4.4.3	Caveats and limitations of the analysis	63
4.5	Global distribution of ephemeral stream - aquifer interactions	63
4.6	Conclusions	67
5	Development of a parsimonious model for quantifying water partitioning in dryland regions: DRYP	70
5.1	Introduction	70
5.2	DRYP: a parsimonious model for DRYland regions water Partitioning	71
5.2.1	Model overview	71
5.2.2	Surface Component	74
5.2.2.1	Infiltration and runoff	74
5.2.2.2	Runoff routing and transmission losses	77
5.2.3	Unsaturated Component	80
5.2.4	Saturated Component	82

5.2.4.1	Unsaturated - Saturated zone interactions	83
5.2.4.2	Groundwater - surface water interactions	84
5.2.5	Numerical implementation and time step	85
5.2.6	Model input files and parameter settings	86
5.3	Model Evaluation	86
5.4	Results	90
5.4.1	Comparing DRYP to MODFLOW: quantitative evaluation . .	90
5.4.2	Evaluation of synthetic experiments	91
5.5	Conclusion	95
6	Characterising water partitioning at catchment scale: Walnut Gulch	
	Experimental Watershed	96
6.1	Introduction	96
6.2	Methods	97
6.2.1	Study site: Walnut Gulch Experimental Watershed-WGEW .	97
6.2.2	DRYP model setting	98
6.2.3	Forcing data, observation and model parameters	98
6.2.4	Model sensitivity analysis and calibration	104
6.2.5	Focused Recharge Evaluation	106
6.3	Results	107
6.3.1	Spatio-temporal visualisation of model process simulation at WGEW	107
6.3.2	Characterisation of the temporal variation in simulated variables	108
6.3.3	Water balance	113
6.4	Conclusions	114
7	Assessing the uncertainty of water partitioning at WGEW: a multi-	
	scale analysis	116
7.1	Introduction	116
7.2	Methods	117
7.2.1	Study Site	117
7.2.2	Model Scale Analysis	117
7.2.3	Model settings and parameterisation	117
7.2.4	Potential Evapotranspiration (PET), latent heat flux, and soil moisture observations	118
7.2.5	Model Calibration, sensitivity and uncertainty analysis	121
7.2.6	Uncertainty due to temporal resolution of rainfall	122

7.3	Results and Discussion	123
7.3.1	Sensitivity and uncertainty analysis	123
7.3.2	Impact of spatial and temporal scales on water partitioning	128
7.3.3	Water balance	132
7.3.4	Impact of temporal resolution of rainfall	133
7.4	Summary and Conclusions	134
8	Characterising water partitioning at regional scale: Upper Ewaso Ng'iro basin, Kenya	138
8.1	Introduction	138
8.2	Methods	139
8.2.1	Study area	139
8.2.2	Conceptual model of the Upper Ewaso Ng'iro basin	141
8.2.3	Model process selection	145
8.2.4	Model spatial resolution	145
8.2.5	Model parameterisation and settings	145
8.2.6	Boundary conditions	148
8.2.7	Model time step	148
8.2.8	Initial conditions	148
8.2.9	Forcing datasets	149
8.2.10	Evaluation datasets	150
8.2.11	Model Calibration, sensitivity and uncertainty analysis	152
8.3	Results	155
8.3.1	Uncertainty of precipitation datasets	155
8.3.2	Model calibration	156
8.3.3	Uncertainty of water partitioning	163
8.3.4	Sensitivity to spatial and temporal distribution of precipitation	179
8.3.5	Water balance of the Upper Ewaso Ng'iro basin	185
8.4	Conclusion	185
9	Conclusions & Outlook	189
9.1	Conclusions	189
9.1.1	Summary of the main outputs	194
9.2	Directions for future work	196
	References	199

A	Governing equations	233
A.1	Overland and channel flow	233
A.2	Variable saturated flow	234
A.3	Saturated flow	235
B	DRYP User Guide	236
B.1	Introduction	236
B.1.1	Running DRYP	236
B.2	Model parameter files	238
B.2.1	Forcing Data	238
B.2.2	Model Parameters	239
B.3	Model results	247
C	Python Code - DRYP	250

List of Figures

1.1	Schematic structure of the present thesis	6
2.1	Global map of dryland regions based on values of the Aridity Index (CGIAR-CSI, 2009; Zomer et al., 2007)	8
2.2	Main hydrological characteristics of arid and semi-arid regions compared to humid regions	9
3.1	Conceptual process model of interactions between ephemeral streams and an underlying homogeneous aquifer for (a) deep and (b) shallow water tables. Dashed lines represent the evolution of the inverted water table (IWT) and the water table mound at time t_i during and after a streamflow event. The hypothetical shape and size of the IWT depend on the magnitude, shape, and duration of the streamflow hydrograph and the antecedent conditions of saturation (inherited from the previous dry period), as well as hydraulic and soil moisture retention properties of the sediments.	21
3.2	a) Shape of the flow event is implemented as a specified head boundary condition at the stream base and sides. Before and after the flow event in the channel, the boundary condition switches to become ‘no flow’; b) cross section of the idealized transect considered in the numerical model, including a list of the boundary conditions and parameters of the base case model.	22

3.3	Variation of hydraulic head and vertical water flux at the centre of the stream, and saturation states for the cross section of the model domain for deep (a-e) and shallow (f-j) initial water table depths during the occurrence of a three-day streamflow event (see stage hydrograph plotted in Figure 3.4a) which otherwise uses the base case scenario parameters and geometry (see Fig. 3.2). Note that the vertical depth axes in (a-e) and (f-j) are different and zero depth corresponds to the base of the channel at an elevation of 57 m used in the calculation of hydraulic head.	30
3.4	Temporal variation modelled at one meter below the centre of stream (left side of model half-space) for the same scenarios of Fig. 3.3: a) infiltration rate, with stream stage shown for comparison on right-hand axis b) pressure head, and c) degree of saturation for deeper (20 m) and shallower (5 m) water tables (WT). Soil parameters correspond to the base case scenario (Fig. 3.2).	31
3.5	Variation of the total infiltrated volume into the streambed during one event against varying: a) dry period durations between events (specified as the number of days with zero streamflow) – with different data series representing a different water table depth, dashed line represents the dry period at which the rate of variation of infiltrated water becomes log - linear, and b) water table depths, with the variation due to different duration of dry periods indicated by the shaded area, dashed line represent the approximate apparent water table depth threshold.	33
3.6	Variation of streambed infiltration volume during a single event as a function of the duration of the streamflow event, the length of dry period between events (shaded range in the style of Figure 3.5), and water table depth.	34
3.7	Variation of infiltrated volume in relation to water table depth for changes in the hydraulic properties: a) hydraulic conductivity, shaded area indicates the range of variation for dry period duration between flow events of 10 to 360 days, b) water retention curve shape, and c) variation of storage capacity; part b) and c) correspond to a seven-day event occurring after a dry period of 360 days (see Table 3.1).	35

3.8	Variation of the infiltrated volume due to variations in the shape of the channel cross section for the flow event defined in the base case scenario. Plotted values correspond to water infiltrated only through the streambanks (red lines)	36
3.9	Channel width analysis: a) Variation from the base-case (BC) scenario of the infiltrated volume per unit length, for different stream channel widths (B) and water table depths; b) variation of the volume infiltrated per metre width through the streambed (solid lines) and streambank (dashed lines) in relation to the channel width for a shallow and deep water table (WTD).	37
4.1	Conceptual representation of groundwater - surface water interactions during a streamflow event: a) dry channel, no groundwater - surface water interaction; b) hydrograph of streamflow event at the upstream end (left) and streamflow event at the downstream end of the channel after transmission losses have occurred (right); c) groundwater - surface water interactions occurring during a streamflow event for deep water table conditions; d) groundwater - surface water interactions for shallow water table conditions. Arrows represent flow directions. . . .	43
4.2	Schematic of the model domain, geometry and boundary conditions corresponding to a typical alluvial aquifer found in arid and semi-arid regions. Not to scale.	46
4.3	Groundwater - surface water interactions for a deep initial water table condition (depth (z) = 20 m). The inverted water table is shown in transparency. $z=0$ corresponds to the elevation of the bottom of the channel. Hydraulic properties of the sediments correspond to the base case sandy loam texture (see Table 4.1). A streamflow influx was used with total magnitude $12 \text{ m}^3 \text{ s}^{-1}$ (see Sect. 4.3.7), the hydrograph and cumulative flux of which is shown in the uppermost panel. Times were selected to indicate an illustrative variety of states of groundwater - surface water interaction.	51

4.4	Temporal and spatial variation of the degree of saturation with depth for selected locations along the channel and longitudinal profile for specific times. Longitudinal saturation profiles along the centre of the channel correspond to deep (dashed red line, depth = 20 m) and shallow (solid blue line, depth = 10 m) initial water table conditions. Hydraulic properties of the sediments correspond to the base case sandy loam texture (see Table 4.1). The based case streamflow hydrograph of $12 \text{ m}^3 \text{ s}^{-1}$ (see Sect. 4.3.7) was used as for Fig 4.3. Times were selected to indicate an illustrative variety of states of groundwater - surface water interaction.	53
4.5	Spatial and temporal variation fluxes and states along the channel for both shallow (left) and deep (right) initial water tables: a) ratio between the total volume of water along the channel, over the entire simulation period and the total volume of water entering the channels as streamflow; b) instantaneous surface water stage profile (stream stages) at specific times indicated in the legend; c) instantaneous infiltration rates at specific times just below the streambed; and d) water table depths for specific times corresponding to panels c and d. Left-hand panels are for initially shallow, 10 m, water table conditions, and deeper, 20 m, initial water table depths in the right-hand panels. Hydraulic properties of the sediments correspond to the base case model with sandy loam texture (see Table 4.1). The streamflow event was generated using a pulse of event of $12 \text{ m}^3 \text{ s}^{-1}$ (see Sect. 4.3.7) - the hydrograph is shown in figure 4.3. Times were selected to indicate an illustrative variety of states of groundwater - surface water interaction.	56
4.6	Temporal and spatial variation of infiltration rates below the stream in relation to the water table depth: a) the ratio between the total infiltrated volume and total input volume in relation to water table depth, b) total cumulative infiltration along the channel, c) temporal variation of total cumulative infiltration, and d) ratio between the cumulative, in the upward direction, total infiltrated volume at each cell along the channel and the total infiltrated volume of the whole channel. Hydraulic properties of the sediments correspond to the baseline sandy loam texture (see Table 4.1). The same streamflow event was generated using a pulse of event of $12 \text{ m}^3 \text{ s}^{-1}$ (see Sect. 4.3.7) as shown in Fig 4.3	58

4.7	Ratio between infiltrated volume and total input streamflow volume in relation to the initial water table depth for different hydraulic properties specified in Table 4.1. Streamflow event was generated using the base case pulse event of $12 \text{ m}^3 \text{ s}^{-1}$ (see Sect. 4.3.7)	60
4.8	Temporal and spatial variation of infiltration rates below the stream in relation to the streamflow duration for shallow (10 m) and deep (20 m) water table depth conditions: a) total cumulative infiltration along the channel, b) ratio between the total cumulative infiltration along the channel and the total infiltrated volume, and c) temporal variation of total cumulative infiltration. Hydraulic properties of the sediments correspond to sandy loam texture (see Table 4.1). Streamflow event was generated using a pulse of event of $12 \text{ m}^3 \text{ s}^{-1}$ (see Sect. 4.3.7)	62
4.9	Global distribution of perennial and non-perennial streams (based on Lehner and Grill (2013); Linke et al. (2019). Dryland and humid regions are based on values of the Aridity Index (CGIAR-CSI, 2009; Zomer et al., 2007)	65
4.10	Water table depth distribution and accumulated water table depth for dryland regions (based on Fan et al. (2013))	66
5.1	Schematic representation of DRYP showing a) the main hydrological processes controlling water partitioning in dryland regions; b) distributed datasets needed to derive input parameters; c) vertical and horizontal discretisation and representation of topographically-driven surface runoff, vertical flow in the unsaturated zone, and hydraulic gradient driven groundwater flow in the saturated component; d) model structure and potential processes within a single grid cell for the surface component (see Sect. 5.2.2), unsaturated zone (see Sect. 5.2.3) and saturated zone (see Sect. 5.2.4). Arrows represent flow directions and red lines represent anthropogenic fluxes.	73
5.2	Schematic illustration of the unsaturated component. The right panel represents the variation of the ratio of potential to actual evapotranspiration in relation to the water content of the soil. Please refer to Sect. 2.2 and 2.3 for a detailed explanation of the terms shown here.	80

5.3	Schematic representation of a) UZ-SZ interactions: 1a) indicates no UZ-SZ interaction whereas 2a) indicates UZ-SZ interaction (soil depth, Droot, is reduced to Duz); b) SW-GW interactions in stream cells: boundary conditions change from no-flow to head dependent flux conditions once the stream bed or ground surface is intersected by the water table. Upper part of panel b) shows the numerical implementation of SW-GW interactions in a stream cell.	85
5.4	Synthetic tilted-V catchment and flow boundary conditions specified for model simulations.	90
5.5	a) Simulated head along the aquifer for different time steps estimated by DRYP (solid lines) and MODFLOW (crosses and dashed lines), and b) temporal variation of the mass balance error for DRYP.	91
5.6	Temporal variation of a) precipitation (black line) and evapotranspiration (grey line), b) water content of the unsaturated zone, c) groundwater recharge, d) runoff/discharge, and e) water table elevations. Right panels represent zoomed-in sections of the shaded areas of the left panels. Solid lines represent the variation at the catchment outlet, whereas dashed lines represent the temporal variation in the stream at 4 km from the catchment outlet. For panels b-e, blue lines represent the ‘infiltration-discharge’ scenario, green lines represent the ‘Infiltration-evapotranspiration-discharge’ scenario, and red lines represent ‘Infiltration-runoff-evapotranspiration-discharge’ scenario.	93
5.7	Long term simulation of scenario “Infiltration-discharge”, steady state is reached after 16,400 hours.	94
5.8	Cumulative volume of main components of the water balance for the simulated scenarios: a) Infiltration – discharge, b) infiltration - evapotranspiration - discharge, and c) infiltration-infiltration excess-evapotranspiration-discharge. P is the precipitation, R is recharge, Q is discharge at the catchment outlet, AET is actual evapotranspiration, GWS is the change in groundwater storage, and Err is the water balance error of the simulation.	94
6.1	a) Geographic location of Walnut Gulch Experimental Watershed and location of monitoring stations, b) topography, c) soil texture, d) Soil land cover, and e) geology	99

6.1	a) Geographic location of Walnut Gulch Experimental Watershed and location of monitoring stations, b) topography, c) soil texture, d) Soil land cover, and e) geology (cont.)	100
6.2	Conceptual model for evaluation of estimated focused recharge, and a diagram for model setup	107
6.3	Spatio-temporal visualisation of model process simulation at WGEW, a) rainfall event, b) soil moisture previous to the rainfall event, c) ephemeral stream for the rainfall event, and c) soil moisture after the rainfall event; x and y axes distance units are in metres.	109
6.3	Spatio-temporal visualisation of model process simulation at WGEW, a) rainfall event, b) soil moisture previous to the rainfall event, c) ephemeral stream for the rainfall event, and c) soil moisture after the rainfall event; x and y axes distance units are in metres (cont.). . . .	110
6.4	Comparison between observed and simulated values of monthly temporal variation (left) and monthly distribution (right) of a) monthly precipitation (left axes) and yearly precipitation (right axes), b) soil moisture at the COSMOS Kendall location, c) actual evapotranspiration at Kendall, d) streamflow at flume F06, e) streamflow at flume F02, and f) streamflow at flume F01. See Fig. 5.4 for station locations.	112
6.5	Comparison of simulated and observed values of water table elevation estimated by the 2D numerical simulation. The modelled recharge obtained from DRYP (grey) was used as model input for the 2D model	113
6.6	Average fluxes of different components of the water budget of WGEW for the simulated period, 01/01/2007 to 01/01/2018. Blue arrows show input fluxes, green arrows represent water leaving the catchment, orange arrows represent internal surface and unsaturated zone fluxes, and yellow arrows represent water moving to the saturated zone (not modelled), values in brackets represent the percentage estimated in relation to the precipitation.	114
7.1	Topography and soil hydraulic characteristics for the three different grid scales (300m, 1km, 5km). AWC = available water content. Values in parenthesis represent the grid size, solid black line represent the WGEW, and solid blue lines represent streams.	119

7.1	Topography and soil hydraulic characteristics for the three different grid scales (300m, 1km, 5km). AWC = available water content. Values in parenthesis represent the grid size, solid black line represent the WGEW, and solid blue lines represent streams.	120
7.2	Indexes estimated for the best models selected according to the combined performance metric 'p' based on the evaluation of flumes F01, F02 and F05, and soil moisture and AET at Kendall. a) Estimated 'p' against the number of valid models resulted from the Monte Carlo analysis for different grid size, time-step, and infiltration approach. b) NSE for the soil moisture (SM) estimated at the Kendall location against NSE of the evapotranspiration at Kendall location. c) R2 of flumes F06 against F01. Part d, e and f) represent the NSE against the PBIAS for the three flumes located along the main channel, flume F01, F02 and F06. Results at 5km grid size were evaluated only at flume F01. Models are represented as P = Philip's, S = Schaake, G = upscaled Green and Ampt, and M = modified Green and Ampt. Models at 5-km grid size were not used to evaluate evapotranspiration	126
7.3	Parameter distributions for acceptable model simulations based on the evaluation at flumes F01, F02 and F06, and soil moisture and AET at Kendall. Results at the 5-km grid size were evaluated only at flume F01	127
7.4	Indices estimated for the best models selected according to the likelihood measure 'p' based on the evaluation of flume F01, and soil moisture and AET at Kendall. a) Estimated 'p' against the number of valid models resulting from the Monte Carlo analysis for different grid sizes, time steps, and infiltration approaches. b) NSE for soil moisture estimated against NSE of the evapotranspiration at Kendall. c) R2 of flumes F06 against F01. Part d, e and f) represent the NSE against the PBIAS for the three flumes located along the main channel, flume F01, F02 and F06. Results at the 5-km grid size were evaluated only at flume F01. Models are represented as P = Philips, S = Schaake, G = upscaled Green and Ampt, and M = modified Green and Ampt. Models at the 5-km grid size do not consider evapotranspiration in the evaluation	129
7.5	Parameter distributions for acceptable model simulations based on evaluation at flume F01 and soil moisture and AET at Kendall. Results for the 5-km grid size were evaluated only at flume F01.	129

7.6	Flux distribution as a percentage of precipitation for behavioural models based on the evaluation of flumes F01, F02 and F06, and soil moisture and AET at Kendall. Results at the 5-km grid size were evaluated only at flume F01	131
7.7	Flux distribution as a percentage of rainfall for behavioural model simulations based on the evaluation at flume F01, and soil moisture and AET at Kendall. Results at the 5-km grid size were evaluated only at flume F01	132
7.8	Percentage of rainfall contributing to the modelled components of the water budget at WGEW (see Fig. 5.1 for model components). Results correspond to the best model structure, the modified Green and Ampt at 300m grid size and 60min time steps. Solid red lines represent the behavioural models for the 3-flume based criteria, green lines represent models for 1-flume criteria, and black solid lines represent all simulations. Arrows outside the catchment represent fluxes entering and leaving the model domain.	133
7.9	Influence of the temporal aggregation of rainfall on water partitioning for the best model: modified Green and Ampt. Left panels show the distribution for the whole simulated period and right panels show the distribution for monthly values for the simulated period. a) represents the actual evapotranspiration at Kendall (see fig. 6.1), b) represents the soil moisture at Kendall (see fig. 6.1), and c) represents the runoff at flume F01 near the catchment outlet (see fig. 6.1)	135
8.1	a) Geographical location of the Upper Ewaso Ng'iro basin, b) geological map, c) soil texture, and d) soil land use.	142
8.1	a) Geographical location of the Upper Ewaso Ng'iro basin, b) geological map, c) soil texture, and d) soil land use (cont.).	143
8.2	Conceptual schematic of the hydrology of the Upper Ewaso Ng'iro basin	144
8.3	Spatial distribution of model parameters: a) river length, b) available water content of the unsaturated zone (Leenaars et al., 2018), c) rooting depth (Leenaars et al., 2018), soil saturated hydraulic conductivity (Dai et al., 2019b), aquifer thickness (Pelletier et al., 2016), and aquifer saturated hydraulic conductivity (Gleeson et al., 2014). Vertical and horizontal axes are in meters and represent the North and East coordinates, respectively.	147

8.4	Scenarios specified for evaluation of the uncertainty of precipitation and model parameters: a) evaluates the uncertainty of model parameters in water partitioning, and b) evaluates the sensitivity of water partitioning to the spatial and temporal characteristic of precipitation.	154
8.5	Climatic zones in the Upper Ewaso Ng'iro basin estimated using MSWEP and IMERG precipitation datasets and hPET dataset for potential evapotranspiration. Climatic zones are based on the Aridity Index (AI) (see Sect. 2.2)	155
8.6	Variation of MSWEP and IMERG precipitation datasets for the Upper Ewaso Ng'iro basin : a) mean annual precipitation totals by climatic region; b) distribution of AI over the basin (top) and mean annual precipitation according to AI (bottom); c) distribution of surface elevation (top), mean annual precipitation totals according to the surface elevation (bottom right), and distribution of mean annual precipitation rates over the basin (right); d) MSWEP, mean annual precipitation; and e) IMERG, mean annual precipitation. Vertical and horizontal axes of panels d) and e) are in meters.	157
8.7	Monthly temporal variation over the whole basin for MSWEP and IMERG datasets of: a) precipitation, b) simulated actual evapotranspiration, c) simulated soil moisture, plotted at log scale in order to compare with ESA product, d) simulated diffuse and focused recharge, e) simulated and observed discharge at the catchment outlet (Archer's Post, see Fig. 8.1), and f) change in total water storage anomalies for model output and the GRACE dataset (solid lines), and monthly precipitation anomalies estimated relative to the mean value over the evaluation period (dashed lines).	159
8.8	Scatter plot between: a) simulated actual evapotranspiration and the MOD16A dataset, b) scaled soil moisture of simulated values and the ESA-CCI-SM dataset, and c) simulated change in total water storage anomalies and the GRACE dataset. Simulated values correspond to MSWEP and IMERG precipitation datasets. Comparison is performed at monthly time steps. The best simulation was considered for comparison.	160

8.9	Correlation between simulated actual evapotranspiration and MOD16A datasets for both MSWEP and IMERG forcing precipitation datasets, and for the best performing parameter sets. Contour lines represent surface elevation in meters above sea level. Vertical and horizontal axes are in meters.	161
8.10	Correlation between simulated soil moisture and the ESA combined (active-passive) product for both MSWEP and IMERG precipitation datasets, and for the best performing parameter sets. Contour lines represent surface elevation in meters above sea level. Vertical and horizontal axes are in meters.	161
8.11	Distribution of parameters of valid simulations (bars), and p-values (eq. 8.4) estimated for valid simulations (dots) for both models, MSWEP and IMERG. Grey bars indicate that IMERG model results are similar than MSWEP.	163
8.12	Variation of actual evapotranspiration for the Upper Ewaso Ng'iro basin estimated using MSWEP and IMERG precipitation datasets: a) distribution of AI over the basin (top) and mean annual actual evapotranspiration according to AI (bottom); b) annual precipitation rate according to climatic region (top) and mean annual actual evapotranspiration according to AI (bottom); and c) evaporation index (AET/P) against dryness index (PET/P), Budyko aridity index (Budyko, 1961)	165
8.13	Mean annual actual evapotranspiration and standard deviation estimated from the ensemble of valid simulation using both IMERG and MSWEP precipitation datasets for the Upper Ewaso Ng'iro basin. Contour lines represent surface elevation in meters above sea level. Vertical and horizontal axes are in meters.	166
8.13	Mean annual actual evapotranspiration and standard deviation estimated from the ensemble of valid simulation using both IMERG and MSWEP precipitation datasets for the Upper Ewaso Ng'iro basin. Contour lines represent surface elevation in meters above sea level. Vertical and horizontal axes are in meters (cont.).	167
8.14	Mean annual relative soil moisture and standard deviation estimated from the ensemble of valid simulation using both IMERG and MSWEP precipitation datasets for the Upper Ewaso Ng'iro basin. Contour lines represent surface elevation in meters above sea level. Vertical and horizontal axes are in meters.	169

8.14	Mean annual relative soil moisture and standard deviation estimated from the ensemble of valid simulation using both IMERG and MSWEP precipitation datasets for the Upper Ewaso Ng'iro basin. Contour lines represent surface elevation in meters above sea level. Vertical and horizontal axes are in meters (cont.).	170
8.15	Normalised cumulative diffuse (left) and focused (right) recharge in relation to precipitation (solid-lines), and probability of exceedance probability of monthly precipitation events (dashed-lines)	171
8.16	Mean annual diffuse recharge and standard deviation estimated from the ensemble of valid simulation using both IMERG and MSWEP precipitation datasets for the Upper Ewaso Ng'iro basin. Contour lines represent surface elevation in meters above sea level. Vertical and horizontal axes are in meters.	172
8.16	Mean annual diffuse recharge and standard deviation estimated from the ensemble of valid simulation using both IMERG and MSWEP precipitation datasets for the Upper Ewaso Ng'iro basin. Contour lines represent surface elevation in meters above sea level. Vertical and horizontal axes are in meters (cont.).	173
8.17	Mean annual focused recharge and standard deviation estimated from the ensemble of valid simulation using both IMERG and MSWEP precipitation datasets for the Upper Ewaso Ng'iro basin. Vertical and horizontal axes are in meters.	175
8.17	Mean annual focused recharge and standard deviation estimated from the ensemble of valid simulation using both IMERG and MSWEP precipitation datasets for the Upper Ewaso Ng'iro basin. Vertical and horizontal axes are in meters (cont.).	176
8.18	Variation of focused and diffuse recharge for the Upper Ewaso Ng'iro basin estimated using MSWEP and IMERG precipitation datasets: a) distribution of AI over the basin (top) and mean annual focused recharge according to AI (bottom); b) distribution of AI over the basin (top) and mean annual diffuse recharge according to AI (bottom); c) focused recharge against surface elevation, d) diffuse recharge against surface elevation, e) annual precipitation according to climatic region (top) and mean annual focused recharge according to AI (bottom); and f) annual precipitation according to climatic region (top) and mean yearly diffuse recharge according to AI (bottom)	178

8.19	Ratio of cumulative focused recharge to cumulative diffuse recharge against aridity index	179
8.20	Mean annual runoff and standard deviation estimated from the ensemble of valid simulation using both IMERG and MSWEP precipitation datasets for the Upper Ewaso Ng'iro basin. Contour lines represent surface elevation in meters above sea level. Vertical and horizontal axes are in meters.	180
8.20	Mean annual runoff and standard deviation estimated from the ensemble of valid simulation using both IMERG and MSWEP precipitation datasets for the Upper Ewaso Ng'iro basin. Contour lines represent surface elevation in meters above sea level. Vertical and horizontal axes are in meters (cont.).	181
8.21	Mean annual exchange surface-groundwater fluxes and its standard deviation estimated from the ensemble of valid simulation using both IMERG and MSWEP precipitation datasets for the Upper Ewaso Ng'iro basin. Positive fluxes indicates groundwater discharging into the stream and negative fluxes indicate transmission losses. Contour lines represent surface elevation in meters above sea level.	182
8.21	Mean annual exchange surface-groundwater fluxes and its standard deviation estimated from the ensemble of valid simulation using both IMERG and MSWEP precipitation datasets for the Upper Ewaso Ng'iro basin. Positive fluxes indicates groundwater discharging into the stream and negative fluxes indicate transmission losses. Contour lines represent surface elevation in meters above sea level (cont.).	183
8.22	Distribution of percentages of main fluxes of the water balance in relation to the input precipitation for the Upper Ewaso Ng'iro basin. Estimated values correspond to valid models for the scenarios specified in Section 8.2.11 (Fig. 8.4) using MSWEP and IMERG datasets. Black lines in evapotranspiration and discharge corresponds to MOD16A AET validation dataset and observed streamflow at Archer's Post station (see Fig. 8.1), respectively.	186
B.1	Location of the GW_1D example	237

List of Tables

3.1	Model scenarios and number of events per scenario. Parameters for the base case scenario are $\alpha = 7.5 \text{ m}^{-1}$; $K = 1.45 \text{ m d}^{-1}$; $n = 1.89$. . .	27
4.1	Aquifer hydraulic properties considered for the analysis (Rawls et al., 1982)	49
4.2	Model scenarios and number of simulations	49
4.3	Distribution of water table depth below streams in dryland regions (based on Fan et al. (2013)), all values represent percentages.	65
5.1	Model parameters for different processes considered in the model, some required parameters depend on the infiltration approach ('Inf. Method'). Default values are specified in brackets. For soil hydraulic properties, default values correspond to a sandy loam soil texture (Clapp and Hornberger, 1978; Rawls et al., 1982)	87
6.1	Soil hydraulic parameters for general textural classes, based on Rawls et al. (1982) and Clapp and Hornberger (1978): n is the porosity, b is the pore size distribution parameter, and ψ is the maximum soil matric potential	101
7.1	Prior parameter range for each component and infiltration approach considered in the Monte Carlo analysis; parameters starting with 'k' mean that it is a factor of the model parameter. Infiltration approaches are specified as P for Philip's model, G for Upscaled Green and Ampt, S for Schaake model, and M for Modified Green and Ampt.	123
8.1	Prior parameter range for each component considered in the Monte Carlo analysis; parameters starting with 'k' mean that it is computed as a factor of the model parameter	153
8.2	Model parameter factors of the best performing model after calibration for IMERG and MSWEP precipitation forced models	162

8.3	Model performance and water partitioning estimated using both MSWEP and IMERG precipitation datasets for the best models. Parameters for the best models were obtained after calibration using each dataset. Values in brackets represent percentage in relation to precipitation . .	184
B.1	Code and Name of variables for input datasets of anthropogenic fluxes	243
B.2	Suffix of model result files stored by DRYP	248
B.3	Model variable name's and codes stored for point result files, for filename see table B.2	249

Chapter 1

Introduction

1.1 Background and Motivation

Drylands are regions characterised by much higher rates of potential evapotranspiration than precipitation, and cover 40 % of the global land surface (Cherlet et al., 2018; Reynolds et al., 2007a). They support a population of around 2.5 billion people (Cherlet et al., 2018; Dai, 2012; Feng and Fu, 2013; Huang et al., 2015; Mortimore, 2009; Reynolds et al., 2007b; Trenberth et al., 2013; White and Nackoney, 2003), with most of this population living in lower income countries where water resources are scarce and tied to rural livelihoods (Cherlet et al., 2018). Dryland environments pose many challenges for water resources allocation for humans and water availability to ecology, yet there are currently major limitations in our ability to assess the water balance in drylands, especially under a changing climate (Green et al., 2011).

Both the availability and quality of global water resources have been under increasing pressure in recent decades due to rising population, increasing urbanisation, and climate change. It has been estimated that by 2030 the global population will rise to around 8.3 billion and over 9 billion by 2100 (UNEP and of Economic and Social Affairs, 2017). A higher population will put more pressure on our planet by increasing the demand for more food, biofuel and urban services (Foley et al., 2011; Rulli et al., 2013). This has potential for increasing degradation of water, land, biodiversity and climatic conditions (Foley et al., 2011) as more resources will be necessary to sustain human activities (Mekonnen and Hoekstra, 2012; Nijdam et al., 2012; SERI, 2013). This may exacerbate existing problems in regions with already over-exploited water resources (Bredehoeft, 1997, 2002; Döll et al., 2012; Jasechko et al., 2017; Sophocleous, 1997; Sophocleous and Devlin, 2004) and may be particularly acute in dryland regions (Alley, 2007; Huang et al., 2017).

Water availability is highly dependent on the spatio-temporal variability of the balance between precipitation and evaporative demand (Aryal et al., 2020; Wheeler et al., 2007; Zoccatelli et al., 2019), yet most precipitation arriving in dryland regions is lost to evapotranspiration. This, in turn, generally results in less surface water available, low soil water content and low groundwater recharge. Spatial variability is also characterised by the concentration of short precipitation events of high intensity over small areas (Goodrich et al., 1997; Pilgrim et al., 1988; Wheeler et al., 2010; Zoccatelli et al., 2019) which leads to the development of ephemeral streams. The loss of water from the streambed of these ephemeral streams, known as transmission losses, is thought to be the main source of groundwater recharge in dryland regions (Abdulrazzak and Morel-Seytoux, 1983; Wheeler et al., 2010). Additionally, precipitation varies significantly through time, over the year or even decades, punctuated by drought periods in some dryland regions (Massuel et al., 2011; Wheeler et al., 1991). These characteristics result in a highly dynamic hydrological system prone to flash flooding, and also to water scarcity and food insecurity, societal risks that are exacerbated by climate change, population growth and dryland expansion (Cuthbert et al., 2019a; Giordano, 2009; Gleeson et al., 2012; Huang et al., 2017, 2015; Reynolds et al., 2007b; Schlaepfer et al., 2017; Siebert et al., 2010; Spinoni et al., 2015; Taylor et al., 2012; Wang et al., 2017b).

Given the limited surface water availability, people in drylands mostly rely on groundwater resources as their primary source of freshwater (Cuthbert et al., 2017; Dai, 2012; Feng and Fu, 2013; Huang et al., 2015; IPCC, 2012; Trenberth et al., 2013). However, due to the widespread ability to access this generally high quality water and relative low sensitivity of groundwater aquifers to drought conditions (Cuthbert et al., 2019b; MacDonald et al., 2012; Taylor et al., 2012; Villeneuve et al., 2015), groundwater withdrawal has considerably risen along with demand for freshwater over recent decades (Altchenko and Villholth, 2015; Gleeson et al., 2012; Jasechko et al., 2017; Wada et al., 2010). This increased abstraction has threatened not only the long-term reliability of groundwater resources, but also its quality, both which can be exacerbated due to climate-related changes and anthropogenic pressures (Jasechko et al., 2017; Padrón et al., 2020; Taylor et al., 2012). Despite the key role of groundwater in water availability in drylands environments, there is still high uncertainty about the impacts of climate change on groundwater resources (Acworth et al., 2021; Ferguson et al., 2020; Taylor et al., 2012).

It is therefore essential to understand and anticipate changes to water partitioning in drylands, i.e. how rainfall is partitioned between infiltration, runoff, and evapotran-

piration, thus affecting water storage in groundwater, soil moisture and streams. This will enable more robust identification, estimation and prediction of the potential impact on these components of the water balance arising due to climate change (Green et al., 2011). Enhancing the understanding of water partitioning and consequently recharge processes in arid and semi-arid regions is a key research gap required to develop sustained management of groundwater resources (Alley and Leake, 2004; Bredehoeft, 1997, 2002; Devlin and Sophocleous, 2005; Kalf and Woolley, 2005; Loáiciga, 2017; Maimone, 2004; Sophocleous, 1997; Sophocleous and Devlin, 2004).

However, assessing water partitioning in dryland regions is difficult due to a variety of challenges such as lack of data (El Khalki et al., 2020; Pilgrim et al., 1988; Shanafield et al., 2021), lack of understanding of the interactions between key processes that control the water balance, such as recharge from ephemeral streams, (Cuthbert et al., 2019b; Taylor et al., 2012), and the lack of efficient numerical tools to evaluate all components of the water balance (Huang et al., 2017) as follows.

Historical data is essential for understanding the relationships between water balance components, yet drylands pose a severe paucity of data not only due to the lack of research studies but also due to the high spatial and temporal variability of hydrological processes that makes it difficult to collect data (i.e. ephemeral flows (Osborn et al., 1979)) (Pilgrim et al., 1988; Taylor et al., 2013; Zimmer et al., 2020). This, in combination with the lack of efficient tools (such as parsimonious modelling approaches), has limited understanding of the functioning and interactions of the water balance components within drylands regions.

Enhancing understanding and quantification of water partitioning in dryland regions requires the development of new techniques that can deal with the spatial and temporal variability of the components of the hydrological processes (Cuthbert et al., 2019a,b; Rassam et al., 2013), as well as the complexity of anthropogenic interactions with water resources (Gorelick and Zheng, 2015). In addition to the high spatial and temporal variability of hydrological processes, modelling water partitioning in dryland regions is challenging due to i) the poor understanding of transmission losses and recharge from ephemeral streams, ii) limited availability of data for model calibration and validation in most dryland environments, and iii) the lack of numerically efficient tools to overcome the computational demand that current hydrological models face.

In this context, hydrological models provide important insights into the translation of climate information to water partitioning at or below the land surface. However, current hydrological models, mainly developed for humid regions, omit several

key hydrological processes that characterise the hydrology of arid and semi-arid regions (Huang et al., 2017). The lack of simple, computationally efficient hydrological models for drylands undermines efforts to anticipate and plan for climatic and anthropogenic changes to water storage and fluxes in catchments, with implications for water resources for ecosystems and society (Huang et al., 2017; Taylor et al., 2012).

1.2 Scope and Objectives

This PhD thesis aims to enhance understanding and quantification of water partitioning and flow pathways in dryland regions. To address shortcomings in existing approaches, I set the following specific objectives:

Objective 1: To enhance understanding of key processes that control the water partitioning of dryland regions, particularly recharge from ephemeral streams, which has been poorly characterised due to the lack of field studies as well as the paucity of generalisable data;

Objective 2: To develop a simple, parsimonious approach to quantify water partitioning in dryland regions;

Objective 3: To evaluate the sensitivity of water partitioning at the relevant spatial and temporal scales of the processes;

Objective 4: To improve estimation of water balance partitioning in dryland basins with limited data; and

Objective 5: To evaluate the sensitivity of water partitioning to the forcing climatic conditions.

To achieve these objectives, in this thesis I have addressed **Objective 1** using physics-based models for characterising the factors that control the infiltration of water through the streambed of ephemeral streams. A physics-based model, if well understood, can give specific details of the sequenced infiltration process. Thus, I designed a set of synthetic experiments that seek to understand the main factors influencing the distribution and magnitude of infiltration rates. To have a better understanding of the infiltration processes across the landscape, the analysis is performed at both transect scale and reach scale.

To address **Objective 2**, a novel and numerically efficient, processes-based, distributed hydrological model is developed. The model considers the hydrological processes deemed to be important to characterise and quantify water partitioning in dryland regions. Knowledge gained from the transect and reach scale analyses is incorporated into the new catchment model.

To address **Objective 3**, the performance of the newly developed model is tested across different scales. Spatial and temporal variation of hydrological processes and their influence on water partitioning is assessed by considering different spatial and temporal aggregation and model structures. The model performance is evaluated using available data from one of the most extensively monitored watersheds of the world, the semi-arid Walnut Gulch Experimental Watershed (WGEW), Arizona, USA.

To address **Objective 4** and **Objective 5**, the developed model is used to characterise the water partitioning at the data-poor Upper Ewaso Ng'iro basin, Kenya. The lack of data is addressed by using global and regional datasets for model parameterisation as well as forcing data. To assess the sensitivity of water partitioning to forcing data, two global datasets of precipitation were used.

1.3 Thesis outline

The present thesis is divided into eight chapters (Fig. 1.1):

Chapter 1 provides the introduction, context, and objectives of the present research, as well as the structure of the thesis.

Chapter 2 gives an overview of the main hydrological processes that control the water partitioning and characterises the main limitations of current numerical models that restrict their use in dryland environments.

Chapter 3 and **4** provides an improved spatial and temporal characterisation of focused recharge as one of the most uncertain components of the water partitioning in dryland regions. **Chapter 3** presents the characterisation of focused recharge at a transect scale, whereas **Chapter 4** complement the characterisation by extending the transect analysis to the reach-scale.

Chapter 5 introduces DRYP, a parsimonious model I developed here for quantifying water partitioning in dryland regions. An evaluation of the model and its capability is also provided in this chapter.

Chapter 6, 7 and **8** present the use of DRYP for characterising water partitioning in two study sites: Walnut Gulch in Arizona, US, and Ewaso Ng'iro basin at Kenya. **Chapter 6** is focused on the evaluation of water partition of Walnut Gulch, whereas **Chapter 7** is focused on the sensitivity of water partition to the temporal and spatial scale of the model process description of DRYP. **Chapter 8** characterises the water partitioning of the semi-arid Ewaso Ng'iro basin, and evaluates the impact of the uncertainty in driving climatological characteristics on the quantification of water partitioning.

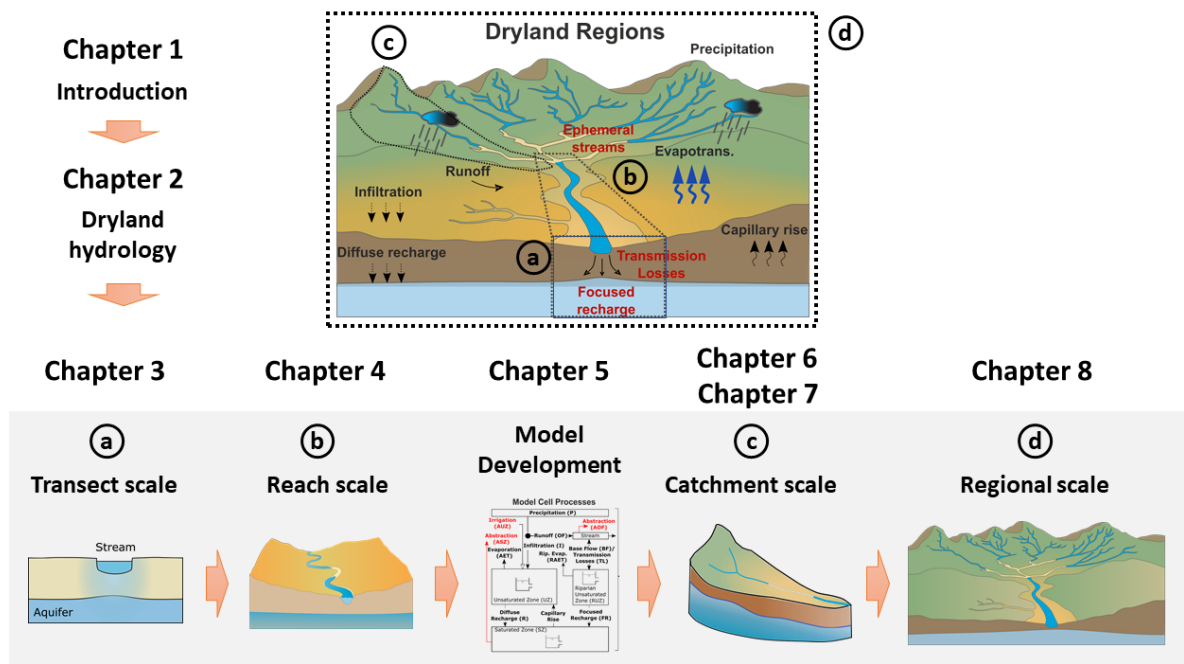


Figure 1.1: Schematic structure of the present thesis

Finally, **Chapter 9** presents a summary and general conclusions of the presented research, as well as recommendations for future research.

Chapter 2

Overview of Dryland Hydrology and Modelling

2.1 Introduction

This chapter provides a general overview of the main hydrological characteristics of dryland regions and also highlights the main limitations of current hydrological models that restrict their use within dryland environments. This chapter begins by introducing the definition and global distribution of dryland regions, and then provide a characterisation of key hydrological processes controlling the water partitioning. Processes such as infiltration, evapotranspiration, runoff, transmission losses, and focused and diffuse recharge are described. Then, an overview of key issues of current numerical hydrological models that limit their utility for drylands have been presented. Finally, a summary of the main concepts have been provided at the end of the chapter.

2.2 Definition of dryland regions

Dryland regions can be defined based on climatic, hydrological, geomorphological, and land cover characteristics (Budyko, 1961; Chen and Sivapalan, 2020; Dai, 2011; Hulme et al., 1992; McKee et al., 1993; Palmer, 1965; Stadler, 1987; Vicente-Serrano et al., 2010). For the purpose of this thesis, drylands have been defined according to the commonly employed ratio between annual precipitation (P) and annual potential evapotranspiration (PET), known as the *Aridity Index (AI)* (Cherlet et al., 2018; D’Odorico and Porporato, 2006; Lerner et al., 1990; Simmers, 2003):

$$AI = \frac{P}{PET} \tag{2.1}$$

Based on *AI*, four climate classes have been specified for drylands (UNEP and of Economic and Social Affairs, 2017): (i) Hyper Arid, with values of *AI* below 0.03; (ii) Arid, with values from 0.03 to 0.2; (ii) Semi-Arid, with values from 0.2 to 0.5; and (iii) Dry sub-humid, with values from 0.5 to 0.65. Regions with values above 0.65 are considered Humid regions.

Based on *AI*, drylands are globally distributed, with 64 % of the global area located in Africa and Asia, 23 % in Australia and North America, and Europe and South America representing 5 and 8 %, respectively. The large extent of these regions also corresponds to their high population; almost 37 % of the world’s population live in dryland regions with a great proportion of located in Asia and Africa (Cherlet et al., 2018).

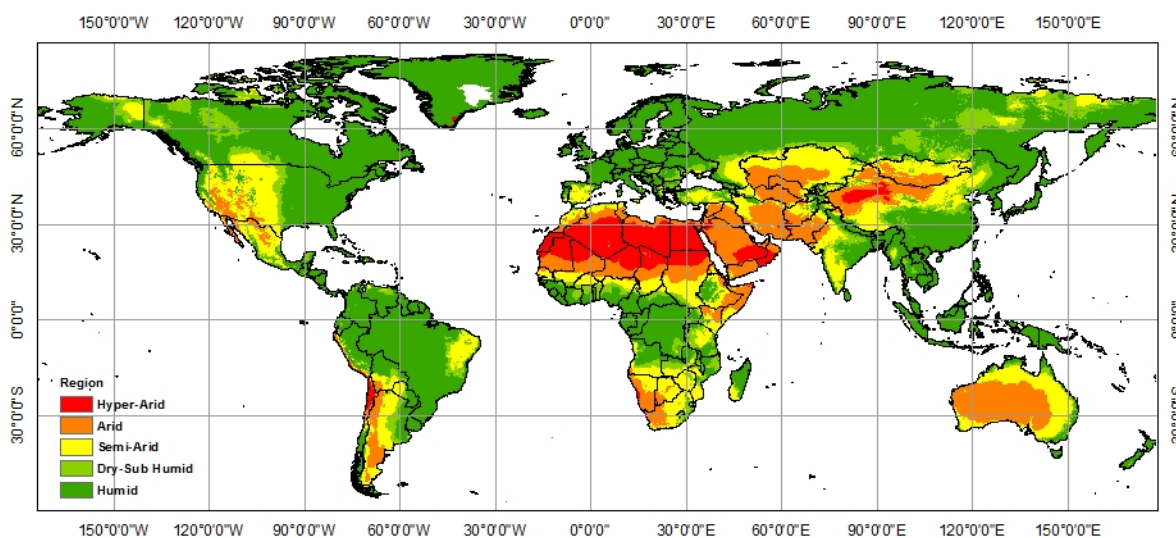


Figure 2.1: Global map of dryland regions based on values of the Aridity Index (CGIAR-CSI, 2009; Zomer et al., 2007)

2.3 Main hydrological processes in dryland regions

In contrast to humid regions, where the amount of annual precipitation generally exceeds annual rates of potential evapotranspiration, dryland regions exhibit key differences in the dominant hydrological processes that can greatly impact the water partitioning of arriving rainfall (see Fig. 2.2).

Drylands characterised by limited availability of seasonal or annual precipitation (Pilgrim et al., 1988; Wheeler et al., 2007). Although scarce, precipitation is delivered in highly intense short precipitation events with great spatial variability, which results in the development of short-lived ephemeral streams and flash floods (Abdulrazzak,

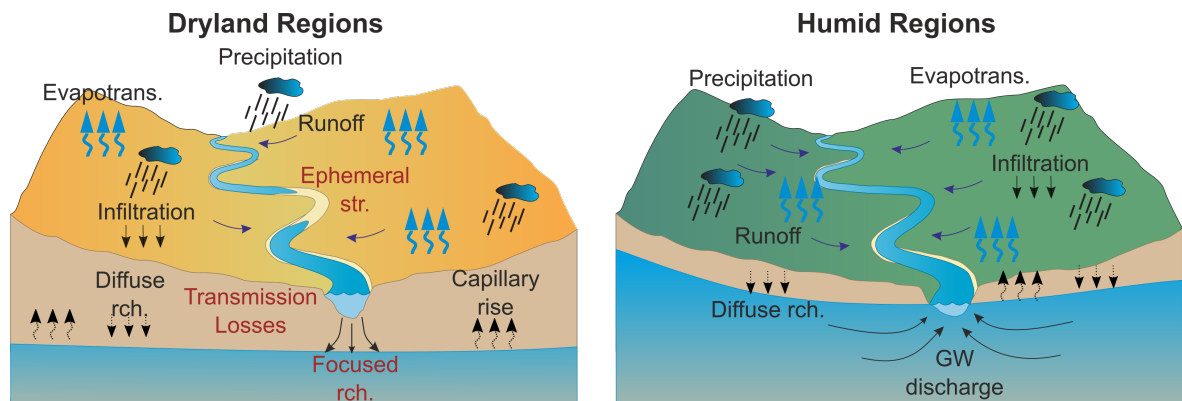


Figure 2.2: Main hydrological characteristics of arid and semi-arid regions compared to humid regions

1995; Aryal et al., 2020; Goodrich et al., 1997; Pilgrim et al., 1988; Wheeler et al., 2007; Zoccatelli et al., 2019). Air temperatures are high which, in combination with lower humidity, results in environments with a high atmospheric demand of water (Simmers, 2003; Wheeler et al., 2007). This can affect plant water consumption and soil water availability due to the high evapotranspiration rates (Huang et al., 2017; Huxman et al., 2005; Kurc and Small, 2004; Liu et al., 1995).

Local rates of infiltration of precipitation into soils vary dramatically mainly due to soil hydraulic properties, temporal variability of precipitation, land cover and surface crusting, and residual water content of the soil prior to the rainfall event (Pilgrim et al., 1988). Shallow soil depths and low soil water retention capacity influence the amount of water that can be stored in the soil. Low water retention capacity is attributed to limited soil organic matter (Pilgrim et al., 1988). Low infiltration rates combined with low precipitation result in less water available for plants. Soil profiles in drylands are often poorly developed which, in combination with the high variability in climatic conditions, results in limited capacity to sustain vegetation and/or produces high vegetation water stress (Sabathier et al., 2021; Warter et al., 2020). Vegetation is limited and restricted to a small variety of species (Deblauwe et al., 2008; Schenk and Jackson, 2002), that may be drastically reduced or even disappear completely during dry periods (Warter et al., 2020).

The high variability of precipitation combined with these dryland soil and vegetation characteristics affect the production of runoff in dryland regions (Favreau et al., 2009; Massuel et al., 2011, 2006; Pilgrim et al., 1988). High-intensity precipitation events, which is often combined with low soil infiltration capacity, lead to a rapid production of (Hortonian) overland flow as a result of the rapid exceedance of soil

infiltration capacity (Pilgrim et al., 1988; Wheeler et al., 2007, 2010; Zocatelli et al., 2020).

Transmission losses from streams, either via infiltration through the streambed or/and direct evaporation (Shanafield and Cook, 2014), is a common process in drylands and can considerably reduce or even totally consume flow in channels. Infiltration through the streambed depends on different factors such as streamflow hydrograph characteristics, channel geometry characteristics, hydraulic properties of the streambed, the antecedent water content within the streambed, and hydraulic characteristics of the underlying aquifer.

Streamflow characteristics include magnitude, shape, duration, and frequency of streamflow events (Dunkerley, 1992; Flug et al., 1980; Knighton and Nanson, 1994, 2001; Lange, 2005; McCallum et al., 2014a; Zocatelli et al., 2020). The hydrograph of a typical flood event in dryland regions is characterised by a sharp increase (rise to peak) followed by a rapid decrease (falling limb) of streamflow and stage, which is typical of a high energy system (Datry et al., 2017; Wheeler et al., 2010; Xie et al., 2014). During long streamflow events and high stream stages, the pressure head increases, consequently increasing the infiltration rate, whereas, short events produce lower transmission losses, due to the limited amount of water available for infiltration (Brunner et al., 2009a, 2017).

Geometrical characteristics and hydraulic properties of the channel boundaries also influence the rate of transmission losses (Cataldo et al., 2005; Dunkerley, 1992, 2008; Hughes and Sami, 1992; Walters, 1990). Increases in the wetted perimeter of the stream during streamflow events increases transmission losses (Brunner et al., 2009a). Additionally, heterogeneity of the streambed influences transmission losses by affecting the wetting time response of the unsaturated zone (Hughes and Sami, 1992) and therefore the spatial distribution of the wetted front (Parissopoulos and Wheeler, 1992; Peterson and Wilson, 1988; Shanafield et al., 2012; Xian et al., 2017). Hydraulic characteristics of the streambed generally produce dynamic responses in which there is significant temporal and spatial variation of hydraulic conductivity values (Wheeler et al., 2008). This variation can be attributed to geomorphic conditions of sediment deposition that subsequently affect flow regimes and may even produce streambed clogging. However, conductivity can even vary over short time scales as was shown by (Wang et al., 2017a) at the ephemeral river Heihe, located in an extreme arid-region in China (Wang et al., 2014).

The degree of saturation of the streambed at the beginning of the streamflow event also influences the infiltration rate such that high negative potentials in the

unsaturated zone as a result of dry conditions may lead to high infiltration rates (El-Kafagee and Rahman, 2011; Hill, 1996). Aquifer properties such as permeability, specific yield, water table depth, and volume of the aquifer may influence surface water interactions (Cuthbert, 2010, 2014; Cuthbert et al., 2016; Sophocleous et al., 1995). However, this process has not been well understood and it is still challenging to evaluate it in ephemeral streams.

Groundwater recharge occurs through two main mechanisms: (i) diffuse recharge, which is the result of infiltrated precipitation flowing vertically through the unsaturated zone into the saturated zone, and ii) focused recharge, which involves ponding or flowing water, which infiltrates via the unsaturated zone to the saturated zone (Healy and Scanlon, 2010). Lerner et al. (1990) and Simmers (2003) use the term *direct recharge* to refer to the mechanism of diffuse recharge and the term *indirect recharge* for the mechanism of focused recharge. Lerner et al. (1990) also distinguish two types of indirect recharge mechanisms: (i) *local indirect recharge*, to describe the recharge from water bodies, and (ii) *localised indirect recharge* to describe the recharge processes through fractures or joints after water concentrates on the surface. Here, the terms diffuse and focused recharge are used to refer to these mechanisms of direct and indirect recharge, respectively.

The interaction between different elements of the hydrological cycle in a dryland environment can exhibit great variation in time and space (e.g.: Cook et al. (1989); Dunkerley (2002); Villeneuve et al. (2015); Wang et al. (2014)). Diffuse recharge in drylands is restricted due to the limited availability of water required to overcome large soil moisture deficits that result from high rates of evapotranspiration combined with the high production of Hortonian overland flow. When combined with low rainfall, such diffuse mechanisms for recharge generation occur much less frequently in dryland regions compared to humid areas (Cuthbert et al., 2019a; Small, 2005). However, diffuse recharge can occur even during low precipitation events in coarse dryland soils, primarily as a result of the rapid advance of the wetting front, the highly seasonal variations of both precipitation and evapotranspiration, and the distribution of storm sizes (Small, 2005). Although diffuse recharge is insignificant in hyper-arid regions, it may increase with the degree of aridity (Cuthbert et al., 2019a; Small, 2005).

Conversely, focused recharge from streams is a much more common process in drylands given the spatial and temporal variability of rapid runoff generation and high transmission losses from ephemeral streams (Houston, 2002; Izbicki et al., 2000; Lerner et al., 1990; Massuel et al., 2006; McCallum et al., 2013; Morin and Benyamini,

1977; Qin et al., 2012; Sanford et al., 2004; Sorman and Abdulrazzak, 1993; Sorman et al., 1997; Wang et al., 2014). Therefore, focused recharge can be a critical source of groundwater in drylands (Favreau et al., 2009; Pool, 2005; Scanlon et al., 2006), particularly as a result of extreme precipitation events (Cuthbert et al., 2019b; Taylor et al., 2013).

Characterising transmission losses and groundwater recharge in dryland regions

Research in different drylands across the globe has contributed to enhance our understanding of key hydrological characteristics of these regions. In this context, transmission losses and groundwater recharge processes play an important role in the hydrological cycle (e.g. China (Wang et al., 2014; Ó Dochartaigh et al., 2010); the Middle East (Dahan et al., 2008; Mansour et al., 2019, 2012; Shentsis et al., 1999; Shentsis and Rosenthal, 2003; Sorman and Abdulrazzak, 1993; Sorman et al., 1997), Southern Asia (Sharma and Murthy, 1995), Europe (Guardiola-Albert and Christopher, 2011; Turner et al., 2015), Africa (Dahan et al., 2008; Hughes, 2019; Hughes et al., 2004), North America (Goodrich et al., 2018; Pacheco-Guerrero et al., 2017; Schoener, 2017; Schreiner-McGraw and Vivoni, 2018; Wallace and Renard, 1967; Walters, 1990), South America (Costa et al., 2012) and Australia (Dunkerley, 2008; Rau et al., 2017). For instance, extensive studies related to the dynamics of streamflow and transmission losses in dryland areas across the USA have shown how the streamflow shape, magnitude, and duration and frequency influence the rate of infiltration through the streambed of arid streams (Cataldo et al., 2005; Schreiner-McGraw et al., 2019; Schreiner-McGraw and Ajami, 2021). Most of this work has been extensively supported by long and high spatial and temporal resolution datasets obtained from well monitored catchments located in Arizona and Colorado, in the USA (Stone et al., 2008). Similarly, studies performed in ephemeral streams in the Middle East have also shown that transmission losses from alluvial channels and their tributaries are well correlated to the upstream flow, channel width and the soil moisture conditions at the beginning of the streamflow event (Abdulrazzak, 1995). Studies performed across arid and semi-arid regions in Southern Africa, Australia and New Mexico have shown the impact of the antecedent moisture conditions of the streambed on infiltration rates (Dunkerley and Brown, 1999; Hughes and Sami, 1992; Lange, 2005; Thomas et al., 2000). Low water content of the streambed increases infiltration rates and consequently increases transmission losses. Reduction of up to 75 % of the streamflow during the first event have been reported in ephemeral streams in Southern Africa (Hughes and Sami, 1992).

Transmission losses also reduce the size and duration of peak discharges, which in turn reduces the impact of flash flood events as reported for ephemeral streams in Australia (Dunkerley and Brown, 1999; Lange, 2005). Water lost from these ephemeral streams can temporarily be stored in sediments underneath the streambed. These in turn provide water for the riparian vegetation close to the stream and/or potentially supply water for domestic and/or livestock uses as in the semi-arid Mara basin in Kenya (Wekesa et al., 2020). Costa et. al. (2011) showed that evapotranspiration from riparian areas is supported by ephemeral streamflow events in the semi-arid basin of Majave, Brazil. Goodrich et.al. (2018) also highlight the hydrological, chemical and ecological connectivity between ephemeral and intermittent streams and riparian zones in the Southwestern U.S. which are mainly influenced by the physical landscape, climate, and human impacts.

Transmission losses by direct evapotranspiration from streams can also play an important role in the water availability along ephemeral streams. Daesslé et al. (2016) found that direct evaporation can take up to 16 – 20 % of the available water in wide channels such as the Colorado river. High values of direct evaporation have also been reported in the Limpopo River in southern Africa (Hughes 2009) and in the Mara River in Southern Kenya (Wekesa et al., 2020).

However, despite the increasing number of studies related to dryland hydrology in general, the interaction between different components, particularly the groundwater – surface water interactions, has not been well understood. In fact, despite the large spatial and temporal distribution of transmission losses along streams, the contribution of focused recharge to total groundwater recharge has not been yet evaluated at regional to global scales. Studies at local scale have shown the importance of considering the spatial distribution of groundwater recharge in dryland environments (e.g. Wang et al. (2017a), Cui et al. (2017), Coelho et al. (2017), Houston (2002); Hughes et al. (2008); Mansour et al. (2019)), however, the likely wide spread interaction of groundwater – surface water has not been yet explored (Cuthbert et al., 2019b; Ferguson et al., 2020; Taylor et al., 2012, 2013), and the impact of climatological disturbances such as natural and human induced climate change at larger scales have not been yet evaluated.

In this context, the use of numerical models developed to account for all the relevant process in dryland environments are considered useful tools to enhance our understanding of key processes and interactions between different components of the water balance in dryland regions. Thus, the following section describe the main

characteristics and limitations of current models to set up the framework of the present thesis.

2.4 Modelling water partitioning in dryland regions

The complexity of rainfall regimes, runoff generation processes and subsurface flow paths in drylands create challenges for data collection, resulting in a paucity of data from which to generalise, and also limits efforts to evaluate numerical models aimed at enhancing understanding of the dryland water balance (Abbot, 1979; Cuthbert et al., 2019b; Ewen et al., 2000; Ivanov et al., 2004; Michaelides and Wainwright, 2002; Noorduijn et al., 2014b; Schreiner-McGraw et al., 2019; Wheeler et al., 2007; Woodward and Dawson, 2000; Woolhiser, 1989; Šimůnek et al., 2006).

Existing hydrological models, operating at catchment to regional scales, are challenged in drylands due to their inherent assumptions about key flow processes. Despite recent improvements (i.e. Hughes et al. (2006), Hughes (2019), Lahmers et al. (2019), Mudd (2006)), the majority of models have been developed based on the theory and hydrological processes of humid regions. This has resulted in models that generally lack the ability to represent the development of ephemeral streams and their potential hydraulic interactions with groundwater systems (Zimmer et al., 2020). This is particularly problematic considering that ephemeral channels represent half of the global stream network length (Datry et al., 2017). The key processes such as transmission losses below streambeds has received little attention by the modelling community, despite the importance of groundwater resources for developed and developing countries in dryland regions. Additionally, due to the inherent spatial variability of streamflow events and the complexity of water movement in the unsaturated zone, transmission losses and consequently focused recharge has been poorly characterised in dryland regions (Cataldo et al., 2005, 2004, 2010; Noorduijn et al., 2014b; Schoener, 2017; Shanafield et al., 2014; Villeneuve et al., 2015; Walters, 1990).

The use of numerical models in drylands has also been restricted due to the complexity and the high computational demand required to describe the highly dynamic behaviour of dryland hydrological processes. These processes, which are highly non-linear, require the use of complex numerical solutions (i.e. Saint-Venant equation for surface flow (de Saint-Venant B., 1871) and Richard's equation for flow through porous media (Richards, 1931)), i.e physically-based models (Abbot, 1979; Kampf and Burges, 2007). **The use of Complex equations, such as the Richard's equation,**

generally assumes homogeneous conditions that limits its application at large scales. Additionally, there are numerical challenges to overcome with the equation and its inability to represent discontinuities (Farthing and Ogden, 2017). This often leads to numerical instabilities and convergence problems in addition to the high computational demand required for model simulations (especially to capture the emergence of wetting and drying). The complexity of these models is also reflected in the usually high number of parameters often included in such models, which are difficult to quantify a priori or even to calibrate due to the high computational demand (Beven, 1989, 2001; Beven and Binley, 1992). Additionally, the degree of complexity of existing models and their inherently high computational cost does not allow for comprehensive sensitivity and uncertainty analysis, which would support the evaluation and interpretation of model results (Beven and Binley, 1992).

At larger scales, regional to global hydrological models rely on coarse and low-quality information available at these scales, so they are subject to great uncertainty in estimating water balance components. Improving the quality, and reducing uncertainty, of model inputs is key to reducing the uncertainty in model results. However, model structure and its internal complexity also play an important role in the parameterisation of large-scale models. In this context, improving the model structure by using parsimonious approaches may enable better evaluation of large-scale models for dryland regions. Understanding the local and regional characteristics of focused recharge supports insights into the main mechanisms and the driving forces that control water partitioning and flow pathways. In turn, it allows for the implementation of focused recharge processes at larger scales - processes that have been neglected in the current generation of large-scale models.

2.5 Summary

Although the understanding of the physical basis of the main hydrological processes in drylands has improved, including flow through porous media or surface flow (particularly at small scales), the interactions between different processes remains unclear. In particular, transmission losses and focused recharge processes are underrepresented in the literature, and their impacts on the water balance are typically neglected, particularly at large scales.

In this context, numerical models have the potential to enhance the understanding and improve the quantification of water partitioning and flow pathways of dryland regions. Thus, it has been proposed here that the development of more efficient and

parsimonious models will help to overcome the current limitations such as lack of data and high computational demand. However, models must include key processes of dryland hydrology in order to understand the main controls of the water balance of these regions.

Furthermore, it has been proposed that understanding the local and regional characteristics of focused recharge will give some insights into the main mechanisms and the driving forces that control this type of recharge. In turn, this will allow the implementation of focused recharge processes at larger scales - processes that have been neglected in all global-scale models to date. Hence, improving our understanding of focused recharge is specifically addressed in the following two Chapters.

Chapter 3

Characterising groundwater - surface water interactions in dryland regions: A transect scale analysis

This chapter is based on the published paper: Quichimbo, E.A., Singer, M.B., Cuthbert, M.O., 2020. Characterising groundwater–surface water interactions in idealised ephemeral stream systems. *Hydrological Processes* 34, 3792–3806. <https://doi.org/10.1002/hyp.13847>

3.1 Introduction

Loss of water through the streambeds of ephemeral streams is a key process for aquifer recharge in arid and semi-arid dryland regions (Costa et al., 2012; Cuthbert et al., 2019b; Keppel and Renard, 1962; Lerner et al., 1990; McCallum et al., 2013; Qin et al., 2012; Renard and Keppel, 1966; Wang et al., 2017a, 2014; Wheeler et al., 2008). Understanding the mechanisms of recharge from ephemeral streams is thus of critical importance for sustainable management of water resources in dryland regions. Key to developing improved understanding of such dryland processes is a better appreciation of the degree and extent of interactions between surface water and groundwater within ephemeral stream systems. Furthermore, improved understanding of the moisture dynamics below and around ephemeral streams would enable a better characterisation of water availability to dryland vegetation and thus climate-groundwater interactions (Cuthbert et al., 2019b), as well as biogeochemical processing of key nutrients and contaminants within the short-lived hyporheic zone (e.g.: Belnap et al. (2005); Meixner et al. (2007); Sargeant and Singer (2016); Singer

et al. (2016); Snyder and Williams (2000); Valett et al. (1990). The current Chapter contributes to this relatively under-studied aspect of dryland hydrology. The focus is on the transect scale in order to develop the necessary understanding of small-scale processes to underpin robust modelling of dryland water partitioning at larger scales developed later in the thesis.

Thus, this chapter first provides an overview of the processes controlling the infiltration through streambeds of ephemeral streams. Second, a conceptual model describing the key factors controlling the infiltration through the streambed is developed. Next, a numerical model to quantify the processes described in the conceptual model is implemented. Then, a sensitivity analysis of the main factors controlling the infiltration process is performed before drawing some conclusions from the analysis.

3.2 An overview of groundwater - surface water interactions

Ephemeral streams are under-represented in existing hydrological research into groundwater - surface water interactions, with much greater emphasis being placed on interactions under perennial streamflow conditions (Jarhani et al., 2015). Nevertheless, insights from studies of perennial losing streams can be useful in informing a deeper conceptual understanding of ephemeral streams. For example, the steady-state loss of water from a perennial stream has previously been characterised as follows (Brunner et al., 2009a,b; Fox and Durnford, 2003; Xian et al., 2017): (i) connected state, in which fully saturated conditions are developed in the region between the stream and the aquifer; (ii) transitional state, characterized by a partially saturated zone between the stream and aquifer; and (iii) disconnected state, in which an unsaturated zone occurs between the stream and the aquifer. For a connected state under steady conditions, the infiltration rate increases linearly with the water table depth, whereas for the disconnected state, the infiltration rate stays at its maximum value regardless of the water table depth, although theoretically, its behaviour is asymptotical. The transitional state is an intermediate state in which the relationship between the infiltration rate and the water table is non-linear. Under transient conditions, for connected streams, the infiltration rate is expected to vary gradually under changes in the river stage, whereas for disconnected streams the infiltration rate will immediately change, reaching a new steady-state, after any change in the stream stage.

Despite this nomenclature becoming widespread in the literature, it is noted that, even during a so-called disconnected state, flow of water still occurs between the

stream and the aquifer - there is no disconnection between surface water and groundwater in real terms. Rather, the term ‘disconnected’ simply refers to the fact that additional lowering of the water table cannot induce a greater loss from the stream for that particular set of conditions. Thus, the interaction between surface and groundwater in the ‘disconnected’ state is still uni-directional, whereas in the ‘connected’ state there can be feedback from the groundwater to the surface water and thus the interaction can be said to be bi-directional. It is also noted that the state of the system may change through time (see for example, (Rau et al., 2017)), a further reason that categorising surface water – groundwater (SW – GW) interactions as connected or disconnected may be misleading.

An important characteristic of SW-GW interactions that has been also shown in previous studies is the development of an inverted water table (IWT) (Peterson and Wilson, 1988; Wang et al., 2016; Xian et al., 2017). The IWT is defined by total pressure being equal to atmospheric pressure (i.e. pressure head equals zero). However, owing to a lack of field observations, the development of the IWT has only been tested using laboratory and numerical experiments (e.g. (Wang et al., 2016)). Such research shows that, under steady-state conditions, the IWT could develop inside the streambed for homogeneous materials and stream stages smaller than the streambed thickness Wang et al. (2016), whereas for thin streambeds it may extend well below the bottom of the streambed (Brunner et al., 2009a, 2011, 2009b; Fox and Durnford, 2003). Under changes in stream stage, for thin streambeds, the extension of the IWT may increase or decrease immediately below the streambed, whereas for thicker streambeds the development of the IWT will gradually increase its size for any change in stream stage (Xian et al., 2017). In ephemeral streams it is anticipated that the development of the IWT should be controlled by factors such as the degree of saturation, water table depth, the magnitude, timing, and sequencing of streamflow events and hydraulic properties of the streambed sediments. However, these factors have not yet been evaluated in the literature, despite recent advances in understanding the nature of groundwater mounding beneath ephemeral streams (Cuthbert et al., 2016).

In this context, in the following sections a general conceptual model is proposed for characterising the main factors that control SW – GW interactions in ephemeral streams and their role in affecting the water balance of arid and semiarid regions. These concepts are then tested using a series of numerical model simulations, enabling the quantitative evaluation of different scenarios of stream-aquifer interactions and leading to some implications for dryland water resource management.

3.3 A conceptual model of ephemeral stream-aquifer interactions

Despite the paucity of research on ephemeral stream-aquifer interactions, existing hydrological theory can inform the likely range of controls on these interactions. It is proposed that the following factors will be most important in controlling the degree of bi-directional interactions: water table depth, stream stage, hydrograph shape, time between events, channel shape, channel boundary permeability and water retention characteristics of the subsurface materials. All these factors may vary individually or in combination in real systems. Nevertheless, it can be characterised in two end-member responses for ‘deep’ and ‘shallow’ water table systems that depend on the variations between these parameters as shown in Figure 3.1.

In the case of a deep water table, the frequency of events will affect the degree of saturation based on the prevailing time of drainage between events and consequently, the rate at which the channel bed can infiltrate newly arrived water. The process of water flowing through a thick variably saturated zone is depicted in Figure 1a in a two-dimensional cross section. When the stream stage starts to rise the IWT starts to develop, at a growth rate and size that are controlled by the antecedent saturation and the hydraulic conductivity of the sediments. Under lower antecedent saturation, which occurs under long time periods between flood events, more water will infiltrate below the streambed due to higher hydraulic gradients. The rate of movement of the IWT will depend on the degree of saturation, and for lower values of saturation the IWT will move more slowly downwards. At the end of the event, the IWT becomes separated from the streambed as it descends due to gravitational drainage. At the same time, it decreases in size (areas decrease from t_1 to t_5 in Fig. 3.1a) due to the losses associated with the spreading of water due to capillary forces. No influence of the water table depth is expected during the advance of the IWT for this case of a deep water table, and the rate of IWT movement is only a function of the saturation state of the sediment surrounding and below the channel.

For the case of a shallow groundwater system, the frequency of streamflow events combined with the antecedent water table depth will influence the infiltration rate. This process is illustrated in Figure 3.1b. Under this scenario, as the IWT develops within the thin variably saturated zone it rapidly interacts with the shallow water table creating a continuous zone of saturation beneath the stream; the hydraulic gradient is thus reduced and consequently the infiltration rate declines.

For both shallow and deep water tables, the change in saturation within the material surrounding and below the channel under different pressure heads will depend on their hydraulic and water retention properties (hydraulic conductivity and soil moisture retention curve).

To quantify the degree of interaction as well as to give insights into a SW-GW processes, this conceptual model is numerically tested by using a physically-based numerical approach.

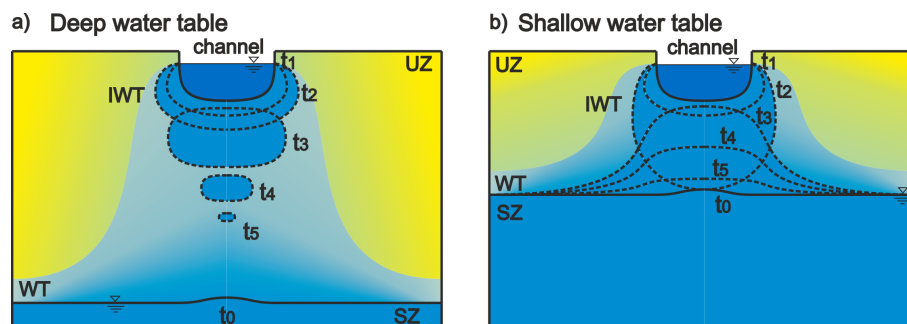


Figure 3.1: Conceptual process model of interactions between ephemeral streams and an underlying homogeneous aquifer for (a) deep and (b) shallow water tables. Dashed lines represent the evolution of the inverted water table (IWT) and the water table mound at time t_i during and after a streamflow event. The hypothetical shape and size of the IWT depend on the magnitude, shape, and duration of the streamflow hydrograph and the antecedent conditions of saturation (inherited from the previous dry period), as well as hydraulic and soil moisture retention properties of the sediments.

3.4 Methods

3.4.1 Numerical modelling

The purpose of the numerical modelling was to quantify the influence of key factors that control transient infiltration rates from ephemeral streams. A set of scenarios was developed to simulate the transient characteristics of the infiltration process under variations in: 1) magnitude/duration of streamflow events; 2) frequency of the events (and inter-arrival times); 3) water table depth; 4) hydraulic properties including soil moisture retention properties of the homogeneous material underlying the channel; and 5) the channel geometry.

3.4.2 Model Geometry

The model was defined as a 2-D cross sectional block containing a rectangular ephemeral channel, and a broad homogeneous aquifer (unconfined and variably saturated) with a water table within it. This configuration is broadly representative of ephemeral streams of dryland regions, which typically express as relatively simple geometrical shapes (Singer and Michaelides, 2014; Sutfin et al., 2014). A homogenous aquifer with a cross-section of 100 m width and 60 m depth was used in which processes are modelled within a ‘half-space’ (Fig. 3.2). The width of the model domain was located at a sufficient distance from the stream to avoid high variations of pressure head close to the boundaries. The width of the stream, which can greatly vary in ephemeral streams, was chosen to be 12 m, which broadly corresponds to the dimensions of an incised alluvial stream located in a piedmont or a lowland zone of an arid or semiarid region (Jaeger et al., 2017).

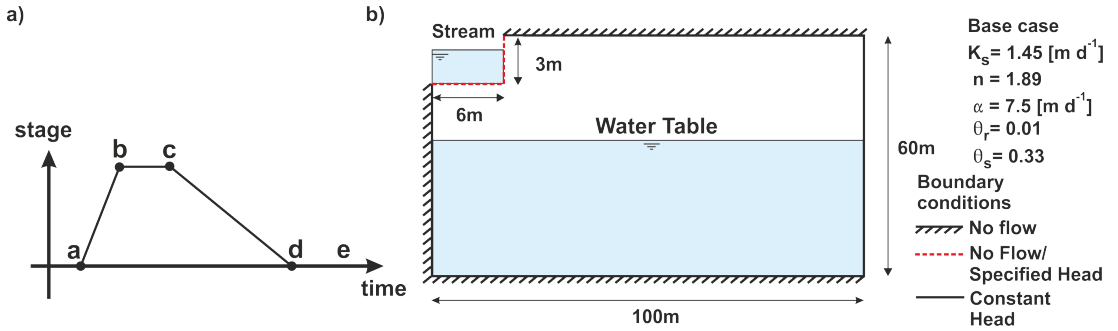


Figure 3.2: a) Shape of the flow event is implemented as a specified head boundary condition at the stream base and sides. Before and after the flow event in the channel, the boundary condition switches to become ‘no flow’; b) cross section of the idealized transect considered in the numerical model, including a list of the boundary conditions and parameters of the base case model.

3.4.3 Governing equations and numerical methods

Flow under unsaturated conditions can be described by Richard’s equation:

$$\left(\frac{C_m}{\rho g} - S_e S \right) \frac{\partial H_p}{\partial t} + \nabla \left(\frac{K}{\rho g} k_r (\nabla H_p + \nabla z) \right) \quad (3.1)$$

where H_p is the pressure head [L], K is the saturated hydraulic conductivity [LT^{-1}], k_r is the relative permeability [-], Q_m is a mass source term [$\text{M}^{-1}\text{L}^{-3}\text{T}^{-1}$], g is the gravity acceleration [LT^{-2}], ρ is the fluid density [ML^{-3}], z is the vertical elevation

[L], S is the storage coefficient [$M^{-1}L^{-2}T^2$], t is time [T], ∇ is the gradient operator, S_e is the effective saturation estimated by:

$$S_e = \frac{\theta - \theta_r}{\theta_s - \theta_r} \quad (3.2)$$

where θ_s and θ_r represent the saturated and residual liquid volume fraction, respectively. θ is described by using the van Genuchten soil moisture retention equation (van Genuchten, 1980):

$$\theta = \begin{cases} \theta_r + \frac{\theta_s - \theta_r}{(1 + |\alpha H_p|^\beta)^m} & H_p < 0 \\ \theta_s & H_p \geq 0 \end{cases} \quad (3.3)$$

where α [L^{-1}], n [-] and m [-] are empirical parameters.

Relative permeability k_r is also estimated by the van Genuchten method in the following way:

$$k_r = \begin{cases} S_e^l \left[1 - \left(1 - S_e^{\frac{1}{m}} \right) \right] & H_p < 0 \\ 1 & H_p \geq 0 \end{cases} \quad (3.4)$$

The specific moisture capacity C_m is defined by the following equation:

$$C_m = \begin{cases} \frac{\alpha m}{1-m} \left[(\theta_s - \theta_r) S_e^{\frac{1}{m}} \left(1 - S_e^{\frac{1}{m}} \right) \right] & H_p < 0 \\ 1 & H_p \geq 0 \end{cases} \quad (3.5)$$

COMSOL V5.1 Multiphysics, which is a numerical platform to solve partial differential equations by using a finite element approach, was chosen for the numerical model in order to have the necessary flexibility in the applied equations and boundary conditions. Thus, COMSOL allows the quick implementation of complex boundary conditions to represent the switch between dry to wet conditions or vice versa, as explained in the following section.

3.4.4 Boundary conditions

Using COMSOL thus allowed the specification of appropriate boundary conditions to represent the switch between ponded and dry channel conditions necessary to simulate ephemeral flows. Since COMSOL does not consider explicitly groundwater - surface water interactions under saturation excess, this condition was implemented by assuming a continuity pressure and flux at the wetted perimeter of the channel. This was specified by using a Cauchy boundary condition (Chui and Freyberg, 2009; Jazayeri and Werner, 2019) to switch between Dirichlet and Neumann boundary

conditions, representing pressure head and flux conditions respectively, by following a similar approach described by Chui and Freyberg (2009):

$$\rho K \nabla (H_p + z) = \rho R (H_r - H) \quad (3.6)$$

where: $H_r = z + y$ represents the hydraulic head in the channel, and $H = z + H_p$ represents the hydraulic head in the streambed, y is the stream stage [L], and R is a conductance term [L^{-1}]. Values of R in eq. 3.6 should be large enough in order to guarantee a pressure continuity at the streambed and to keep at the same time the pressure head similar to the stream stage at the bottom of the channel. In the present simulation, a value of 1000 d^{-1} for R was specified in order to assure the accuracy and convergence of the model results in acceptable simulation times.

In order to simulate ephemeral channel conditions, the parameter R was switched to zero when the stream stage was zero, creating a no-flow boundary condition. This switching was applied gradually over a period of two hours prior and after the event by using a smoothing function. A smooth transition enables the convergence of the model during large changes in hydraulic gradient due to dry to wet conditions (Chui and Freyberg, 2009; Chui et al., 2011).

In order to define the size and distribution of the finite element model mesh, various geometrical distributions were analysed in order to ensure the accuracy and convergence of the results. As a result, a triangular mesh was specified for the entire model domain, in which the size of the elements varies between 0.05 to 1.0 m, according to the characteristics of the flow and the balance between the model accuracy and efficiency. Elements with a minimum size of 0.05 m were specified in the region below the corresponding to the flux boundary condition representing the stream (Fig 3.2). The mesh was also refined in the region located between the water table and the streambed as well as above the water table. These refined regions allowed for a better representation of the highly non-linear behaviour of the unsaturated zone at the region corresponding to the capillary fringe.

The solution for the numerical model was obtained using the numerical solver MUMPS (MUltifrontal Massively Parallel sparse direct Solver) in COMSOL v5.1. MUMPS, which is based on the lower-upper (LU) decomposition, used an adaptive time step with a minimum time step of 0.001 d, although the time step for the model output was specified as 1 hour in order to optimize computational resources.

3.4.5 Initial conditions

Choice of initial conditions in ephemeral streams is non-trivial due to complex antecedent moisture conditions implicit in such systems. Two options for initial conditions often used in unsaturated zone models are either a hydrostatic initial state of the water table and unsaturated zone or a periodic steady state for a specific dry period length. However, both of these can be unrealistic considering the typically highly variable frequency of flow events in ephemeral systems. Thus, a compromise between these end members has been implemented as follows. First, a steady-state condition for a small stream stage corresponding to 0.5 cm was specified in order to raise the moisture state of the unsaturated zone above the unrealistically dry conditions that hydrostatic conditions would imply. Second, using this initial steady state condition the stream stage was then set to zero in order to let the sediment drain and to allow the dissipation of groundwater mound for a period of approximately a year (360 days) of no flow. Third, at the end of this no flow period, a pair of identical flow events were modelled using the various types of flow event described below, separated in time by a dry period whose duration was also varied as described below. The second event of the pair was then analysed and included in the results presented in the following sections.

3.4.6 Base Case scenario and sensitivity analysis

A base case model was defined with a K of 1.45 m day^{-1} , which corresponds to sandy loam sediments (Carsel and Parrish, 1988). This is consistent with the permeability of a sandy streambed typical of ephemeral streams characterised as high-energy environments due to high flow velocities that can reduce the chance of the deposition of fine sediments on the bottom of stream (Peterson and Wilson, 1988; Xie et al., 2014). While it is recognised that clogging layers can be deposited as ephemeral flows abate, they are also often scoured out during the first stages of the next event (Lerner et al., 1990). Given the objectives of the modelling to determine behaviour in a homogeneous system, this complication is out of scope of this paper but will be included in future work.

Unsaturated soil parameters for the van Genuchten soil water-retention curve of a sandy loam sediment were assigned as 7.5 m^{-1} and 1.89 for α and n , respectively and 0.01 and 0.33 for residual, θ_r , and saturated, θ_{sat} , moisture water content, respectively (Carsel and Parrish, 1988). A pair of trapezoidal, seven-day flow events were then simulated, in which the rising limb lasted one day, the peak was represented as a flat

period of one day, and the falling limb comprises five days. The dry period between the pair of events was 10 days for the base case.

Ephemeral streamflow events can show a huge variation in hydrograph shape, return period and duration. In small ephemeral streams, streamflow shape is characterized by a rapid increase and decrease of the stream stage (Costigan et al., 2017; Malmom et al., 2004). Streamflow durations can vary from several hours up to several days (Cataldo et al., 2004; Constantz and Thomas, 1997; Knighton and Nanson, 1994; Wheater et al., 2008) or even weeks (Rau et al., 2017). Therefore, variations from the base case were simulated in order to assess the sensitivity of the stream-aquifer interactions to the aspects hypothesised to be important (see conceptual model description, Section 3.3) as follows: stream flow duration, dry period length between flow events, and hydraulic properties.

Streamflow duration and water table depth

The shape of the event hydrograph was varied by changing the total duration of the event from seven days to 16 days. The rising and falling limb of the hydrograph were kept the same as the base case scenario (i.e. one day and five days for the rising and falling limb respectively) but the duration of the peak of the event was varied with values of one (base case), five, and ten days.

Length of dry period between stream flow events

The influence of the dry conditions is evaluated by two streamflow events separated by a specific period of time. Time periods between events allow the drainage of water from the unsaturated zone and the dissipation of the water table mound after a streamflow event occurs, these conditions are reflected in the degree of saturation and water table depth and they become the initial condition for the next event.

Duration of the dry period shows great variability in real ephemeral streams (Costigan et al., 2017), in part due to the high spatio - temporal variability in runoff - generating rainfall events (e.g., Michaelides et al. (2018); Singer and Michaelides (2017)). Therefore, a range of 10 to 360 days for the duration of the dry period has been considered in order to include seasonal variations (Table 3.1). The analysed event corresponded to an event peak of five-day duration event for the simulations.

Soil hydraulic and water retention properties

The characteristics considered in the sensitivity analysis were: i) hydraulic conductivity, ii) water retention curve, and iii) storage capacity. These were evaluated separately and are summarised in Table 3.1. Values of K were varied between 1.0 m d^{-1} and 2.0 m d^{-1} in addition to the base case value of 1.45 m d^{-1} . For the water retention curve, its shape was varied by changing the α and n parameters (Table 3.1).

Table 3.1: Model scenarios and number of events per scenario. Parameters for the base case scenario are $\alpha = 7.5 \text{ m}^{-1}$; $K = 1.45 \text{ m d}^{-1}$; $n = 1.89$.

Parameter being varied	Range of variation	Other parameters that were varied in combination (number of combined simulations in brackets)
Length of dry period between stream flow events	10 days (base case)	Water table depth (72)
	30 days	
	60 days	
	90 days	
	150 days	
Event peak duration	360 days	Water table depth Dry period (72)
	1 day (Base case)	
	5 days	
	10 days	
Saturated hydraulic conductivity, K	1 m d^{-1}	Water table depth Dry period (72)
	1.45 m d^{-1} (Base Case)	
	2 m d^{-1}	
Soil hydraulic (van Genuchten) parameters, α and n	Coarse Material: $\alpha = 10.4 \text{ m}^{-1}$; $n = 2.28$	Water table depth Dry period (72)
	Base Case: $\alpha = 7.5 \text{ m}^{-1}$; $n = 1.89$	
	Fine material: $\alpha = 3.6 \text{ m}^{-1}$; $n = 1.56$	
Transmissivity	Aquifer thickness of 60 m (Base Case)	Water table depth (72)
	Increase of 10 m of the aquifer thickness	
	Decrease of 10 m of the aquifer thickness	
Storage capacity	-10%: $\theta_r = 0.01$, $\theta_{sat} = 0.300$	Water table depth (72)
	Base Case: $\theta_r = 0.01$, $\theta_{sat} = 0.33$	
	+10%: $\theta_r = 0.01$, $\theta_{sat} = 0.373$	
Cross section shape	Rectangular (base case)	Water table depth (72)
	Triangular	
	Trapezoidal	
Cross section width	1 m	Water table depth (72)
	2 m	
	6 m (base case)	
	12 m	
	24 m	
Total number of simulations		252

Note: Each analysed event corresponds to the second streamflow event for each event pair simulated (see section 3.4.3). Scenarios of water table depths ($\times 6$) were 1, 3, 5, 10, 15 and 20m below stream bed. Dry period between events ($\times 6$) modelled were 10, 30, 60, 90, 150 and 360 d. Total number of events are in parenthesis. Parameters for the base case scenario are $\alpha = 7.5 \text{ m}^{-1}$; $K = 1.45 \text{ m d}^{-1}$; $n = 1.89$.

Higher values of α and n correspond to coarser material with higher content of sand while low values of these parameters correspond to finer material with higher clay content. Finally, the available storage capacity of the material ($\theta_{sat} - \theta_r$) was varied by increasing and decreasing the saturated water content by $\pm 10\%$.

Transmissivity

The influence of aquifer transmissivity was evaluated by increasing and reducing the height of the model domain by 10 m while keeping the K value constant.

Channel cross-section shape and channel width

Channel cross-section was evaluated by changing the channel width in relation to the base case scenario. For a channel width larger than the base case scenario, the model domain was also increased in order to reduce the influence of lateral boundary conditions. Since it is intuitive that the increase in channel width increases the total infiltration, the infiltration per unit length flowing through the streambed was used for comparative analysis. Channel cross section shape was also considered by simulating and comparing results for rectangular, triangular and trapezoidal shapes. For the latter two cross sections, a slope of 1:1 was specified for the channel banks.

Combinations of parameters used in sensitivity simulations

All variations of the above parameter variations were carried out in combination with variations in initial water table depth values of: 1, 3, 5, 10, 15, 20 metres below the streambed (Table 3.1). In addition, the length of dry period and event peak duration were also varied in combination (Table 3.1).

3.5 Results

3.5.1 Conceptualising a single flow event in time and space

Based on the results of the numerical simulations, the hydraulic processes governing the loss of water from an ephemeral stream transect can be described as follows for a three-day streamflow event with a 1 d peak (Figure 3.3), stage hydrograph illustrated in Figure 3.4). During a streamflow event occurring after a dry period of no flow in the stream (Fig. 3.3a, f), as the stream stage starts to rise a saturated zone and IWT start to develop at the bottom of the channel (Fig. 3.3b, g).

For deep water tables, an IWT forms by the time the streamflow hydrograph has reached its peak value. In this case, the hydraulic head at the bottom of the channel is equal to the stream stage (2 m) plus the elevation (57 m), as shown in Fig 3.3b. At the IWT, where the pressure head equals zero, the hydraulic head is equal to the elevation head and consequently intersects the gravity drainage line.

Immediately below the IWT, the hydraulic head plots above the gravity drainage line indicating unsaturated conditions. In the deeper water table case, the zone of saturation below the streambed continues expanding during the event until the streamflow ceases (Fig. 3.3c), after which the IWT starts to move downward until it disappears as a result of lateral spreading dominated by capillary forces and downward spreading dominated by gravity forces (Fig. 3.3d). Much of the remaining water above the water table, which is temporally stored in pores, continues to move downward through the unsaturated profile until it eventually reaches the water table producing recharge (Fig. 3.3e). Since this process is relatively slow, no significant groundwater mound develops underneath the stream as the lateral movement of water in the aquifer towards the lateral boundary keeps pace with the rate of recharge.

In contrast, for the case of an initially shallower water table, the IWT quickly expands downwards developing a fully saturated zone between the stream and the aquifer (Fig. 3.3g). However, the water table drops below the channel once the stream event ceases (Fig. 3.3i). In this case, lateral groundwater flow cannot keep pace with the rate of recharge during the event and a groundwater mound is created beneath the stream (Fig. 3.3j). For shallow water tables, the pressure head and the infiltration rate at the peak of the event are similar to those within deep water table simulations. However, fully saturated conditions between the stream and the aquifer are reached faster after the onset of the event for shallow water tables (Fig. 3.3g) as a result of the reduced storage capacity and a higher antecedent moisture content arising from the initial conditions. Hence, at later times the infiltration rates are lower for a shallow water table compared to the deeper water table case (Figs. 3.3c, h), due to the lower hydraulic gradients produced by the quicker development of fully saturated conditions between stream and aquifer.

Figure 3.4 shows how vertical flow rate at the bottom of the channel and pressure head and saturation at 1.0 m below the bottom of the channel vary during the same streamflow event plotted in Figure 3.3, for both the shallow and deeper water table cases. At the beginning of the event ($t = 0$ d), the infiltration rate suddenly increases as a result of the rapid change of the pressure head in the stream from zero to positive values, which in turn produces high hydraulic gradients driving flow as a result of the beginning of the development of a thin IWT. A short step-decrease of the infiltration rate follows due to the rapidly declining hydraulic gradient at the streambed as the IWT continues to develop. As the stream stage rises the pressure head also rises but at a slightly slower rate, which in combination with the slower rate of development

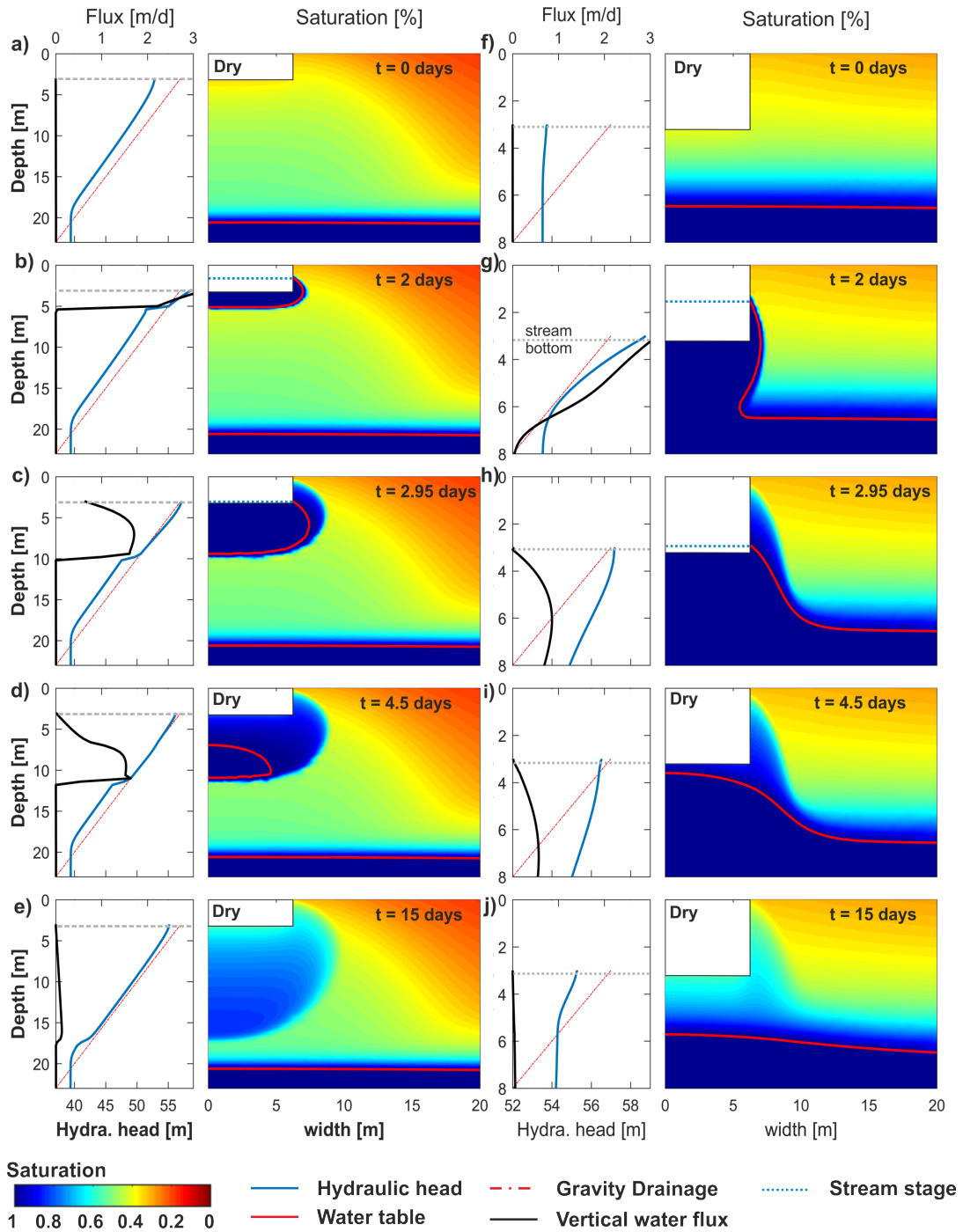


Figure 3.3: Variation of hydraulic head and vertical water flux at the centre of the stream, and saturation states for the cross section of the model domain for deep (a-e) and shallow (f-j) initial water table depths during the occurrence of a three-day streamflow event (see stage hydrograph plotted in Figure 3.4a) which otherwise uses the base case scenario parameters and geometry (see Fig. 3.2). Note that the vertical depth axes in (a-e) and (f-j) are different and zero depth corresponds to the base of the channel at an elevation of 57 m used in the calculation of hydraulic head.

of the IWT results in the overall increase of the infiltration rate ($0 < t < 1$ d, Fig. 3.4a).

When the stream stage reaches its peak ($t = 1$ d), the infiltration rate reaches its maximum values and suddenly declines due to the reduction of hydraulic gradient as a results of the continuous rise of the pressure head beneath the stream and development of the IWT ($1 \leq t < 2$ d, Fig. 3.4a; 3.4b). The rate of rising of the pressure head for shallow water tables is larger than that for deep water tables due to the quicker feedback of the water table (Fig. 3.4b). Finally, when the stream stage starts to fall ($t = 2$ d), the pressure head also decreases and becomes negative by the end of the flow event. This results in the decrease of the hydraulic gradient and consequently the reduction of the infiltration rate (Fig. 3.4a).

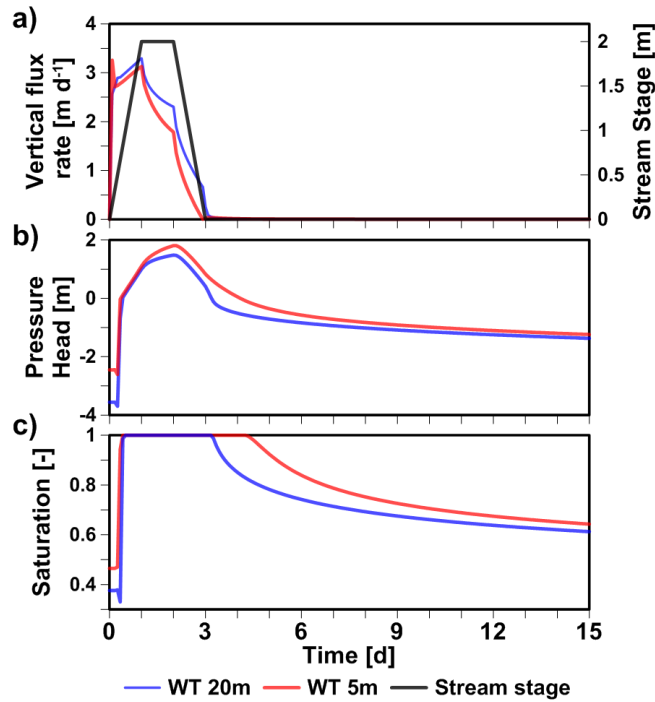


Figure 3.4: Temporal variation modelled at one meter below the centre of stream (left side of model half-space) for the same scenarios of Fig. 3.3: a) infiltration rate, with stream stage shown for comparison on right-hand axis b) pressure head, and c) degree of saturation for deeper (20 m) and shallower (5 m) water tables (WT). Soil parameters correspond to the base case scenario (Fig. 3.2).

3.5.2 The influence of dry period duration between flow events and water table depth on streambed infiltration rates

As dry period duration between flow events varied, it is found that total streambed infiltration increased with the length of dry periods, irrespective of water table depth (Fig. 3.5a). The total volume of infiltration shows a particularly high range of variation for dry periods with a duration of less than ~ 35 days (Fig. 3.5a). For longer dry period durations, the total volume of transmission losses approaches a constant value. As water table depth varied, it is found that for water tables shallower than ~ 10 m, infiltrated volumes increase significantly with water table depth. For water tables deeper than 10 m, the variation of the total infiltrated volumes is relatively unaffected by any further increases in water table depth, although there are still small variations ($<10\%$), associated with variations in dry period duration (Fig. 3.5b).

These results are intuitive because for events occurring after short dry periods, it is expected that the rate of decay of the degree of saturation to be higher after the event has ceased caused by the downward movement of the IWT (Fig. 3.5c). For longer dry periods following an event, the rate of change in the degree of saturation decreases considerably, and becomes nearly constant (Fig. 3.5c). This reduced variation of saturation states for long dry periods between events means that the infiltrated volume does not vary much when an event occurs, reaching an almost constant value depending on the depth of the water table (Fig. 3.5a).

For shallow water tables of <3 m in the present study, the range of variation of total infiltrated volume due to the length of dry period is also restricted, but for a different reason, in this case due to the rapid connection of the IWT with the water table and the influence of the capillary fringe (Fig. 3.5a). The extension of the capillary fringe represents a region in which the degree of saturation reaches a constant value. Therefore, the initial conditions for a shallow water table will be similar for any dry period length, which in consequence will result in a similar volume of water losses for events, irrespective of dry period duration between events.

3.5.3 The influence of streamflow duration

A summary of the simulation results used to test the influence of streamflow duration on total streambed infiltration volumes are shown in Figure 3.6. As expected, infiltrated volumes increase with the duration of the event. Variation in flow event duration shows that the maximum value of infiltrated volume is asymptotically reached

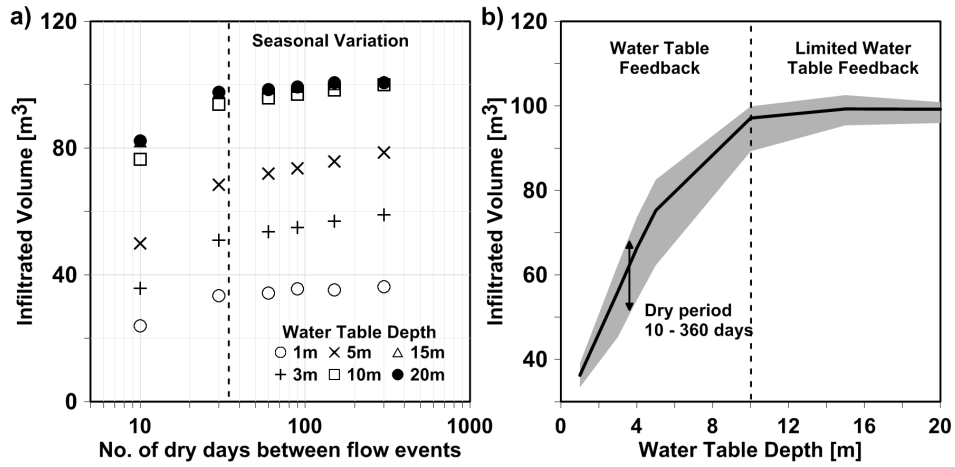


Figure 3.5: Variation of the total infiltrated volume into the streambed during one event against varying: a) dry period durations between events (specified as the number of days with zero streamflow) – with different data series representing a different water table depth, dashed line represents the dry period at which the rate of variation of infiltrated water becomes log - linear, and b) water table depths, with the variation due to different duration of dry periods indicated by the shaded area, dashed line represent the approximate apparent water table depth threshold.

later for longer stream flow durations and for deeper water table depths. For example, the increase in infiltrated volume reaches a steady value at water table depths of around 10 m, 15 m, and >20 m for one-, five- and ten-day long flow events respectively.

For shallow water tables, the increase of infiltration losses is limited due to the rise and lateral expansion of the groundwater mound below the stream which quickly reduces the hydraulic gradient and regulates the infiltration rate (Fig. 3.3i). For deep water tables, there is more pore-space available to enable continued lowering of the IWT which enables higher infiltration and, consequently, a larger increase in total infiltration volume (Fig. 3.6). As the streamflow duration increases, the maximum depth at which this feedback from the water table occurs is therefore also greater. Thus, the limit to the depth of eventual SW - GW bi-directional interactions may be 10s of metres in the scenarios simulated, but in principle even greater for other combinations of high permeability sediment and long flow durations.

3.5.4 The influence of sediment properties

Simulations showed that the total streambed infiltration volume per event increases as the sediment hydraulic conductivity increases (Fig. 3.7a), the 'coarseness' of moisture-retention curve increases (Fig. 3.7b), or the amount of total pore space available increases (Fig. 3.7c).

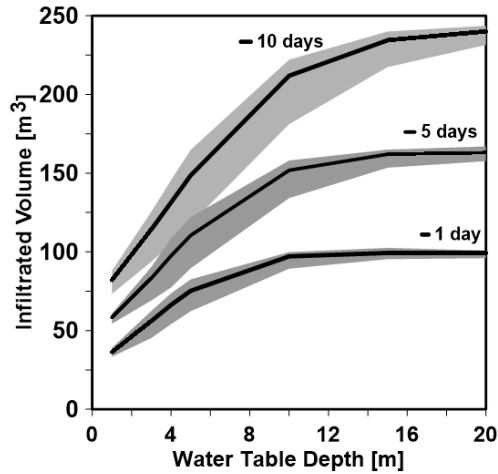


Figure 3.6: Variation of streambed infiltration volume during a single event as a function of the duration of the streamflow event, the length of dry period between events (shaded range in the style of Figure 3.5), and water table depth.

Total infiltration is particularly sensitive to changes in hydraulic conductivity due to the fact that infiltration rate is proportional to the hydraulic conductivity and the hydraulic gradient. For a specific stream stage, the hydraulic head and consequently the hydraulic gradient remain similar. The opposite occurs for low values of hydraulic conductivity. However, when the shape of the moisture-retention curve is changed, rates of infiltration also change due to changes in hydraulic gradients. Higher changes of hydraulic gradients are expected for coarser material, particularly at low degrees of saturation, due to the sharper change of pressure head in relation to water content.

Total infiltration increases with increasing storage capacity, it is expected since there is more pore space available under partly saturated conditions that can be filled at higher rates of infiltration when the material is partially saturated. However, this effect is quite small. This suggests that the capacity for water to flow through the streambed and underlying sediments, rather than the absolute volume of storage available beneath the stream, is the primary control on the overall volume of streambed infiltration.

For the relatively high transmissivity values ($68.2\text{-}95.7 \text{ m}^2 \text{ d}^{-1}$) considered in the analysis, simulations (not shown) showed that the infiltration rates and water table depth thresholds are relatively insensitive to changes in this parameter. A small variation which varies from 5 % for shallow water tables to 0.3 % for the deeper water table was observed of the total infiltration rate in relation to the base case scenario due to the development and dissipation of the groundwater mound and its interaction with the IWT. For deep water tables, the interaction with the water table

was limited and consequently the variation of the total infiltration due to changes in transmissivity was negligible.

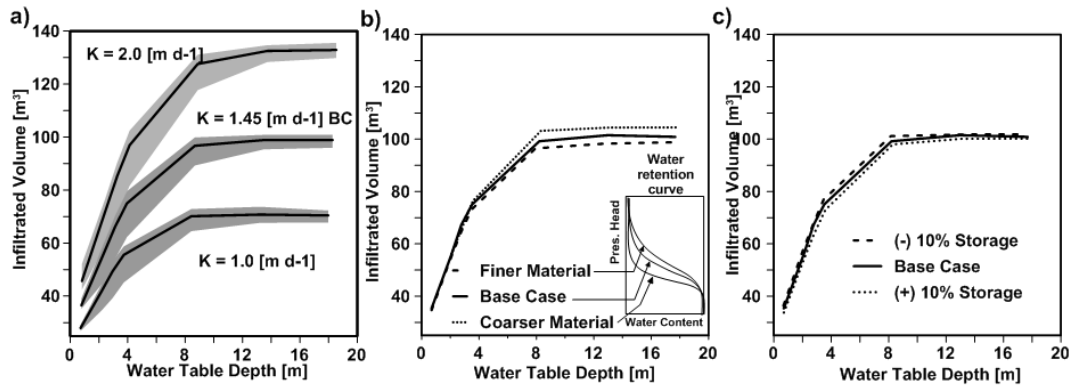


Figure 3.7: Variation of infiltrated volume in relation to water table depth for changes in the hydraulic properties: a) hydraulic conductivity, shaded area indicates the range of variation for dry period duration between flow events of 10 to 360 days, b) water retention curve shape, and c) variation of storage capacity; part b) and c) correspond to a seven-day event occurring after a dry period of 360 days (see Table 3.1).

3.5.5 The influence of geometrical characteristics of the stream channel

It is found that infiltration through the streambed for both trapezoidal and rectangular channel geometries showed differences with higher values (6 %, not shown) for the rectangular shape which are consistent with the shorter wetted perimeter in comparison with the trapezoidal shape that reduces the influence of lateral flow due to capillary flux during the advance of the IWT. Since the triangular channel geometry does not have a ‘streambed’ as such, for comparison of all three geometries tested, just the infiltration through the streams’ banks was considered. Figure 3.8 shows that the total bank-infiltrated volume increases substantially for both the triangular and trapezoidal shapes in comparison with the base case rectangular shape. The increase is also affected by the water table depth, although a threshold for maximum infiltration rates is still reached for deeper water tables for all cross-section shapes.

The increase of the bank-infiltrated volume for triangular and trapezoidal shapes is intuitive due to the increase of the wetted perimeter. The combination of both vertical and lateral flow driven by gravity and capillary forces plays an important role in total stream losses. The higher stream bank losses for a triangular cross section is explained by the smaller perimeter of the wetted front which makes the combined

horizontal-vertical flow reach higher values. For the trapezoidal shape, the base of the channel increases the perimeter of the overall wetted front affecting both the lateral flow due to capillary forces and the vertical flow which in turn results in less infiltration in comparison to the triangular shape. In the case of the rectangular channel, the low infiltrated volume at the banks is the result of the short wetted perimeter of the channel and the lower influence of lateral flow which in turn makes the vertical flow higher than the streambed flow of the trapezoidal shape section (Xian et al., 2017).

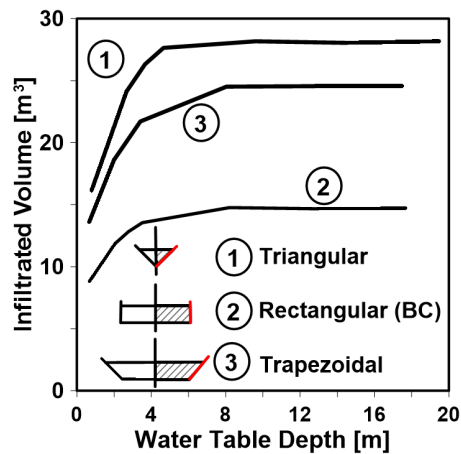


Figure 3.8: Variation of the infiltrated volume due to variations in the shape of the channel cross section for the flow event defined in the base case scenario. Plotted values correspond to water infiltrated only through the streambanks (red lines)

Figure 3.9 indicates that the infiltration per unit length varies for different combinations of changes in channel width and water table depth. For example, for wider channels, the infiltration per unit length receives feedback from the water table at deeper water tables whereas for narrow channels this interaction only occurs for shallower water tables (Fig. 3.9a). The smaller degree of interaction with the water table for narrower channels is explained by the shorter wetted perimeter of the IWT which results in a rapid advance, at highest rates of infiltration, of the IWT. When the IWT reaches the water table, the development of a groundwater mound, which is also narrower, is more easily spread laterally due to the higher hydraulic gradient, resulting in less feedback to the infiltration rate. As the channel width increases, the interaction with the water table last longer due to the development of a bigger groundwater mound which reduces the hydraulic gradient and consequently the infiltration rate.

The variation of the infiltration rate through both the streambed and streambank shows a non linear relation with the stream width. Figure 3.9b shows how the infiltration per unit length through the streambed changes from higher values for narrow

channels to almost a constant value for wider channels. For shallow water tables, the streambed infiltration reaches a constant value for channels wider than 5 m, whereas for a deep water table of 20 m, the infiltration through the streambed only reaches a constant value for channel greater than 15 m. This result shows that lateral flow has greater influence in narrow channels than in wide channels. Additionally, the infiltration rates through the streambanks increase as the water table depth increases as shown for the two end members plotted in Figure 3.9.

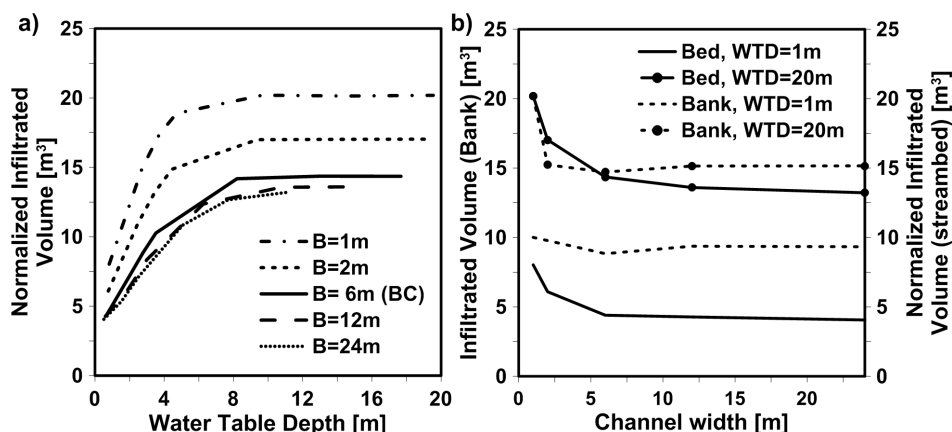


Figure 3.9: Channel width analysis: a) Variation from the base-case (BC) scenario of the infiltrated volume per unit length, for different stream channel widths (B) and water table depths; b) variation of the volume infiltrated per metre width through the streambed (solid lines) and streambank (dashed lines) in relation to the channel width for a shallow and deep water table (WTD).

3.5.6 Caveats and limitations of the analysis

Evapotranspiration processes as well as preferential flow are not considered in present analysis. For evapotranspiration, it is expected to increase the infiltration rates due reduction of water in the unsaturated zone by direct evaporation from the streambed or plant transpiration. This effect may be even more significant for wider channels were a great area is exposed to evaporation processes. Additionally, evapotranspiration may extract a significant amount of water for cases in which the water table is shallow, it will affect the degree of saturation of the unsaturated zone and consequently lead to changes in infiltration rates. In the case of preferential flow, flow paths can pathways with higher rates of infiltration resulting in higher volumes of transmission losses and consequently the potential increase of focused recharge (Zarate et al., 2021).

Additionally, the analysis considers the development of ponded conditions due to a water accumulation rate higher than the infiltration capacity of the streambed by using a constant head boundary condition. This condition restricts the appropriate evaluation of the initial infiltrated volume, since in a 2-D model the pressure head boundary condition supplies an infinite amount of water which can result in an unrealistic infiltrated volume. It also implies that the only limitation to provide water is the duration of streamflow event.

It is also known that streamflow events show a stochastic behaviour and the saturation and water table depth can show highly ranges of variation, this condition has not been in order to take control of the degree of saturation and the water table depth which in turn will allow a comparison between different dry condition and streamflow events.

3.6 Conclusion

A conceptual model of factors that control infiltration through the variably saturated zone around, and below, an ephemeral streambed has been developed. Then a quantification of the relative importance of these factors using a suite of numerical model simulations was performed. Specifically, streamflow characteristics, time duration between streamflow events, water table depth, aquifer hydraulic properties and channel geometry have been evaluated in the present chapter.

For a given streamflow event, the initial saturation conditions characterised by the duration of the antecedent dry period, the hydraulic conductivity of the sediments, and the water table depth all provide strong controls of the infiltration rates lost from the stream. As expected from the conceptual model, deeper water tables combined with longer dry periods and higher hydraulic conductivity increase the amount of infiltrated water; the opposite occurs when these parameters decrease.

Analyses of the variability of infiltration rates when the geometrical characteristics of the channel change, have important implications for hydrologic and land surface models, especially for large scale models where narrow channels are difficult to represent, which can result in the gross underestimation of infiltration rates. At smaller scales, the variation of infiltration rates through streambanks due to changes in the cross section will also impact the availability of water for biochemical processes occurring within the streambed.

Simulations also show that infiltration rates vary non-linearly with water table depth, although they become constant, dependent on the local conditions, when a

threshold in the water table depth is reached. For a homogeneous aquifer with hydraulic properties corresponding to a sandy loam material, the threshold for a 7-day streamflow event (with a 1 day peak) is reached for water table depths greater than approximately 10 meters. This threshold, beyond which bi-directional SW – GW interactions become limited, increases for longer events and can be 10s of metres in some of the scenarios tested.

In all these cases, the initial condition beneath the stream is one of partial saturation, and yet it has been demonstrated that feedback from the underlying groundwater is common during the simulated ephemeral stream flow events. Hence, it is concluded that the paradigm of characterising streams as either ‘connected’ or ‘disconnected’ derived from studies of perennial streams (Brunner et al., 2009a; Winter et al., 1998) is not applicable to ephemeral stream systems. In fact, caution should be considered against the current practice of using the term ‘disconnected’ streams at all, in favour of referring to unidirectional or bi-directional SW – GW interactions, depending on the relative extent of feedback given by groundwater to stream losses.

Chapter 4

Characterising groundwater - surface water interactions in dryland regions: A reach scale analysis

4.1 Introduction

Chapter 3 outlined and quantified the key processes controlling transmission losses in typical ephemeral stream transects. Factors such as duration, frequency, shape and magnitude of streamflow events, in addition to aquifer hydraulic characteristics, water table depth and channel characteristics were shown to play an important role in groundwater - surface water interactions (see Chapter 3). However, that analysis did not address the spatial variation of groundwater - surface water interactions longitudinally along an ephemeral channel. This has also received little attention in the literature (Cuthbert et al., 2019a; Green et al., 2011). While it is expected that the same controls and processes seen in the 2-D transect analysis will also operate longitudinally down an ephemeral stream network, the changing availability of the streamflow available for infiltration will also vary. This may potentially lead to complex patterns of transmission losses downstream, which are important to understand for the wider aim of improving dryland water balance partitioning. To enhance such an understanding of the spatial extent of ephemeral groundwater - surface water interactions, a series of 3-D numerical simulations using a fully coupled physically-based distributed model was carried out, and this forms the basis for the current Chapter.

4.2 A conceptual model of groundwater - surface water interactions in ephemeral streams

Transmission losses and subsequent focused recharge from ephemeral streams is a common feature of mountain front basins of arid and semi-arid regions (Lerner et al., 1990; Pool, 2005; Simmers, 1997). In these settings, recharge mainly occurs by streamflow losses during episodic streamflow events received from upstream (commonly more humid) headwaters. Extending the concepts outlined in Chapter 3 (Fig 3.1) into 3-dimensions, a conceptual model representing focused recharge processes from an idealised ephemeral stream into a homogeneous isotropic aquifer is represented in figure 4.1. In addition to the initial water content of the streambed, which has been evaluated in the Chapter 3, infiltration and consequently the development of the IWT along the channel is mainly influenced by available water for infiltration along the channel, the lateral movement of water below the channel, and the water table depth.

The amount of water available along the channel depends on the balance between how fast the streamflow moves along the channel and the streambed infiltration rates. When a streamflow event enters a reach from upstream, water flowing in the channel starts to infiltrate into the shallow alluvial aquifer. Higher infiltration rates are expected at the onset of the streamflow event depending on the degree of saturation of the streambed prior to the event (see Chapter 3). If the amount of water flow in the channel is less than the infiltration rate, the downstream end of the channel will become dry. The extent of the IWT below the streambed is expected to vary along the channel due to infiltration rates and the lateral flow below the channel. The water moving within the streambed in the direction parallel to the channel will influence the degree of saturation along the channel and consequently the infiltration rates. If the water table is deep, infiltration rates along the channel will be higher due to higher hydraulic gradients in the IWT (Fig. 4.1b and c), which in turn result in higher values of total infiltration rates. However, if the water table depth is shallow enough, a fully saturated zone along the channel may develop between the stream and the aquifer as the IWT joins up with the water table below (Fig. 4.1d). This will likely result in lower infiltration rates due to lower hydraulic gradients between the stream and the aquifer and eventually result in lower transmission loss from the stream.

A groundwater mound will be developed as a result of infiltrated water reaching the water table, and its width and height is expected to vary longitudinally and transversely to the channel, depending particularly on the infiltration rates and hydraulic

properties of the aquifer. The height of the water table mound will decrease along the channel as long as the infiltration rates along the channel are lower than hydraulic-driven recession rates of the aquifer. Otherwise, or for initially shallow water table conditions, the groundwater mound is more likely to intersect the channel streambed.

When there is no more inflow into the channel at end of the streamflow event, the channel becomes dry and the water table or the IWT starts to separate from the streambed (see Chapter 3). Depending on the presence of an unsaturated condition between the stream and the aquifer, the rate at which the water table/IWT separates from the streambed will depend on the location in relation to the source point and the hydraulic properties of the aquifer. Locations far from the upstream boundary are expected to result in a faster rate of separation due to the influence of the higher recession rate closer to the upstream inflow as rates of recharge tend to reduce with distance from source. Groundwater mounding will start to recede once recharge rates decline below the groundwater hydraulic-driven recession rate (Cuthbert, 2010; Cuthbert et al., 2016; Healy and Scanlon, 2010). Eventually, the groundwater mound will become fully dissipated as it spreads out laterally and longitudinally.

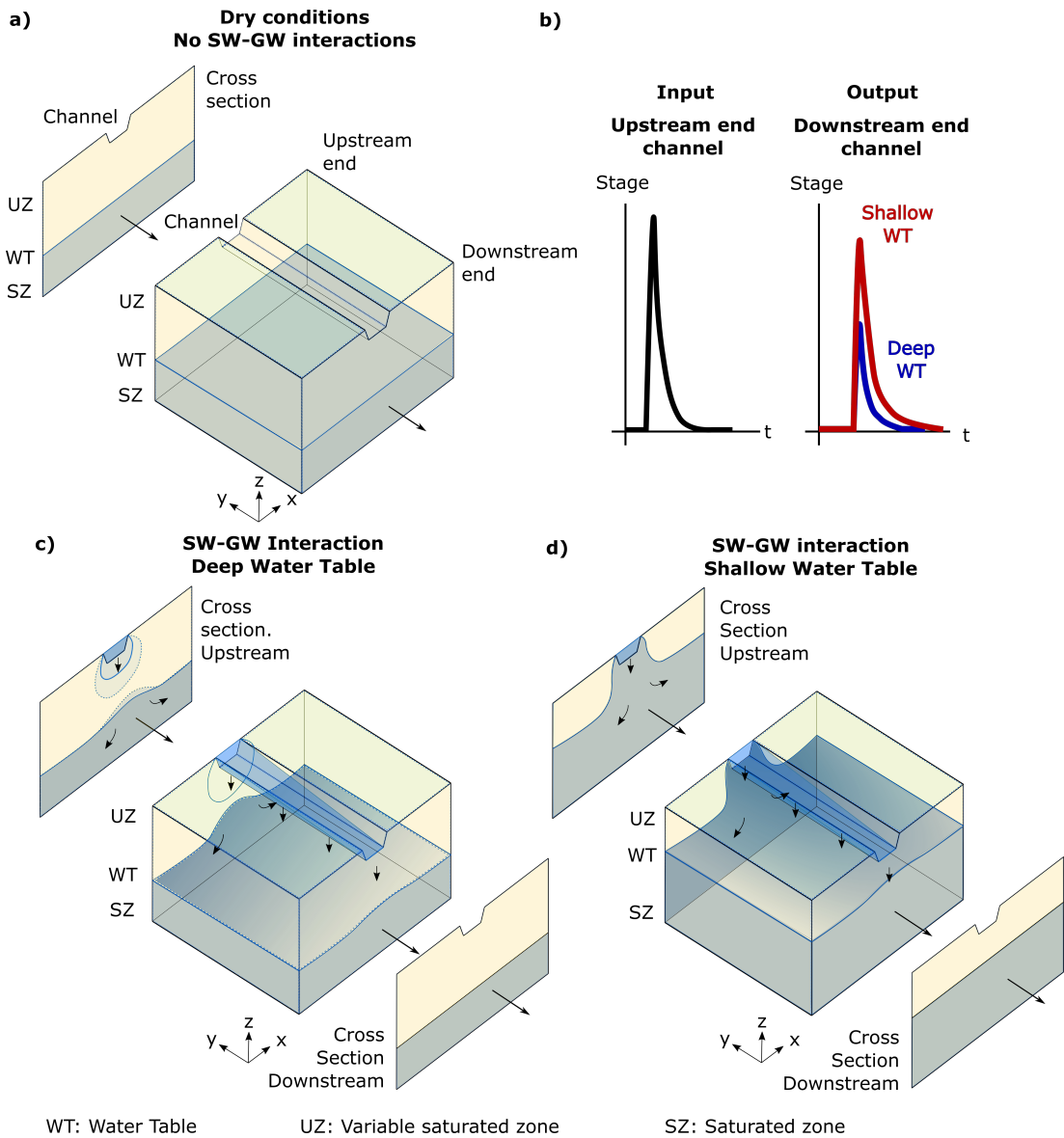


Figure 4.1: Conceptual representation of groundwater - surface water interactions during a streamflow event: a) dry channel, no groundwater - surface water interaction; b) hydrograph of streamflow event at the upstream end (left) and streamflow event at the downstream end of the channel after transmission losses have occurred (right); c) groundwater - surface water interactions occurring during a streamflow event for deep water table conditions; d) groundwater - surface water interactions for shallow water table conditions. Arrows represent flow directions.

4.3 Methods

4.3.1 Numerical modelling

The purpose of the numerical modelling undertaken here was to quantify the influence of key factors controlling the spatial variation of transient infiltration rates along idealised ephemeral streams. A set of scenarios was developed to simulate the spatial variability of the infiltration process under variations in: 1) streamflow event duration; 2) initial water table depth; and 3) hydraulic properties of the homogeneous material underlying the channel. Other factors such as magnitude and frequency of streamflow events and channel geometry also influence infiltration rates below the channel (Chapter 3). However, their influence on the spatial variability along the channel can intuitively be extended to the reach scale, since those parameters will directly increase or decrease the rate at which groundwater - surface water interactions take place. Therefore, in this Chapter 3 only the three scenarios listed above have been considered, since they govern the longitudinal controls on water partitioning along the streambed.

4.3.2 Distributed River Flow and Sediment Transport Modelling System, SHETRAN

SHETRAN is a physically-based distributed modelling system, which is able to model water flow, sediment and solute transport in a river basin (Birkinshaw et al., 2010; Ewen, 2001; Ewen et al., 2000). SHETRAN allows for the characterisation of surface-subsurface processes in a fully 3-D environment and hence is an ideal choice for the purpose of the present analysis. The model uses a fully coupled finite difference scheme to solve the Richards equation (see Appendix A, eq. A.1) for a variable saturated zone, and the diffusive-wave equation for overland flow and channel flow (see Appendix A, eq. A.3). SHETRAN represents the different components of the hydrological cycle by using three basic elements: (i) rectangular grid elements representing surface and subsurface stores; (ii) channel links representing rivers and streams between grid cells; and (iii) bank elements located on both sides of the channel links. A full description of all modules as well as the binary files can be found in <https://research.ncl.ac.uk/shetran/>. Only the water flow module was needed for the following analysis.

4.3.3 Model Geometry

As in Chapter 2, the geometry of the model was defined according to common values from ephemeral streams in arid and semi-arid environments (Chen et al., 2019; Singer and Michaelides, 2014; Sutfin et al., 2014). The aquifer system was parameterised to represent typical characteristics of mountain front aquifer systems (Sutfin et al., 2014), where groundwater is mainly recharged by the loss of water from ephemeral streams (Lerner et al., 1990). Thus, the model domain was specified as a rectangular basin 2 km wide and 10 km long with a stream located in the middle along the longest dimension (see Fig. 4.2). The aquifer depth was specified as 60 m, typical of alluvial aquifers in arid and semi-arid regions (Lerner et al., 1990; Pool, 2005). Channel cross sections were specified as rectangular and 12 m wide (see Fig. 4.2) (Jaeger et al., 2017).

The dimensions of the domain were chosen in order to reduce the influence of the boundary conditions on the simulated processes. Thus, the specified model width is wide enough to support a groundwater mound underneath the channel, as a result of focused recharge, which is subsequently dissipated within the domain. The main direction of groundwater flow is assumed to be parallel to the stream except when mounding occurs during/after flow events, when there will be a transverse component. Stream slope and surface slope were specified as 1 ‰, consistent with common dryland channel gradients (Chen et al., 2019; Singer and Michaelides, 2014).

To capture the spatial variation of groundwater - surface water interactions, the model was discretised horizontally in 47×53 rectangular elements. Grid elements vary in area but have the same length (200 m) in the direction parallel to the stream. In the direction perpendicular to the stream, grid cells below and around the stream were refined in order to properly capture the spatial and temporal variation of infiltration as well as the dissipation of the groundwater mound in the aquifer. Thus, cells below the stream have a width of 3 m (3 cells) and cells on both sides of the stream have a width of 5 m. The remaining cells varied with distance to the stream from 10 to 100 m with the first 5 cells increasing to 10 meters up to a maximum of 50 m width. Then, the following 13 cells were specified as 50 m width each. Finally, the last 3 cells had 100 m width each.

Vertically, the model was discretised into 40 elements. In order to capture the highly nonlinear variation of the wetting front below the stream, the first 100 cm of the variable saturated zone was discretised in 10 elements of 10 cm depth each. Then, the subsequent 200 cm were discretised with 20 elements of 20 cm, followed by 19 elements of 1 m depth. Finally, one element of 38 m to reach a depth of 60 m.

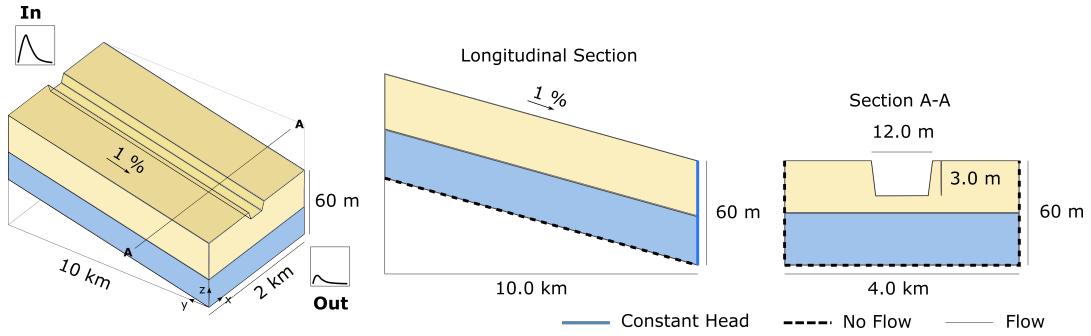


Figure 4.2: Schematic of the model domain, geometry and boundary conditions corresponding to a typical alluvial aquifer found in arid and semi-arid regions. Not to scale.

4.3.4 Boundary conditions

Boundary conditions of the aquifer were assumed to be no-flow conditions for the bottom and both sides of the model domain. A no-flow boundary condition on the sides assumes a system of parallel streams, a simplified condition that is a reasonable assumption in arid and semi-arid mountain basins (Kernodle, 1999; Morin et al., 2009). The downstream end of the model was specified as a constant head boundary condition. This condition represents a discharge (exfiltration) zone such as lakes, perennial streams, or wetlands.

To best observe the behaviour of the development and dissipation of the groundwater mounding, the initial water table elevation in the model was set parallel to the ground. Therefore, the relative behaviour of any groundwater mounding should result only as a response to recharge and the global water table gradient, with no influence from the shape of the initial water table. The upstream end of the model was specified as a lateral flux boundary condition which implicitly assumes that a steady-state condition has been reached prior to the start of an infiltration event. Use of a flux boundary condition as opposed to, for example, a head boundary, also restricts the unrealistic outflow of water from the top end of the model domain, which may otherwise be produced by a change in direction of the hydraulic gradient. The flow rate at the boundary was estimated as:

$$q = K_{sat}\Delta y h S_o \quad (4.1)$$

where: q is the flow rate [$L^3 T^{-1}$], K_{sat} is the saturated hydraulic conductivity, Δy is the grid size in the direction parallel to the stream [L], h is the saturated thickness of the aquifer [L], and S_o is the surface slope [$L L^{-1}$].

The use of these improved boundary conditions overcomes a major shortfall in an analogous modelling analysis previously attempted for my MSc dissertation which led to ambiguous results (Quichimbo, 2016).

Input flow to the stream was imposed as a flux boundary at the upstream end of the channel (see Fig. 4.2). The boundary was specified only on the stream cell of the uppermost layer, so it has no direct influence on the aquifer. The boundary condition at the downstream end of the channel was specified as a head dependant flux boundary, called a weir link in SHETRAN (Ewen, 2001).

4.3.5 Model time step

Since highly non linear conditions are developed in the unsaturated zone, the time step is automatically adjusted in SHETRAN in order to guarantee numerical convergence and stability of the model (Ewen, 2001). Nevertheless, model results were reported at 1 h time steps.

4.3.6 Model parameters

4.3.7 Test case scenarios and sensitivity analysis

A base case model was defined with a K_{sat} of 1.05 m day^{-1} , which corresponds to sandy loam sediments (Carsel and Parrish, 1988). This is consistent with the permeability of a sandy streambed typical of ephemeral streams, characterised as high-energy environments due to high flow velocities that limit the deposition of fine sediments on the streambed (Peterson and Wilson, 1988; Xie et al., 2014). While it is recognised that clogging layers can be deposited as ephemeral flows abate, they are also often scoured out during the rising stage of the next event (Lerner et al., 1990). Channel hydraulic properties were specified using a Manning's roughness of 0.035 [-] (Strickler coefficient, $M = 20$), which corresponds to coarse sandy material within a regular cross section (Phillips and Tadayan, 2006).

Unsaturated soil parameters for the van Genuchten soil water-retention curve of a sandy loam sediment were assigned as 7.5 m^{-1} and 1.89 for α and n , respectively and 0.01 and 0.33 for residual, θ_r , and saturated, θ_{sat} , moisture water content, respectively (Carsel and Parrish, 1988).

Streamflow event characteristics

Ephemeral streamflow events may show a huge variation in hydrograph shape, return period and duration. In ephemeral streams, hydrograph shape is characterised by a rapid increase and decrease of the stream stage (Costigan et al., 2017; Malmon

et al., 2004). Streamflow durations can vary from several hours up to several days (Cataldo et al., 2004; Constantz and Thomas, 1997; Knighton and Nanson, 1994; Wheater et al., 2008) or even weeks (Rau et al., 2017). Therefore, to simulate an event with such characteristics, a linear reservoir model was used to create synthetic hydrographs (Beven, 2004).

A linear reservoir model assumes that water discharged from the reservoir Q [$L^3 T^{-1}$] is proportional to its storage S [L^3]:

$$Q = kS \quad (4.2)$$

where: k is proportionality constant [T^{-1}].

By applying a mass balance for the reservoir:

$$\Delta S = I - Q \quad (4.3)$$

and combining Eq. (4.2) and Eq. (4.3). The resulting equation was discretised over time, and then solved by a finite difference approach. The final equation for discrete streamflow event resulted in:

$$Q_t = (1 - k\Delta) Q_{t-\Delta} + k\Delta I_t \quad (4.4)$$

Parameter k of the above discrete transfer function represents the inverse of the residence time of the reservoir T_r [T], which in the case of a continuous time model can be specified as:

$$T_r = -\frac{\Delta t}{\ln(1 - k\Delta t)} \quad (4.5)$$

The hydrograph obtained from eq. 4.4 for a rectangular pulse event results in a hydrograph with a sharp rise at the beginning of the event, followed by an exponential decay of flow rate.

Using eq. 4.4, a streamflow event with a mean residence time of one day was specified as the base case scenario. The streamflow was generated considering a pulse event of $12 \text{ m}^3 \text{ s}^{-1}$ applied for one day. This large event size was chosen to allow for the evaluation of infiltration rates under the influence of high streamflow stages (pressure head), as well as infiltration rates dominated by capillary forces at lower stages.

Water table depth

In order to evaluate the influence of the water table depth on transmission losses, a set of scenarios was defined by fixing the baseline hydraulic properties and flow hydrograph but varying the water table depth between a specified range (2 and 20

meters, with 2 m increments) below the streambed. Flux at the upstream end of the aquifer was estimated using Eq. (4.1).

Streamflow variation

In order to evaluate the impact of hydrograph shape on infiltration rates along the channel, the residence time of the linear reservoir controlling the streamflow (Eq. 4.5) was varied between 1 and 10 days with 1 day increments, while the hydraulic properties were fixed and in combination with shallow and deep initial water table scenarios. The total magnitude of the event ($12 \text{ m}^3 \text{ s}^{-1}$) was held constant. A summary of model scenarios is presented at the end of this section in Table 4.2.

Aquifer hydraulic properties

In order to evaluate the influence of the sediment hydraulic properties, two different sets of substrate properties characterising high and low permeabilities were analysed in addition to the base case scenario: loamy sand (high) and loam (low). The hydraulic properties are specified in Table 4.1. For these scenarios, all the simulations were performed for the same ranges of initial water table depth (2-20 m) (see Table 4.2).

Table 4.1: Aquifer hydraulic properties considered for the analysis (Rawls et al., 1982)

Sediment Texture	Sediment hydraulic properties					
	θ_s [$\text{m}^3 \text{ m}^{-3}$]	θ_r [$\text{m}^3 \text{ m}^{-3}$]	n [-]	α [m^{-1}]	K_{sat} [m d^{-1}]	$\theta_s - \theta_r$ [$\text{m}^3 \text{ m}^{-3}$]
Loam (fine)	0.43	0.045	1.56	3.6	0.2496	0.39
Sandy loam (medium)	0.41	0.065	1.89	7.5	1.0608	0.35
Loamy sand (coarse)	0.41	0.057	2.28	12.4	3.5016	0.35

Table 4.2: Model scenarios and number of simulations

Parameter	Scenario	Range of variation [d]	Water Table [m]	Number of simulations
Hydraulic properties	Loam (fine)	-	0 - 20	10
	Sandy loam (Base case)	-	0 - 20	10
	Loamy sand (coarse)	-	0 - 20	10
Residence time	Shallow water table	1 - 10	10	10
	Deep water table	1 - 10	20	10
Total				50

4.4 Results

4.4.1 Characterisation of groundwater - surface water interactions

The model results show highly dynamic interactions between surface and groundwater components, which is illustrated for the deep initial water table base case model in Fig. 4.3. When the streamflow event starts ($t = 0$ d), an inverted water table (IWT) starts to develop below the bottom of the channel. The IWT initially keeps expanding longitudinally and below the stream as more water infiltrates into the aquifer. However, sometime between day 2 and 3, the IWT starts to shrink as the amount of water provided by the streamflow is less than the rate of infiltration. At day 5, infiltrated water starts to impact the water table depth, hence a groundwater mound has started to develop (Fig. 4.3). As the groundwater mound keeps rising in a direction parallel to the channel, it is also transversely and longitudinally dissipated towards the boundaries (Fig. 4.3b, day 6).

The size of the groundwater mound depends on the amount of recharge. Hence, as the amount of water infiltrated along the channel decreases with distance to source point, the height of the groundwater mound also decreases in the downstream direction of the channel.

From day 6, streamflow rates have decreased to a value lower than the saturated hydraulic conductivity, so no additional ponding occurs in the channel and the IWT dissipates. The wetting front keeps moving downward, eventually causing an abrupt rise in the water table on day 6 (see Fig. 4.3). From day 6 until the end of the streamflow event (day 10), groundwater recharge occurs only at the upstream end of the channel. Therefore, a further increase in the groundwater mound is expected in locations below the streamflow source point (i.e. Fig. 4.3, day 10). Finally, from day 10 onward the groundwater mound starts to dissipate longitudinally and transversely to the channel, as infiltration rates become zero.

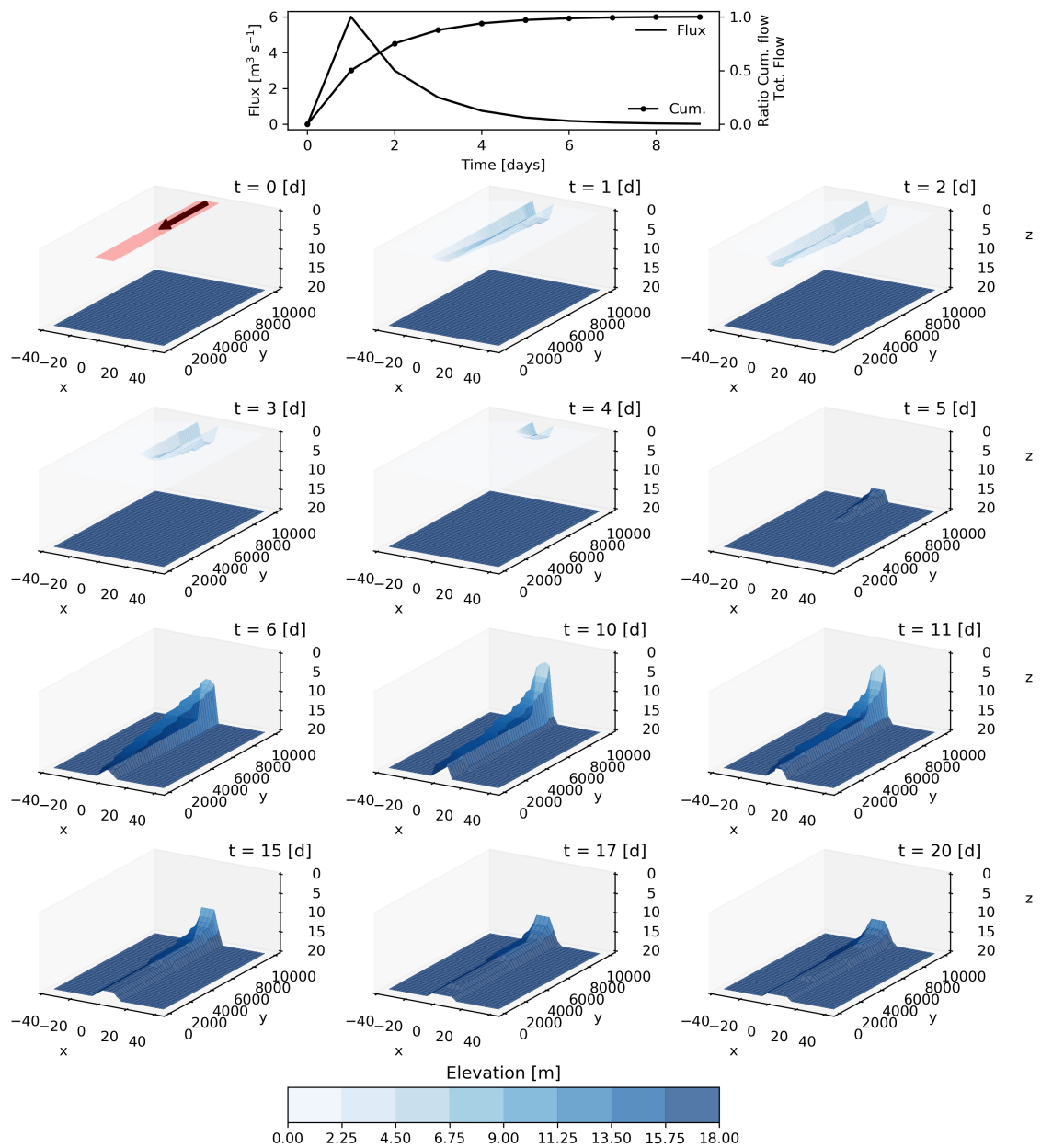


Figure 4.3: Groundwater - surface water interactions for a deep initial water table condition (depth (z) = 20 m). The inverted water table is shown in transparency. $z=0$ corresponds to the elevation of the bottom of the channel. Hydraulic properties of the sediments correspond to the base case sandy loam texture (see Table 4.1). A streamflow influx was used with total magnitude $12 \text{ m}^3 \text{ s}^{-1}$ (see Sect. 4.3.7), the hydrograph and cumulative flux of which is shown in the uppermost panel. Times were selected to indicate an illustrative variety of states of groundwater - surface water interaction.

The development of the IWT during the streamflow event can be clearly observed

in figure 4.4, where there is variation in the degree of soil saturation with depth for both shallow and deep water tables and at specific locations along the channel. The variation of the saturation is reported at the beginning of each time step. For both initial water table depths, the state of full saturation defines the extent of the IWT. The size of the IWT along the stream decreases with distance from the source point, located at 10 km on the y axis (Fig. 4.4, right panels). There is a relatively linear decrease in the depth of the IWT along the channel for both deep and shallow water table conditions (days 1 to 4) (see Fig. 4.4, shallow and deep saturation profiles).

Fig.4.4 shows a comparison of the responses for the deep and shallow initial water table conditions. For a shallow initial water table (solid blue line in Fig.4.4), the IWT grows at a rate similar to the deep water table case. However, as less water is required to fill the unsaturated zone, the interaction between the IWT and the water table starts earlier (during day 3). A fully saturated zone between the surface water and groundwater is already developed at day 3, and infiltration rates decline as a result of lower driving hydraulic gradients.

A similar initial rate of development of the IWT for both deep and shallow initial water tables can be attributed to an initially similar water content within the unsaturated zone and there is no upward hydraulic feedback from the water table in either case.

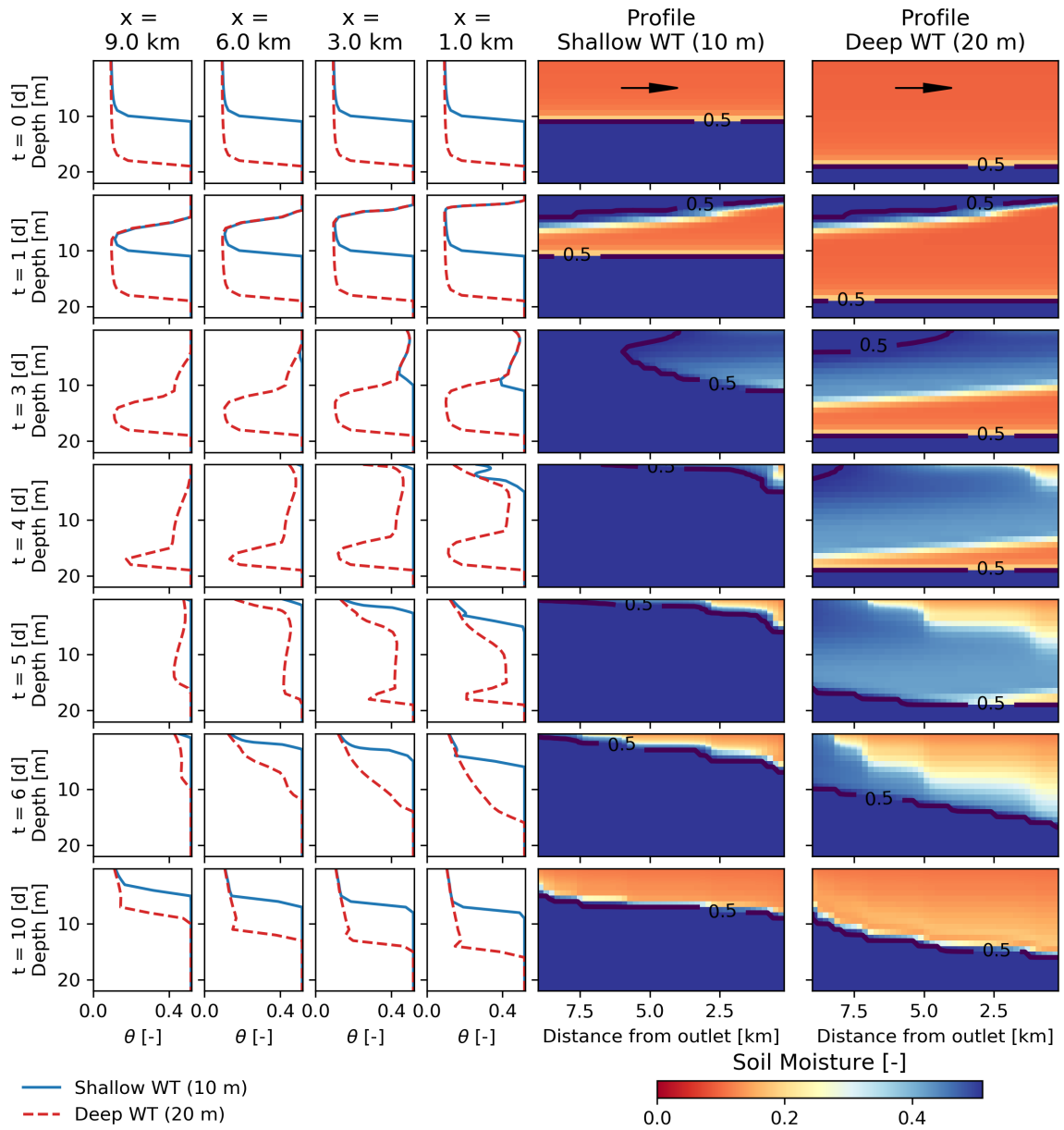


Figure 4.4: Temporal and spatial variation of the degree of saturation with depth for selected locations along the channel and longitudinal profile for specific times. Longitudinal saturation profiles along the centre of the channel correspond to deep (dashed red line, depth = 20 m) and shallow (solid blue line, depth = 10 m) initial water table conditions. Hydraulic properties of the sediments correspond to the base case sandy loam texture (see Table 4.1). The based case streamflow hydrograph of $12 \text{ m}^3 \text{ s}^{-1}$ (see Sect. 4.3.7) was used as for Fig 4.3. Times were selected to indicate an illustrative variety of states of groundwater - surface water interaction.

Variation of infiltration rates along the channel

Variation in infiltration rates along the channel as well as in stream stage and water

table depth for both shallow and deep initial water tables are shown in figure 4.5. The total available water along the channel in relation to the total amount of water entering the channel at the upstream boundary is mainly characterised by a smooth variation for both shallow and deep water tables (Fig. 4.5a). Small fluctuations along the channel are attributed to high infiltration rates occurring under unsaturated conditions below the channel.

For both shallow and deep initial water table conditions, rates of infiltration at the beginning of the streamflow event (day 1) are very similar, as expected given the previous analyses (see Fig. 4.4 and also Sect. 3.5.2). Infiltration rates increase closer to the downstream outlet due to the lag caused by the flow routing along the channel (Fig. 4.5d day 1). Higher rates of infiltration correspond to lower values of stream stage, attributed to initially lower levels of saturation below the streambed that result in higher hydraulic gradients that push water faster into the subsurface. At the onset of the streamflow event, the growth of the IWT is fastest at the upstream end of the channel. This influences the degree of saturation of downstream cells by lateral flow and consequently, the infiltration rates. As the influence of hydraulic feedback of the IWT decreases with distance from the upstream boundary (10 km), this results in higher infiltration rates at distances closer to the downstream channel outlet (0 km, day 1).

At the beginning of day 2, hydraulic feedback from the water table on infiltration below the streambed is still limited, so infiltration rates for both shallow and deep initial water tables are similar. Infiltration rates are less influenced by the stream stage and there are nearly constant values of infiltration rates observed along the channel (see Figs. 4.5 c and d).

At the beginning of day 3, infiltrated water for the shallow initial condition reached the water table as recharge. A fully saturated zone developed beneath the stream at distances between 6.2 km to 9.0 km (Fig. 4.5d left). This results in the reduction of the infiltration rates as the hydraulic gradient under unsaturated conditions is reduced by the change from negative to zero matric potentials. Values of infiltration rates stay high for the region of the channel that has not developed a fully saturated zone between the channel and the water table. This condition is also observed at the beginning of day 4 between 1 and 6 km, where higher infiltration rates, regardless of stream stage, are observed in areas where a fully saturated condition has not been reached during the event. However, the further increase in infiltration rates at day 4 between 1 and 2 km is mainly attributed to the rapid change of saturation conditions

as the water table quickly decreases as a result of a combination of lower recharge values and pressure wave propagation (Fig. 4.5e, left)

For initially deep water table conditions, infiltration rates remain high for a longer time, almost until the end of the streamflow event (day 5). Temporal and spatial reductions of infiltration rates along the channel are mainly attributed to the lateral movement of water in the unsaturated zone and the stream stage. It can also be seen that as more water infiltrates, less surface water is available as the stream stage decreases faster and ultimately all water in the channel is consumed by transmission losses.

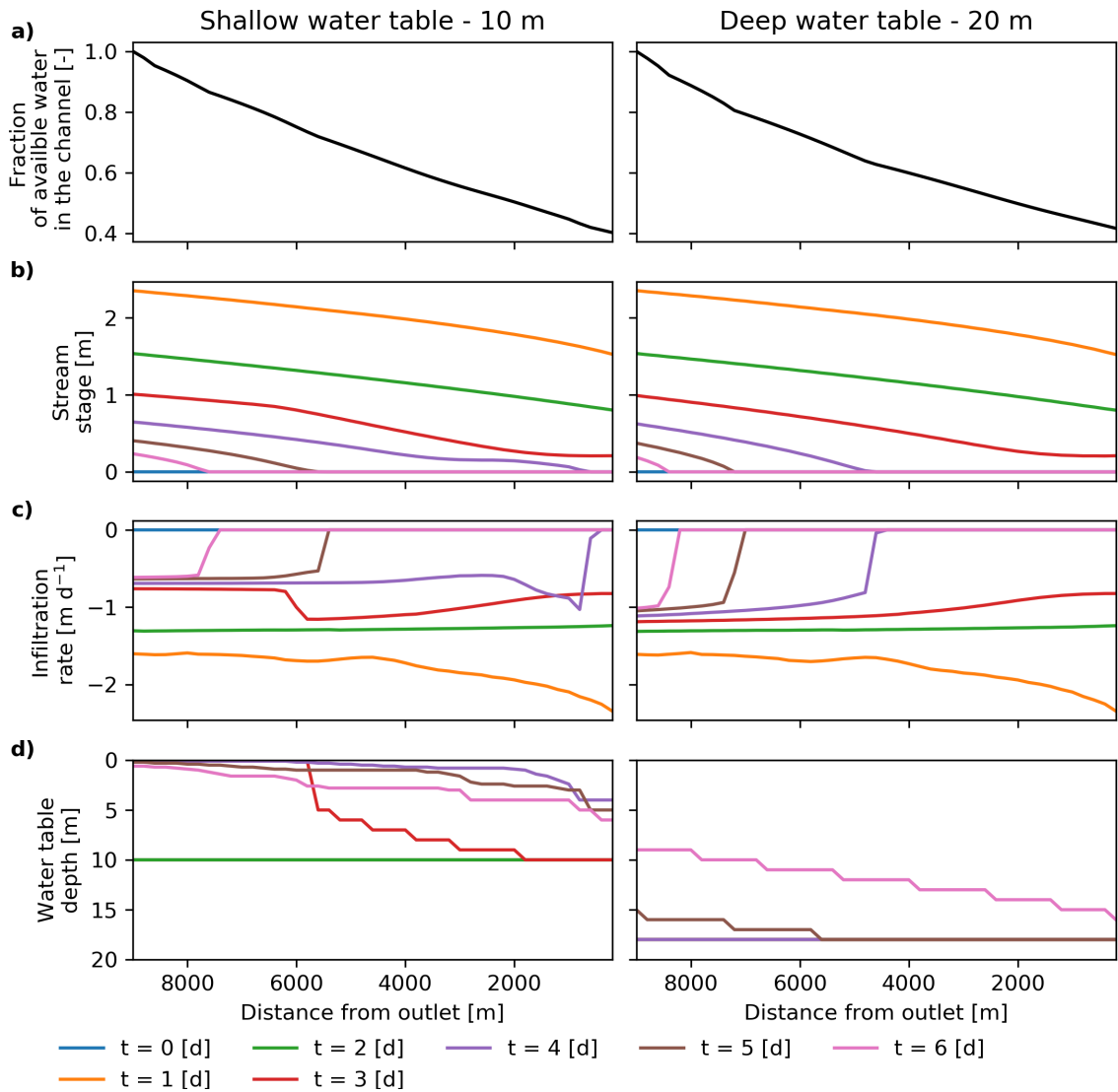


Figure 4.5: Spatial and temporal variation fluxes and states along the channel for both shallow (left) and deep (right) initial water tables: a) ratio between the total volume of water along the channel, over the entire simulation period and the total volume of water entering the channels as streamflow; b) instantaneous surface water stage profile (stream stages) at specific times indicated in the legend; c) instantaneous infiltration rates at specific times just below the streambed; and d) water table depths for specific times corresponding to panels c and d. Left-hand panels are for initially shallow, 10 m, water table conditions, and deeper, 20 m, initial water table depths in the right-hand panels. Hydraulic properties of the sediments correspond to the base case model with sandy loam texture (see Table 4.1). The streamflow event was generated using a pulse of event of $12 \text{ m}^3 \text{ s}^{-1}$ (see Sect. 4.3.7) - the hydrograph is shown in figure 4.3. Times were selected to indicate an illustrative variety of states of groundwater - surface water interaction.

4.4.2 Assessing the sensitivity of transmission losses

Sensitivity to initial water table depth variation

The influence of the initial water table position on transmission losses is presented in figure 4.6. The total amount of water lost by the stream increases non-linearly with depth to the water table (see Fig. 4.6a) up to a threshold above which the total volume of water lost by the stream becomes almost constant. As shown in the previous section (4.4.1), high infiltration rates that contribute to the total infiltrated volume are the result of the limited hydraulic feedback between the IWT and the water table. However, as the water table elevation decreases, there is increased negative feedback between the water table elevation, resulting in lower infiltration rates (see Fig. 4.5d and also Chapter 3). This is consistent with the transect results of Chapter 3, but the 3-D analysis here also enables the variations along the channel longitudinally to be seen.

Infiltration rates along the channel vary depending on the presence or absence of a fully saturated zone between the stream and the aquifer (Fig. 4.6c). Lower total infiltration rates generally occur for shallower water table conditions. Ups and downs in total infiltration rates indicates that a unsaturated condition has been developed along the channel during either wetting or drying conditions (see also left panel of figure 4.5). For depths greater than 10 m, total infiltration rates increase with distance from the downstream outlet at higher rates in comparison to shallow water tables. This occurs because there is limited hydraulic feedback from the water table (see Fig. 4.6c), which is in agreement with the rates of total infiltrated water shown in figure 4.6a.

Initial infiltration rates at the beginning of the streamflow event contribute considerably to the total infiltration, as can be seen in the steep increases at early times (see Fig. 4.6b). However, this steep increase slows down as the feedback from the water table increases, as can be seen in the departure off the cumulative infiltration curve as the water table depth decreases. This is because infiltration rates remain high as long as unsaturated conditions develop between the stream and the aquifer. Cumulative infiltration keeps rising until the streamflow event ends or infiltration has consumed all available water in the channel (see Fig. 4.6b).

To evaluate the contribution of infiltration rates along the channel in relation to the total infiltrated volume, the cumulative infiltration in the upstream direction was calculated. Thus, the ratio between the cumulative total infiltrated volume at each cell along the channel and the total infiltrated volume from whole channel (Fig. 4.6d) shows how channel sections contribute to the total infiltrated water over the

whole channel length. Thus, for shallowest water table condition, total infiltrated volume along the channel is almost constant (Fig. 4.6c). Therefore, the percentage of cumulative infiltration follows a straight line (Fig. 4.6d). As the water table depth increases, small deviations from the straight line are observed. This small variation indicates that each part of the channel contributes nearly proportionally to the total infiltrated water along the channel, regardless of the proportion of streamflow in the channel. Therefore, despite the highly non-linear behaviour in groundwater - surface water interactions along the channel, a simple constant rate may be considered enough to represent water losses along the channel.

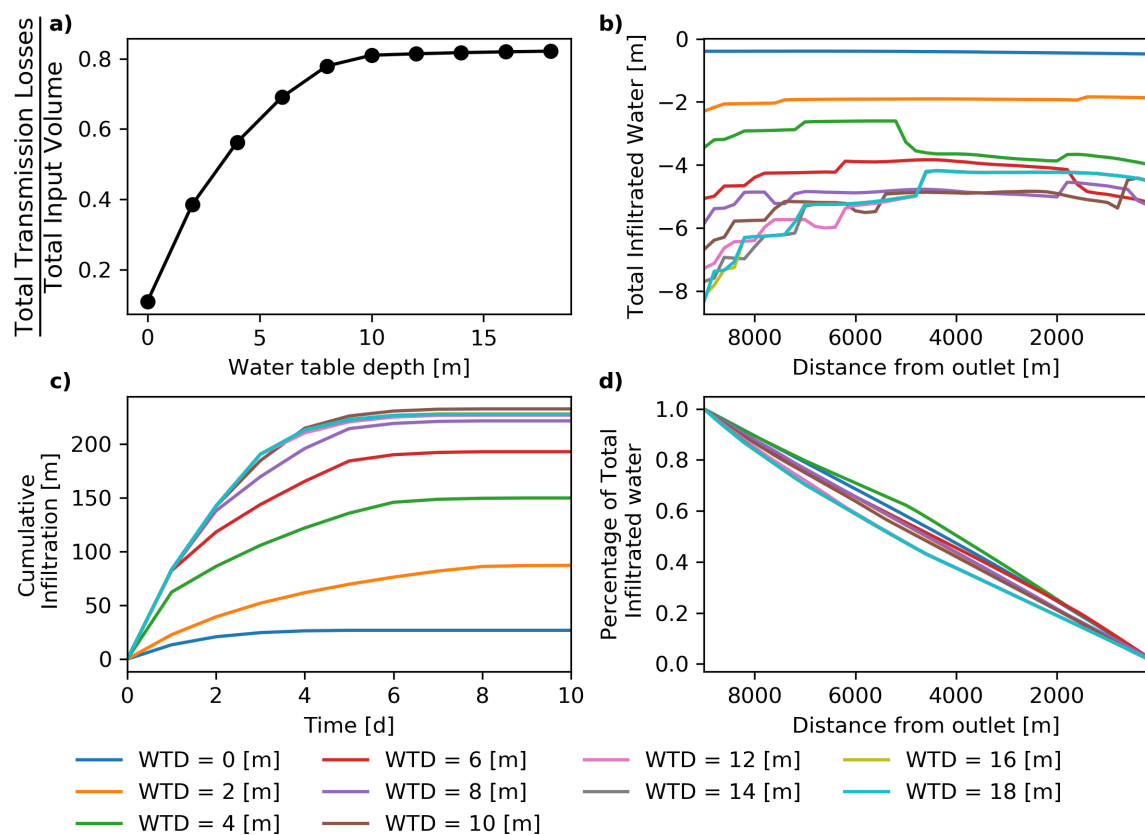


Figure 4.6: Temporal and spatial variation of infiltration rates below the stream in relation to the water table depth: a) the ratio between the total infiltrated volume and total input volume in relation to water table depth, b) total cumulative infiltration along the channel, c) temporal variation of total cumulative infiltration, and d) ratio between the cumulative, in the upward direction, total infiltrated volume at each cell along the channel and the total infiltrated volume of the whole channel. Hydraulic properties of the sediments correspond to the baseline sandy loam texture (see Table 4.1). The same streamflow event was generated using a pulse of event of $12 \text{ m}^3 \text{ s}^{-1}$ (see Sect. 4.3.7) as shown in Fig 4.3

Sensitivity to the choice of hydraulic properties

Hydraulic properties directly impact the rate of total infiltrated water volumes, as shown by different gradients of the loss ratios (total infiltrated volume over total streamflow volume) in relation to the water table depth (Fig 4.7). These properties are also reflected in different thresholds at which the water table reduces its influence on infiltration rates as follows.

For finer materials, the overall sensitivity of loss ratios to water table depth changes is relatively low. Infiltrated water moves slowly through the unsaturated zone, which in turn delays the development of a fully saturated zone between the stream and the aquifer, hence limiting any bi-directional interactions. A threshold in water loss of around 41 % is reached at shallow depths (6 m), suggesting that a further decrease in the water table will have minimal impact on infiltration rates.

For medium materials, groundwater - surface water interactions increase with depth, as can be seen in higher loss ratios in comparison to the scenario with finer materials. A threshold is reached at a greater depth, around 13 m, which results in higher volumes of water loss from the stream. The maximum amount of water loss reaches ≈ 82 % of the volume of the streamflow event.

Coarser materials result in faster groundwater - surface water interactions due to high infiltration rates, as a result of the high saturated hydraulic conductivity. This water quickly reaches the aquifer and produces a groundwater mound. However, although more water is supplied to the aquifer, the high saturated hydraulic conductivity of the material quickly dissipates it laterally and the bi-directional feedback is potentially more limited as a result. For these coarser materials, transmission losses from the stream are high enough that they consume the total volume of water supplied by the streamflow event at the upstream boundary. The plateau seen in figure 4.7 is due to this effect and not a threshold effect of the water table feedback. However, for larger streamflow events, the depth at which the water table shows no further impact on infiltration rates is expected to be higher for coarse materials than for medium and fine materials (i.e. greater than 13 m).

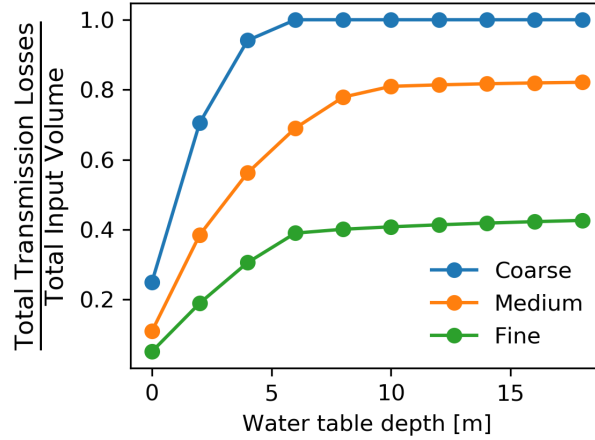


Figure 4.7: Ratio between infiltrated volume and total input streamflow volume in relation to the initial water table depth for different hydraulic properties specified in Table 4.1. Streamflow event was generated using the base case pulse event of $12 \text{ m}^3 \text{ s}^{-1}$ (see Sect. 4.3.7)

Sensitivity to the duration of streamflow events

The duration of a streamflow event also has a substantial impact on the total volume of water losses from the channel as can be seen in figure 4.8b. For the initial shallow water table depth scenario higher residence times (6) result in increased water losses up to a maximum equal to the amount of the streamflow event. For a deep initial water table depth scenario, all water entering into the channel is consumed by transmission losses for all residence times analysed.

For a shallow initial water table (depth = 10 m) (Fig. 4.8c left panels), total infiltrated water along the channel does not show great variations. This is because a fully saturated zone develops between the stream and the channel at early times so the feedback from the water table quickly regulates infiltration rates. For residence times >5 days, streamflow is totally consumed before it reaches the downstream end of channel (i.e. the channel become dry at 2 km for a $T_r = 9$ days). This is, as expected, due to higher infiltration rates in relation to the rates of the streamflow event.

For the deep water table condition (Fig. 4.8a right panel), total infiltrated volumes along the channel are higher in relation to shallow water table conditions. The higher volumes result in water losses that consume the total streamflow event at distances closer to the source point at larger residence times (i.e. the channel become dry at 6 km for a $T_r = 9$ days). The higher infiltration rates are attributed to the limited feedback from the water table, which is the result of unsaturated conditions between the

stream and the aquifer. However, as the residence time decreases, the feedback from the water table increases and consequently infiltration rates also decrease. Therefore, the residence time in combination to infiltration rates, directly impact the temporal availability of water along the channel.

The ratio between the total cumulative infiltration along the channel and the total infiltrated volume shows that the contribution of infiltrated water at different sections of the channel varies smoothly along the channel for both shallow and deep water table conditions (Fig. 4.8d). However, the shape of the hydrograph has a greater impact on the amount of total water infiltrated along the channel. Thus, for shallow water tables and longer residence times there is an increase in the rate of change of the relative cumulative infiltration rate along the channel in relation to short residence times. However, the rate of change does not show a great variation for the residence times analysed here (Fig. 4.8d, left). This is mainly attributed to higher water table feedback at shallow conditions that quickly regulate infiltration rates along the channel. For deep water table conditions, the range of variation of the relative cumulative infiltrated water increases considerably as the residence time increases. Thus, for longer residence times there is a steep decrease of the relative cumulative infiltration in relation to short residence times (Fig. 4.8d, right). This is mainly attributed to the higher rates of infiltration rates developed under unsaturated conditions as a result of the limited feedback from the water table underneath the channel.

There is a significant temporal variation in cumulative total infiltration for different hydrograph durations for both shallow and deep initial water table conditions (see Fig. 4.8e). Cumulative total infiltration is greater for initially deep water table conditions, with especially high contributions to the total infiltrated water at early time steps (see Fig. 4.8e right). The high infiltration rates at the beginning of the streamflow event are attributed to the limited feedback from the water table. Thus, for a shallow water table and longer residence times, the interaction between the water table and stream along the channel is limited. This, in combination with the low amount of water entering into the stream, result in lower infiltration rates that slowly increases the total infiltrated water. As the residence time decreases, there is more water available along the channel, so more water can infiltrate into the streambed. This results in slightly increased cumulative infiltrated water. Similar conditions are developed for deep water tables. Larger residence times results in small increases in infiltration rates over time, whereas short residence times result in high infiltration rates that produce a more steep increase in the cumulative infiltrated water.

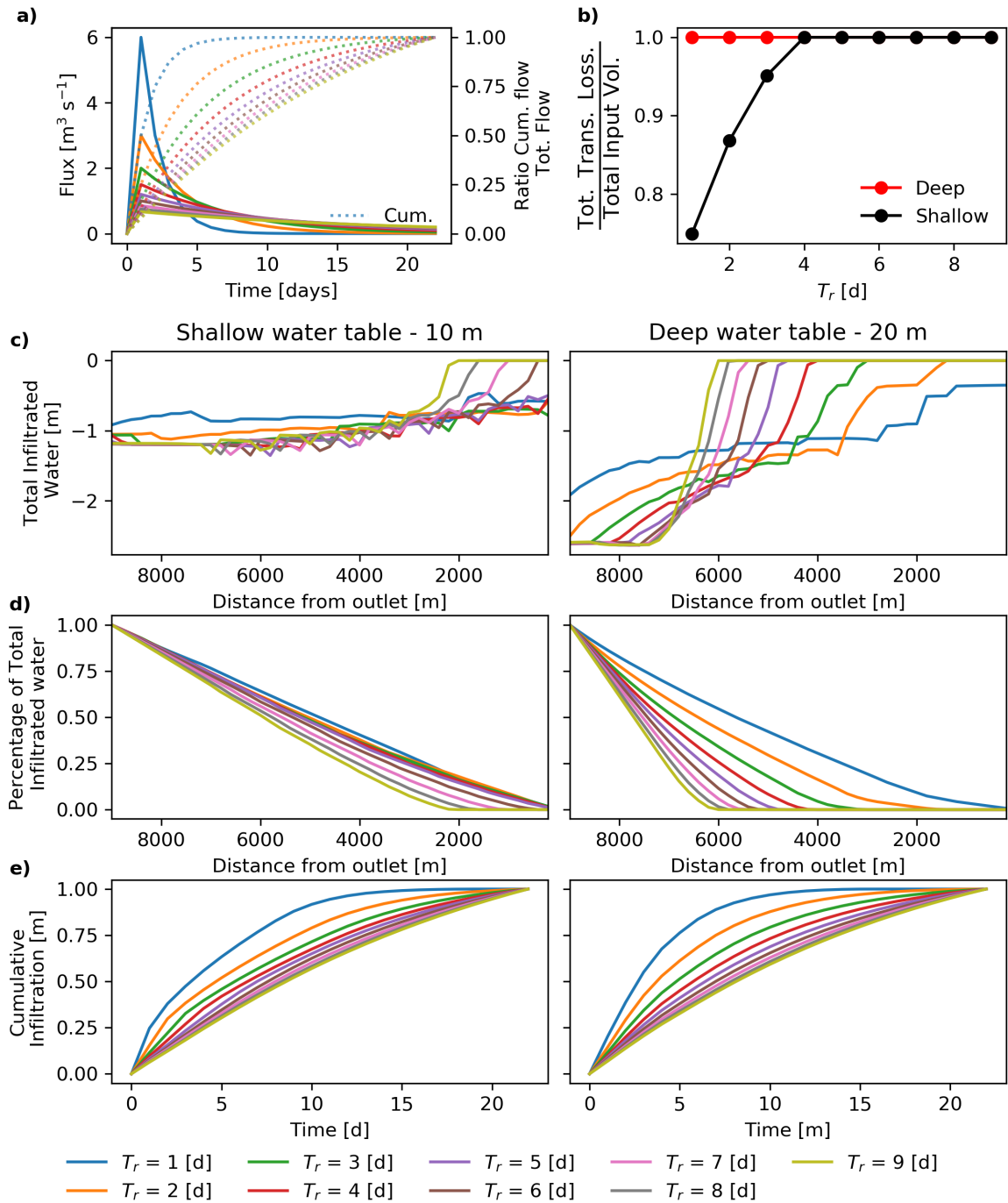


Figure 4.8: Temporal and spatial variation of infiltration rates below the stream in relation to the streamflow duration for shallow (10 m) and deep (20 m) water table depth conditions: a) total cumulative infiltration along the channel, b) ratio between the total cumulative infiltration along the channel and the total infiltrated volume, and c) temporal variation of total cumulative infiltration. Hydraulic properties of the sediments correspond to sandy loam texture (see Table 4.1). Streamflow event was generated using a pulse of event of $12 \text{ m}^3 \text{ s}^{-1}$ (see Sect. 4.3.7)

4.4.3 Caveats and limitations of the analysis

The present analysis neither considers the effect of evapotranspiration nor the influence of preferential flow (e.g., macropores). As indicated in Chapter 3, evapotranspiration is expected to increase infiltration rates by inducing lower degrees of saturation either as direct evaporation from the streambed or as riparian plant transpiration from banks and floodplains. This effect may be even more significant for wider channels where a greater area is exposed to evaporative processes. For shallow water tables, plant evapotranspiration may also take water directly from the aquifer, which in turn will affect the degree of saturation of the unsaturated zone and consequently lead to changes in infiltration rates (Wang et al., 2017a). Preferential flow may create pathways with higher rates of infiltration resulting in higher volumes of transmission losses and consequently affect the potential increase of focused recharge (Zarate et al., 2021). These pathways, which can be the result of faults, heterogeneity, or even anthropogenic activities, may exert great control on focused recharge due to their flow regulation capacity (Zarate et al., 2021). Additionally, floodplains and stream banks may also impact infiltration rates by increasing the infiltrated area and/or by the flow regulation capacity of bank storage (Dunkerley, 2008; Zarate et al., 2021).

4.5 Global distribution of ephemeral stream - aquifer interactions

Global distribution of ephemeral streams

In order to estimate how significant the influence of different water table depths may be on infiltration rates from ephemeral streams globally, water table depth distributions below all dryland streams was estimated. The analysis was restricted to dryland regions, since stream networks in these regions are likely to develop losing and ephemeral conditions. For the analysis, databases of equilibrium water table depth, global stream networks, and aridity index were taken into account.

Unfortunately, field observations of water table depth are quite limited globally and restricted to small areas generally located in developed countries. However, a simulated equilibrium water table depth dataset at the global-scale has been estimated by Fan et al. (2013) and it is available on www.sciencemag.org/cgi/content/full/339/6122/940/DC1 at a 30" grid size. The water table at each location has been estimated under steady-state assumptions and it does not represent the effect of locally perched conditions developed above regional groundwater systems. The equilibrium

water table considers vertical flow as recharge and lateral movement of water in the saturated zone driven by topography (Fan et al., 2013; Miguez-Macho et al., 2007). The model does not consider the influence of focused recharge, an omission that can lead to an overestimation of water table depth in certain regions (Reinecke et al., 2019).

Information about stream networks was obtained from Lehner and Grill (2013); Lehner et al. (2008) and is available on <http://www.hydrosheds.org/>. These data are available at scales above 15" in vector and raster formats. The analysis was performed using the 15" database. This dataset also provides stream flow information based on discharge estimation from the global WaterGap model (Döll et al., 2014). This information was then used to map perennial streams, specified as stream flow $>0.001 \text{ m}^3 \text{ s}^{-1}$ considering the uncertainty of stream flow estimates (Döll et al., 2012, 2014). Although the uncertainty of stream flow estimation is high, especially in arid and semi-arid regions (Döll et al., 2014), this method provides a global map of the distribution of perennial streams.

Dryland regions were delimited using the aridity index (AI), estimated by Trabucco and Zomer (2009) (information available on <http://www.cgiar-csi.org/data/global-aridity-and-pet-database>). Dryland regions ($\text{AI} \leq 0.65$) were selected for the analysis. Datasets of water table depth and AI were resized to a common scale of 15" in order to obtain a uniform grid size. Stream networks were mapped onto the global water table depths in order to assess their relationships. Then, streams were classified according to region and water table depth. The grid-based analysis includes the whole stream network, including rivers located in regions where the water table depth is shallow (below 0.25 m). Regions with water table depth below 0.25 m generally correspond to areas where groundwater is discharged or permanently inundated areas (Fan et al., 2013). A summary of the analysis, representing the percentage of the river network classified by water table depth, aridity index (AI), and flow above $0.001 \text{ m}^3 \text{ s}^{-1}$ is presented in Table 4.3.

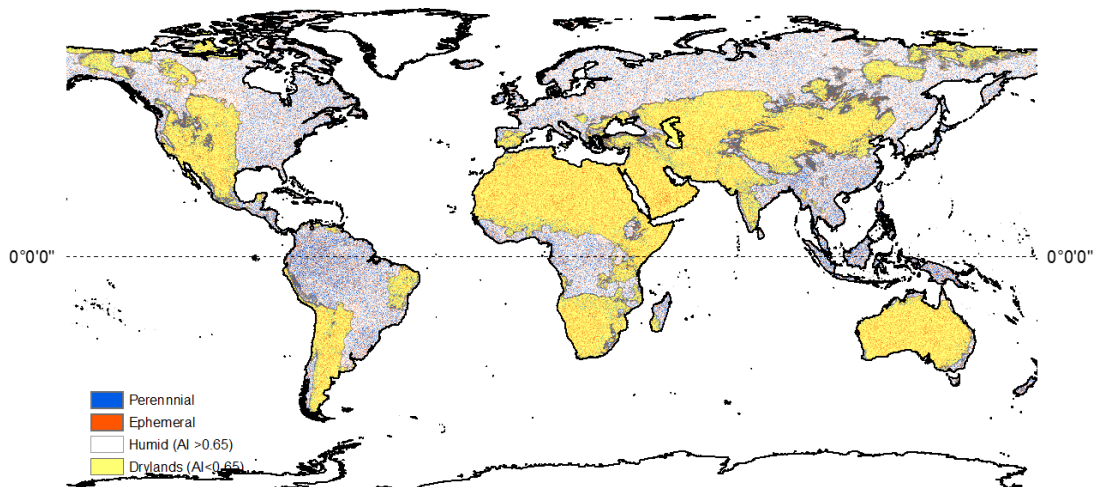


Figure 4.9: Global distribution of perennial and non-perennial streams (based on Lehner and Grill (2013); Linke et al. (2019)). Dryland and humid regions are based on values of the Aridity Index (CGIAR-CSI, 2009; Zomer et al., 2007)

Streams in dryland regions represent $\approx 60\%$ of the global river network, despite the fact that dryland regions ($AI < 0.65$) represent $\approx 44\%$ of the total continental area excluding Antarctica (see Chapter 2). Within dryland, including dry-humid regions, streams in arid and semi-arid areas represent around 33% and 36% , respectively, whereas hyper-arid region rivers represent just 12% of the total river network.

Table 4.3: Distribution of water table depth below streams in dryland regions (based on Fan et al. (2013)), all values represent percentages.

Region	Water Table Depth												Total Rivers	
	$\leq 0.25\text{m}$		$\leq 5\text{m}$		$\leq 10\text{m}$		$\leq 15\text{m}$		$\leq 20\text{m}$		$> 20\text{m}$		Tot	Per
	Tot G	Per G	Tot	Per	Tot	Per	Tot	Per	Tot	Per	Tot	Per		
Hyper-arid	7	0.2	13	0.2	11	0.1	9	0.1	8	0.0	53	0.3	12	0.1
Arid	22	2	22	1	12	1	8	0	6	0	31	2	33	1.9
Semiarid	36	13	21	6	10	3	6	2	5	1	23	6	36	11.0
Dry-Humid	43	31	21	15	11	8	6	4	4	3	16	9	20	13.9
Total	29	11	20	6	11	3	7	2	5	1	28	4	100	27

Tot = total river network, Per = perennial rivers, Tot G = total gaining river network, Per G = perennial gaining rivers.

Comparing water table depths across the global stream network indicates that potentially losing rivers in dryland regions account for 70% of the total river cells (depth $> 0.25\text{ m}$). As expected, the percentage of perennial streams decreases with aridity and also with water water table depth. Note that rivers with water table depths $\leq 0.25\text{ m}$ in Table 4.3 all should be considered as perennial.

Potential groundwater - surface water interactions in ephemeral streams

Based on the analysis of groundwater - surface water interactions using the transect (Chapter 3) and reach scale models (this Chapter), typical water table depths of ≈ 5 to 10 m can be considered as the threshold above which any increase in water table depth will not significantly exert changes on infiltration rates below the stream. Although the uncertainty of this threshold is high, given the assumption and limitation of the analysis, it is considered conservative.

Looking at the cumulative distribution of water table depth below the stream presented in figure 4.10, it can be seen that the proportion of streams with water table depths less than 10 m decreases as the aridity increases e.g. dry-humid regions have $\approx 75\%$ of rivers with water table depths less than 10 m, whereas in hyper-arid regions this values decreases to 35%. For a more conservative threshold of 5 m, the proportion of rivers in the dry-humid regions decreases to 65%, although still high, whereas in hyper-arid regions it reduces to 20%. This indicates that hyper-arid regions are less sensitive to changes to water table depths, and consequently to focused recharge as a consequence of the limited hydraulic feedback. However, it markedly contrasts with the rest of the AI regions, where a great proportion of rivers are underlain by water tables with depths less than ten meters. This implies that focused recharge in dry-humid regions could be seriously affected by changes in water table depth, due to the potential bi-directional feedback from the water table. As was shown in previous sections, depending on aquifer properties, variations of water table depth of just 1.0 m may increase transmission losses and consequently potential recharge by around 10 % (based on coarser material).

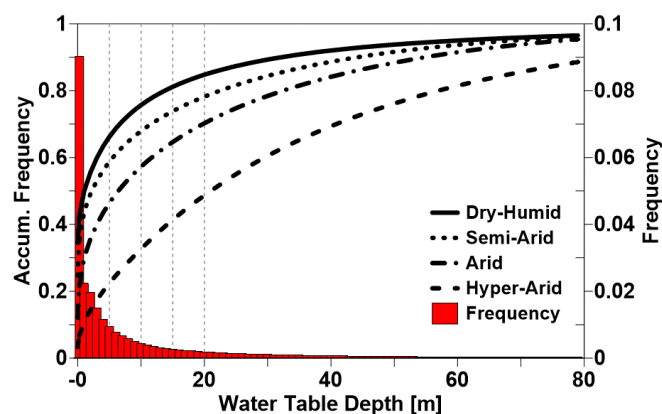


Figure 4.10: Water table depth distribution and accumulated water table depth for dryland regions (based on Fan et al. (2013))

However, despite the fact that this analysis shows broadly that changes in water table depth may affect focused recharge over large parts of the Earth's surface, the

magnitude of this effect as a proportion of total aquifer recharge in dryland regions is still unknown. Additionally, there is significant uncertainty in the values of water table depth and ephemeral stream network used in the present analysis, and hence the specific percentage values presented should be viewed with caution.

4.6 Conclusions

A spatial and temporal characterisation of groundwater - surface water interactions has been performed in order to enhance the understanding of transmission losses from ephemeral streams. The analysis applied a fully coupled physically-based distributed model in order to capture the high spatial and temporal variation of infiltration rates along the channel. The findings enhance the understanding gained from the transect analysis performed in Chapter 3 as follows:

- the temporal and spatial variation of infiltration rates along the channel is highly influenced by streamflow duration, water table depth and hydraulic properties of the streambed. Longer streamflow events in combination with deep water tables can more quickly reduce the streamflow along the channel, resulting in complete loss of inflows and dry channels over shorter distances from the source point.
- short residence times result in water reaching location far from the source which in turn increase the channel surface for infiltration to occur. However, this effect can be counterbalanced by shorter periods of available water in channel, which may ultimately lead to less recharge per channel length. Conversely, long residence times will result in more available water for infiltration, and if the rate of water flowing along the channel is equal to, or less than, infiltration rates, infiltration will exhaust water at short distances from the input source.
- the contribution of early infiltration during the onset of a streamflow event (rising limb) can reach up to 25 % of the total infiltration. However, this contribution is reduced to 6 % for longer residence times ($T = 9$ d). Hence, for working at larger scales, in many instances it may be reasonable to simplify the infiltration rate to a steady rate during an event.
- the contribution of local infiltration along the channel to the total infiltrated volume is only slightly non-linear (4.6c and 4.8d). Therefore, a temporally

variable but constant-in-space infiltration rate may be used to represent the longitudinal infiltration along channels, particularly at larger scales.

- global comparisons of water depth and ephemeral stream networks (although rather uncertain) show that potential losses from a large percentage of dryland streams may be sensitive to changes in water table depths. Feedbacks between rates of recharge and changes in water table depths due to, for example, climate change or pumping may have important implications for the availability and consequently, management of water resources in dryland regions.

The models presented here have been kept deliberately simple in order to quantify a first conceptual outline of the dynamics of groundwater - surface water interactions in ephemeral systems. Overall, the analysis highlights the importance of spatially and temporally variable groundwater - surface water interactions for the availability of surface water along the channel. Further work will also explore the influence of evapotranspiration as well as heterogeneity and layering of sediments. Nevertheless, these results give an improved insight into the possible importance of bi-directional feedback between groundwater systems and ephemeral streams. Such interactions may have several implications at increasing scales, anthropogenic activities or natural or human-induced climate change.

In the context of climate change, it is highly likely that changes in climatic conditions will result in short but more intense precipitation events that in turn will result in the development of flash flood events (IPCC, 2013; IPCC6, 2021). Such short but high magnitude events may result in less focused recharge per unit length along ephemeral streams. These changes could have a great impact on the temporal and spatial availability of groundwater resources that may threaten its sustainability (Ferguson et al., 2020).

Human interventions may also have an impact on groundwater - surface water interactions. As the demand for water resources increases with population growth, the increasing use of flow regulation systems, such as dams, may have impacts on surface and groundwater resources. Flow regulation in streams will result in changes of the frequency, shape and magnitude of streamflow events (McCallum et al., 2014b), which in turn will affect the transmission losses and focused recharge, and consequently the availability of groundwater resources.

Groundwater - surface water interactions may be very widespread across dryland regions, where water tables are typically within a few tens of metres of the surface (Fan

et al., 2013). Oversimplified categorisations of ephemeral streams that assume ‘hydraulic disconnection’ between surface water and groundwater in dryland regions for water management purposes may therefore be highly misleading, since any increase or decrease in water table depth caused by natural or human activities could still affect the amount of recharge that the aquifer receives in many cases. Such ‘capture’ of additional recharge (Theis, 1940) is generally ignored for dryland regions (Bredehoeft, 1997; Bredehoeft et al., 1982; Bredehoeft, 2002). Since dryland groundwater aquifers supply a significant proportion of the world’s water for irrigated agriculture, the depletion of groundwater from such regions is a major global issue. Additional research into the potential feedbacks between SW and GW in these contexts is still needed.

It is therefore important to develop models that take into account focused recharge from ephemeral streams and their interactions with the underlying groundwater system. Including such processes will enhance the the understanding and quantification of water partitioning. However, the highly non-linear behaviour of such processes may create challenges in terms of numerical and computational demands.

Given that channel losses depend on the amount of water available along the channel, which is in turn highly dependent on streamflow characteristics and the temporal variation of infiltration rates, the lateral flow in the unsaturated zone between the stream and the aquifer becomes less significant in relation to the longitudinal variation of infiltration rates. Therefore, for large scale models, a 1-D vertical flow for infiltration below the channel may be considered as a good approximation for estimating channel transmission losses as long as the longitudinal variation of infiltration rates is included. This will also reduce the computational demand, especially for longer simulations. However, in the case of shallow water tables, the transverse flow of the saturated zone should still be considered where possible, as it will more significantly affect the infiltration rates.

Chapter 5

Development of a parsimonious model for quantifying water partitioning in dryland regions: DRYP

This chapter is partially based on the paper: Quichimbo, E.A., Singer, M.B., Michaelides, K., Hobley, D.E.J., Rosolem, R., Cuthbert, M.O., 2021. DRYP 1.0: A parsimonious hydrological model of DRYland Partitioning of the water balance. *Geosci. Model Dev. Discuss.* 2021, 1–34.
<https://doi.org/10.5194/gmd-2021-137>. (*Under review*)

5.1 Introduction

Modelling water partitioning in drylands regions gives rise to a variety of challenges due to spatial and temporal characteristics of key hydrological processes, paucity of data, and the lack of computationally efficient hydrological models (see Chapter 1). Key processes such as transmission losses and focused recharge have been underrepresented despite the potential impact on water partitioning in dryland regions (see Chapter 3 and 4). These processes also show high temporal and spatial variation driven by the combination of spatio-temporal characteristics of precipitation, soil hydraulic properties, groundwater system, and anthropogenic activities.

In this chapter, a novel parsimonious model, DRYP, is developed to quantify water partitioning in dryland regions using a combination of insights from the previous Chapters, and from the existing literature on dryland hydrological modelling. The model considers the main processes that control the water partitioning, fluxes, and changes in water storage in dryland regions for estimation of runoff, soil moisture,

actual evapotranspiration and groundwater recharge. First the main characteristics and processes included in DRYP are described in detail, as well as their numerical implementation. Second, the ability of the model to describe hydrological processes is demonstrated using synthetic experiments before some conclusions are drawn from the analysis.

5.2 DRYP: a parsimonious model for DRYland regions water Partitioning

5.2.1 Model overview

The main hydrological processes that control fluxes and storage of water in dryland regions are shown schematically in Fig. 5.1a. The movement of water through the different storage components within the catchment is characterised as follows: spatially distributed rainfall falling during individual events over the surface is partitioned into infiltration and runoff, depending on the temporal and spatial characteristics of the rainfall and the antecedent soil moisture conditions at the beginning of the rainfall event (Goodrich et al., 1997; Zocatelli et al., 2019). Water infiltrated into the soil can be extracted by plant evapotranspiration and/or soil evaporation, or it can percolate to the water table as diffuse recharge. Runoff is routed to the nearest stream based on topographic gradient. In each stream reach, water may be added through groundwater discharge as baseflow or water may be lost through the porous boundaries by transmission losses as it moves downstream. The volumes of both baseflow and transmission losses are dependent on the water table depth. Transmission losses into the near-channel alluvial sediments increase the water available for plant evapotranspiration in the riparian zone and also generate focused recharge when the water holding capacity of the sediments in the riparian zone is exceeded (a la Schreiner-McGraw et al. (2019)). Groundwater discharge into streams depends on the hydraulic gradient, occurring when the water table elevation is higher than streambed elevation. Additionally, when the water table is close to the surface, capillary rise increases the root zone water availability for riparian plant evapotranspiration. Finally, anthropogenic activities, such as localised stream and groundwater abstraction as well as irrigation, may affect the storage and fluxes of the water balance.

The only forcing variables in DRYP are spatially explicit fields of precipitation and potential evapotranspiration. The partitioning of the water balance then depends on

the combination of this forcing and its interactions with spatially distributed parameters representing topography, land cover, soil hydraulic properties, hydrogeological characteristics of the aquifer, and anthropogenic activities (Fig. 1b). Hydrological processes in DRYP are structured into three main components: i) a surface water component (SW) where precipitation is partitioned into infiltration and overland flow, which is then routed through the model domain based on the topographic gradient; ii) an unsaturated zone (UZ) component that represents the soil and a riparian area parallel to streams; and iii) an saturated zone (SZ) component which represents groundwater flow (Fig. 5.1c). All three components in DRYP are discretized as square grid cells, and all components are vertically integrated into a computational one-way sequential scheme (Fig. 5.1c). However, all components are hydraulically interconnected, allowing for gradient-driven, and potentially bi-directional water exchange (Fig 5.1c and d).

DRYP is written in Python and uses the Python-based Landlab package, which has versatility to handle gridded datasets and model domains (Barnhart et al., 2020; Hobbey et al., 2017). DRYP is structured in a modular way to allow user flexibility to control the desired level of process and parameter complexity, as well as the grid size and time-stepping choices appropriate for the desired application of the model. The grid size is the same for all layers, but the time step for different components may vary flexibly as described below. Each grid cell potentially consists of all the process elements shown in Fig. 1d. However, the stream and riparian components can be excluded if stream channel characteristics are not provided, in which case all generated runoff in a cell will simply be routed to the next downstream cell with no additional losses or interactions.

For all cells, at the beginning of every time step, the input rainfall (P) is partitioned into surface runoff (RO) and infiltration (I) depending on the available water content of the unsaturated zone (UZ). Water in the UZ can be extracted as actual evapotranspiration (AET), a combination of soil evaporation and plant transpiration, and/or percolate (R) to the saturated zone (SZ), depending on the water content and hydraulic properties of the unsaturated zone. If a cell is defined as a stream, transmission losses (TL) or groundwater discharge contributing to base flow (BF) and a riparian unsaturated zone (RUZ) are included in the local partitioning. The riparian zone is defined as an area parallel to the stream with a specified width. The riparian zone receives contributions from TL and a volume of infiltrated water proportional to the riparian area. Water within the riparian zone can either percolate,

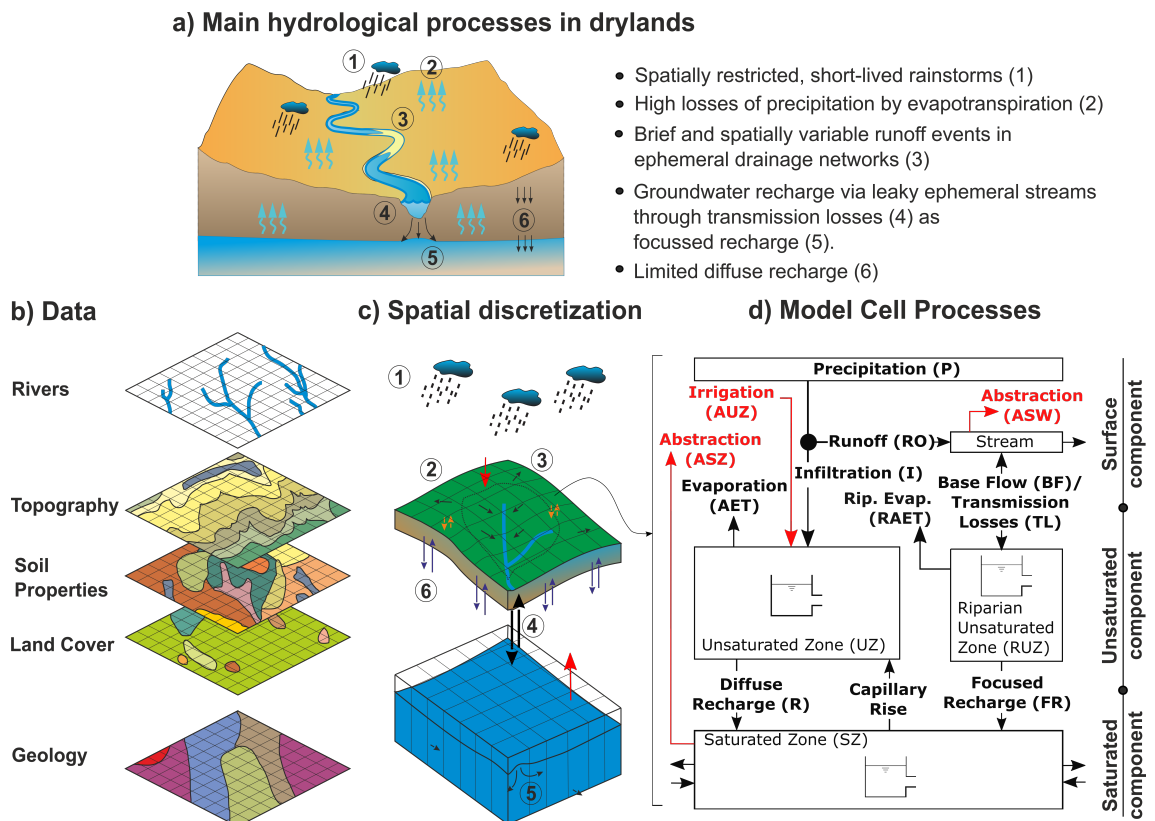


Figure 5.1: Schematic representation of DRYP showing a) the main hydrological processes controlling water partitioning in dryland regions; b) distributed datasets needed to derive input parameters; c) vertical and horizontal discretisation and representation of topographically-driven surface runoff, vertical flow in the unsaturated zone, and hydraulic gradient driven groundwater flow in the saturated component; d) model structure and potential processes within a single grid cell for the surface component (see Sect. 5.2.2), unsaturated zone (see Sect. 5.2.3) and saturated zone (see Sect. 5.2.4). Arrows represent flow directions and red lines represent anthropogenic fluxes.

becoming focused recharge or it can be extracted by plants as riparian evapotranspiration. Focused and diffuse recharge are combined as the main inputs to the SZ, which may also interact with the UZ depending on the water table elevation as it rises and falls through the simulation. The movement of water in SZ is driven by the lateral hydraulic gradient. Additionally, anthropogenic interactions in the model are implemented as localized fluxes from the saturated zone (ASZ) and streams (AOF), whereas water abstraction for irrigation (AUZ) is delivered to the surface where it then contributes to infiltration into the unsaturated zone.

5.2.2 Surface Component

Two main processes are considered in the surface component: i) the partitioning of precipitation into infiltration and runoff, and ii) runoff routing and the partitioning of runoff into streamflow and transmission losses in stream cells. These are described below.

5.2.2.1 Infiltration and runoff

The partitioning of precipitation into infiltration and runoff at the land surface is a key process in drylands and a potentially major source of uncertainty in the overall water partitioning for these regions. Hence, four different infiltration approaches have been included in DRYP, which can be toggled on or off within the main control file (prior to simulation) to allow the user to experiment with different infiltration model structures. These approaches include two point-scale methods: the Philip infiltration approach and the Modified Green Ampt method; and two upscaled methods for summarising infiltration over larger areas: the Upscaled Green Ampt and the Multiscale Schaake approach.

Method 1: Infiltration based on Philip's equation

In this option, infiltration, f [$L T^{-1}$] during a rainfall event is based on the explicit solution of the infiltrability depth of Philip's equation (Philip, 1957).

$$f(t_c) = \frac{1}{2} S_p t_c^{-\frac{1}{2}} + K_{sat} \quad (5.1)$$

where: K_{sat} is saturated hydraulic conductivity [$L T^{-1}$], S_p is sorptivity [$L^2 T^{1/2}$], and t_c is time since the beginning of the precipitation event [T]. The sorptivity term is estimated by using the following equation (Rawls et al., 1982):

$$S_p = [2K_s (\theta_{sat} - \theta) |\psi_f|]^{\frac{1}{2}} \quad (5.2)$$

where: θ is volumetric water content [$L^3 L^{-3}$], θ_{sat} is volumetric water content at saturated conditions [$L^3 L^{-3}$], and ψ_f is suction head [L] estimated as (Clapp and Hornberger, 1978):

$$|\psi_f| = \psi_a \frac{2\lambda + 2.5}{\lambda + 2.5} \quad (5.3)$$

where: ψ_a is maximum suction head [L], and λ is a parameter that represents the pore size distribution of the soil [-] (Clapp and Hornberger, 1978).

The total infiltration depth in any given cell, I [L], during a precipitation event is estimated by solving the integral of Eq. 5.1 over the event duration. The integral of Eq. 5.1 is solved using the time compression approach (TCA) (Holtan, 1945; Mein and Larson, 1973; Sherman, 1943; Sivapalan and Milly, 1989), assuming that infiltration after ponding depends on the cumulative infiltrated volume. Therefore, to match the initial infiltration rate at the beginning of each time step with the infiltration at the end of the previous time step, the start time of infiltration is shifted to match the total cumulative infiltration. A more detailed description and the analytical solution of the approach can be found in Assouline (2013) and Chow et al. (1988).

Method 2: Infiltration based on a Modified Green - Ampt method

A modified version of Green - Ampt approach defined by the following equation has been implemented (Michaelides and Wilson, 2007; Scoging and Thornes, 1979):

$$f(t_c) = K_{sat} + \frac{B}{t_c} \quad (5.4)$$

where: B represents initial suction head [L], t_c is the same as Eq. 5.1; here I use sorptivity (Eq. 5.2) as a proxy of the initial head owing to the nonlinear dependency of sorptivity on the water content of the soil.

The integral of Eq. 5.4 was also solved using the time compression approach (Holtan, 1945; Mein and Larson, 1973; Sherman, 1943; Sivapalan and Milly, 1989). However, since there is no explicit solution for Eq. 5.4, an implicit solution has been used.

Method 3: Infiltration based on an Upscaled Green - Ampt method

This method is based on the semi-analytical solution of the Green and Ampt equation for spatially heterogeneous hydraulic conductivity developed by Craig et al. (2010):

$$\begin{aligned}
\bar{I}(t) = & \frac{p}{2} \operatorname{erfc} \left(\frac{\ln(pX) - \mu_Y}{\sigma_Y \sqrt{2}} \right) \\
& + \frac{1}{2X} \log |K_{sat}| \operatorname{erfc} \left(\frac{\sigma_Y}{\sqrt{2}} - \frac{\ln(pX) - \mu_Y}{\sigma_Y \sqrt{2}} \right) \\
& + p \int_0^{X(t)} \varepsilon(X(t), K_s) \cdot f_k(K_s) dK_s
\end{aligned} \tag{5.5}$$

where: \hat{I} is the mean infiltration rate [L T⁻¹], p is the precipitation rate [L T⁻¹], t_c the same as Eq. 5.1, f_k is the probability density function of K_{sat} , μ_Y and σ_Y are mean and standard deviation of the log saturated hydraulic conductivity,

$$\mu_Y = \ln |K_{sat}| - \frac{1}{2} \sigma_Y$$

, X is a dimensionless time estimated as:

$$X = \frac{1}{1 + \frac{\alpha}{Pt_c}} \tag{5.6}$$

where: $\alpha = |\psi_f|(\theta_{sat}\theta)$, with ψ_f representing the suction head.

The $\varepsilon(X, K_s)$ in Eq. 5.5 is an error function that can be estimated by the following approximation (Craig et al., 2010):

$$\varepsilon \approx 0.3632 \cdot (1 - X)^{0.484} \cdot \left(1 - \frac{K_{sat}}{pX}\right)^{1.74} \left(\frac{K_{sat}}{pX}\right)^{0.38} \tag{5.7}$$

The $f_k(K_s)$ is assumed as a lognormal distribution following Craig et al. (2010):

$$f_K(K_{sat}) = \frac{1}{K_{sat}\sigma_Y\sqrt{2\pi}} \exp \left\{ \left(-\frac{(\ln(K_{sat}) - \mu_Y)^2}{2\sigma_Y^2} \right) \right\} \tag{5.8}$$

As suggested by Craig et al. (2010), the integral of the Eq. 5.5 was efficiently solved using a 2-point Gauss-Lagrange numerical integration method.

Method 4: Infiltration based on the Multi-scale Schaake method

The Schaake et al. (1996) approach is based on the assumption that rainfall and infiltration rates follow an exponential distribution to approximate spatial heterogeneity of soil properties. Therefore, the spatially averaged infiltration I [L] is estimated as:

$$I = \frac{PI_c}{P + I_c} \tag{5.9}$$

where: P is total rainfall [L] and I_c is cumulative infiltration capacity [L].

Infiltration capacity is estimated as (Schaake et al., 1996):

$$I_c = (\theta_{sat} - \theta) (1 - \exp(-k_{dt})) \quad (5.10)$$

where k_{dt} is a constant that depends on soil hydraulic properties.

Following Chen and Dudhia (2001), k_{dt} was defined as:

$$k_{dt} = k_{dtref} \frac{K_{sat}}{K_{ref}} \quad (5.11)$$

where: K_{ref} [$L T^{-1}$] is a reference hydraulic saturated conductivity equal to 2×106 $m s^{-1}$ (Chen and Dudhia, 2001; Wood et al., 1998) and the parameter, K_{dtref} , is specified as a scale calibration parameter.

5.2.2.2 Runoff routing and transmission losses

Rainfall that does not infiltrate (i.e. precipitation, P, minus infiltration, I) into the unsaturated component is routed over the model domain based on topography. This feature of the model is critically important based on the results presented in Chapter 3 and 4 of this thesis, and often missing from existing, particularly large-scale, dryland models. The flow routing scheme varies depending on whether a cell is defined as a stream or not. A simple flow accumulation approach is used in cells without a defined stream, whereas for defined stream cells, an additional flux term is added to the flow accumulation approach to account for groundwater interactions via the riparian zone. This flux will either be a transmission loss or a baseflow contribution from the saturated component.

Flow routing in cells without streams

Runoff produced in any given cell is instantaneously routed to the next downstream cells using the flow accumulation approach implemented in Landlab (Braun and Willett, 2013; Hobbey et al., 2017). The next downstream cell is estimated using a D8 flow direction approach (8 potential directions based on adjacent cells). The flow accumulation method adds the amount of runoff from the upstream cells:

$$Q_i = \sum_{i=1}^N Q_{ini} \quad (5.12)$$

where: Q_{in} [L^3] is the volume of water that discharges from upstream cells into the current cell i , N is the number of upstream cells discharging into the current cell. and Q_i [L^3] is the volume of water in the cell.

Flow routing in stream cells

In defined stream cells, the amount of water entering the cell, q_{in} [$L^3 T^{-1}$], is instantly reduced by any transmission losses, i_{ch} [$L^3 T^{-1}$], and any remaining water, q_{out} [$L^3 T^{-1}$], is moved to the next downstream cell:

$$q_{out} = q_{in} - i_{ch} \quad (5.13)$$

Water from the upstream cell, q_{in} , is assumed to be released to the next cell following a linear reservoir approach:

$$q_{in} = q_0 e^{-k_T t^*} \quad (5.14)$$

where: k_T [T^{-1}] is a recession term that is equal to the inverse of the residence time of the streamflow at each cell, t^* represents time [T], and q_0 is the initial flow rate of water entering the channel, estimated as:

$$q_0 = (Q_{in} + S_{SW} - Q_{ASW}) k_T \quad (5.15)$$

where: Q_{ASW} [L^3] is the volume of water abstracted from the stream, and S_{SW} [L^3] is water stored in the channel.

It is assumed that the sediments in the streambed are homogeneous. Consequently, the rate of infiltration depends on the wetted perimeter of the channel, and the infiltration rate, i_{ch} at the stream cell is estimated assuming a unit gradient Darcian flow across the wetter perimeter:

$$i_{ch} = K_{ch} (2y + W) L_{ch} \quad (5.16)$$

where K_{ch} [$L T^{-1}$] is saturated hydraulic conductivity of the streambed, L_{ch} [L] is channel length for a given cell, W is channel width [L], and y is streamflow stage [L]. For the purposes of modelling at larger scales, this implicit assumption of 1-D vertical flow beneath the channel is justified on the basis of the results from Chapter 3 and 4, which indicated that channel losses are more influenced by the longitudinal contribution of infiltration as streamflow in channel moves downstream. If the rate of water entering the stream cell is less than the potential channel infiltration rate, flow to the next downstream cell is set to zero (all water is lost via infiltration) and

$$i_{ch} = q_{in}$$

Stream stage, y , is estimated by assuming that flow velocity does not change along the channel in any given cell (no flow acceleration). Therefore, the streamflow stage and the volume at any time along the channel are kept constant in any given stream

cell. A constant-velocity approach assumes that there are no backward effects on the streamflow routing approach. Thus, the stream stage is estimated as the height of the rectangular prism with area

$$A = WL_{ch}$$

and volume at time t as:

$$y = \frac{q_{in}}{A} \quad (5.17)$$

After substituting Eq. (17) into Eq. (16) and then into Eq. (13), the time integral of Eq. (13) represents the total amount of water, Q_{out} [L³], that moves to the next downstream channel cell (becoming Q_{in}):

$$Q_{out} = \int_0^{\min[t_q=0, \Delta t]} \left[q_0 e^{-k_T t} - L_{ch} K_{ch} \left(2q_0 e^{-k_T t} W L_{ch} + W \right) \right] dt \quad (5.18)$$

Note that the time step choice is important to bear in mind with respect to the size of the catchment modelled, since it represents the minimum travel time for flow to reach the catchment outlet.

The amount of water stored in the channel is estimated by applying a mass balance of all inputs and outputs of the channel:

$$S_{RO}^t = Q_{in} + S_{SW}^{t-1} - Q_{ASW} - Q_{TL} - Q_{out} \quad (5.19)$$

where: t represents the current time step, and Q_{TL} [L³] is transmission losses estimated as the integral of the second term of Eq. (5.18). The total of Q_{TL} is restricted to the storage available in the aquifer:

$$Q_{TL} = \min[Q_{TL}, \max[(z - h) A S_y, 0]] \quad (5.20)$$

where: z is the surface elevation [L], h is water table elevation [L], A is the area of cell [L²], and S_y is aquifer specific yield [-]. This simplification not only results in the reduction of the computational demand, but also considers the feedback from the water table (Chapters 3 and 4). Thus, when the water table is deep, there is more space available for channel losses, whereas for shallow water tables, channel losses will be limited. However, one of the main limitations is that the non-linear feedback from the water table (Chapters 3 and 4) will not be adequately represented, and if the saturated zone is modelled at larger time steps, the behaviour will likely become linear. Additionally, local groundwater mounding in stream cells is not considered in the model, although this effect is expected to be reduced at small spatial-scales (Brunner et al., 2011) (see Chapter 3). This condition could result in more channel losses.

5.2.3 Unsaturated Component

Water infiltrated into the soil or through the stream channel becomes a flux input to the UZ (Fig. 5.1d). The unsaturated component comprises the soil and the riparian zone, explained below, both of which are simulated using a linear ‘bucket’ soil moisture balance model (Fig. 5.2a), following an approach similar to the FAO water balance model (Allen et al., 1998):

$$\Delta S_{UZ} = I + Q_{TL}AET - R \quad (5.21)$$

where: ΔS represents storage change [L], AET represents actual evapotranspiration rate [$L T^{-1}$] and R represents potential recharge rate [$L T^{-1}$]. The term Q_{TL} is only defined for stream cells. Diffuse potential recharge results from the local vertical percolation of the unsaturated zone, whereas focused potential recharge is produced in the riparian unsaturated zone (see Fig. 5.1).

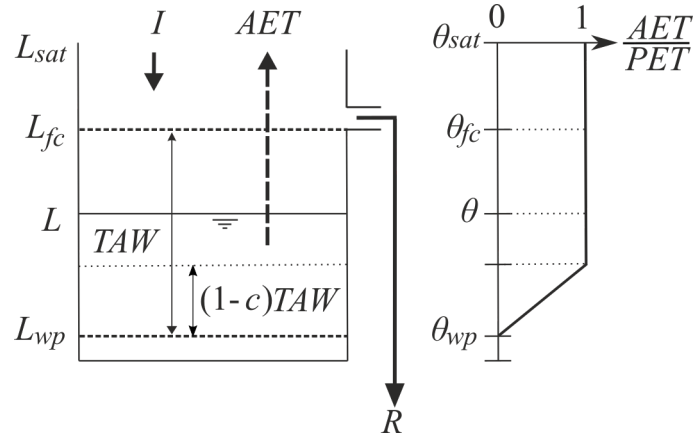


Figure 5.2: Schematic illustration of the unsaturated component. The right panel represents the variation of the ratio of potential to actual evapotranspiration in relation to the water content of the soil. Please refer to Sect. 2.2 and 2.3 for a detailed explanation of the terms shown here.

The amount of water available for plant evapotranspiration in the UZ, L [L], is estimated as the product of the rooting depth, D_{root} [L], and the relative water content, θ [$L^3 L^{-3}$]. The maximum amount of water that the soil can store is limited by the field capacity of the soil (L_{fc}), whereas the minimum amount is constrained by the wilting point (L_{wp}). Thus, the total available water for plant transpiration, L_{TAW} , is estimated by the difference between L_{fc} and L_{wp} (see Fig. 5.2).

The potential amount of water that plants can remove water from the UZ as transpiration, PET [$L T^{-1}$], which is the result of the product between a crop coefficient,

k [-], and the reference potential evapotranspiration, ET_0 [L T⁻¹] (Allen et al., 1998). When there is enough water to supply plant energy demands, water can be extracted from the UZ at a rate equal to PET . However, when there is not enough water in the UZ to supply the PET , plants are considered to be under stressed conditions and the actual evapotranspiration (AET) is constrained as:

$$AET = I + \beta (PET - I) \quad (5.22)$$

where: β is a dimensionless parameter that depends on the water content and is estimated by:

$$\beta = \frac{L - L_{TAW}}{L_{TAW} (1 - c)} \quad (5.23)$$

where: c is the fraction of L_{TAW} [-] at which plants can extract water from the UZ without suffering water stress, and set to 0.5 as recommended by the FAO guidelines (Allen et al., 1998), although this can be varied in DRYP.

If after accounting for infiltration and AET , there is a surplus of water in the soil that exceeds the field capacity, diffuse recharge (R) to the groundwater system occurs. If the model is run at daily time steps, it is assumed that all water content above field capacity will percolate and produce R . However, for sub-daily time steps it is more realistic to assume that the soil slowly releases water as R when it is above the field capacity, depending on the soil water retention curve. Hence, in this case it is assumed that percolation to the water table depends on the water content and occurs only under the influence of gravity as follows:

$$D_{UZ} \frac{d\theta}{dt} = -K(\theta) \quad (5.24)$$

where $K(\theta)$ is estimated by using the Brooks and Corey (1964) relations and Clapp and Hornberger (1978) (see Eq. (5.3)):

$$K(\theta) = K_{sat} \left(\frac{\theta}{\theta_{sat}} \right)^{(2\lambda+2.5)} \quad (5.25)$$

Assuming that the soil drains immediately into the groundwater component after evapotranspiration loss, and substituting Eq. (5.25) into Eq. (5.24), an analytical solution based only on drainage without considering other inputs or outputs is specified by:

$$\theta = \exp \left\{ \left(- (2\lambda - 1.5) \log \left| \theta^{-2\lambda-1.5} - \frac{\Delta t (2\lambda + 1.5) K_{sat}}{D_{UZ} \theta_{sat}^{2\lambda+2.5}} \right| \right) \right\} \quad (5.26)$$

The UZ model component in DRYP can also change its behaviour when the head in the SZ component beneath restricts downward movement of water. This case is described below in Section 5.2.4 (Unsaturated – Saturated zone interactions).

Riparian zone component

The riparian component is an area parallel to the stream, with length similar to the river but different width W_{RUZ} [L], which is a user-defined parameter. Flow in the riparian component is assumed to be unsaturated. Riparian soil parameters are assumed to be the same as the unsaturated zone (θ_{sat} , θ_{fc} , θ_{wp} , D_{root}), and the saturated hydraulic conductivity is assumed as K_{ch} .

5.2.4 Saturated Component

Lateral saturated flow underneath the unsaturated zone assumes Dupuit-Forchheimer conditions for the Boussinesq equation and Darcian conditions for flow in/out of each model cell:

$$\frac{\partial h}{\partial t} + q_s + q_{riv} = \frac{1}{S_y} \nabla \cdot (-K_{sat} h \nabla h) + R - Q_{ASZ} \quad (5.27)$$

where: K_{aq} is the saturated hydraulic conductivity of the aquifer [L T⁻¹], S_y is the specific yield [-], q_s is saturation excess [L T⁻¹] (see Sect. 5.2.4.1), q_{riv} is discharge into stream [L T⁻¹] (see Sect. 5.2.4.2), Q_{ASZ} [L T⁻¹] is any groundwater abstraction, ∇ represents the gradient operator and $\nabla \cdot$ represents the divergence operator. Where the saturated thickness of the aquifer is relatively constant over the simulation period, transmissivity, T [L² T⁻¹], (the product of the aquifer thickness and the saturated hydraulic conductivity of the aquifer), may be held constant, hence linearising Eq. (5.27). Additionally, an exponential function based on Fan et al. (2013) has been added to represent the reduction of transmissivity in relation to depth:

$$T = K_{sat} f_D \exp\left(-\frac{z-h}{f_D}\right) \quad (5.28)$$

where: f_D is effective aquifer depth [L]. These different transmissivity parameterisation options can be toggled on or off in the main model control file.

Equation (5.27) is solved using a forward time central space (FTCS) finite difference approach. FTCS is an explicit finite difference approximation whose solution is sensitive to grid size and time step. Thus, in order to obtain a stable convergence of Eq. (5.27), a time variable approach was adopted. The maximum allowable time step for the saturated component is estimated based on the Courant number criteria (a value of 0.25 was set as a default but this may be changed by the user):

$$\frac{T \Delta t}{S_y \Delta x^2} \leq 0.25 \quad (5.29)$$

If the maximum time step of the SZ component is greater than the time step of the minimum time step of the any other component of the model, the time step of the SZ

component is reduced to the time step of the minimum time step of the model (see Sect. 5.2.5 for more details of the model time step options).

5.2.4.1 Unsaturated - Saturated zone interactions

Unsaturated - saturated zone interactions are implemented using a variable depth unsaturated zone as follows (Fig. 5.3a). Unsaturated zone thickness (D_{uz}) is equal to the rooting depth when the water table elevation (h) is below the rooting depth, but when the water table is above the rooting depth the thickness of the unsaturated zone is reduced to the depth of the water table:

$$D_{uz} = \min [D_{root}, z - h] \quad (5.30)$$

When the water table is below the rooting elevation, z_{root} , there is no two-way interaction between the soil and the groundwater compartment (only one-way, as recharge), so no updates to the water table elevation are required (see Fig. 5.3a, left panel). However, when the water table crosses the z_{root} threshold, either via recharge or lateral groundwater flow, the water table is updated depending on the change in groundwater storage:

$$\frac{\Delta S_{SZ}}{\Delta t} = \nabla \cdot (-K_{sat} h \nabla h) + R - Q_{ASZ} \quad (5.31)$$

where: ΔS_{SZ} is the change in groundwater storage per unit area [$L^3 L^{-2}$]. Specifically, if an SZ cell is being recharged and the water table rises past the rooting depth in a given time step, the water table is updated according to:

$$h_t = \frac{1}{\theta_{sat} - \theta_t} [\Delta S_{SZ} - (z_{uz} - h_{t-1}) S_y] + z_{uz} \quad (5.32)$$

whereas, when the water table is draining and passes the rooting depth in a given timestep:

$$h_t = -\frac{1}{S_y} [\Delta S_{SZ} - (h_{t-1} - z_{root}) (\theta_{sat} - \theta_{fc})] + z_{root} \quad (5.33)$$

When the water table is above the rooting depth elevation, the water table elevation will be updated according to:

$$h_t = \frac{\Delta S_{SZ}}{\theta_{sat} - \theta_{fc}} + h_{t-1} \quad (5.34)$$

while if it is below the rooting depth elevation, the water table elevation is simply:

$$h_t = \frac{\Delta S_{SZ}}{S_y} + h_{t-1} \quad (5.35)$$

When the water table is above z_{root} , there is more water potentially available for evapotranspiration, since it can be taken from the groundwater reservoir via capillary rise or direct root water uptake. Thus, the potential maximum amount of water taken up from the groundwater reservoir, $PAET_{SZ}$ [$L T^{-1}$], is computed as the remaining PET after AET from the unsaturated component as:

$$PAET_{SZ} = PET - AET \quad (5.36)$$

For a shallow water table, upward capillary fluxes may also be taken from the groundwater reservoir. The rate of actual evapotranspiration from the SZ (AET_{SZ}), including both plant water uptake and capillary rise, is thus estimated as a linear function of the water table depth as follows:

$$AET_{SZ} = \max \left[PAET_{SZ} \left(\frac{h - z_{root}}{D_{root}} \right) \Delta t, 0 \right] \quad (5.37)$$

5.2.4.2 Groundwater - surface water interactions

Groundwater - surface water interactions are characterised in DRYP through transmission losses as described in Sect. 5.2.2.2. In addition, when the water table intersects a cell's defined streambed elevation it produces discharge into the stream, q_{riv} [$L T^{-1}$], and when the water table reaches the ground surface it produces saturation excess, q_s [$L T^{-1}$] (Fig. 5.3b) (Eq. (5.27)).

Discharge into streams, q_{riv} , is quantified using a head-dependent flux boundary condition (similar to that used in MODFLOW (Harbaugh, 2005)) as:

$$q_{riv} = C (h - h_{riv}) \quad (5.38)$$

where: C is a conductance term [$L^2 T^{-1}$] estimated as:

$$C = \frac{K_{ch} L_{ch} W}{0.25 \Delta x} \quad (5.39)$$

To avoid numerical instabilities, a regularisation approach was implemented via a smooth switch between the flux boundary condition and a constant head boundary (and vice versa) using a convex function (Marçais et al., 2017):

$$q_s = f_u \left(\frac{h - h_b}{z - hb} \right) f_g (\nabla \cdot (-K_{sat} h \nabla h) + R - q_{riv}) \quad (5.40)$$

where: h_b is aquifer bottom elevation [L], f_u is the continuous function between $[0,1]$ specified as (Marçais et al., 2017):

$$f_u = \exp \left\{ \left(-\frac{1 - u}{r} \right) \right\} \quad (5.41)$$

where r is a dimensionless regularisation factor $r > 0$, which has been specified as 0.001 following Marçais et al. (2017). f_g is the Heaviside step function.

$$f_g = 0, u < 0; u, u \geq 0 \quad (5.42)$$

After both q_s and q_{riv} are estimated, their corresponding volumes are estimated by multiplying the flow rate, the time step and the corresponding surface area (cell or stream). The volume is then added as additional runoff in the surface component (Sect. 5.2.2). The water table is updated to its topographical elevation and kept as a constant head boundary condition. The boundary switches back to a flux condition if the water table drops back below the water table.

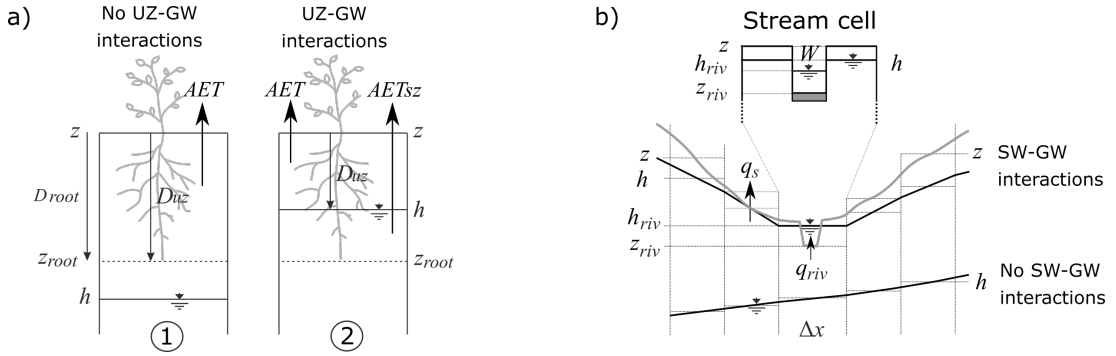


Figure 5.3: Schematic representation of a) UZ-SZ interactions: 1a) indicates no UZ-SZ interaction whereas 2a) indicates UZ-SZ interaction (soil depth, D_{root} , is reduced to D_{uz}); b) SW-GW interactions in stream cells: boundary conditions change from no-flow to head dependent flux conditions once the stream bed or ground surface is intersected by the water table. Upper part of panel b) shows the numerical implementation of SW-GW interactions in a stream cell.

5.2.5 Numerical implementation and time step

DRYP is a fully open-source, grid-based model with a layer-based structure, developed using the Landlab architecture (Hobley et al., 2017) and its Python library. Landlab was chosen due to the versatility and its modular design that allows the user to plug in multiple modules for different levels of complexity and processes using grid-based objects (Barnhart et al., 2020; Hobley et al., 2017).

Since most hydrological processes in DRYP, except the SZ component and the modified Green-Ampt infiltration, are described according to explicit-analytical solutions, it is possible to run DRYP at hourly or sub-hourly time steps at low computational cost.

The three main DRYP components (i.e. surface, unsaturated and saturated components), can run at different time steps, from sub-hourly to daily. The riparian zone of the unsaturated component can be also run at a different time step to that of the unsaturated component. Where different time steps are used between components, the fluxes and state variables are temporally aggregated in DRYP by accumulating and/or averaging them over the specified time step as appropriate and then transferring them to the next component. In addition, and as described above, for the saturated component, an internal time step is also automatically considered to ensure the stability of the numerical solution.

5.2.6 Model input files and parameter settings

DRYP requires spatial characterisation of key input parameters and data including a digital elevation model (DEM), channel properties in cells where streams are explicitly defined (length, width and saturated hydraulic conductivity), land cover (plant rooting depth), various soil hydraulic properties, and aquifer properties (specific yield, aquifer thickness, and saturated hydraulic conductivity) (Fig. 5.1). A summary of model parameters for the different model components and structures is presented in Table 5.1. If parameters are not provided, ‘global’ default values are used as defined in Table 5.1.

Precipitation and potential evapotranspiration are the only forcing variables required as either spatially variable gridded datasets in netCDF format or as spatially uniform values for each time step. Gridded datasets must be interpolated or aggregated to match the model grid resolution.

5.3 Model Evaluation

The use of synthetic experiments is an important aspect of model development in hydrology which is welcome but not used often (Clark et al., 2015). The objective of synthetic experiments is to better understand the structural controls on the physical processes represented in the model, for example, on groundwater-soil interactions (Batelis et al., 2020; Rahman et al., 2019). Here, a set of numerical experiments have been performed to evaluate the stability and convergence of DRYP components, particularly the coupling of both the surface and unsaturated zone with the groundwater component. Convergence and stability of the numerical solution of the groundwater component using the FTCS finite difference approach and regularisation have been well documented in different studies (e.g. Anderson et al. (2015); Marçais et al. (2017);

Table 5.1: Model parameters for different processes considered in the model, some required parameters depend on the infiltration approach ('Inf. Method'). Default values are specified in brackets. For soil hydraulic properties, default values correspond to a sandy loam soil texture (Clapp and Hornberger, 1978; Rawls et al., 1982)

Parameter	Description	Dimension	Default Values	Inf. Method
Overland flow				
k_T	Recession time for channel streamflow	[T ⁻¹]	0.083 h ⁻¹ *	-
W	Channel width	[L]	10 m	-
L_{ch}	Channel length	[L]	grid size	-
K_{ch}	Channel saturated hydraulic conductivity	[L T ⁻¹]	10.9 mm h ⁻¹	-
Unsaturated zone				
θ_{wp}	Water content at wilting point	[-]	0.07	All
θ_{fc}	Water content at field capacity	[-]	0.17	All
θ_{sat}	Saturated water content	[-]	0.41	All
ψ	Suction head	[L]	110.1 mm	All
γ	Soil pore size distribution	[-]	4.9	All
σ_Y	Standard deviation of the log saturated hydraulic	[LT ⁻¹]	0.5 mm h ⁻¹	Up-GA
K_{sat}	Saturated hydraulic conductivity	[L T ⁻¹]	120.9 mm h ⁻¹	All
D	Rooting depth	[L]	800 mm	All
kdt	Schaake reference parameter	[-]	1.0	Schaake
k	Crop coefficient	[-]	1.0	-
Saturated Zone				
Sy	Specific yield	[-]	0.01	-
Kaq	Aquifer Saturated hydraulic conductivity	[L T ⁻¹]	1 m h ⁻¹	-
T	Aquifer Transmissivity (for constant values)	[L T ⁻¹]	60 m ² h ⁻¹	-
f_D	Effective aquifer depth (for exponential function)	[L]	60 m	-
h_b	Aquifer bottom elevation	[L]	0 m	-

Wang and Anderson (1982)). Hence, for model evaluation two sets of analysis were considered: (i) a quantitative evaluation of the model performance in relation to the well know numerical model, MODFLOW (Harbaugh, 2005; Harbaugh et al., 2000), for a simple groundwater - surface water interaction test represented as a draining condition, and (ii) a qualitative evaluation of the model performance with respect to the desired skill of the model to seamlessly allow interactions between groundwater and the land surface and surface water components.

For the *quantitative evaluation*, a 1-D synthetic experiment considering an inclined plane aquifer was specified as a model domain (see Fig. 5.4a). The length and width of the model domain were specified as 10 km and 1 km, respectively. Hydraulic saturated conductivity and aquifer specific yield were specified as 1.2 m d^{-1} and 0.01, respectively. Boundary conditions were specified as no-flow for both the right and left side as well as the bottom of the model domain. Model grid size was set to $1 \text{ km} \times 1 \text{ km}$. The top boundary condition was considered as seepage face.

For comparison, a model with similar geometry, grid size and hydraulic properties was built in MODFLOW using the FLOPY python package (Bakker et al., 2016a,b). Boundary conditions for the MODFLOW model were the same as DRYP except for the top boundary condition, which was specified by using the 'drain package' (Harbaugh et al., 2000). The elevation at which the water starts to drain was specified as the surface elevation of the model domain. A high value of the conductivity term ($500 \text{ m}^2 \text{ d}^{-1}$) was implemented in order to capture the seepage process and to assure convergence as well as minimal water balance errors (Batelaan and Smedt, 2004).

The synthetic test consisted of a free-draining condition for an unconfined aquifer with a water table depth equal to zero (at the surface level). The time step considered for evaluation was 1 day. The evaluation considered the temporal variation of the water table for both DRYP and MODFLOW models, as well as the water balance errors. Errors were evaluated at all locations along the aquifer considering the mean square errors:

$$RMSE = \sqrt{\frac{1}{n} \sum_{i=1}^n (S_i - O_i)^2} \quad (5.43)$$

where: O represent values from the MODFLOW and S represent simulated values from DRYP, and n is the number of values compared.

The geometry of the model domain for these tests consisted of a tilted-V catchment (Fig. 5.4b) with a size of 7×10 square cells on a 1-km resolution grid. Land use and soil hydraulic characteristics were specified as uniform over the entire model domain, and the saturated zone was considered as a homogeneous and unconfined aquifer.

Boundary conditions were specified as no-flow boundaries for all sides as well as at the bottom of the model domain. The initial water table was set as a horizontal plane at the level of the catchment outlet (100 m) for all simulations (Fig. 5.4). For experimental purposes, hydraulic characteristics of both the unsaturated and saturated zone were arbitrarily chosen. Thus, a loamy sand soil texture with $K_{sat} = 29.9 \text{ cm h}^{-1}$, $\theta_{sat} = 0.40$, $\theta_{fc} = 0.175$, and $\theta_{wp} = 0.075$ was chosen for the unsaturated zone, whereas, for the saturated zone, the hydraulic conductivity of the aquifer (K_{aq}) was specified as 6 m d^{-1} and the specific yield (S_y) was set as 0.01. The high value of K_{aq} combined with S_y and boundary conditions of the aquifer were applied in order to allow a fast increase/decrease of the water table and the observation of groundwater - surface water interaction in a short period of time.

For the *qualitative evaluation*, three main scenarios were analysed by using synthetic time series of precipitation and evapotranspiration and changing hydraulic parameters of the UZ as follows:

1. An 'Infiltration - discharge' scenario, where all precipitation was allowed to infiltrate into the catchment and no infiltration excess was produced over the model domain.
2. An 'Infiltration-evapotranspiration-discharge' scenario was simulated by adding a time variable potential evapotranspiration as input into the model.
3. An 'Infiltration-runoff-evapotranspiration-discharge' scenario was designed to evaluate the production of runoff and focused groundwater recharge, as well as groundwater discharge. For this last scenario, the saturated hydraulic conductivity of the soil was decreased by one order of magnitude to produce infiltration excess and consequently, runoff.

For all three scenarios, precipitation events were specified at a constant value of $0.25 \text{ [mm h}^{-1}\text{]}$ over 10 days followed by a 20-day dry period of response to the rainfall input. Potential evapotranspiration was specified as a sinusoidal function with a 24-hour period and a maximum rate of $0.10 \text{ [mm h}^{-1}\text{]}$. These experimental values of precipitation and evapotranspiration combined with the hydraulic properties of the unsaturated and saturated zone allowed for a visual evaluation of groundwater - surface water interactions under different conditions, such as increasing and decreasing water table through the model run and its interaction with the unsaturated zone.

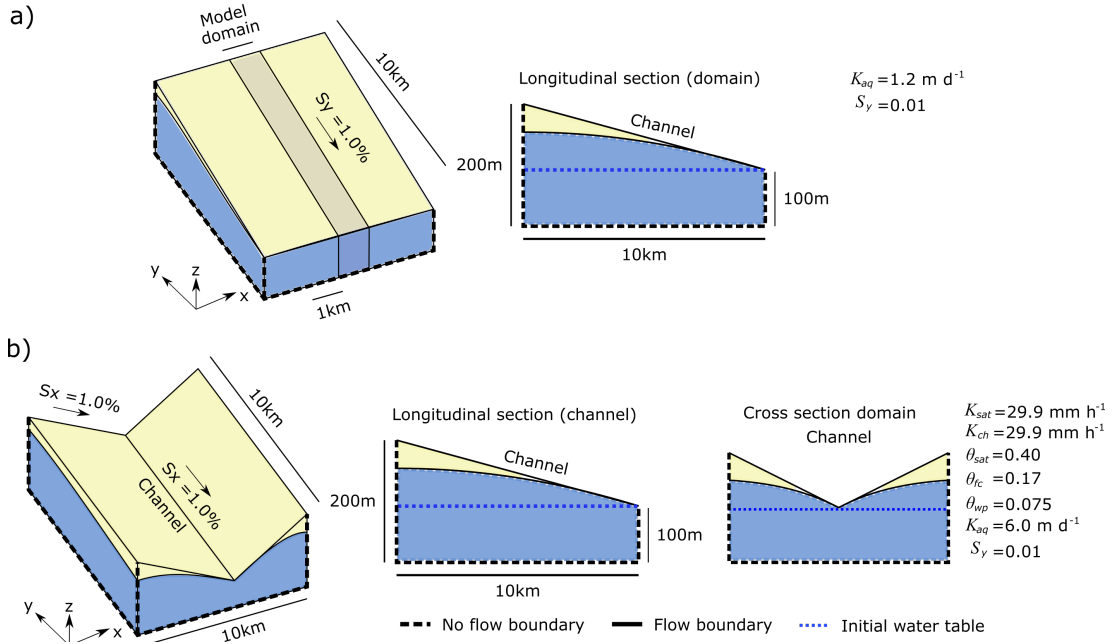


Figure 5.4: Synthetic tilted-V catchment and flow boundary conditions specified for model simulations.

5.4 Results

5.4.1 Comparing DRYP to MODFLOW: quantitative evaluation

Modelling results show a good agreement between DRYP and MODFLOW models (water balance error: $1.79\text{e-}15 \text{ m}^3$ for DRYP, and $6.95\text{e-}8 \text{ m}^3$ for MODFLOW) (see Fig. 6.3) both temporally and spatially. Differences in water table elevations are in the range of 0.022 m at the beginning of the simulation when the aquifer starts to drain, but then decrease as the water table decreases (see Fig. 6.3a). Temporal variation of the groundwater storage for both models show good consistency, with higher values due to higher gradients at the beginning of the simulation and lower values as the water table decreases (see Fig. 6.3b). However, more fluctuations are observed on MODFLOW simulations (see inset plot in figure 6.3b). This can be attributed to the time step used for the simulation, which would need to be reduced further in order to more smoothly capture the variation in water table depth as the model switches boundary conditions. DRYP captures this variation more smoothly due to the exponential function used (eq. 5.41) and by automatically reducing the time step to assure numerical convergence.

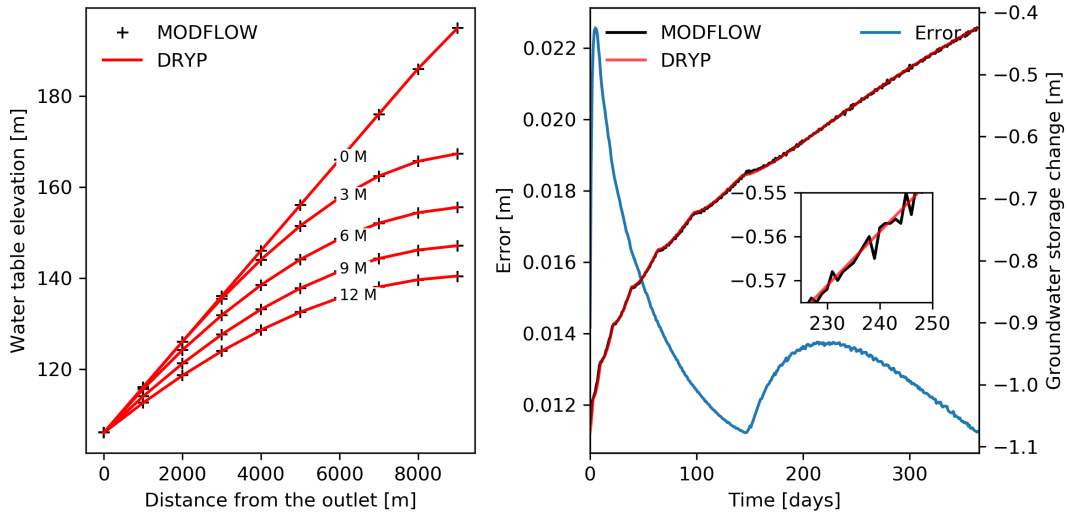


Figure 5.5: a) Simulated head along the aquifer for different time steps estimated by DRYP (solid lines) and MODFLOW (crosses and dashed lines), and b) temporal variation of the mass balance error for DRYP.

5.4.2 Evaluation of synthetic experiments

Figure 5.6 shows the temporal variation of fluxes and state variables for the three simulated scenarios at two evaluation points located along the channel, one at the catchment outlet and the second 4 km from the catchment outlet. These results are in turn described below:

1. 'Infiltration - discharge' scenario (blue lines): when the precipitation falls over the catchment (Fig. 5.6a) it immediately infiltrates into the unsaturated zone, increasing the water content of the soil. Since there are no losses due to evapotranspiration, the water content steadily increases until it reaches field capacity (Fig. 5.6b). At field capacity, given that the soil cannot hold any excess water, it starts to release water as diffuse recharge. The soil remains at field capacity for the rest of the simulation, allowing the water from the next rainfall event to move directly to the saturated zone producing recharge (Fig. 5.6c). Recharge produces an increase in groundwater storage and consequently increases the discharge at the outlet of the catchment (Fig. 5.6d). In the early precipitation events, the contribution of groundwater discharge is minimal. However, this contribution keeps increasing until a dynamic steady-state is eventually reached (by 16400 hours, see Fig. 5.7). Discharge closely follows the temporal variation of the precipitation, due to the high transmissivity of the aquifer and the saturation of the soil; a sharp increase in discharge means that precipitation

has become the main contributor to discharge changes because the water table is at the surface (Fig. 5.6d).

2. . ‘Infiltration-evapotranspiration-discharge’ (green lines): the addition of evapotranspiration in this experiment produces a reduction in soil water content (Fig. 5.6b). Since precipitation is much higher than evapotranspiration, soil moisture quickly reaches a dynamic steady-state at the end of the second precipitation event. At cells located close to the catchment outlet, the rise of the water table to ground level reduces the thickness of the unsaturated zone to zero, as no water can be infiltrated, the soil water content is kept at its highest value during the precipitation event. After the precipitation event, the rate of evapotranspiration, which is greater than the rate of lateral groundwater inflow, gradually reduces the amount of water in the cell. However, since the storage of the SZ keeps increasing, the thickness of the UZ decreases and the rate of lateral groundwater flow becomes greater than the rate of evapotranspiration. It also results in quick changes in the water content of the soil (Fig. 5.6b). Recharge is also reduced and, as expected, only occurs when the soil moisture reaches field capacity (Fig. 5.6c). Discharge is also reduced as a result of decreased aquifer recharge due to upward losses by AET. For cells close to saturation, the storage in the groundwater reservoir is affected by evapotranspiration losses (not observed in right panel due to the y-axis scale), which in turn results in daily fluctuations in discharge that are inverse of evapotranspiration fluctuations.
3. . ‘Infiltration-runoff-evapotranspiration-discharge’ scenario (red lines): a reduced K_{sat} results in the development of infiltration excess overland flow. The rate of infiltration at the beginning of the precipitation event is high enough to provide water for evapotranspiration without reducing the soil water storage (Fig. 5.6b), which explains the similarity in soil moisture behaviour with the second scenario. When cells start to produce runoff as a result of infiltration-excess, discharge also starts to rise. At stream cells with a deep water table, the increase in streamflow is the result of flow accumulation along the channel during the precipitation event (e.g. Fig. 5.6d, left panel at 6600 to 6700 hours). At cells where the water table interacts with the surface, groundwater discharge gradually increases the streamflow at the catchment outlet at much longer temporal scales (Fig. 5.6d). At the catchment outlet, streamflow is also affected by the fluctuation of the water table due to the daily variation of evapotranspiration losses (Fig. 5.6d).

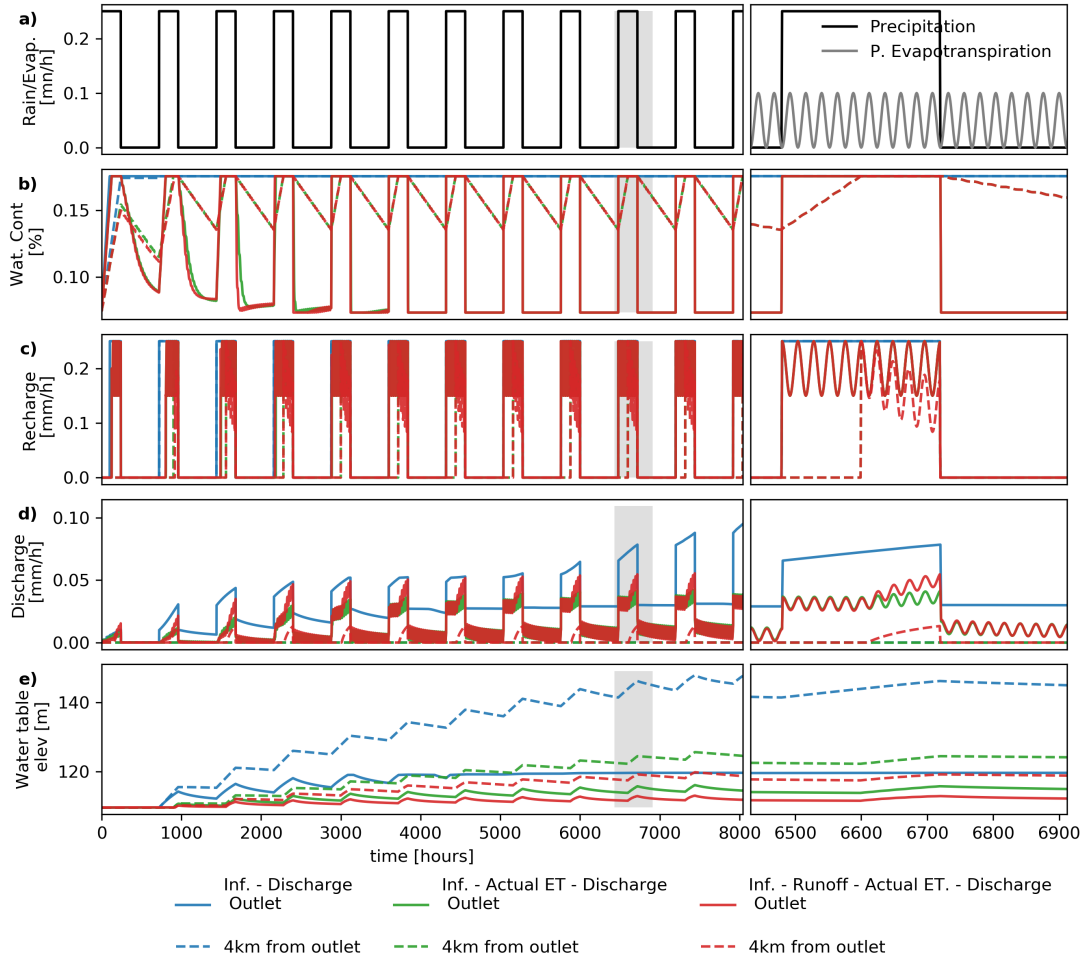


Figure 5.6: Temporal variation of a) precipitation (black line) and evapotranspiration (grey line), b) water content of the unsaturated zone, c) groundwater recharge, d) runoff/discharge, and e) water table elevations. Right panels represent zoomed-in sections of the shaded areas of the left panels. Solid lines represent the variation at the catchment outlet, whereas dashed lines represent the temporal variation in the stream at 4 km from the catchment outlet. For panels b-e, blue lines represent the ‘infiltration-discharge’ scenario, green lines represent the ‘Infiltration-evapotranspiration-discharge’ scenario, and red lines represent ‘Infiltration-runoff-evapotranspiration-discharge’ scenario.

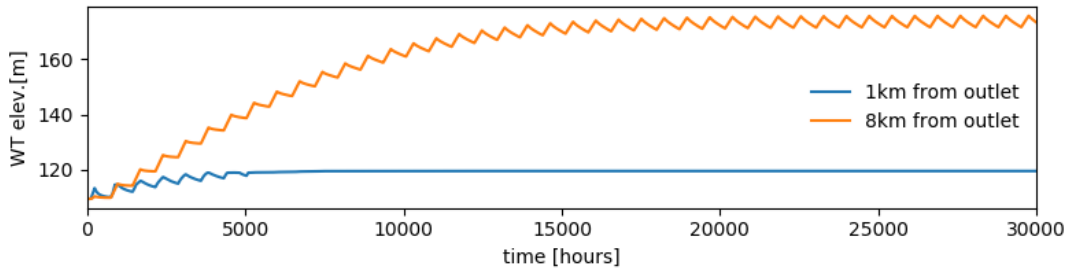


Figure 5.7: Long term simulation of scenario "Infiltration-discharge", steady state is reached after 16,400 hours.

Figure 6.5 shows the cumulative volumes of different components of the water balance as well as the cumulative mass balance error of the model. Mass balance errors are low in comparison to the total amount of water entering the catchment, with values less than 0.12 % for the first case (only precipitation). For the other two cases where evapotranspiration is included, errors are less than 0.02 %. The higher error for the first case scenario is attributed to the concentration of flow at the catchment outlet, which leads to an increase in the number of cells discharging into the surface and the channel and the resulting minor numerical artefacts.

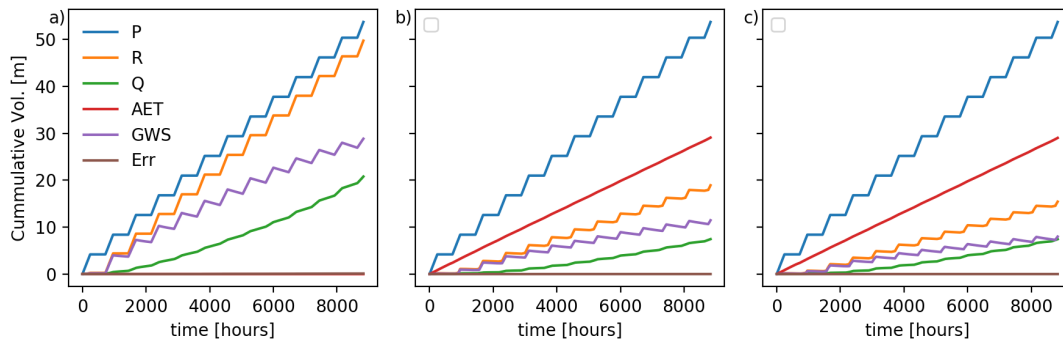


Figure 5.8: Cumulative volume of main components of the water balance for the simulated scenarios: a) Infiltration – discharge, b) infiltration - evapotranspiration - discharge, and c) infiltration-infiltration excess-evapotranspiration-discharge. P is the precipitation, R is recharge, Q is discharge at the catchment outlet, AET is actual evapotranspiration, GWS is the change in groundwater storage, and Err is the water balance error of the simulation.

Coupling of surface and groundwater processes often results in numerical instabilities and in convergence problems (Batelaan and Smedt, 2004; Marçais et al., 2017). However, the results of these synthetic experiments illustrate DRYP's ability to produce realistic hydrological process behaviours by providing a stable solution for rep-

representing groundwater - surface water interactions without producing numerical artefacts. DRYP is effective at handling the complex coupling and dynamic switching of different types of hydraulic boundary conditions, producing acceptable results with negligible mass balance errors.

5.5 Conclusion

This chapter has presented a parsimonious model to estimate water partitioning in dryland regions (“DRYP”). It provides a technical description of all the components of DRYP and its evaluation under different scenarios. The ability of DRYP to provide stable numerical simulations of the interaction of surface and subsurface components through synthetic model experiments was demonstrated in addition to excellent agreement to an industry standard (MODFLOW) groundwater model. Numerical experiments over a synthetic model domain also showed that DRYP shows skill at producing stable simulations for the main components of the water balance with low mass balance errors ($< 0.12\%$). Thus, it has been demonstrated that DRYP shows the potential to be applied in environments where groundwater - surface water interactions play an important role in the overall mass balance of the catchment. Subsequent chapters build on this analysis first applying DRYP to a data rich part of the world in the USA for further testing in a real catchment, before applying it an even larger scale to a data-sparse region of the world in Kenya).

Chapter 6

Characterising water partitioning at catchment scale: Walnut Gulch Experimental Watershed

This chapter is partially based on the paper: Quichimbo, E.A., Singer, M.B., Michaelides, K., Hobley, D.E.J., Rosolem, R., Cuthbert, M.O., 2021. DRYP 1.0: A parsimonious hydrological model of DRYland Partitioning of the water balance. *Geosci. Model Dev. Discuss.* 2021, 1–34.
<https://doi.org/10.5194/gmd-2021-137>.

6.1 Introduction

In this chapter, the performance of DRYP (see Chapter 5) is evaluated with respect to characterising key processes that control the water partitioning in the semi-arid Walnut Gulch Experimental Watershed (WGEW), in SE Arizona, USA. This catchment was chosen based on its comprehensive availability of high-resolution data for a dryland basin, supporting thorough evaluation of the performance of the model. In this chapter, the main objective of DRYP modelling is to capture the long-term behaviour of the water balance in the basin. The Chapter thus describes the main hydrological characteristics of the WGEW, the numerical implementation of DRYP and a sensitivity analysis that was undertaken to support model evaluation. Finally, after quantitatively characterising the water balance of the WGEW, some conclusions are presented.

6.2 Methods

6.2.1 Study site: Walnut Gulch Experimental Watershed-WGEW

The model was evaluated at the Walnut Gulch Experimental Watershed (WGEW), a 149 km² basin near Tombstone, Arizona, USA (31° 43'N, 110° 41'W) (Fig. 6.1). The climate of the region is semi-arid with low annual rainfall – mean of 312 mm yr⁻¹ for the period 1956–2005 (Goodrich et al., 2008).

WGEW was chosen because it has the longest global record of runoff in a semi-arid site (Stone et al., 2008), covering the period 1954–2015. Historical records of event discharge at WGEW exist for this period at seven flumes along the main channel and at seven flumes on tributaries. Event-based rainfall data exist for the same period at many of the 95 operational rain gauging stations across all of WGEW (Goodrich et al., 2008). These historical records of rainfall and discharge provide the opportunity to assess many components of DRYP (Emmerich and Verdugo, 2008; Goodrich et al., 2008; Keefer et al., 2008; Scott et al., 2015; Stone et al., 2008). Additionally, although groundwater has been less well monitored at WGEW, patchy records of water table levels from three wells located close to the catchment outlet are available for assessing the model capability for representing groundwater recharge.

The catchment is underlain by deep Tertiary and Quaternary alluvium sediments. Depths of alluvial sediments are generally >400 m and are composed of different clastic materials, typical of dryland fluvial systems, with a wide range of variation in particle size (clays to well-cemented boulders) (Osterkamp, 2008). The water table is deep below the surface (\approx 145 m at flume 6, fig. 6.1) and shallower (\approx 50 m deep) close to the catchment outlet. A small shallow perched aquifer has been found around flume F02 (see fig. 6.1) (Osterkamp, 2008; Renard et al., 1964).

WGEW is mainly covered by shrubs and grasses, with a high concentration of trees and shrubs along the channels (Skirvin et al., 2008) (Fig. 6.1b). Hillslopes are dominated by gravelly and fine sandy loam soil texture, which generally have high values of hydraulic conductivity (Becker et al., 2018). Streambed sediments are composed of gravel and coarse sand with high values of porosity, supporting high infiltration rates.

Runoff generation is highly spatially and temporally variable, depending on rainfall intensity-duration, rainfall spatial location, antecedent soil moisture, and soil infiltration rates (Becker et al., 2018; Goodrich et al., 1997; Yatheendradas et al., 2008). When the runoff generated on the hillslope is intense and for a long enough duration,

it may result in the accumulation of water in ephemeral channels as streamflow (including as flash floods). Streamflow infiltrates into the channel bed as transmission losses as it moves downstream (e.g. Chen et al. (2019)), supporting both riparian zone moisture availability and focused groundwater recharge.

Lorem ipsum dolor sit amet, consectetur adipiscing elit. Ut purus elit, vestibulum ut, placerat ac, adipiscing vitae, felis. Curabitur dictum gravida mauris. Nam arcu libero, nonummy eget, consectetur id, vulputate a, magna. Donec vehicula augue eu neque. Pellentesque habitant morbi tristique senectus et netus et malesuada fames ac turpis egestas. Mauris ut leo. Cras viverra metus rhoncus sem. Nulla et lectus vestibulum urna fringilla ultrices. Phasellus eu tellus sit amet tortor gravida placerat. Integer sapien est, iaculis in, pretium quis, viverra ac, nunc. Praesent eget sem vel leo ultrices bibendum. Aenean faucibus. Morbi dolor nulla, malesuada eu, pulvinar at, mollis ac, nulla. Curabitur auctor semper nulla. Donec varius orci eget risus. Duis nibh mi, congue eu, accumsan eleifend, sagittis quis, diam. Duis eget orci sit amet orci dignissim rutrum.

6.2.2 DRYP model setting

Model simulations were performed using the modified Green and Ampt infiltration approach (see Chapter 5) because of its ability to describe the high potential infiltration rates at the beginning of the precipitation event, which is particularly important in this setting (Schreiner-McGraw and Vivoni, 2017). The time step of both the surface component and unsaturated component was set to one hour, whereas a time step of one day was used for the riparian zone to reduce computational time. The high temporal resolution for the unsaturated component was used to capture the observed high intensity, low duration rainfall at WGEW, as well as the influence of diurnal fluctuations in evapotranspiration. Since the water table is deep below the ground surface and surface water groundwater interactions are known to be limited (see Chapter 3), the groundwater component was not included in model simulations for WGEW in this chapter.

6.2.3 Forcing data, observation and model parameters

Spatial and temporal information required as inputs and for model parameters were obtained for WGEW from <https://www.tucson.ars.ag.gov/dap/>. A model domain of 104×41 square cells on a 300-m resolution grid was developed. A digital elevation model with a spatial resolution of 30×30 metres was obtained from SRTM

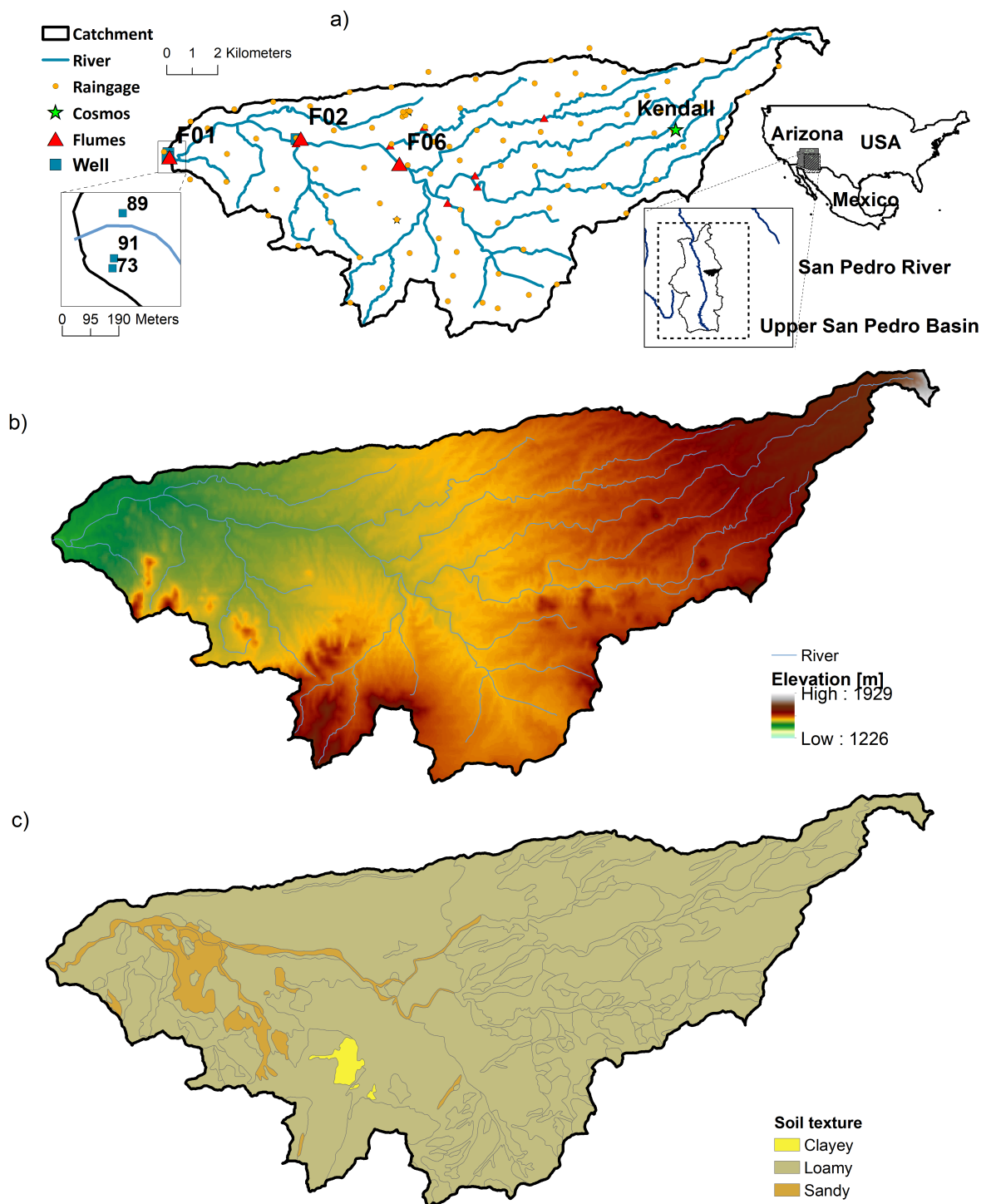


Figure 6.1: a) Geographic location of Walnut Gulch Experimental Watershed and location of monitoring stations, b) topography, c) soil texture, d) Soil land cover, and e) geology

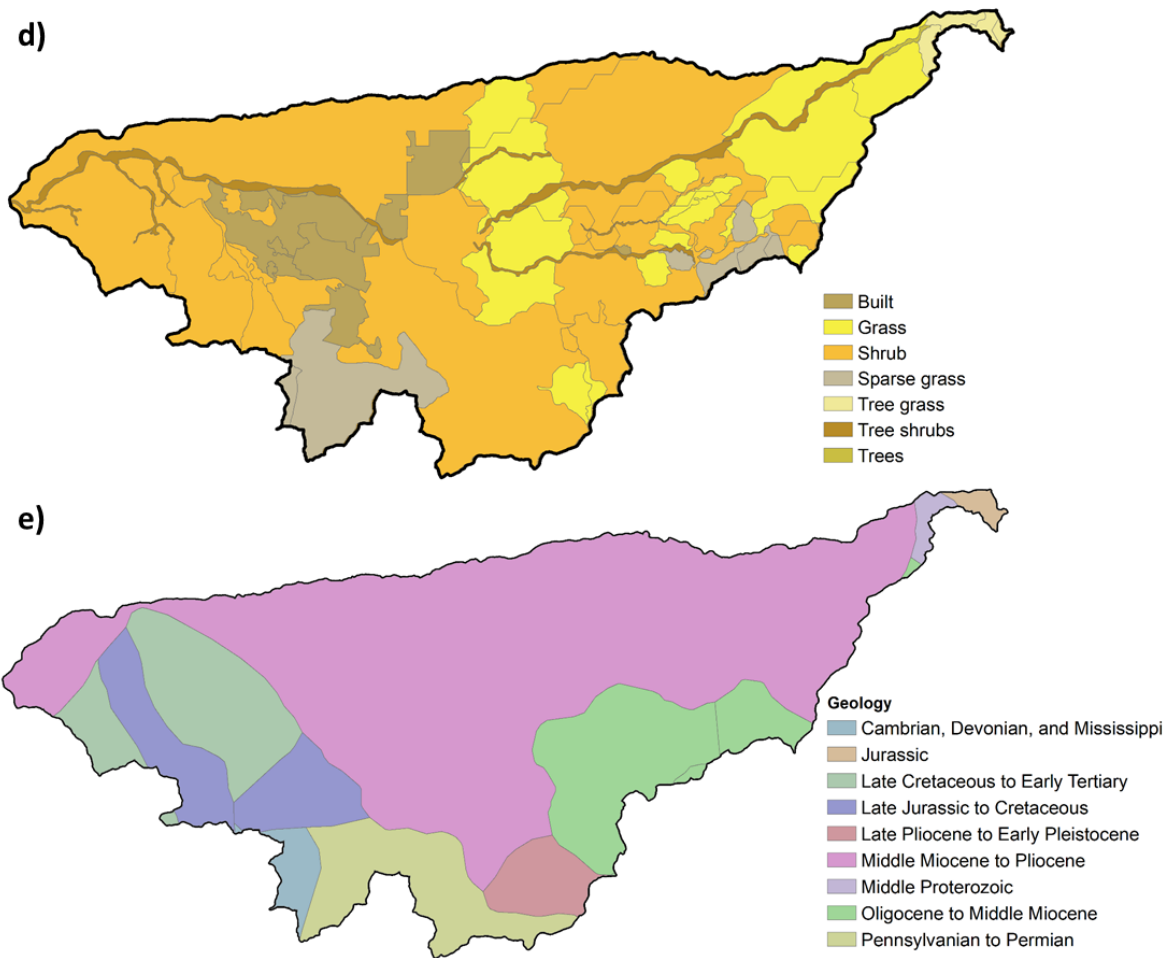


Figure 6.1: a) Geographic location of Walnut Gulch Experimental Watershed and location of monitoring stations, b) topography, c) soil texture, d) Soil land cover, and e) geology (cont.)

Table 6.1: Soil hydraulic parameters for general textural classes, based on Rawls et al. (1982) and Clapp and Hornberger (1978): n is the porosity, b is the pore size distribution parameter, and ψ is the maximum soil matric potential

Texture	n	$K_{sat}[mmh^{-1}]^a$	b^b	$\psi[cm]$
Sand	0.437	117.8	4.05	12.1
Loamy sand	0.437	29.9	4.38	9
Sandy loam	0.453	10.9	4.9	21.8
Loam	0.463	3.4	5.39	47.8
Silt loam	0.501	6.5	5.3	78.6
Sandy clay loam	0.398	1.5	7.12	29.9
Clay loam	0.464	1	8.52	63
Silty clay loam	0.471	1	7.75	35.6
Sandy clay	0.43	0.6	10.4	15.3
Silty clay	0.479	0.5	10.4	49
Clay	0.475	0.3	11.4	40.5

^a Rawls et al. (1982)

^b Clapp and Hornberger (1978)

1 Arc-Second Global map (available at <https://earthexplorer.usgs.gov>). The DEM was aggregated by averaging cells to the 300-m grid size. Textural characteristics of soil and land cover, obtained as polygon files from <https://www.tucson.ars.ag.gov/dap/>, were converted into model gridded data by assigning the value of the polygon feature to the raster value. If there were various features falling into one cell, the value of the local feature with maximum size were assigned as the raster value. Based on the soil texture, baseline hydraulic properties required for modelling were obtained from Rawls et al. (1982) and Clapp and Hornberger (1978) (see Table 6.1). Values of field capacity and wilting point required to estimate L_{TAW} (see Fig. 5.2) were obtained assuming a matric potential of -33 kPa and -1500 kPa following FAO guidelines (Walker, 1989). Soil rooting depth was specified according to land cover, using reference values for different types of vegetation from (Lesschen et al., 2004).

Stream positions were estimated from the 30×30 m DEM. The routing network at the 30×30 m grid resolution was specified by defining a minimal upstream drainage area threshold of 65 ha, which corresponds to the medium stream network resolution specified in Heilman et al. (2008). Stream cells were then aggregated to the model grid size, 300×300 m, to obtain the stream length at any given cell.

Stream width has a great variation over the catchment varying from 2 m in low order streams up to 30 m in the trunk stream (Miller et al., 2000). However, as there was not a source of the spatial variation of stream width for the catchment,

stream width was assumed as 10 m for the whole model domain based on average values observed across the whole catchment (Miller et al., 2000). A sensitivity of channel width was not performed because in the model the channel width and the saturated hydraulic conductivity are directly proportional to the transmission losses. Hence, any change in any of these parameters will result in proportional changes in transmission losses. Additionally, the riparian zone at stream cells was specified with a 40 m width, 15 m at each side of streams, based on measurements from publicly available Google Earth imagery.

Rainfall

Point measurements of rainfall from 95 rainfall stations were used in the analysis. Data is publicly available and was downloaded from <https://www.tucson.ars.ag.gov/dap/>. Rainfall data was processed in two main stages. First, time series of rainfall at every location (see Fig. 6.1) were aggregated at the specified model time step and then spatially interpolated to the 30×30 m grid size using a Natural Neighbour algorithm. In the second stage, the temporally gridded rainfall was spatially aggregated at the resolution of the spatial domains considered for the analysis (300 m).

The timing and rainfall amount of the digital rain gauges at WGEW are regularly calibrated (Goodrich et al., 2008) by comparing digital and analog gauges, therefore, it is assumed that precipitation measurements have low uncertainty. However, interpolation and aggregation processes are highly likely to introduce error into the rainfall estimation. Therefore, a source of uncertainty in the model can be attributed to rainfall. Spatial and temporal aggregation of rainfall have been shown to severely affect the performance of hydrological models (Faurès et al., 1995; Goodrich et al., 1997, 1994; Yatheendradas et al., 2008). Errors up to 130 and 90 % for runoff volume and peak discharge, respectively, have been reported on WGEW by previous studies due to spatial aggregation in rainfall for specific events (Lopes, 1996).

Potential Evapotranspiration (PET) and latent heat flux observations

Potential evapotranspiration (PET) was calculated using hourly data from ERA5-Land reanalysis (Hersbach et al., 2020) because this dataset enabled high temporal resolution (1-hour) and owing to its potential to drive hydrological and land surface models (Albergel et al., 2018; Alfieri et al., 2020; Tarek et al., 2020). Data from ERA5 have a spatial resolution of ≈ 9 km at the equator.

The Penman-Monteith approach, considered a standard method by the FAO (Food and Agriculture Organization of the United Nations) (Allen et al., 1998), was chosen

to estimate hourly PET due to its high accuracy to produce evapotranspiration values under different climates and locations:

$$ET_o = \frac{0.408\Delta (R_n - G) + \gamma \frac{37}{T_{hr}+273} u_2 (e^\circ(T_{hr}) - e_a)}{\Delta + \gamma (1 + 0.34u_2)} \quad (6.1)$$

where ET_o is the reference evapotranspiration [mm h^{-1}], R_n is the net radiation at the grass surface [$\text{MJ m}^{-2} \text{h}^{-1}$], G is the soil heat flux density [$\text{MJ m}^{-2} \text{h}^{-1}$], T_{hr} is the mean hourly air temperature [C], δ is the saturation slope vapour pressure curve at T_{hr} [kPa C^{-1}], γ is the psychrometric constant [kPa C^{-1}], $e^\circ(T_{hr})$ is the saturation vapour pressure at air temperature T_{hr} [kPa] e_a is the average hourly actual vapour pressure [kPa], and u_2 is the average hourly wind speed [m s^{-1}] at 2 m above the surface.

Data from two AmeriFlux eddy covariance flux tower sites located within WGEW, Lucky Hills (ES-SRC) and Kendall Grassland (US-Wkg), were available at the study site for model evaluation of AET (Glenn et al., 2015; Scott, 2010). However, only one site, US-Wkg, was considered for model evaluation due to its location far from the influence of model boundary domain. Uncertainty in flux tower data is mainly attributed to instrumental and random errors and it increases with flux magnitude (Richardson et al., 2006; Schmidt et al., 2012). Mean relative errors for AmeriFlux sites are approximately -5 % with deviations of ± 16 % (Schmidt et al., 2012). Historical records from mid-2006 to 2018 were available for model evaluation. AmeriFlux data are publicly available and were downloaded from <https://ameriflux.lbl.gov/sites/siteinfo/US-Wkg>.

Soil moisture measurements

To evaluate modelled soil moisture, data from a cosmic-ray neutron sensor station from the COSMOS network (Zreda et al., 2012) was used. The COSMOS station is located within the Kendall subcatchment of WGEW (see Fig. 6.1). The raw data (publicly available at <http://cosmos.hwr.arizona.edu/Probes/StationDat/010/index.php>) were corrected for atmospheric pressure (Desilets et al., 2010; IAEA, 2017; ?), atmospheric vapour pressure (Rosolem et al., 2013), above ground biomass and variation in background intensity using the standardised data processing Cosmic-Ray Sensor Python tool (Power et al., 2021) for the period between mid-2010 and 2018.

Runoff measurements

Runoff at 11 small watersheds and the catchment outlet is regularly measured by critical and subcritical depth flumes. However, due to the spatial scale and grid size

of the model, three main flumes (F01, F02, F06) located along the main channel were considered for the analysis (see Fig. 6.1). Flumes at WGEW have been designed to capture the high variability of flow. Therefore, the reliability and accuracy of the measurements have low uncertainty (Stone et al., 2008).

Groundwater observations

Available groundwater measurements at WGEW are very limited. Consequently, the evaluation of surface-groundwater processes at the study site is very restricted. Patchy information from three wells located close to the catchment outlet were available for the evaluation of model focused recharge (see Fig. 6.1). Daily and hourly records for two periods: 16/07/1999-14/01/2004 and 08/08/2017-15/03/2019 were available for the analysis.

Large gaps in water table records restrict the proper characterisation of the number and magnitude of recharge events. However, the information available allows the estimation of the overall change in the groundwater storage due to recharge occurring between the two periods. Thus, these short but high resolution periods allow the characterisation of the hydraulic characteristics of the aquifer system.

6.2.4 Model sensitivity analysis and calibration

An initial trial-and-error calibration of the model was performed to explore the parameter sensitivities of DRYP and to reduce the a priori parameter ranges used in the second step. This first trial-and-error calibration considered only the performance of the model to represent streamflow at the catchment outlet (flume F01). The calibration was performed by applying spatially constant multiplicative factors (kK_{sat} , kD , kK_{ch} , kk_T) to model parameters (K_{sat} , D , K_{ch} and k_T , respectively). These parameters were used because they control the storage and the water partitioning of components (surface and subsurface components) in the DRYP model for WGEW. Parameters W , K_{ch} , and k_T were assumed to be uniform over the entire catchment due to the lack of spatial information, whereas the rest of parameters listed in Table 5.1 vary depending on their mapped spatial distribution. The initial manual calibration enabled a set of parameter ranges to be defined for a Monte Carlo experiment to analyse the multi-parameter uncertainty of the model results. Then, a set of 1000 realisations was implemented for the analysis with parameters randomly generated using a uniform distribution.

The Generalized Likelihood Uncertainty Estimation (GLUE) framework (Beven and Binley, 1992) was used as the uncertainty analysis framework. The GLUE framework considers that, owing to the uncertainty of the input data, model structure and

limitations of boundary condition, there are multiple set of parameters that can produce acceptable simulations. To determine which simulations were considered as acceptable (i.e. behavioural), a combination of two different 'goodness of fit' indices was used: Nash–Sutcliffe Efficiency (NSE) (Nash and Sutcliffe, 1970), and per cent bias (PBIAS) defined as follows:

$$NSE = 1 - \frac{\sum_{i=1}^n (O_i - S_i)^2}{\sum_{i=1}^n (O_i - \bar{O})^2} \quad (6.2)$$

$$PBIAS (\%) = 100 \cdot \frac{\sum_{i=1}^n O_i - \sum_{i=1}^n S_i}{\sum_{i=1}^n O_i} \quad (6.3)$$

where: O represents the observation, \hat{O} is the arithmetic mean of observations, S represents the model simulations, and n is the number of observations.

In order to define behavioural models, a set of thresholds was specified for the three indices. For streamflow, values of NSE higher than 0.50 and $PBIAS$ less than 20 % (i.e. less than 1 % of the total water budget of the study area) were considered as acceptable simulations. For soil moisture and actual evapotranspiration, only values of NSE greater than 0.5 was used.

In order to combine these measures into a single performance metric, models which did not meet these conditions were assigned a value of zero, whereas the indexes were linearly scaled between 0 and 1 for rest of models. Scaling of NSE values was performed according to the following range: 0 for the minimum value ($NSE = 0.5$) and 1 for the maximum value of NSE which is also 1. For $PBIAS$, absolute values were scaled by considering the maximum value ($PBIAS = 20$ %) equal to 0 and the minimum ($PBIAS = 0$) equal to 1. The combined performance measure was calculated as the product of all indexes considered in the analysis:

$$p_i = \prod_{k=1,2,6} NS_k^* \cdot PBIAS_k^* \quad (6.4)$$

where p_i is the combined performance measure for the i -th parameter set, the * signifies scaled values, and k represents the variable considered in the analysis.

For soil moisture, a direct comparison between observation and simulations was not possible due to differences between the representative soil depths of measurements and simulations. Modelled soil moisture represents the water content of the entire soil column specified by the rooting depth, whereas the observed soil moisture represents the water content over a depth-averaged value, which can be characterised by an effective soil depth that depends on the soil moisture itself (Franz et al., 2012). A

direct comparison would result in the misrepresentation of high values of observed soil water content by the model due to the attenuation of peak values over larger soil depths. This problem has been solved by using exponential models that need to be calibrated by using measurements at different soil depths (e.g. Albergel et al. (2008); Wagner et al. (1999)). Therefore, to enable model-data comparisons that capture the variation of both high and low values of soil moisture observations, scaling of observed soil moisture was performed by the following expression:

$$O^* = O^\alpha + S_{min} \quad (6.5)$$

where: O^* refers to the scaled value, and α is estimated by:

$$\alpha = \frac{\log |S_{max} - S_{min}|}{\log |O_{max} - O_{min}|} \quad (6.6)$$

The period between 01/01/2007 and 01/01/2018 was the temporal domain for model simulations at WGEW, with a warm-up period of one year prior to this period. This period matches the overlapping period of streamflow observations and flux tower observations. Soil moisture was evaluated for a shorter period of available data 01/10/2010 and 01/01/2018. Additionally, modelled soil moisture for the COSMOS site was obtained by spatial averaging the 9 cells located around the COSMOS station to match the effective COSMOS footprint diameter (700m) (Desilets and Zreda, 2013).

6.2.5 Focused Recharge Evaluation

Owing to the deep water table, groundwater - surface water interactions are considered to be uni-directional (see Chapter 3 and 4). Given the spatial and temporal scales of the model, this was required to give a more detailed representation of hydraulic head resulting from the simulated recharge. Therefore, the evaluation of the modelled recharge was performed separately by developing a 2D transect model. The groundwater component of DRYP was used 'offline' from the catchment model, to represent the changes in the water table due to recharge generated from the DRYP catchment model.

The 2D model was set in order to capture the small spatial influence of focused recharge on the water table. Focused recharge will produce a local mounding within the water table that will lead to an initial steep recession due to the nonequilibrium flow. The steep recession will eventually be attenuated and will reach a linear shape governed by the regional groundwater recession (Cuthbert, 2014). This is a common

process in dryland regions where the recharge is sporadic. This linear recession has also been reported by Goodrich et al. (2013) at WGEW.

A schematic representation of the model and the geometrical characteristics of the model domain are shown in figure 6.2. The model domain consisted of 1×100 grid shape and one layer. Grid size elements were specified as 100×15 metres. Values of specific yield, S_y [-], were assumed to vary between 7-9% according to hydrogeological reports of aquifers with similar geological characteristics (cemented conglomerates), taken from locations close to WGEW (Pool and Schmidt, 1997; USBR, 1977). Flow rates for the linear recession were calculated considering the head changes over a period between 2002-2004. This period corresponds to water table changes at which the groundwater mounding dissipated due to the input pulse (see Fig. 5.2). Considering the range of variation of S_y , the flux boundary conditions varies from 0.00007 - 0.00009 $\text{m}^3 \text{d}^{-1}$.

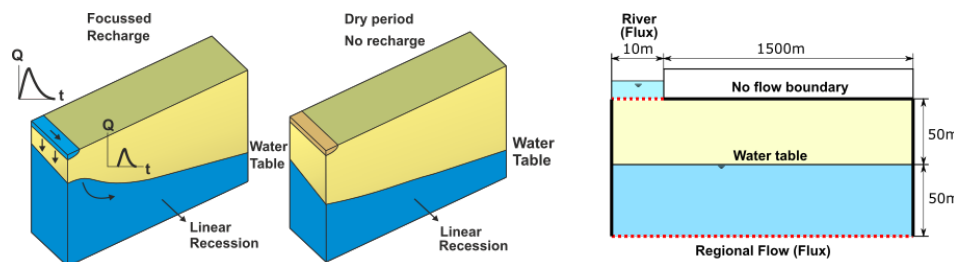


Figure 6.2: Conceptual model for evaluation of estimated focused recharge, and a diagram for model setup

6.3 Results

6.3.1 Spatio-temporal visualisation of model process simulation at WGEW

The ability of the model to capture the dynamics of dryland hydrological processes is illustrated for WGEW in Figure 6.3. The best model (see following section) captures the emergence of ephemeral flow conditions for specific storms, as well as the spatio-temporal changes in soil moisture. It can be seen how, for a given initial soil moisture condition, the production of runoff due to a rainfall event falling over only the central part of catchment results in the concentration of flow along the stream. As water moves downstream, the stream loses water via transmission losses, which ultimately consumes almost all the available water by the time runoff reaches the catchment outlet (flume F01 in Figure 6.3c).

Lorem ipsum dolor sit amet, consectetur adipiscing elit. Ut purus elit, vestibulum ut, placerat ac, adipiscing vitae, felis. Curabitur dictum gravida mauris. Nam arcu libero, nonummy eget, consectetur id, vulputate a, magna. Donec vehicula augue eu neque. Pellentesque habitant morbi tristique senectus et netus et malesuada fames ac turpis egestas. Mauris ut leo. Cras viverra metus rhoncus sem. Nulla et lectus vestibulum urna fringilla ultrices. Phasellus eu tellus sit amet tortor gravida placerat. Integer sapien est, iaculis in, pretium quis, viverra ac, nunc. Praesent eget sem vel leo ultrices bibendum. Aenean faucibus. Morbi dolor nulla, malesuada eu, pulvinar at, mollis ac, nulla. Curabitur auctor semper nulla. Donec varius orci eget risus. Duis nibh mi, congue eu, accumsan eleifend, sagittis quis, diam. Duis eget orci sit amet orci dignissim rutrum. Nam dui ligula, fringilla a, euismod sodales, sollicitudin vel, wisi. Morbi auctor lorem non justo. Nam lacus libero, pretium at, lobortis vitae, ultricies et, tellus. Donec aliquet, tortor sed accumsan bibendum, erat ligula aliquet magna, vitae ornare odio metus a mi. Morbi ac orci et nisl hendrerit mollis. Suspendisse ut massa. Cras nec ante. Pellentesque a nulla. Cum sociis natoque penatibus et magnis dis parturient montes, nascetur ridiculus mus. Aliquam tincidunt urna. Nulla ullamcorper vestibulum turpis. Pellentesque cursus luctus mauris.

Nulla malesuada porttitor diam. Donec felis erat, congue non, volutpat at, tincidunt tristique, libero. Vivamus viverra fermentum felis. Donec nonummy pellentesque ante. Phasellus adipiscing semper elit. Proin fermentum massa ac quam. Sed diam turpis, molestie vitae, placerat a, molestie nec, leo. Maecenas lacinia. Nam ipsum ligula, eleifend at, accumsan nec, suscipit a, ipsum. Morbi blandit ligula feugiat magna. Nunc eleifend consequat lorem. Sed lacinia nulla vitae enim. Pellentesque tincidunt purus vel magna. Integer non enim. Praesent euismod nunc eu purus. Donec bibendum quam in tellus. Nullam cursus pulvinar lectus. Donec et mi. Nam vulputate metus eu enim. Vestibulum pellentesque felis eu massa.

6.3.2 Characterisation of the temporal variation in simulated variables

Calibration using the trial-and-error method showed that streamflow showed particular sensitivity to the parameters K_{sat} , D , K_{ch} and k_T . This informed a set of parameter ranges that were used in the Monte Carlo analysis as follows: for hydraulic conductivity at the channel, kK_{ch} , 0.10 and 0.30, for kK_{sat} 0.20 and 0.50, for kk_T 3-10, and k_D 0.80 and 1.20. The Monte Carlo analysis resulted in 21 behavioural models with values of p above zero. The calibrated parameters for the best simulation were kK_{ch}

$= 0.21$, $kAWC = 1.02$, $kK_{sat} = 0.30$, and $kk_T = 7.7$. A factor of $kk_T = 7.7$ applied to default value of k_T (0.083) represents a flow velocity of 0.41 m s^{-1} in the channel.

Soil moisture

The DRYP model demonstrates skill at capturing the dynamics of the soil moisture (Fig. 6.4b) with values of NSE around 0.69. Discrepancies in the magnitude of peak values are likely the result of scaling, so simulations are not able to account for the variation of the effective measurement depth of COSMOS water content estimates (Franz et al., 2012, 2013). The effective COSMOS measurement depth is greater for low values of soil water content ($\approx 33 \text{ cm}$), whereas, for higher values of water content

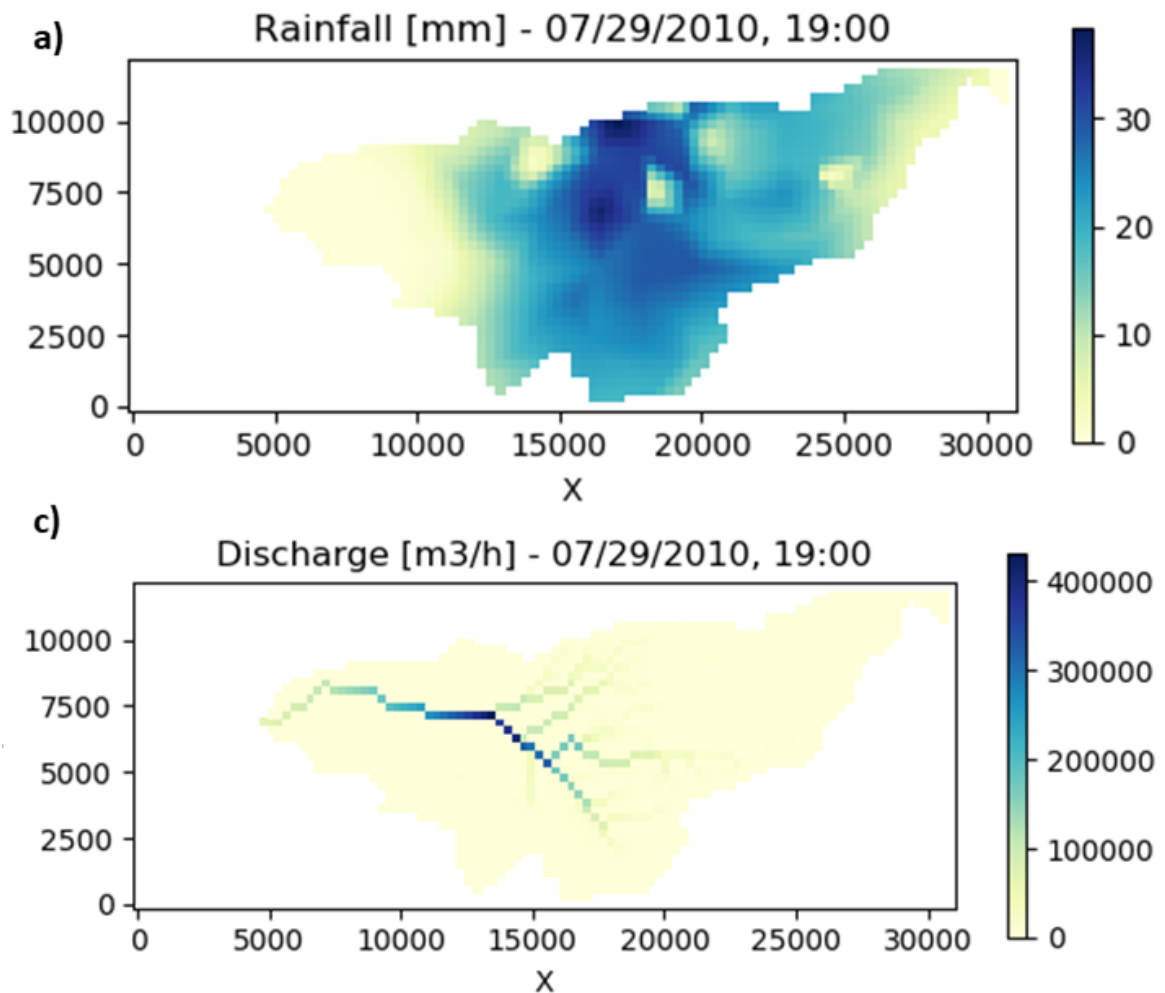


Figure 6.3: Spatio-temporal visualisation of model process simulation at WGEW, a) rainfall event, b) soil moisture previous to the rainfall event, c) ephemeral stream for the rainfall event, and d) soil moisture after the rainfall event; x and y axes distance units are in metres.

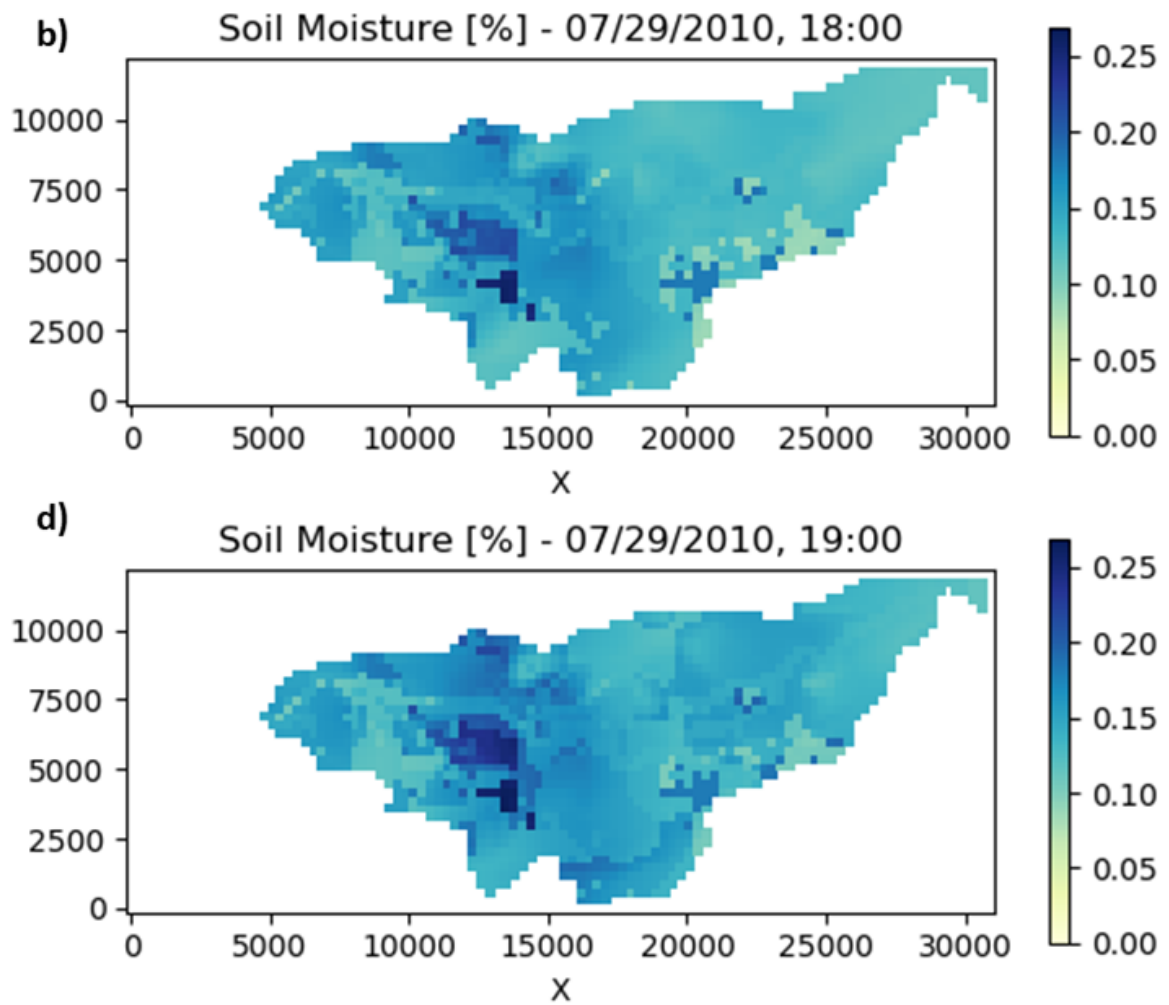


Figure 6.3: Spatio-temporal visualisation of model process simulation at WGEW, a) rainfall event, b) soil moisture previous to the rainfall event, c) ephemeral stream for the rainfall event, and c) soil moisture after the rainfall event; x and y axes distance units are in metres (cont.).

the effective measurement depth is shallow (≈ 16 cm). However, discrepancies may also reflect the limited ability of the soil moisture model to represent high variations occurring at shallow depths of the soil layer, due to the use of a single store. Nevertheless, it is encouraging that DRYP captures the time series dynamics of the soil moisture signal recorded at the COSMOS station.

Evapotranspiration

The DRYP model also captures ($NSE \approx 0.7$) the seasonality and the overall temporal variation in evapotranspiration, a dominant component of the water budget in drylands (Fig. 6.4b), although peak values are generally overpredicted after long dry periods. Nevertheless, discrepancies between flux tower data and simulated AET up to 15% for one year have been reported for grassland vegetation in previous studies (Scott, 2010; Twine et al., 2000), and such errors are mainly attributed to the inherent uncertainty in rainfall and latent heat flux measurements (Scott, 2010).

Streamflow

DRYP is also able to reproduce the seasonality and the monthly production of runoff at the outlet of the catchment (F01, $NSE = 0.9$) (Fig. 6.4c), as well as at the two upstream flumes (F02, F06) considered in the analysis ($NSE \approx 0.60$) (Figs. 6.4d and 6.4e). However, monthly values at flumes F02 and F06 are overpredicted in 2012, perhaps reflecting the development of a crusting layer in previous dry years (e.g. 2009, 2011), a process not included in the model. On the other hand, low production of runoff during wet years (e.g. 2015) may be attributed to the energy of high intensity rainfall events removing such a crusting layer from the top of the soil, which in turn results in the increase of infiltration rates (Becker et al., 2018). Additionally, the spatial aggregation of the DEM causes slight inaccuracies in the estimated contributing areas for different streams. This affects not only the volume but also the timing of streamflow events, which may result in over/under prediction of streamflow events and may ultimately affect the overall water budget.

Groundwater recharge

Owing to the short period of available data to evaluate the simulations of groundwater recharge, the simulation period for the best model was extended to a period between 01/01/2000 and 01/01/2019. Results of the 2D model show how the amount of water percolated from the streambed via focused recharge affects the water table elevation (see Fig. 6.5). It can be seen that for the last period of available data, mid 2017 to late 2018, the model captures the changes in the water table due to focused recharge. For the period between 01/01/2000 and 01/01/2004, at which the model was not evaluated for streamflow, soil moisture or AET, the model is still able to capture

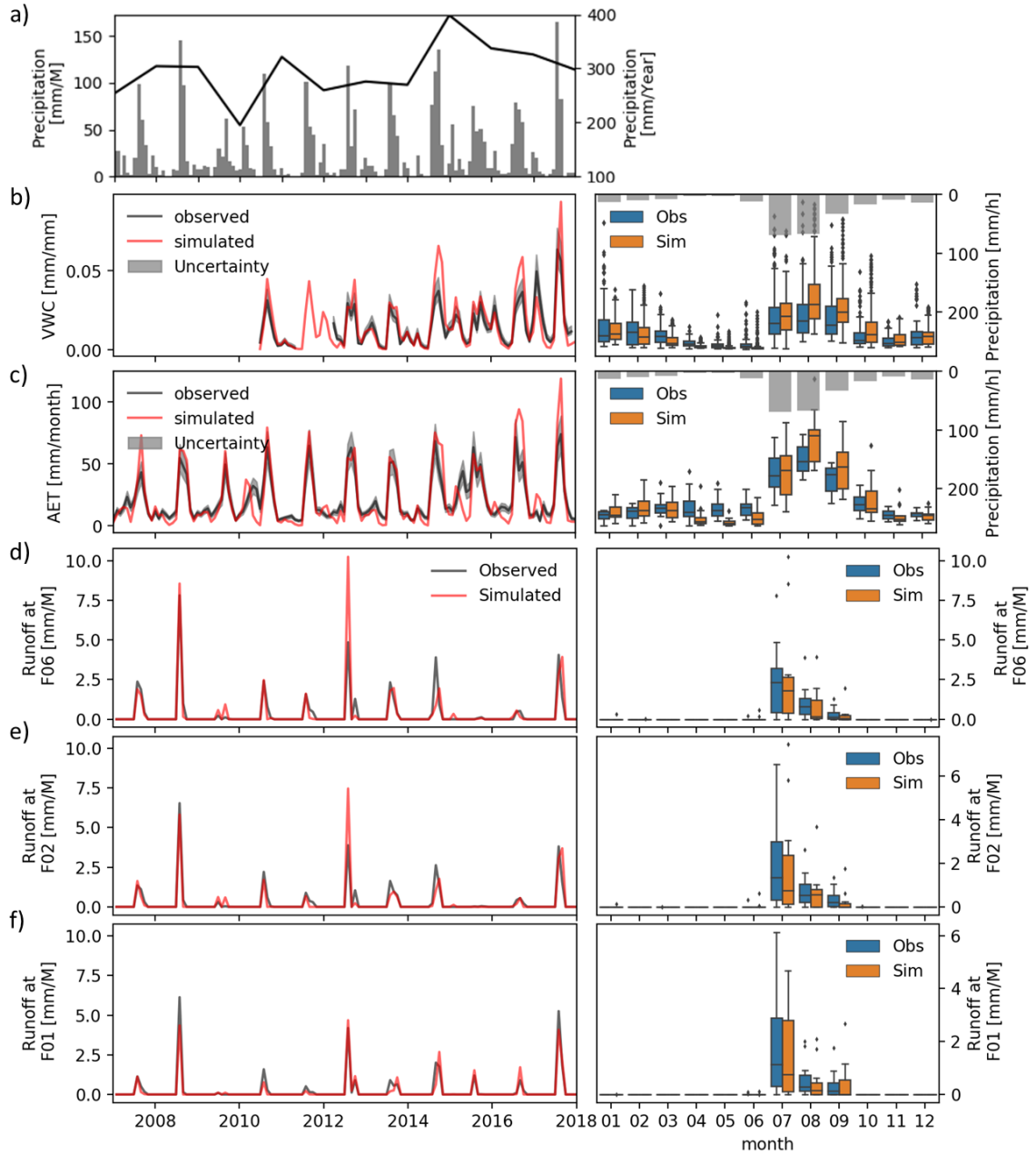


Figure 6.4: Comparison between observed and simulated values of monthly temporal variation (left) and monthly distribution (right) of a) monthly precipitation (left axes) and yearly precipitation (right axes), b) soil moisture at the COSMOS Kendall location, c) actual evapotranspiration at Kendall, d) streamflow at flume F06, e) streamflow at flume F02, and f) streamflow at flume F01. See Fig. 5.4 for station locations.

the recharge from the year 2002. This shows that DRYP is able to represent well the spatial and temporal variation of water partitioning between precipitation and runoff, and despite the simplicity of the flow routing and transmission losses approach, the model shows that is robust to represent the focused groundwater recharge. For the year 2001, where a high streamflow event is not captured by DRYP, the recharge is underestimated and consequently, so is groundwater mounding. However, the overall linear recession rate, which expresses the ratio of long term recharge to specific yield (Cuthbert, 2014; Cuthbert et al., 2016), is simulated well.

In general, results from DRYP suggest that the model has good skill to simulate the water partitioning for the evaluated period. The amount of water required to produce and increase the water table matches the observations for the aquifer properties specified for the study area.

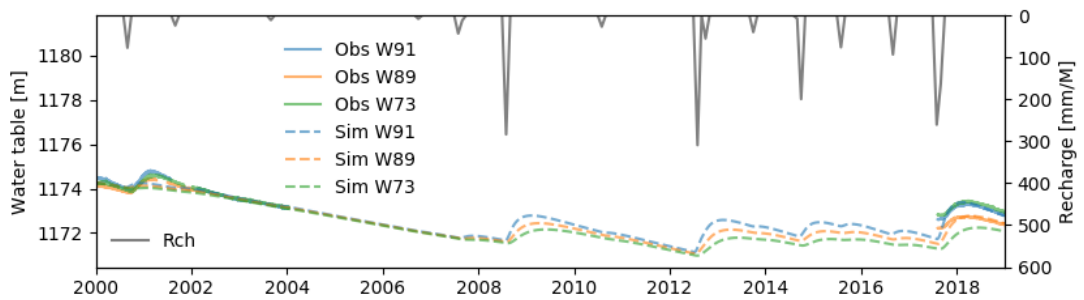


Figure 6.5: Comparison of simulated and observed values of water table elevation estimated by the 2D numerical simulation. The modelled recharge obtained from DRYP (grey) was used as model input for the 2D model

6.3.3 Water balance

Precipitation shows a high annual variability for the evaluated period in relation to the mean value (295 mm yr^{-1}). The range of variation includes the lowest value of 200 mm yr^{-1} corresponding to the 2011 and reaches a value of up to $\approx 400 \text{ mm yr}^{-1}$ in 2015 (Fig. 6.4a). This variability in input precipitation translates into variability in the annual water partitioning for WGEW. For the evaluation period, 01/01/2007 to 01/01/2018, water balance estimates from the best model show that 92 % of the total precipitation infiltrates into the soil (see Fig. 6.6). However, almost all infiltrated water returns to the atmosphere as evapotranspiration, representing 89 % of the total precipitation. A small proportion, $\approx 3 \%$ of the total precipitation, remains in the soil, and this stored water corresponds mainly to wetter years of the simulation

period (2014, and 2015). Only a small percentage, less than 0.03 %, percolates as diffuse recharge contributing to groundwater storage. Water that does not infiltrate into the soil (8 % of the precipitation) is routed downstream. However, this amount of water is consistently reduced by transmission losses, representing ≈ 7 % of the precipitation. Water entering the riparian zone via transmission losses is partitioned into evapotranspiration and focused recharge.

Evapotranspiration consumes up to 60 % of these transmission losses representing ≈ 4.5 % of the total precipitation. This shows how transmission losses play an important role in the availability of water for plant evapotranspiration and ecohydrological process occurring in riparian areas. This result is broadly consistent with previous studies showing values of 20 mm yr^{-1} or 5.5 to 7 % of the total precipitation (Renard, 1970; Renard et al., 2008). The amount of surface water leaving the catchment represents less than 1.0 % of the total amount of precipitation falling over the catchment. These values highlight the impact of transmission losses on the streamflow and aquifer recharge. The main contributor to the total amount of groundwater recharge is focused recharge (≈ 2.5 % of precipitation).

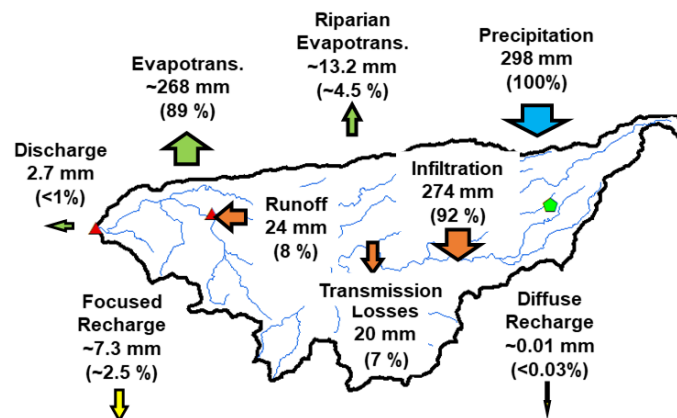


Figure 6.6: Average fluxes of different components of the water budget of WGEW for the simulated period, 01/01/2007 to 01/01/2018. Blue arrows show input fluxes, green arrows represent water leaving the catchment, orange arrows represent internal surface and unsaturated zone fluxes, and yellow arrows represent water moving to the saturated zone (not modelled), values in brackets represent the percentage estimated in relation to the precipitation.

6.4 Conclusions

The performance of the parsimonious model, DRYP, to quantify water fluxes and partitioning was evaluated by using stream flow, soil moisture, evapotranspiration

and groundwater level data from the semi-arid Walnut Gulch Experimental Watershed (Arizona, USA). The ability of the model to produce behavioural simulations that match observed phenomena was evaluated based on multi-parameter Monte Carlo experiments for a range of objective performance metrics.

Overall, DRYP is demonstrably effective for estimating the spatio-temporal variation in the main components of the dryland water balance. It is both parsimonious and computationally efficient, enabling a wide range of parameter and structural uncertainties to be resolved. For Walnut Gulch, it was found that focused recharge represents between $\approx 2.5\%$ the total amount of rainfall, whereas diffuse recharge is below 0.03% . Evapotranspiration is the dominant process above 90% of water leaving the catchment. The results also show that evapotranspiration from riparian areas also plays an important role in groundwater recharge since the amount of water becoming focused recharge is only around 40% of the transmission losses.

Chapter 7

Assessing the uncertainty of water partitioning at WGEW: a multi-scale analysis

7.1 Introduction

Chapter 6 showed that DRYP has the ability to effectively estimate the main components of the water balance in the semi-arid Walnut Gulch Experimental Watershed. However, the influence of the spatio-temporal scale of processes description within DRYP has not yet been evaluated. Spatial and temporal scales of model processes and underlying model structure influence the quantification of water partitioning into fluxes and storage comprising the water balance (Blöschl et al., 1995; Blöschl and Sivapalan, 1995a; Kipkemoi et al., 2021; Scheidegger et al., 2021). At different scales, different processes may become dominant (Barthel and Banzhaf, 2016; Beven, 1991, 1995, 2001; Blöschl and Sivapalan, 1995b; Fenicia et al., 2008; Merz et al., 2009). Therefore, assessing the scale-dependence of dominant hydrological processes is of key importance for understanding the main controls on water partitioning for a catchment. Given the spatial-temporal variability of hydrological processes in arid and semi-arid regions, understanding the sensitivity of factors controlling water partitioning at different spatial-temporal scales will not only give insights into the transferability of processes at different scales, but it will also enhance understanding of the likely impacts of variation in climatic forcing on quantification of water balance components.

To meet this research challenge, the influence of model structure as well as the spatial and temporal scaling of processes within DRYP is investigated in this Chapter. The Walnut Gulch Experimental Watershed (WGEW) was again used for the analysis,

given its unparalleled density of available high quality hydrometeorological data. The impact of model resolution on fluxes and states was investigated by changing model grid size, time step, and the temporal resolution of forcing data. In addition, model structure was evaluated by comparing several infiltration approaches for surface water partitioning.

7.2 Methods

7.2.1 Study Site

A full description of the WGEW study site is presented in Chapter 6, including locations of observation stations for rainfall, streamflow, soil moisture, and latent heat, shown in Chapter 6, figure 6.1.

7.2.2 Model Scale Analysis

Scale dependence of modelled water partitioning at WGEW was evaluated by considering different spatial and temporal scales. This was done by using three model grid sizes (300m, 1km, and 5km) and three model time steps (15min, 1h and 24h). In most dryland regions, the lack of data (especially streamflow measurements) severely restricts hydrological model evaluation, yet such models are sorely needed in data-sparse areas. Therefore, in order to evaluate DRYP's efficacy in representing the key hydrological processes with limited data available for evaluation, two scenarios of data availability were considered for this analysis: i) use of data from three streamflow flumes along the main channel, along with soil moisture and evapotranspiration data, and ii) use of only one flume at the catchment outlet as well as evaporation and soil moisture. For both data scenarios, the Kendall station (see Fig. 6.1) was used for evaluation of soil moisture and evapotranspiration, as described in more detail below.

7.2.3 Model settings and parameterisation

Topography and surface characteristics

Topography for each grid size (300m, 1km, and 5km) used in the analysis was obtained by spatially aggregating the digital elevation model (DEM) of WGEW (SRTM 1 Arc-Second Global map, see Section 6.2.3 for more details).

Stream location and stream length for each grid size were also estimated from the 30×30 m grid size DEM following a similar approach described in section 6.2.3 (see Fig. 7.1b).

Hydraulic properties derived from soil texture required in DRYP were obtained from Rawls et al. (1982) and Clapp and Hornberger (1978) (see Table 6.1 and section 6.2.3). Soil rooting depth was specified according to land cover and using reference values for different types of vegetation from Lesschen et al. (2004) (see Fig. 7.1e).

Lorem ipsum dolor sit amet, consectetur adipiscing elit. Ut purus elit, vestibulum ut, placerat ac, adipiscing vitae, felis. Curabitur dictum gravida mauris. Nam arcu libero, nonummy eget, consectetur id, vulputate a, magna. Donec vehicula augue eu neque. Pellentesque habitant morbi tristique senectus et netus et malesuada fames ac turpis egestas. Mauris ut leo. Cras viverra metus rhoncus sem. Nulla et lectus vestibulum urna fringilla ultrices. Phasellus eu tellus sit amet tortor gravida placerat. Integer sapien est, iaculis in, pretium quis, viverra ac, nunc. Praesent eget sem vel leo ultrices bibendum. Aenean faucibus. Morbi dolor nulla, malesuada eu, pulvinar at, mollis ac, nulla. Curabitur auctor semper nulla. Donec varius orci eget risus. Duis nibh mi, congue eu, accumsan eleifend, sagittis quis, diam. Duis eget orci sit amet orci dignissim rutrum.

Rainfall

Rainfall data (see Section 6.2.3) was processed in two main stages: first, per minute time series of rainfall at every location (see Fig. 6.1) were aggregated to the specified model time step and then spatially interpolated to a 30×30 m grid size using a Natural Neighbour algorithm. In the second stage, the temporally gridded rainfall was spatially aggregated to the resolution of the spatial domains considered for the analysis (300m, 1km, and 5km).

7.2.4 Potential Evapotranspiration (PET), latent heat flux, and soil moisture observations

A complete description of the potential evapotranspiration (PET) is presented in Chapter 6. Similarly, latent heat flux at Kendall Grassland (US-Wkg) from the AmeriFlux eddy covariance flux tower site (Fig. 6.1) and soil moisture data from Kendall Cosmos station (Fig. 6.1) used for model evaluation are also presented in Chapter 6,

Runoff measurements

The spatial aggregation of the DEM of the study site have a major impact on the distribution of contributing areas at subcatchment level (see Chapter 6). Variations in areas of up to 800 % for small catchments were found when comparing gridded data and values reported by Heilman et al. (2008) (considered here as a baseline). Therefore, only three flumes (F01, F02 and F06) along the main channel were used

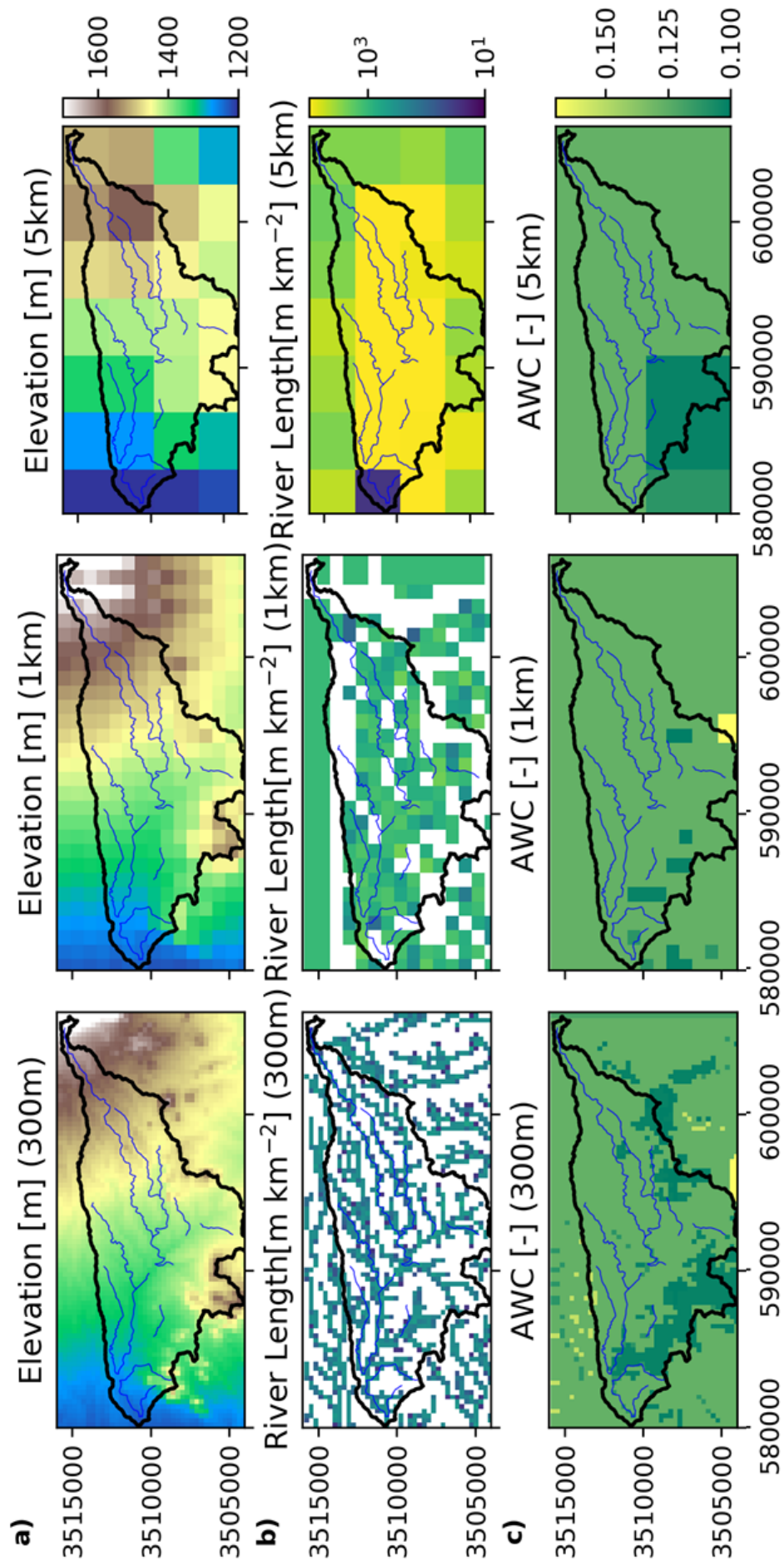


Figure 7.1: Topography and soil hydraulic characteristics for the three different grid scales (300m, 1km, 5km). AWC = available water content. Values in parenthesis represent the grid size, solid black line represent the WGEW, and solid blue lines represent streams.

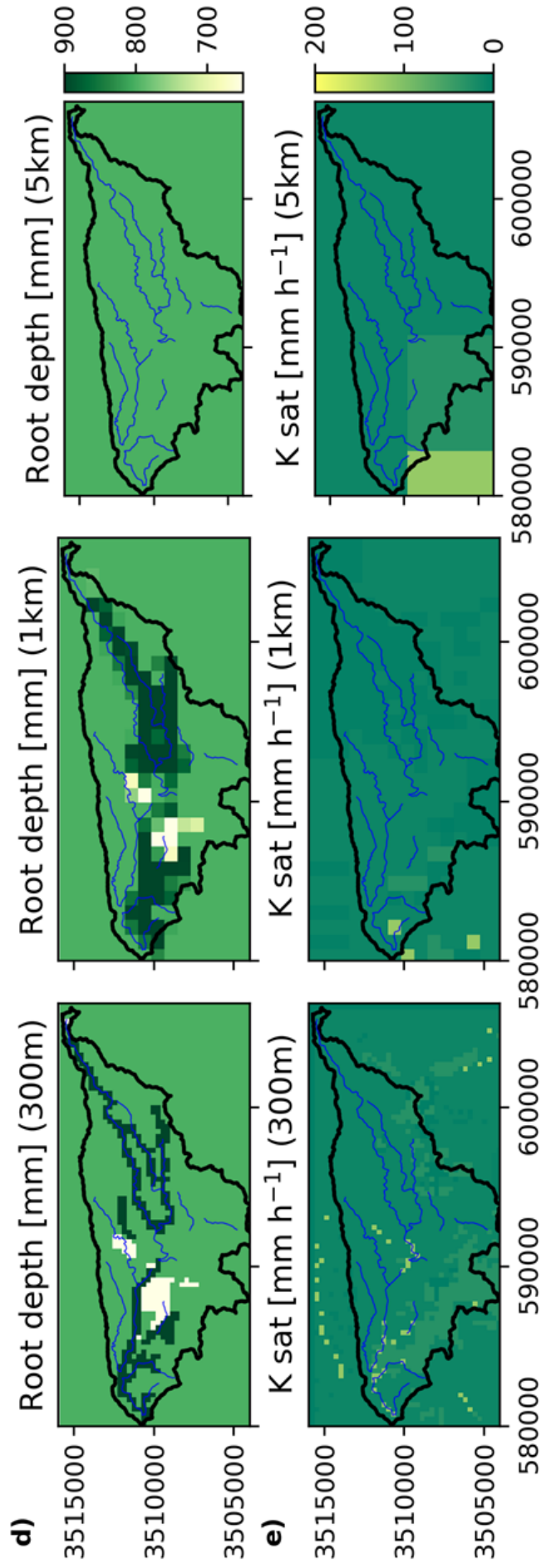


Figure 7.1: Topography and soil hydraulic characteristics for the three different grid scales (300m, 1km, 5km). AWC = available water content. Values in parenthesis represent the grid size, solid black line represent the WGEW, and solid blue lines represent streams.

for the analysis (see Fig. 6.1). For the three flumes considered in the analysis, the following variations were estimated: at the catchment outlet, flume F01, the contributing area for the three model grid sizes (300 m, 1 km, and 5 km), varied from the baseline by 2, 8.5 and -2 %, respectively. At flume F02, contributing area varied by 3, 13, and -2 % for the 300 m, 1 km, and 5 km model grid sizes, respectively. At flume F06, it varied by 4, -5, and -42 %. A more detailed description of the streamflow data is presented in section 6.2.3.

7.2.5 Model Calibration, sensitivity and uncertainty analysis

The calibration was performed following a similar approach considered in the section 6.2.4 of chapter 6 where multiplicative factors kK_{sat} and $kAWC$ were applied to K_{sat} (hydraulic conductivity) and L_{TAW} (available water content), respectively. Parameters K_{ch} (channel hydraulic conductivity) and T (recession time of streamflow) were changed globally (see Table 5.1 and Chapter 5 for parameter descriptions).

Similar to Chapter 6, the Generalised Likelihood Uncertainty Estimation (GLUE) framework (Beven and Binley, 1992) was considered to evaluate the uncertainty of the model due to parameter sets. However, in addition to the Nash–Sutcliffe Efficiency (NSE) (Nash and Sutcliffe, 1970) (Eq. 6.2) and the per cent bias (PBIAS) (Eq. 6.3), the coefficient of determination (R^2) was also used for selecting behavioural models:

$$R^2 = \frac{(n \cdot \sum_{i=1}^n O_i \cdot S_i - \sum_{i=1}^n O_i \cdot \sum_{i=1}^n S_i)^2}{\left[n \cdot \sum_{i=1}^n O_i^2 - (\sum_{i=1}^n O_i)^2 \right] \left[n \cdot \sum_{i=1}^n S_i^2 - (\sum_{i=1}^n S_i)^2 \right]} \quad (7.1)$$

where: O represents the observation, \hat{O} the arithmetic mean of observations, S the model simulations, and n the number of observation available.

Similarly to section 6.2.4, values of NSE greater or equal to 0.50 and PBIAS less or equal to 20 % were used to select acceptable simulations when streamflow was evaluated. However, for the number of events, values of R^2 greater than 0.5 were considered to be good behavioural models. For soil moisture and actual evapotranspiration, values of NSE greater than 0.5 were included. Soil moisture values were scaled by using the equations 6.5 and 6.6 before the comparison.

All these parameters were again combined into a single performance metric after scaling all values between 0 and 1 as follows (see Section 6.2.4 for more details):

$$p_i = \prod_{k=1,2,6} NS_k^* \cdot PBIAS_k^* \cdot R^2 \quad (7.2)$$

where p_i is the combined performance measure for the i -th parameter set, the * means scaled values, and k represents the variable considered in the analysis.

The period between 01/01/2006 and 01/01/2018 was used for model simulations, with a warming-up period of one year. This period matches the period of eddy flux tower observations. Soil moisture was only evaluated for the period of available data.

A total of 36000 simulations were performed in the uncertainty analysis. This total number is comprised of: 1000 simulations based on random combinations of parameters from a uniform distribution for each Monte Carlo realisation of each of the four infiltration approaches (Philip's, Schaake, upscaled GA, and modified GA), three time resolutions (15min, 60min, and 24h), and three grid resolutions (300m, 1km and 5km).

Parameters and their ranges of variation for each model structure, grid size and temporal scale are shown in Table 7.1. Selected parameters and their corresponded ranges were chosen based on their sensitivity, which was evaluated in a preliminary analysis. The production of runoff was the main focus of this preliminary analysis. Thus, by trial and error, the parameters that control infiltration (e.g. K_{sat}) and channel transmission losses (e.g. K_{ch} and T) were varied until runoff and streamflow reached values 20% and 5% of the total precipitation. This percentages were assumed reasonable considering that previous studies reported values of 8% and <1% for runoff and streamflow, respectively (Renard, 1970; Renard et al., 2008).

7.2.6 Uncertainty due to temporal resolution of rainfall

In drylands, rainfall is typically short-lived but delivered in intense bursts, where storms often last less than an hour. This high intensity, short duration rainfall is an important control on the water balance in drylands. Therefore, the representation of the temporal resolution of rainfall is a key component of DRYP. In order to understand how rainfall resolution affects hydrological partitioning in the model, a set of numerical simulations was performed which systematically varied the temporal resolution of rainfall (from 3 h to 24 h to 7 days). These simulations were used to test the sensitivity of streamflow, actual evapotranspiration and soil water content to input rainfall resolution.

Table 7.1: Prior parameter range for each component and infiltration approach considered in the Monte Carlo analysis; parameters starting with 'k' mean that it is a factor of the model parameter. Infiltration approaches are specified as P for Philip's model, G for Upscaled Green and Ampt, S for Schaake model, and M for Modified Green and Ampt.

Component		Parameter					
		Infiltration				Transmission losses	
Model		kKsat [-]			kdt [-]	Kch [m/d]	T [h]
Grid	Time	P	G	M ^a	S ^b	All ^c	
300m	15min	0.05-0.20	0.20-0.40	0.30-0.50	4.9-4.5	0.30-0.60	0.1-0.3
	60min	0.015-0.20	0.05-0.20	0.10-0.30	2.2-2.8	0.20-0.50	0.1-0.3
	24h	0.005-0.025	0.015-0.045	0.005-0.025	10.0-15.0	0.005-0.0245	0.1-0.3
1km	15min	0.05-0.20	0.75-0.25	0.55-0.75	5.5-6.5	0.02-0.060	0.1-0.3
	60min	0.01-0.10	0.05-0.35	0.15-0.30	5.5-6.5	0.50-0.90	0.1-0.3
	24h	0.005-0.025	0.02-0.06	0.04-0.06	10.0-16.0	0.02-0.060	0.1-0.3
5km	15min	0.07-0.27	0.23-0.43	0.003-0.023	14-18	7.0-8.0	0.1-0.4
	60min	0.055-0.075	0.1-0.3	0.03-0.23	3.0-5.0	2.0-5.0	0.1-0.5
	24h	0.003-0.023	0.027-0.047	0.013-0.036	0.35-0.65	0.07-0.28	0.1-0.6

^a σK_{sat} for the upscaled GA was assumed to vary uniformly between [0.1-1.5] (see eq: 5.5)

^b kK_{sat} for the Shaake model was assumed 1

^c kAWC was assumed to vary uniformly between [0.9-1.1]

7.3 Results and Discussion

7.3.1 Sensitivity and uncertainty analysis

Three flume evaluation criterion

Figure 7.2a shows the overall performance (p -value) against the number of valid models. Only the best model for each structure, grid and time step are plotted. Model characteristics are labelled according to the following nomenclature: infiltration model-grid-time step. Models at the 5-km resolution are not included in the plots because simulated catchment areas at flumes F02 and F06 did not match the topographical areas with sufficient accuracy (see Sect. 7.2.5).

The performance of the model varies highly with space, time, and model structure. Although not shown, models were mostly rejected due to higher values of streamflow PBIAS and low correlation on the number of events. More behavioural models are represented by the modified GA approach, but no behavioural models resulted from the Schaake approach. The best model uses the modified GA at the spatial and spatial resolution of 300 m and 60 min, respectively (M/300m/60min) followed by the Philip's model at the spatial and temporal resolution of 300 m and 15 min, respectively (P/300m/15min).

Valid models show good skill at representing both the soil moisture and AET with NSE values > 0.65 (Fig. 7.2b). The model, M/300m/60min, best represented the dynamic of soil moisture, whereas the M/1km/15min is the best for representing actual evapotranspiration. At a temporal resolution of 15 min, the modified GA model shows a slight reduction in the performance for both AET and soil moisture outputs when the spatial resolution is increased from 1 km to 300 m. When the temporal resolution is decreased from 15 min to 60 mins, the representation of the soil moisture improves, but the AET performance declines from NSE values above 0.70 to a value around 0.63. The results show that the temporal scale of the model substantially affects the performance of the model to represent evapotranspiration more than soil moisture. The latter result can be attributed to the better representation of the temporal variability of rainfall and its influence on water availability for evapotranspiration at small time steps in the model. The temporal aggregation also affects those processes that have a high frequency, such as channel routing as described below.

Figure 7.2c shows model performance in relation to the number of streamflow events for flume F01 against flume F06. Models at spatial resolution of 5 km have also been added to the figure in order to evaluate temporal variability of the model at coarser scales (even though they were rejected based on mismatching contributing areas-see above). Again, both model scale and model structure greatly influence DRYP's performance. In general, the analysis shows a high R^2 index (>0.6) for all models, and the P/300m/15min demonstrates the best performance at both flumes. For the 5-km grid size, the best models are the ones that use the Philips approach at both 15 min and 60 min time steps. Models with a time step of 24 h also appear to have good performance, despite the coarser temporal and spatial scale. This is attributed to less restrictions applied at 24 models, since they are only evaluated at flume F01. However, high values of R^2 are attributed to the high correlation between precipitation and streamflow event combined with the ability of the model to capture the development of ephemeral streams.

The bottom panels of figure 7.2 show the estimated NSE against the PBIAS for streamflow at the three flumes considered in the analysis. Results for models at 5-km grid size were only evaluated at flume F01 because at upstream flumes the simulated catchment areas differed substantially from measured contributing drainage areas, as stated in section 7.2.5. In general, accepted models capture the dynamics of streamflow events, represented by high values of NSE (>0.5), but they have less skill at capturing the overall mass fluxes at flume F01, indicated by high values of

PBIAS. The best model in this case is also the M/300m/60min, which has the lowest PBIAS and a very high NSE value, similar to the P/300m/15min and M/300m/15min models. The skill of DRYP to capture streamflow dynamics at the upstream flumes decreases with distance to the catchment outlet, as can be seen in figures 7.2e and 7.2f. At flume F02, the best model is P/300m/15min (fig. 7.2e), whereas at flume F06, the best model is M/300m/60min (fig. 7.2e). Only one model was found to be valid at the 1-km grid size, which is likely attributed to great variation in the contributing areas at flume F02 for this coarser spatial resolution.

Figures 7.2d, e and f show that the flow routing approach plays an important role in the model performance for both runoff and transmission losses. Therefore, streamflow is the main factor that controls the selection of valid DRYP models. However, for the WGEW basin it is also important to consider that the proportion of streamflow in relation to other components of water balance is small, with values $<1\%$ at the catchment outlet. Therefore, a PBIAS threshold of 20% can yield accurate results for the study area, as it will only represent $\approx 0.2\%$ of the amount of precipitation. The results of this multi-scale also illustrate the importance of rainfall partitioning between runoff and infiltration which, in addition to the flow routing approach, can lead to great uncertainty in model estimations. Results show that the highly dynamic temporal variation of streamflow flow events is influenced by the temporal scale of the model, which in turn impacts the timing and consequently spatial variation of streamflow events. Finally, these results show the challenges for a simple model in capturing the strong spatial and temporal variations of streamflow present in drylands.

For behavioural models with $p > 0$, the distribution of parameters which greatly impact the model performance are shown in figure 7.3. Results show a narrow distribution for parameters that control the production of runoff (Fig. 7.3a) and the corresponding transmission losses (Fig. 7.3b), whereas parameters that control the flow routing show a broader distribution (Fig. 7.3c). A narrow distribution of a fitted parameter from the Monte Carlo analysis means that model results are quite sensitive to such model parameters.

Figure 7.3a shows that values of kK_{sat} depend on the model structure and the spatial and temporal scales. Values of kK_{sat} for the modified GA model are greater than those of the Philips model. This variation indicates that the model structure greatly impacts the production of runoff. Models with the modified GA produce high volumes of infiltration at the onset of a rainfall event, which in turn influences the production of runoff and consequently transmission losses. It can also be seen on

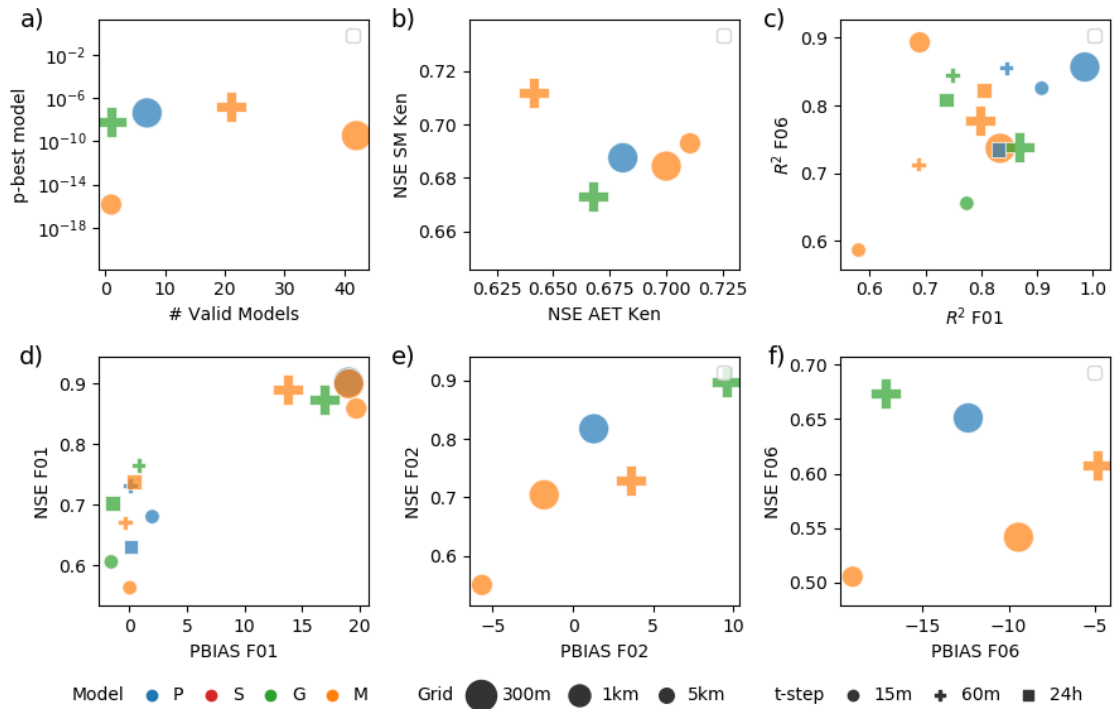


Figure 7.2: Indexes estimated for the best models selected according to the combined performance metric 'p' based on the evaluation of flumes F01, F02 and F05, and soil moisture and AET at Kendall. a) Estimated 'p' against the number of valid models resulted from the Monte Carlo analysis for different grid size, time-step, and infiltration approach. b) NSE for the soil moisture (SM) estimated at the Kendall location against NSE of the evapotranspiration at Kendall location. c) R^2 of flumes F06 against F01. Part d, e and f) represent the NSE against the PBIAS for the three flumes located along the main channel, flume F01, F02 and F06. Results at 5km grid size were evaluated only at flume F01. Models are represented as P = Philip's, S = Schaake, G = upscaled Green and Ampt, and M = modified Green and Ampt. Models at 5-km grid size were not used to evaluate evapotranspiration

figure 7.3a, that as the spatial or temporal scale of the model increases, the magnitude of the K_{sat} has to be reduced in order to capture the production of runoff. This is understandable, since the peaks of rainfall events are flatter as the spatial and temporal aggregation of the model increases (coarser and longer duration) and lower rates of infiltration are needed to produce runoff. For example, for the modified GA, the multiplicative factor kK_{sat} for hydraulic conductivity was reduced from 0.4 for the 300m/15min models to 0.01 for the 5km/24h models. Similarly, the magnitude of the parameter that controls the transmission losses was reduced in order to capture the influence of the temporal scale of the model (Fig. 7.3b). However, less variation between model structures was observed in comparison to model the spatial and temporal resolution.

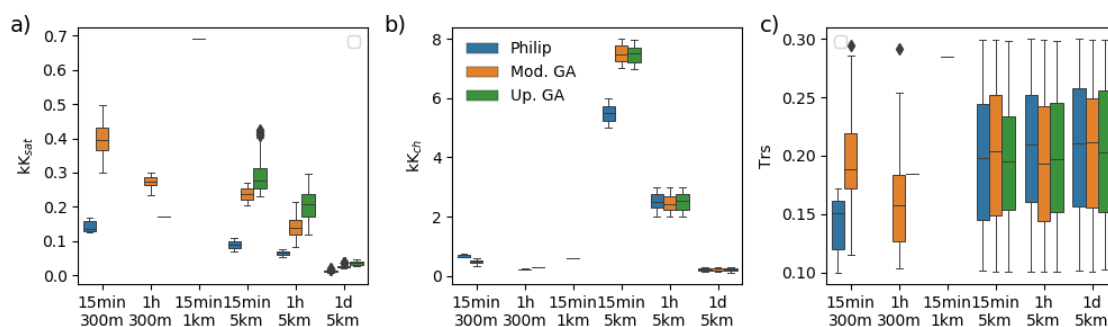


Figure 7.3: Parameter distributions for acceptable model simulations based on the evaluation at flumes F01, F02 and F06, and soil moisture and AET at Kendall. Results at the 5-km grid size were evaluated only at flume F01

Single flume evaluation criterion

Figure 7.4 shows the results of the model evaluation using the combined performance metric (p) (Eq. 7.2) using only one flume (F01 – at the catchment outlet). Figure 7.4a shows the overall model performance against the number of valid models. Models with a grid size of 5 km have been excluded here because it was not possible to evaluate their performance for soil moisture and evapotranspiration outputs.

Using only one flume in evaluation, results in valid models with very similar performance and only slight variations between them. Due to this less restrictive evaluation criterion, more models are considered behavioural. However, for this scenario all models at the 24-h time step and those using the Schaake infiltration structure failed to meet the behavioural criteria. For this single flume scenario, behavioural models generally show variations in performance depending on their structure, grid size and time step, with the best model being the P/300m/15min, a result that contrasts with the 3-flume evaluation criteria, where M/300m/60min was the best model.

The performance of DRYP for the 1-flume evaluation criterion with respect to soil moisture and evapotranspiration show slightly higher values in relation to the 3-flume evaluation criteria with values of NSE for evapotranspiration above 0.65 (fig. 7.4b). Models at the 1-km spatial resolution and 60-min time step perform better in terms of representing evapotranspiration, a result that agrees with the 3-flume scenario. These results show that the model is robust in representing the evapotranspiration.

Behavioural models also perform well in terms of representing the number of streamflow events with values of R^2 above 0.6 (fig. 7.4c). The Philips and upscaled GA models show the best performance in this regard, with both showing similar values of R^2 . Almost all 5-km grid size models appear to perform well for representing the number of streamflow events (fig. 7.4c).

In terms of representing streamflow, models show good performance at flume F01 with values of NSE >0.85 and PBIAS $<3\%$ (fig. 7.4d). The best model is the Philips at 300-m grid size and 15-min time step, which has the highest NSE (>0.9) and PBIAS close to zero. Models at 5-km grid size resolution also performed well evidenced by high values of NSE and low PBIAS. However, at flumes F02 and F06 (see Fig. 7.4e and f, respectively), these models perform poorly with values of PBIAS above 20 % for flume F02 and $>30\%$ for flume F06.

The distributions of parameter sets for behavioural models are presented in figure 7.5. In general, a similar behaviour with relation to the 3-flume evaluation scenario can be observed. Model parameters related to infiltration on hillslopes needed to be reduced as the temporal scale increases in order to capture the production of runoff. However, these parameter reductions do not depend on the spatial scale but only on the temporal scale. The distribution of parameters is wider as more models are valid due to the less restrictive validation criteria imposed. Figures 7.5a and b show that the distribution of hydraulic conductivity below channels and hillslopes increases as the grid size increases from 300 m to 1 km for models with the same time step. Additionally, values of kK_{sat} are slightly higher than those of the 3-flume criteria. These results illustrate the important impact that spatial resolution of streamflow observations have on the model evaluation. As fewer restrictions are set, only runoff events that satisfy the performance criteria are required.

7.3.2 Impact of spatial and temporal scales on water partitioning

Results of the water partitioning obtained from the behavioural models for the two-flume-based evaluation scenarios are shown in figures 7.6 and 7.7. These figures

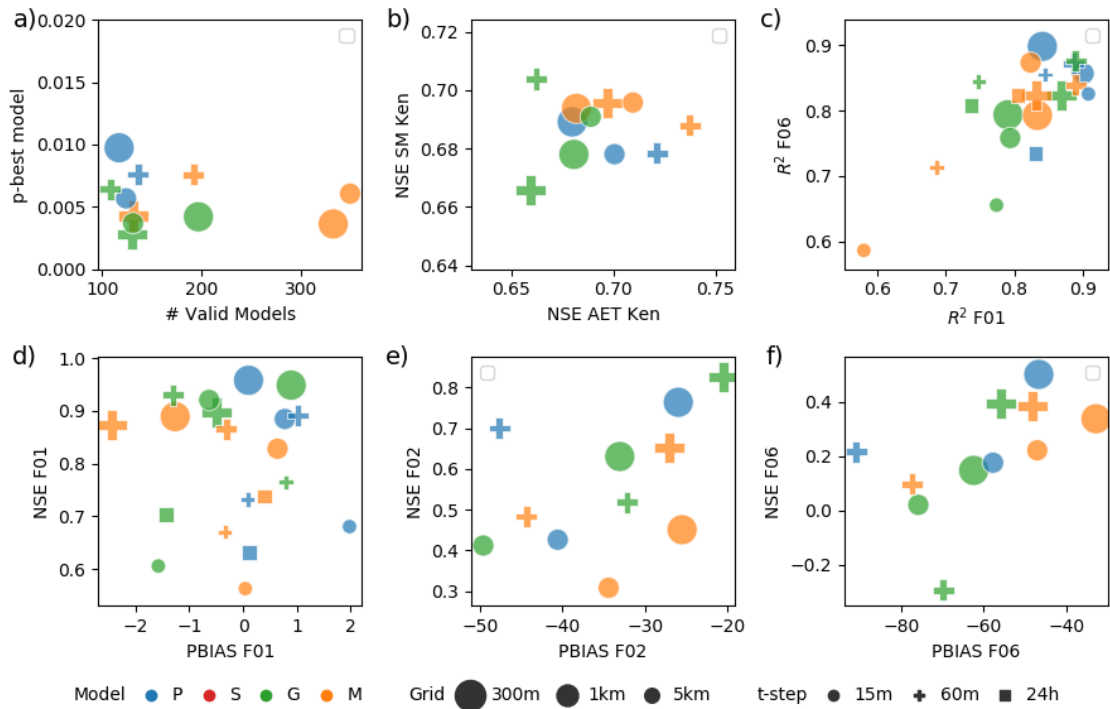


Figure 7.4: Indices estimated for the best models selected according to the likelihood measure 'p' based on the evaluation of flume F01, and soil moisture and AET at Kendall. a) Estimated 'p' against the number of valid models resulting from the Monte Carlo analysis for different grid sizes, time steps, and infiltration approaches. b) NSE for soil moisture estimated against NSE of the evapotranspiration at Kendall. c) R2 of flumes F06 against F01. Part d, e and f) represent the NSE against the PBIAS for the three flumes located along the main channel, flume F01, F02 and F06. Results at the 5-km grid size were evaluated only at flume F01. Models are represented as P = Philips, S = Schaake, G = upscaled Green and Ampt, and M = modified Green and Ampt. Models at the 5-km grid size do not consider evapotranspiration in the evaluation

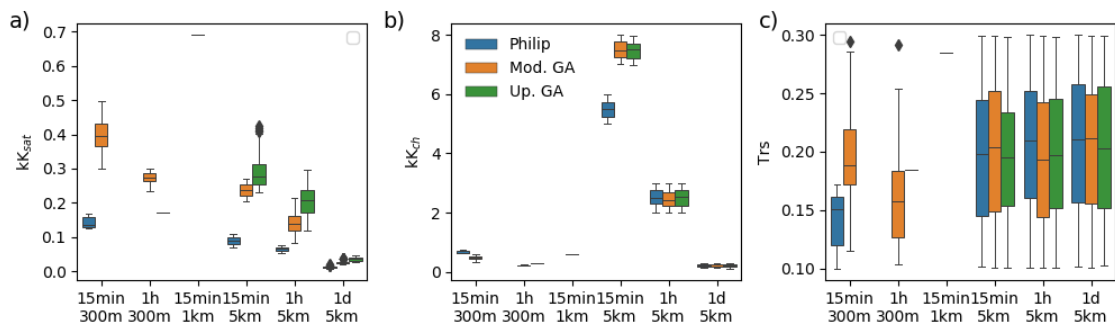


Figure 7.5: Parameter distributions for acceptable model simulations based on evaluation at flume F01 and soil moisture and AET at Kendall. Results for the 5-km grid size were evaluated only at flume F01.

show the distribution of each component of the water balance in relation to the precipitation.

Using the three main flumes along the main channel considerably influences model selection and reduction of the uncertainty in the model results, as indicated by narrow distributions of fluxes in figure 7.6. The model structure mainly influences the production of runoff via the K_{sat} parameter, and good simulations of discharge at the catchment outlet are sensitive to the channel infiltration parameter (K_{ch}). Therefore, the two infiltration parameters (on hillslopes and in the channel) play an important role in the performance of the model. In general, the production of overland flow for all models varies from 4-14 %, with most model structures showing a mean value of runoff of \approx 8-11 % (fig. 7.6f). Transmission losses vary between 3-13 % with most models producing mean values around 9 % (fig. 7.6b).

Evaporation consumes almost all infiltrated water with varying from 85-94 %. Evapotranspiration is low for models at spatial resolutions of 5 km compared to models at 300 m and 1 km (fig. 7.6e). This is attributed to low infiltration rates as a result of the spatial aggregation of rainfall. Low infiltration rates result in low values of soil water content which put vegetation under stressed conditions and consequently reduce rates of evapotranspiration. Also, models at the 5-km grid size and 24-h time step show an increase in diffuse recharge (fig. 7.6d), which is attributed fewer intense rainfall events along with high initial infiltration rates, which combined support percolation of soil water.

The simulated transmission losses for the best model structure (M/300m/60min) are \approx 5 % of the rainfall, and are low compared to other models (mean values \approx 8-10 % of rainfall). The low percentage of transmission losses in the modified GA arise from high volumes of infiltration (see fig. 7.4c), due to the high K_{sat} values which consequently results in low runoff production (Fig. 7.4f). To compensate for the low production of runoff and to get a better estimate of discharge at the outlet, the parameter K_{ch} also had to be reduced (Fig. 7.4b).

For the single flume evaluation scenario (figure 7.7), the uncertainty in water partitioning increases due to the increase in the number of valid models as restrictions on flumes F02 and F06 are lifted. Both the flow routing and the transmission losses approach play an important role in the modelled infiltration, which ultimately results in increased uncertainty, particularly for the Philip's models. Philip's models at the 300-m grid size and 15-min time step exhibit variations in the modelled infiltration component between 75-92 % with a mean \approx 87 % (Fig. 7.7c). These variations have knock-on consequences for uncertainty in the modelled runoff and transmission losses

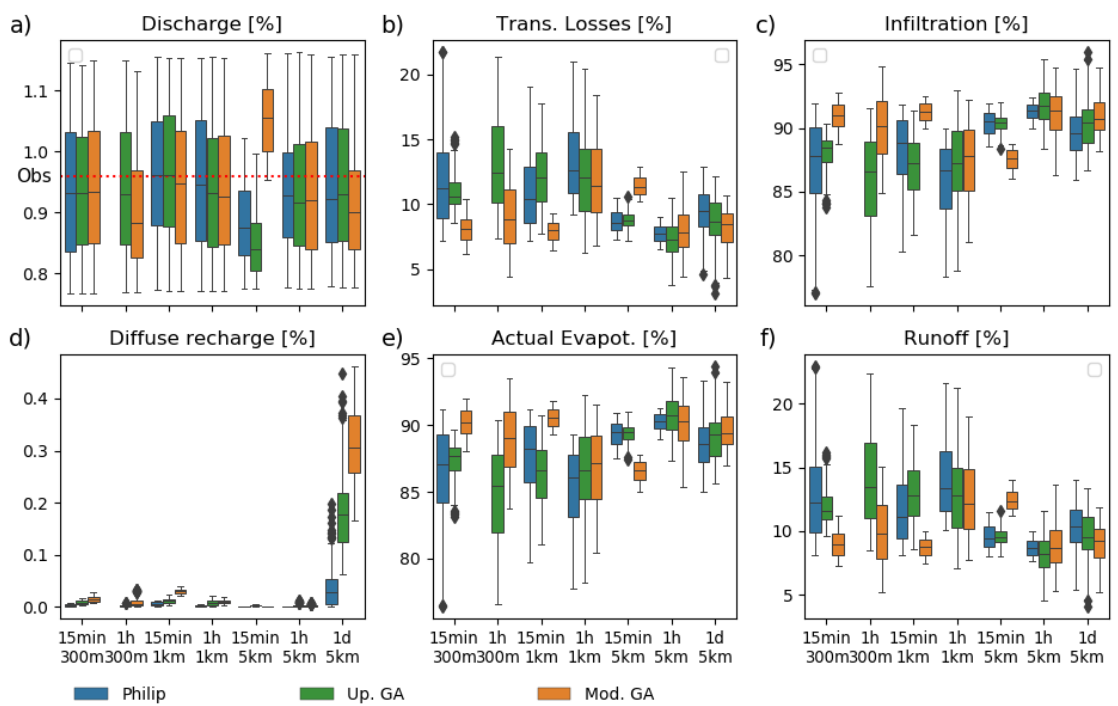


Figure 7.6: Flux distribution as a percentage of precipitation for behavioural models based on the evaluation of flumes F01, F02 and F06, and soil moisture and AET at Kendall. Results at the 5-km grid size were evaluated only at flume F01

(varying from 5-22 %). In general, all models show an increase in the transmission losses due to high infiltration rates, despite having a narrow range of variation in water leaving the catchment with values ranging from 0.75-1.15 %. All models produce average values of evapotranspiration >80 %, suggesting that they are robust for representing these losses to the atmosphere. Finally, the best models (the modified GA) produce a better representation of water partitioning as less uncertainty in fluxes is observed in all modelled water cycle components.

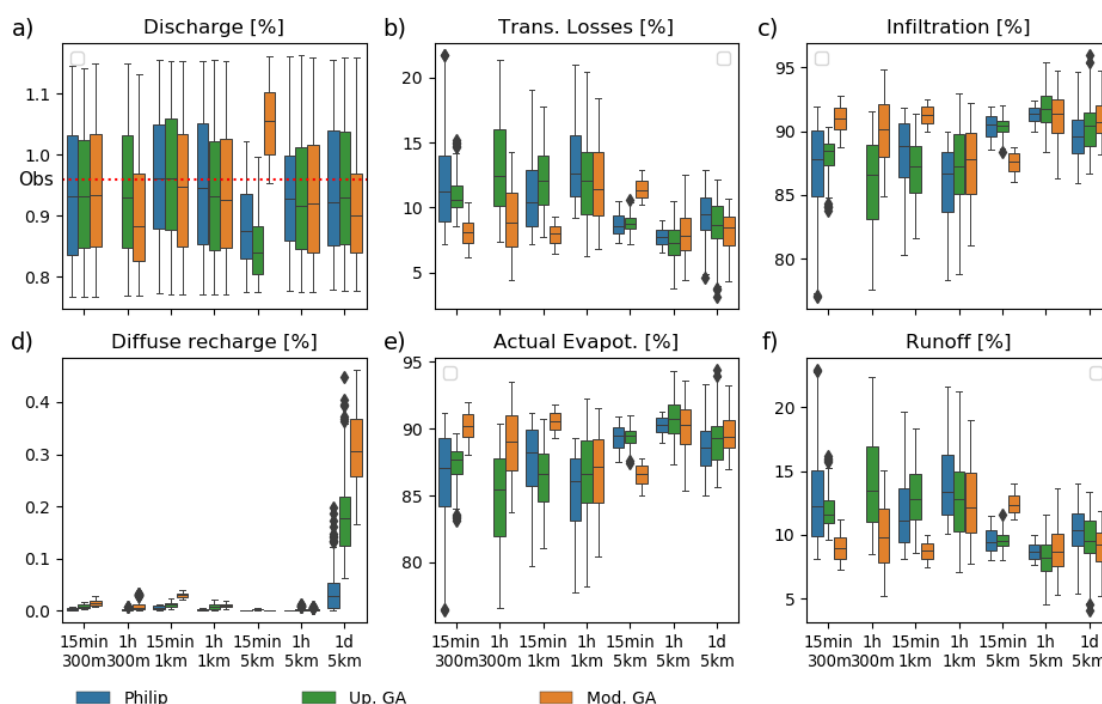


Figure 7.7: Flux distribution as a percentage of rainfall for behavioural model simulations based on the evaluation at flume F01, and soil moisture and AET at Kendall. Results at the 5-km grid size were evaluated only at flume F01

7.3.3 Water balance

A summary of the main components of the water balance for the best model structure (M/300m/60min) for WGEW is presented in figure 7.8. Model fluxes are represented as a percentage of the input precipitation. Figure 7.8 also shows the distribution of behavioural models depending on the performance criteria: default parameters, three-flumes and one flume criteria. It can be seen that these results clearly show how the impact of the information available for evaluation constrains the modelled water budget for WGEW. In particular, streamflow data at one or several locations along

the stream has a great impact on the model evaluation. The figure also highlights the impact of transmission losses on streamflow and on recharge of the aquifer. The main contributor to total groundwater recharge is focused recharge ($\approx 2.2\%$), which represents between 40-50% the total transmission losses.

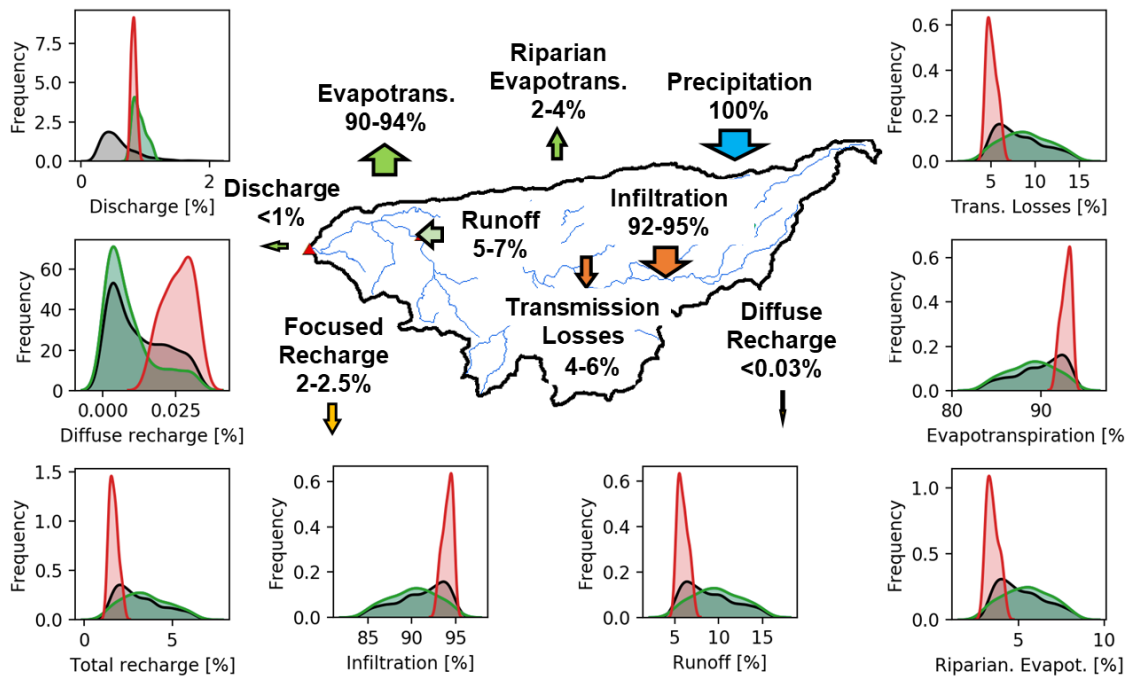


Figure 7.8: Percentage of rainfall contributing to the modelled components of the water budget at WGEW (see Fig. 5.1 for model components). Results correspond to the best model structure, the modified Green and Ampt at 300m grid size and 60min time steps. Solid red lines represent the behavioural models for the 3-flume based criteria, green lines represent models for 1-flume criteria, and black solid lines represent all simulations. Arrows outside the catchment represent fluxes entering and leaving the model domain.

7.3.4 Impact of temporal resolution of rainfall

The model was tested for different temporal resolutions of rainfall forcing and the results are shown in figure 7.9. For this analysis, parameters of the modified Green and Ampt model at the 300-m grid size and 60-min time step from the 3-flume evaluation criteria were selected.

Temporal resolution of rainfall does not have a large impact on mean values of modelled evapotranspiration (fig. 7.9a). However, models do show small variations as the temporal aggregation of rainfall increases, particularly on the AET for wet

months (fig. 7.9a right panel). For the weekly rainfall resolution, evapotranspiration model output from DRYP has a narrow distribution when the wet season starts, and a wider distribution for dry months. This can be attributed to low values of antecedent soil water content at the beginning of the season.

The temporal resolution of rainfall significantly impacts modelled soil moisture. Mean values of soil moisture output from DRYP decrease and the distributions narrow as the temporal resolution of rainfall increases. The variation of the soil moisture for different models over the whole period is also consistent on a monthly basis (figure 7.9b, right panel), but for all months soil moisture systematically declines as the temporal resolution in rainfall increases. The reduction in soil moisture results from the continuous depletion of water by evapotranspiration.

However, the most impacted component of the water balance from DRYP simulations is runoff production (figure 7.9c). Streamflow at the catchment outlet decreases as the temporal resolution in rainfall increases, becoming zero at the lowest resolution (1 week). This was expected since the lower temporal resolution in rainfall reduces the number of peak streamflow events in channels due to a reduction in runoff generation from hillslopes.

7.4 Summary and Conclusions

The ability of DRYP to produce behavioural simulations at WGEW based on multi-parameter Monte-Carlo experiments was tested. The model was evaluated against a range of objective performance metrics.

Using this approach, combinations of spatial grid discretisations (300 m to 5 km), time steps (15 min to 1 day), and runoff-infiltration model structures (the dominant process control on the overall water balance) was evaluated in order to investigate which combinations give robust results on the partitioning of the observed range of hydrological fluxes. For the best performing models, model sensitivity to different timescales (1 h to 1 week) of aggregated rainfall time series forcing is also assessed. A number of general conclusions can be made about DRYP:

- good prediction of the number of flow events is easier to achieve under a much wider range of model structures and grid and time resolutions than accurate volumetric discharge estimates. While this indicator may not be a good metric for the overall water balance, it may be very useful to capture basin dynamics and responses and for predicting the probability of wetting events that may have local significance for dryland water uses. For example, the filling of sand

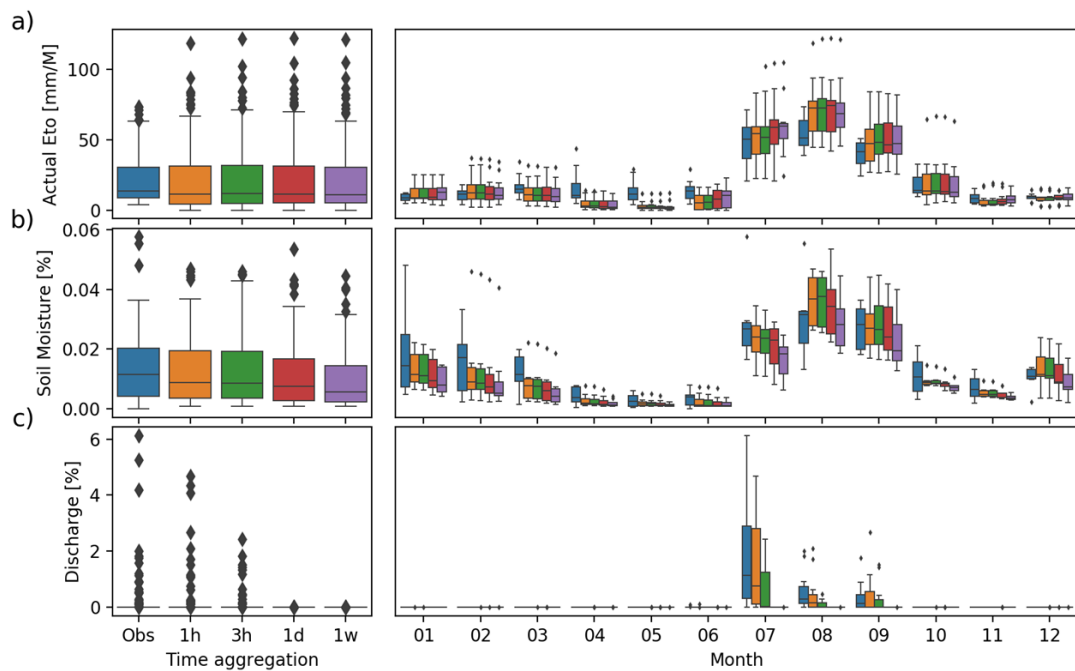


Figure 7.9: Influence of the temporal aggregation of rainfall on water partitioning for the best model: modified Green and Ampt. Left panels show the distribution for the whole simulated period and right panels show the distribution for monthly values for the simulated period. a) represents the actual evapotranspiration at Kendall (see fig. 6.1), b) represents the soil moisture at Kendall (see fig. 6.1), and c) represents the runoff at flume F01 near the catchment outlet (see fig. 6.1)

dams or small earth dams in developing countries is a critical issue for rural dry season water supply for households, livestock, fodder production and small scale irrigation.

- estimates of actual evapotranspiration and soil moisture are better simulated by a larger range of models than streamflow discharge.
- owing to the trade-offs between runoff generation and transmission losses leading to equifinality in simulating flow at a particular flow gauge, estimates of transmission losses are highly uncertain without additional observational constraints from multiple flow gauges. This indicates the importance of DRYP for application to other dryland regions of the world which are typically data sparse, since its simplicity and efficiency enables the range of uncertainty to be fully explored, something that would not be possible with a more complex, and highly parameterised model.
- considering observations of soil moisture and evapotranspiration in the selection of behavioural models reduces the uncertainty of the estimation of most of the water balance components. However, the uncertainty in measured soil moisture and estimated AET may be larger than for streamflow discharge in absolute terms in dryland settings. Hence, the relative accuracy of the streamflow estimation may still be very uncertain, for example as measured as PBIAS.
- of the infiltration approaches implemented, it was found that high infiltration rates at the onset of the rainfall event play an important role in the development and distribution of runoff events which ultimately affect the water balance of the model,
- the water partitioning is highly sensitive to the spatial and temporal scales considered in the model domain. In general, behavioural models required smaller values of saturated hydraulic conductivity for longer time steps or larger grid sizes when using a multi-flume evaluation. When only a single flume was used, this relationship held for different time steps, but was more complex for varying grid size due to the lesser influence of the spatial distribution of rainfall in the production of runoff at the catchment outlet. However, model results also suggest that in order to reduce the computational demand, good predictions can still be achieved at grid sizes of 1 km.

- in order to capture the main characteristics of the streamflow and focused recharge components of the water balance, a high temporal resolution (<1 day) of rainfall forcing is required for model simulations. In contrast, soil moisture and AET are much less sensitive to larger aggregations of rainfall forcing above 1 day.

Finally, understanding how water partitioning is controlled in dryland regions is of key importance to understand the future impacts of climate change and anthropogenic activities. In this context, the quantification of water fluxes and their interaction with different components, especially groundwater - surface water interactions, will help to reduce the uncertainty and will contribute to understanding of the impact of groundwater depletion on surface water availability (Bredehoeft, 1997, 2002), which has been misrepresented or neglected in current hydrological models. This study paves the way for consideration of how larger-scale hydrological models can improve their process representation in drylands.

Chapter 8

Characterising water partitioning at regional scale: Upper Ewaso Ng'iro basin, Kenya

8.1 Introduction

In recent years, the Upper Ewaso Ng'iro basin, Kenya, has experienced a dramatic increase in water resource demands due to population growth and the increase of unregulated agricultural and pastoral activities (Aeschbacher et al., 2005; Koech et al., 2020; Mati et al., 2006; Muriithi, 2016). This has put more pressure on the already limited availability of water resources and has also increased water related conflicts in the area (Kiteme and Gikonyo, 2002; Mutiga et al., 2010a; Wiesmann et al., 2000). The problem has been intensified by climate change, which has resulted in long and severe drought events (Muriithi, 2016; Ojwang', 2010). Therefore, understanding and quantifying the main mechanisms that control the water partitioning and flow pathways in the Upper Ewaso Ng'iro basin is of key importance not only to improve the management of limited water resources, but also to understand the future impacts of climate change on the spatial and temporal variability of water resources in the basin.

In this context, the hydrological model, DRYP, is used in the present chapter to characterise the water partitioning of the Upper Ewaso Ng'iro basin. The area poses a variety of challenges in terms of highly spatial variability in groundwater - surface water interactions and limited data availability, both of which restrict the straightforward characterisation of the basin water balance. Modelling the Upper Ewaso basin therefore has the potential to enhance the understanding of water partitioning mechanisms and their influence at larger regional scales. The objectives of this chapter are

as follows: i) to test the ability of DRYP to accurately partition the water balance in a climatically, topographically and geologically diverse, data sparse environment, using only readily available regional-global datasets for parameterisation and forcing; ii) to identify the key mechanisms that control the water partitioning in the study area; and iii) to evaluate the sensitivity of water partitioning to the spatial and temporal variation of precipitation and model parameters which would support the transferability of this approach to other basins with a substantial dryland component. The following sections describe the study area and model characteristics, after which a description of data availability and model parameterisation is presented. Finally, after presenting and analysing model results, some conclusions are drawn from the analysis.

8.2 Methods

8.2.1 Study area

The upper Ewaso Ng'iro basin is located northwest of Mt. Kenya (see Fig. 8.1), a region characterised by dry-humid climatic conditions. The basin has an area of approximately 15,200 km² with elevations ranging from \approx 800 m in its lower part in the northeast (Archer's Post) to \approx 4700 m at the top of the Mt. Kenya in the south.

The area experiences different hydrological regimes depending on elevation, latitude, and the location of the Intertropical Convergence Zone over the year. Precipitation has a unimodal distribution in the western part of the basin, whereas two well defined rainy seasons characterise the climate of the Mount Kenya area and the lower parts of the basin. In the bimodal locations, a long rainy season occurs between March-May whereas the short rainy season occurs in September-December. Precipitation also varies from year to year depending on the elevation, with average annual precipitation being \approx 1700 mm at high elevations ($>$ 3300 m), \approx 800 mm at elevations between 2000 and 1700m on the Laikipia plateau, and \approx 350 mm in lower elevations around the catchment outlet (Archer's Post) (Gichuki, 2002; Liniger et al., 2005; Muriithi, 2016; Mutiga et al., 2010b; Notter et al., 2007). Rates of potential evapotranspiration also show great spatial variation with mean annual values of \approx 500 mm at high elevations to \approx 1700 at lower ones (Ngigi et al., 2007). The low annual precipitation combined with high rates of potential evapotranspiration results in high aridity at lower elevations (Gichuki, 2004; Liniger et al., 1998; Ngigi et al., 2007).

Spatially variable geological, topographical and climatic conditions enabled the development of a variety of ecological zones (Decurtins, 1992). Alpine characteristics occur at higher altitudes on Mount Kenya, with moorland and forest on its slopes

and foot zones, whereas savannahs occur in the more arid lower parts of the basin. Hence, the study catchment is mostly covered by woody vegetation, shrublands, and grasses. (Muriithi, 2016). The woody vegetation is dominated by acacia (Franz et al., 2010; Gichuki, 2004; Mati et al., 2006; Muriithi, 2016; Mutiga et al., 2010a), a species which is drought tolerant, allowing it to survive under arid conditions (Dharani, 2009; Ludwig et al., 2003).

The upper part of the basin is characterised by perennial streams, whereas the lower part is dominated by ephemeral streams (Aeschbacher et al., 2005; Mutiga et al., 2010a). Perennial streams are the result of a combination of high annual orographic precipitation and the modulation of rainfall owing to the high storage capacity of the forest, moorland, and the glacier on the top and flanks of Mount Kenya. Streams in the lower parts of the basin are fed by perennial upstream rivers. However, as they flow downstream, transmission losses substantially reduce the streamflow. Flow in lower areas of the basin is also reported to have been impacted by anthropogenic water abstractions occurring at upstream locations, which has also resulted in water conflicts in the area (Gichuki, 2004). However, no abstraction data are available to quantify this aspect of the water balance and this chapter only considers the natural flow regime of the streams.

The geology of the study site is characterised by Quaternary and Tertiary volcanic sediments overlaying the metamorphic rocks of the Basement System (Gichuki, 2004; Muriithi, 2016). Metamorphic rocks from the Basement System are mainly composed of gneiss, schists, quartzite, and marbles. Major outcrops of the Basement System inside the study basin occur in the west part of Isiolo. The Tertiary sediments (Simbara, Rumuruti, and Thomson's Falls formations) consist of tuffs, phonolites, basalts and agglomerates. Outcrops of Tertiary rocks, mainly consisting of basalts, cover a great part of the Laikipia plateau. Quaternary sediments (Mount Kenya, Aberdare Suite, Nanyuki Formation, and alluvial sediments) mainly consist of porphyritic phonolites, pyroclasts, trachytes, and basalts resulted from a sequence of eruptive events. The Nanyuki formation is reported to have a thickness of around 60-100 meters, whereas the thickness of alluvial sediments varies from 6-40 meters depending on the underlying geological formation.

Lorem ipsum dolor sit amet, consectetur adipiscing elit. Ut purus elit, vestibulum ut, placerat ac, adipiscing vitae, felis. Curabitur dictum gravida mauris. Nam arcu libero, nonummy eget, consectetur id, vulputate a, magna. Donec vehicula augue eu neque. Pellentesque habitant morbi tristique senectus et netus et malesuada fames ac turpis egestas. Mauris ut leo. Cras viverra metus rhoncus sem. Nulla et lectus

vestibulum urna fringilla ultrices. Phasellus eu tellus sit amet tortor gravida placerat. Integer sapien est, iaculis in, pretium quis, viverra ac, nunc. Praesent eget sem vel leo ultrices bibendum. Aenean faucibus. Morbi dolor nulla, malesuada eu, pulvinar at, mollis ac, nulla. Curabitur auctor semper nulla. Donec varius orci eget risus. Duis nibh mi, congue eu, accumsan eleifend, sagittis quis, diam. Duis eget orci sit amet orci dignissim rutrum.

8.2.2 Conceptual model of the Upper Ewaso Ng'iro basin

The Upper Ewaso Ng'iro basin is characterised by highly spatially variable hydrological and hydrogeological settings. The Precambrian rocks of the Basement system, which crop out mainly in the lower areas of the basin, are thought to represent a regional aquifer (Hackman, 1988). In contrast, in the upper parts of the catchment, local aquifer systems are developed in volcanic sediments of Mount Kenya and the Laikipia plateau (see Fig. 8.2) (Baker, 1967; Gregory, 1900). These volcanic sediments are characterised by medium porosity values (1 - 10%) (WRAP, 1987), which is in agreement with the range of volcanic sediments (Courtois et al., 2010; Custodio, 1989; Taylor et al., 2010). Transmissivity of the volcanic material of Laikipia plateau, estimated from four boreholes, varies between 2.6 - 30.7 m² d⁻¹ (WRAP, 1987). Transmissivity values for the basement rocks reported in the area vary from 5 - 30 m² d⁻¹ (Bianchi et al., 2020), consistent with values reported for the metamorphic rocks of other basement systems in the region (Bianchi et al., 2020; Carrier et al., 2011; Chilton and Foster, 1995; Holland, 2012; Taylor and Howard, 2000; Taylor et al., 2010), whereas effective porosity values for these metamorphic rocks have been reported to vary between 0.001 - 0.01 (Bianchi et al., 2020; Courtois et al., 2010; Maréchal, 2004).

Soil characteristics and their distribution over the study site are strongly influenced by the topographical, geological, and climate characteristics. For example, in the upper part of the basin, mountain slopes (Mount Kenya and Aberdares), soils are characterised as clay and clay-loam texture type with high moisture storage capacity, well drained, and deep to very deep soil profiles (> 800 mm) (Mainga and Mbuvi, 1994; Mbuvi and Kironchi, 1994). In foot slopes and plateau areas (Laikipia), soils have clay to sandy-clay texture characteristics, with well to moderately well drained characteristics, and deep to very deep soil profiles (Liniger et al., 1992). In contrast, soils in the lower part of the basin's basement area are poorly developed with low to

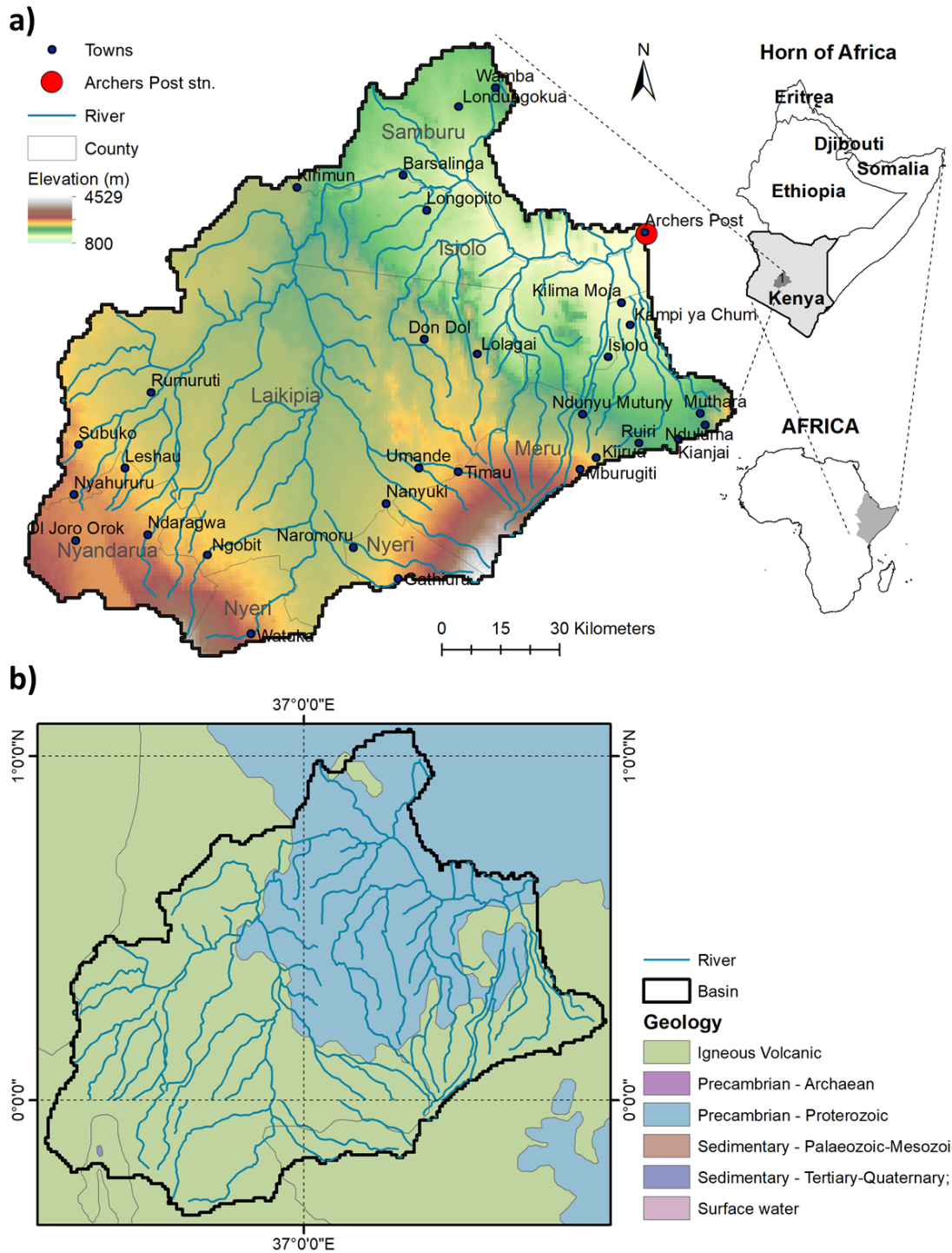


Figure 8.1: a) Geographical location of the Upper Ewaso Ng'iro basin, b) geological map, c) soil texture, and d) soil land use.

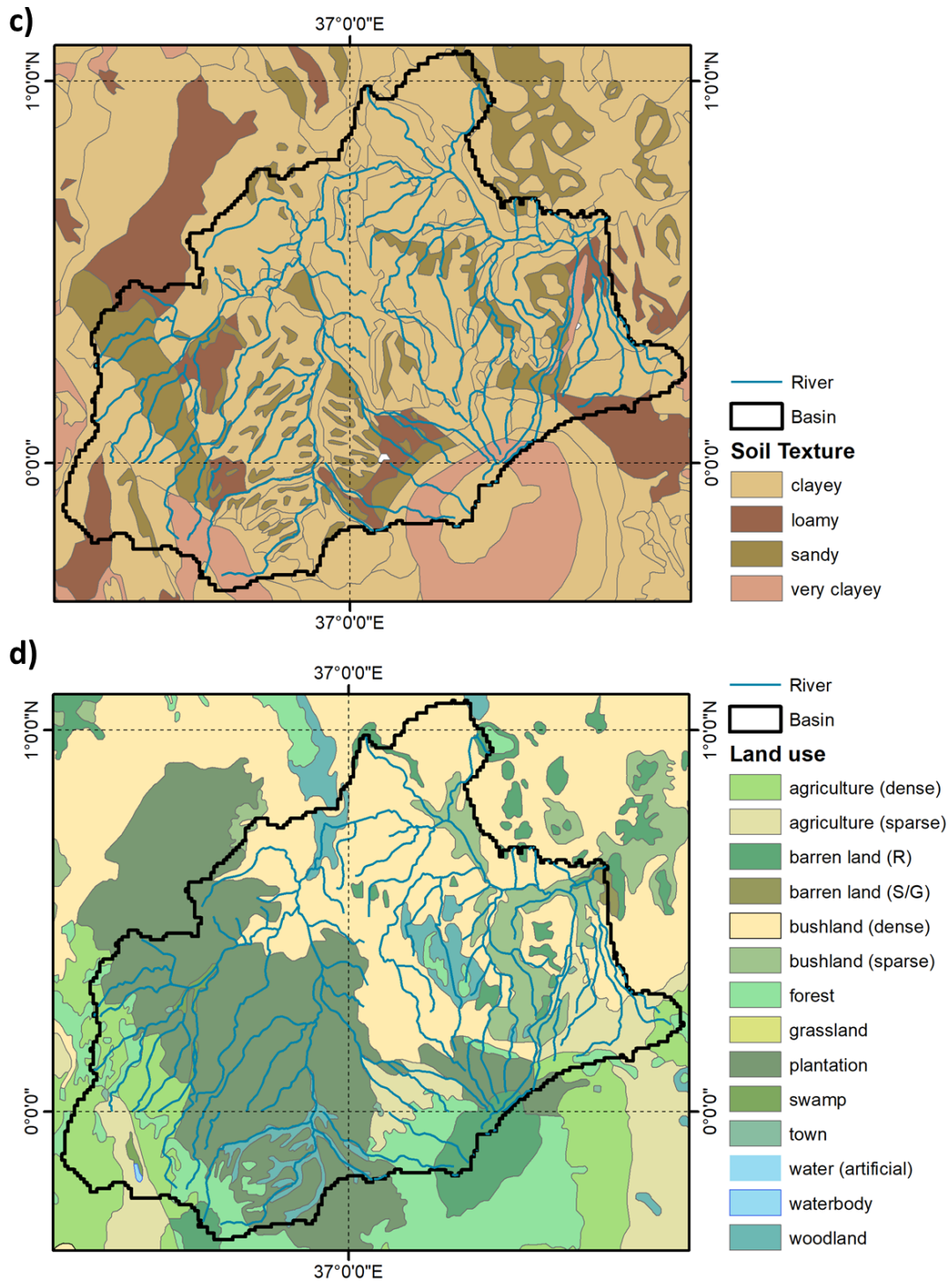


Figure 8.1: a) Geographical location of the Upper Ewaso Ng'iro basin, b) geological map, c) soil texture, and d) soil land use (cont.).

very low storage capacity and shallow profiles. Soils at lower elevations tend to develop crust sealing layers which result in high runoff production as Hortonian overland flow (Mbuvi and Kironchi, 1994).

There is a strong precipitation gradient with much higher rates of precipitation falling over the upper parts of the basin. It is anticipated that this higher precipitation at higher elevations, combined with low rates of potential evapotranspiration for the upper basin, results in water surplus and potentially high rates of water recharge into the groundwater system in this part of the catchment. Precipitation is therefore likely partitioned into infiltration and runoff by both infiltration excess or saturation excess processes and then routed downstream to lower elevations. Groundwater is discharged at springs feeding streams located on the lower flanks of Mount Kenya (see Fig. 8.2) and also in contact areas between volcanic and basement rocks on the break in slope on the margins of the Laikipia Plateau. In the lower parts of the basin, the relief is lower, but runoff is also likely to develop by short but intense precipitation events occurring on lower permeability soils via infiltration excess (Hortonian overland flow). In these lower areas, streamflow supplied with water from the upper part of the catchment loses flow due to transmission losses, and flows are often ephemeral, flowing infrequently during the year. It is anticipated that a component of water lost as leakage through the streambeds of ephemeral channels reaches the water table producing focused recharge, whereas the rest is lost as evapotranspiration from vegetative uptake occurring on riparian areas.

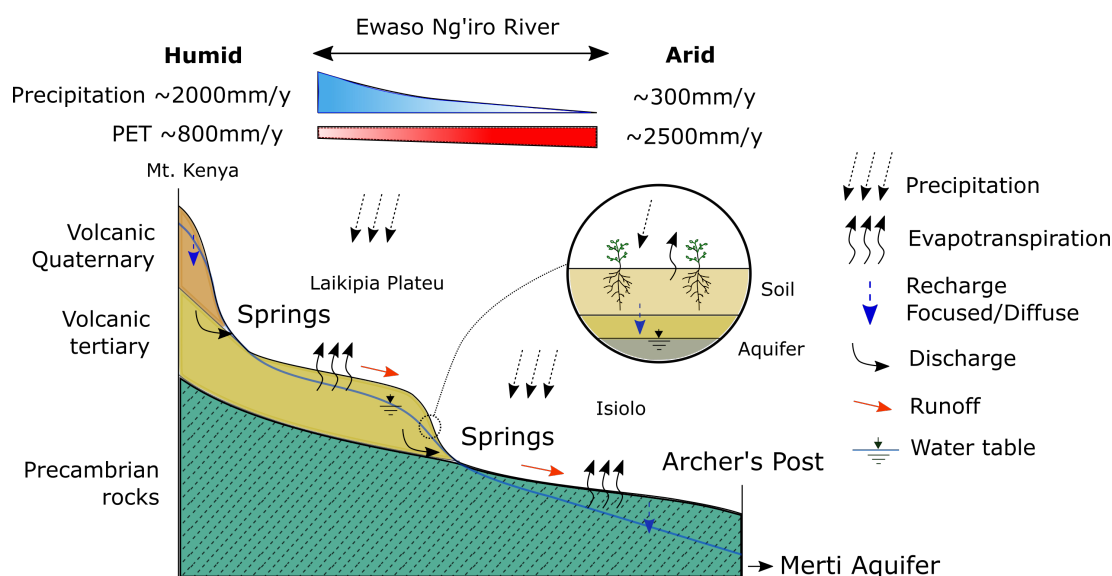


Figure 8.2: Conceptual schematic of the hydrology of the Upper Ewaso Ng'iro basin

8.2.3 Model process selection

Water partitioning was modelled using DRYP (see Chapters 5 and 6). To reduce the computational demand, a Philips infiltration approach was implemented, which uses an explicit approach, as this method has shown good performance for modelling water partitioning in the semi-arid Walnut Gulch Experimental Watershed (see Chapter 6 and 7).

For the groundwater component, given the great uncertainty in the hydrogeological characteristics of the basin, a variable hydraulic conductivity with depth approach was specified for representing flow below the surface (Bianchi et al., 2020; Bonsor et al., 2014). This allows for the representation of high transmissivities due to weathered conditions at shallow depths and the reduction of transmissivity as depth increases, consistent with typical behaviour of basement aquifers (Bianchi et al., 2020).

8.2.4 Model spatial resolution

The spatial resolution of the model influences the water partitioning (see Chapter 7). Therefore, in order to reduce the computational demand without significantly affecting the necessary model process description (see Chapter 7), the spatial resolution of the model was set on a 1×1 km grid. Hence, a grid of 201×174 cells was required to cover the study area.

8.2.5 Model parameterisation and settings

Given the data scarcity for the basin, the main hydrological and hydrogeological processes in the basin have been characterised using global and regional datasets at the basin scale.

Surface elevation and channel streambed elevations were obtained from NASA's 30-m resolution SRTM 1 Arc-Second Global dataset (available at <https://earthexplorer.usgs.gov>). The surface elevation was aggregated by averaging the 30-m cells to the 1 km resolution, whereas streambed elevations were obtained by estimating the 30th percentile of cells inside the 1-km cell of the model spatial resolution following Fan et al. (2013); Reinecke et al. (2019). Stream locations were estimated from the 30×30 m DEM. To capture the potential temporal variation of streamflow along the channel (see Chapter 4), the routing network was generated at the 30×30 m grid resolution by defining a minimal upstream drainage area threshold of 10 km^2 . This contributing area corresponds to first-order streams in this region and is in agreement with global dataset products of river networks, such as HydroRIVERS (Lehner and

Grill, 2013). Stream cells were then aggregated to the model grid size, $1 \text{ km} \times 1 \text{ km}$, to obtain the stream length at any given cell (see Fig. 8.3a).

Soil properties and land cover were obtained from global datasets at the model spatial resolution (1 km) as follows (see Fig. 8.3), which supports. Soil hydraulic conductivity (K_{sat}) (Fig. 8.3d), pore size distribution index (λ), and saturated capillary potential (ψ) (Dai et al., 2019a,b) were sourced from publicly available data archives at <http://globalchange.bnu.edu.cn/research/dtbd.jsp>. Land cover specified by plant rooting depth (D_{root}) (Fig. 8.3c), available water content (AWC) (Fig. 8.3b), saturated water content (θ_{sat}), and wilting point (θ_{wp}) (Leenaars et al., 2018) were downloaded from <https://data.isric.org/geonetwork/srv/api/records/10aa9a8f-1433-11e9-a8fa-a0481ca9e724>.

Reliable hydrogeological information that allows a proper characterisation of the groundwater system at local and regional scales is not currently available. Since topography in mountainous regions influences the partitioning and distribution of surface and groundwater flow over the basin (Prancevic and Kirchner, 2019), a global dataset of modelled depth to bedrock was used to characterise the geometrical characteristics of the aquifer system (Pelletier et al., 2016) (see Fig. 8.3e). These data were then combined with hydraulic characteristics for the aquifer sediments, such as permeability and porosity, obtained from GLHYMPS (Gleeson et al., 2014) (<https://dataverse.scholarsportal.info/dataset.xhtml?persistentId=doi:10.5683/SP2/DLGY0>). Saturated hydraulic conductivity was obtained from permeability assuming a fluid viscosity of 0.001 Pa s and water density of 999.7 kg m^{-3} for an average water temperature of $12 \text{ }^\circ\text{C}$ (Fig. 8.3f). Specific yield was assumed as the porosity due to the low range of variation of GLHYMPS dataset (0.01-0.09), which is in agreement with values reported for the study area (see Section 8.2.2). However, two main limitations need to be considered regarding the assumed equivalence of specific yield and porosity: i) this can result in the overestimation of aquifer storage since it considers all the connected and interconnected pores, and ii) it does not consider the influence of capillary forces in small pores, which limits the amount of water that can drain under gravity forces, thus also overestimating the specific yield.

Although these large-scale datasets are very uncertain in absolute parameter values, they give a first indication of the possible spatial variation in hydraulic properties which are then later varied in a Monte Carlo analysis to derive reasonable local parameter values for the basin grid.

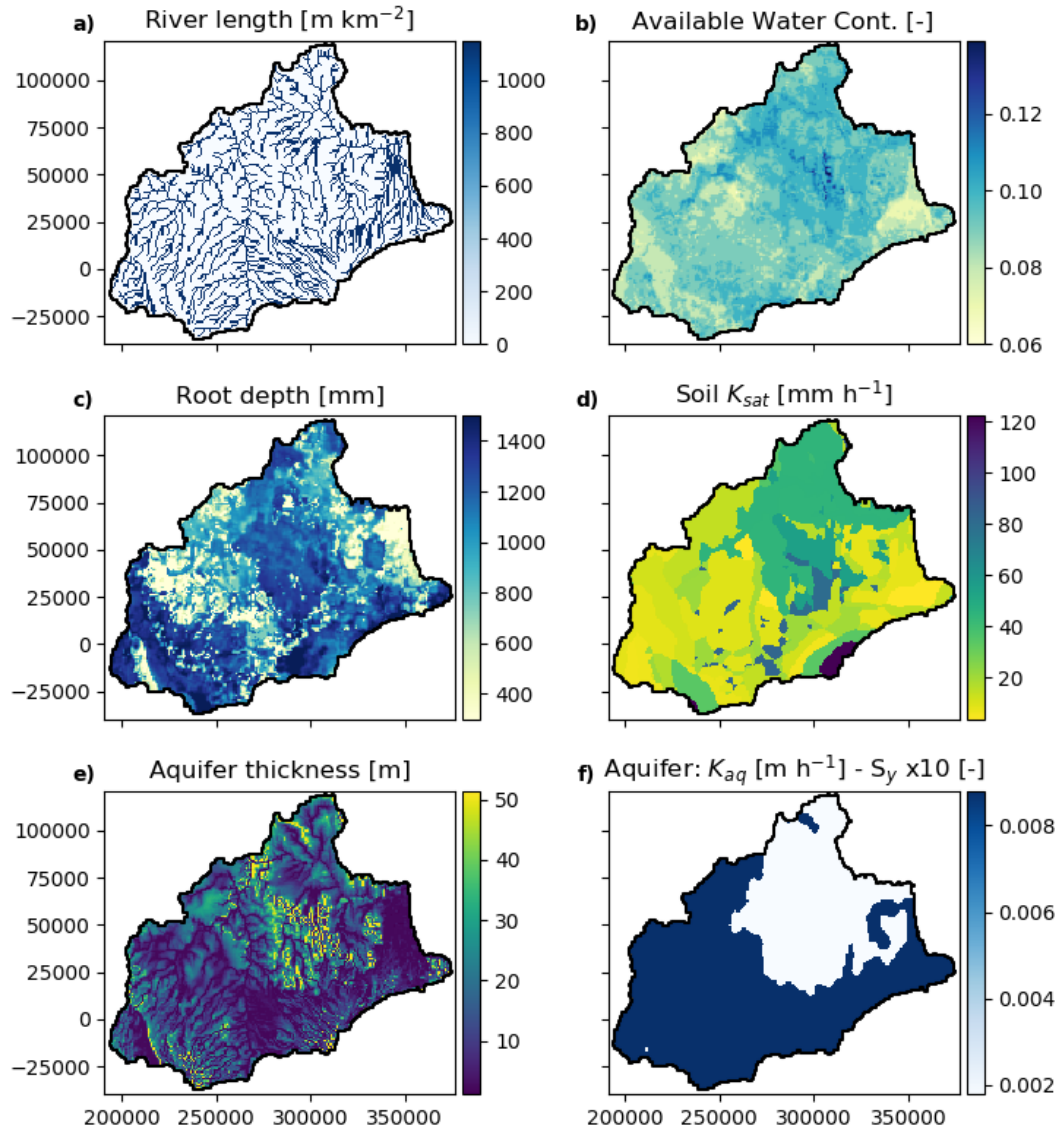


Figure 8.3: Spatial distribution of model parameters: a) river length, b) available water content of the unsaturated zone (Leenaars et al., 2018), c) rooting depth (Leenaars et al., 2018), soil saturated hydraulic conductivity (Dai et al., 2019b), aquifer thickness (Pelletier et al., 2016), and aquifer saturated hydraulic conductivity (Gleeson et al., 2014). Vertical and horizontal axes are in meters and represent the North and East coordinates, respectively.

8.2.6 Boundary conditions

The model domain was defined by the catchment of the Upper Ewaso Ng'iro basin (see Fig. 8.1) downstream to the Archer's Post flow gauge. Since the groundwater system is assumed to be shallow, it interacts with surface flow processes. Thus, the basin is defined according to the topographic characteristics that control the contributing area. Therefore, no-flow boundary conditions for the groundwater domain were specified along the boundaries of the basin. To avoid the artificial accumulation of water in lower parts of the basin due to the specified no-flow boundary conditions and the specified parameterisation of the aquifer transmissivity (groundwater flow is likely to follow the topographical gradients), a constant flux of 0.0005 m d^{-1} was specified for the bottom boundary of the model. This flux boundary condition was applied only in the area corresponding to the outcrop of the Basement system (see Fig. 8.3f, the white area inside the basin) and is consistent with the known hydraulic gradient in the area (WRAP, 1987).

8.2.7 Model time step

Hydrological processes in arid and semi-arid regions are characterised by their high spatial and temporal variability (see Chapter 5). Further, to capture the main processes that control the water partitioning in the basin, a time step of 3 hr was implemented, based on the results of previous testing of DRYP in the Walnut Gulch catchment (see Chapter 7). The chosen 3-hour time step is considered reasonable for two main reasons: i) it is a trade-off between the computational time and process description representation (see Chapter 7), and (ii) it matches the temporal resolution of available precipitation datasets (3 hr). The 3-hour time step simulation also allows for a fair comparison between the two subdaily precipitation datasets, IMERG and MSWEP (see Section 8.2.9 for further details).

8.2.8 Initial conditions

Initial conditions in hydrological models are known to impact the water partitioning and consequently the model performance (Ajami et al., 2014; Cosgrove et al., 2003; Levis et al., 1996; Rodell et al., 2005, 2004; Shrestha and Houser, 2010). Temporal and spatial variations within forcing data as well underlying parameterisation influence the best choice of initial conditions (Cosgrove et al., 2003; Rodell et al., 2005). Therefore, given the seasonal and spatial variation of precipitation over the basin, as well as the uncertainty of the extent of groundwater - surface water interactions across the

area, a dynamic cyclic equilibrium approach was used to assign the initial conditions of the unsaturated and saturated zone of the model. Dynamic cyclic conditions were reached after running the model repeatedly for the period 01/01/2001-01/01/2011. The starting year of this period coincides with average annual wet conditions. Therefore, the spin-up period avoids the influence of extreme wet years. The very first simulation was specified as a relatively wet initial condition with a water table situated just below the rooting depth and the soil moisture at field capacity. Then, subsequent simulations were initialised with state conditions estimated at the end of the simulation period. The spin-up loop continues until changes in state variables, soil moisture and water table, reached less than 0.1 %, for at least 1 % of the model domain (≈ 180 cells). This was achieved after 13 iterations. Finally, to reduce the influence of initial conditions in model evaluation, the first year of the simulation period 2001-2017, was skipped in model evaluation (see Sect. 8.2.11 for further details about the evaluation).

8.2.9 Forcing datasets

Precipitation

Owing to their high temporal and spatial resolution, the following two global datasets of precipitation were used as forcing data for water partitioning evaluation: (i) Multi-Source Weighted-Ensemble Precipitation (MSWEP) V2 Global 3-Hourly 0.1°, and (ii) the Integrated Multi-satellitE Retrievals for Global Precipitation Measurement (IMERG) V06A. These two products were chosen due to the high temporal and spatial resolution necessary to characterise the main hydrological processes within the basin (Chapter 7). MSWEP is a global precipitation product that combines point measurements (76,747 gauges worldwide), satellite products (Climate Prediction Center morphing technique (CMORPH), Gridded Satellite (GridSat), Global Satellite Mapping of Precipitation (GSMaP), and Tropical Rainfall Measuring Mission (TRMM) Multisatellite Precipitation Analysis), and global atmospheric models (European Centre for Medium-Range Weather Forecasts (ECMWF) interim reanalysis (ERA-Interim) and Japanese Reanalysis (JRA)) (Beck et al., 2019). MSWEP is bias corrected and covers the period between 1979 and 2017 with a 3-hourly temporal resolution and 0.1 degree spatial resolution.

IMERG is multi-satellite precipitation product resulting from a combination of measurements from passive microwave sensors (Huffman et al., 2015). The product is also bias corrected by using monthly rain gauge measurements (Huffman et al., 1997). IMERG spans the period from 2001 to 2017 and has a spatial and temporal resolution

of 0.1° and 30 min, respectively. Three IMERG products are available depending on the sensor latency: Early (4 h), Late (14 h), and Final (3.5 months). Early and Late products are not bias corrected and are generally used for flood forecasting applications. Therefore, the bias corrected IMERG Final satellite-gauge product was used in the present simulation, which is publicly available from https://gpm1.gesdisc.eosdis.nasa.gov/thredds/catalog/aggregation/GPM_3IMERGHH.06/2000/catalog.html.

Evapotranspiration

Owing to its high-resolution, spatially and temporally, the global dataset hourly Potential Evapotranspiration (hPET) (Singer et al., 2021) was used as a forcing variable for driving plant and soil evaporation water demands. hPET is a product based on ERA5-Land reanalysis dataset with a spatial resolution of 0.1 (9 km at the equator). hPET estimates potential evapotranspiration by using the Penman-Monteith approach at hourly time steps. hPET is publicly available from <https://doi.org/10.5523/bris.qb8ujazzda0s2aykkv0oq0ctp>.

8.2.10 Evaluation datasets

Actual Evapotranspiration

Owing to the high spatial resolution, a 500 m 500 m grid size and the global coverage, the actual evapotranspiration (AET) product MOD16 ET (Mu et al., 2007; Running et al., 2017) developed from the MODerate Resolution Imaging Spectroradiometer (MODIS) was used for model evaluation for the AET component. MOD16 ET has a temporal resolution of 8-days and is publicly available from <https://lpdaac.usgs.gov/products/mod16a2v006/>.

Remote sensing products have shown good performance in representing seasonality in ET over different regions around the world (Cleugh et al., 2007; Mayes et al., 2020; Mutiga et al., 2010b) although estimations have shown large biases particularly under dry conditions (Jahangir and Arast, 2020; Miralles et al., 2016; Weerasinghe et al., 2020). Therefore, to evaluate the agreement between the spatial and temporal variation in simulated and MOD16 ET values, a correlation analysis was performed rather than comparing values in absolute terms.

Soil moisture

In situ measurements of soil moisture over the Ewaso basin are non-existent. Remote-sensing data represent a reasonable alternative for sites where no information is available (Lettenmaier et al., 2015; Liu Guoxiang et al., 2011; McNally et al., 2016). Therefore, due its global coverage and its high temporal resolution (1-day),

the soil moisture product ESA-CCI-SM (developed by the European Space Agency - Climate Change Initiative, ESA-CCI) was used for model evaluation. ESA-CCI-SM is produced by combining passive (radiometer) and active (scatterometer/radar) sensors (Dorigo et al., 2017; Liu et al., 2011; Preimesberger et al., 2021). ESA-CCI-SM provides information at 0.25 (25 km) spatial resolution.

However, soil moisture from ESA-CCI is only representative of the soil depth between 2 - 5 cm (Brocca et al., 2017). Therefore, it cannot be directly compared to the DRYP model results, which resolves a single depth integrated soil store. Therefore, to evaluate the performance of DRYP in relation to ESA-CCI-SM, a correlation analysis was performed instead of comparing absolute values.

Total water storage

Total water storage anomalies (TWSA) derived from the Gravity Recovery and Climate Experiment (GRACE) were used to evaluate the ability of the model to simulate changes in the combined hydrological storage. GRACE satellite observations need to be post-processed to produce gravity and mass change solutions and two main post-processed products are available at the global scale: i) the CSR solution from the Center for Space Research at University of Texas, Austin (Landerer and Swenson, 2012), and ii) the JPL Mascons solution from the Jet Propulsion Laboratory (Watkins et al., 2015; Wiese et al., 2016). The CSR solution is based on spherical harmonic functions, whereas JPL Mascons uses mass concentration functions based on regularisation information derived from geophysical models or by GRACE itself (Rowlands et al., 2005; Save et al., 2016; Watkins et al., 2015). Mascons solutions are considered to better represent hydrology as well as ocean and ice mass changes, since there is no need of a destriping function or reduction of signal leakage (Rowlands et al., 2005; Save et al., 2016; Watkins et al., 2015). Hence, in the present study, the mascons solutions from CSR and JPL, at 1° spatial resolution and at monthly time steps were obtained from <http://grace.jpl.nasa.gov>. These datasets were then combined by averaging in order to include the uncertainty of the two approaches (Bonsor et al., 2018). The four grid cells analysed are those which covered the study basin.

Uncertainty of GRACE estimations depends on factors such as the post-processing approach, region, and spatial scale. Uncertainty associated to these factors increases even further for basins smaller than 200,000 km² (Landerer and Swenson, 2012; Longuevergne et al., 2010; Scanlon et al., 2012). Therefore, the model results of the present study have been cautiously assessed in relation to the GRACE datasets to avoid misinterpretation of simulated TWSA.

8.2.11 Model Calibration, sensitivity and uncertainty analysis

A similar approach followed in Chapter 6 was carried out here to calibrate model parameters. First, an initial trial-and-error calibration of the model was performed to explore the parameter sensitivities and to reduce the a-priori parameter ranges used in the second step. The calibration was performed by applying spatially constant multiplicative factors kK_{sat} , kD_{root} , kK_{ch} , kk_T , kK_{aq} , and kS_y to model parameters K_{sat} , D_{root} , K_{ch} , k_T , K_{aq} , and S_y respectively. The channel width, W , which was assumed constant over the model domain, was not evaluated because it is combined proportionally with the conductivity in the model equations, and thus its sensitivity to change can be represented by the parameter kK_{sat} . These parameters were used because they represent the dominant controls on the storage and water partitioning of the surface and subsurface components (see also Chapter 7). The initial manual calibration enabled a set of parameter ranges to be defined for a Monte Carlo experiment to analyse the multi-parameter uncertainty of the model results (see Table 8.1).

Chapter 7 showed that the soil parameter K_{sat} has to be reduced in order to enable good model performance with temporal and spatial aggregation of the precipitation. In the same context, the parameter K_T also has to be reduced. For specific yield, S_y , a short range of variation ($\pm 20\%$) was specified due to the big contrast between the metamorphic ($\approx 1\%$) and volcanic sediments ($\approx 10\%$) (Fig. 8.3), although this short range also cover the likely range of variation reported in the area (see Sect. 8.2.2). A big range will results in unrealistic values, particularly, for volcanic sediments. Finally, for the Monte Carlo analysis a set of 200 realisations for each precipitation dataset was used to drive DRYP for the analysis with parameters randomly generated using a uniform distribution.

Similarly to chapters 7 and 7, the Generalized Likelihood Uncertainty Estimation (GLUE) framework (Beven and Binley, 1992) was used as the uncertainty analysis framework. However, in order to determine which simulations were considered as acceptable (i.e. behavioural), a combination of two different 'goodness of fit' indices was used: per cent bias (PBIAS) (eq. 6.3), and Kling-Gupta Efficiency (KGE) (Gupta et al., 2009) defined as follows:

$$KGE = 1 - \sqrt{(r - 1)^2 + (\alpha - 1)^2 + (\beta_n - 1)^2} \quad (8.1)$$

Table 8.1: Prior parameter range for each component considered in the Monte Carlo analysis; parameters starting with 'k' mean that it is computed as a factor of the model parameter

Factor	Parameter affecting	Range of factor
Overland flow		
kk_T	k_T , Recession time for channel streamflow	0.15-0.35
kK_{ch}	K_{ch} , Channel saturated hydraulic conductivity	0.50-1.50
Unsaturated zone		
kK_{sat}	K_{sat} , Saturated hydraulic conductivity	0.10-0.20
kD_{root}	D_{root} , Rooting depth	0.75-1.50
Saturated Zone		
kS_y	S_y , Specific yield	0.80-1.20
kK_{aq}	K_{aq} , Aquifer Saturated hydraulic conductivity	1-10

$$\alpha = \frac{\sigma_S}{\sigma_O} \quad (8.2)$$

$$\beta_n = \frac{\mu_S - \mu_O}{\sigma_O} \quad (8.3)$$

where: O represents the observation, \hat{O} the arithmetic mean of observations, S the model simulations, and n the number of observation available, μ is the mean and σ is the standard deviation.

The KGE index has the ability to assess the temporal variability, bias and correlation between observed and simulated data. Nash Sutcliffe (NSE) generally over-represents peak values because it uses standard error for the estimation (Gupta et al., 2009; Krause et al., 2005). Therefore, given that baseflow from upstream areas plays an important role in supplying water for downstream areas where the evaluated streamflow station is located, NSE was not considered for this analysis.

After scaling both KGE and PBIAS between 0 and 1, these metrics were combined into one metric by calculating their product (see section 6.2.4 and 7.2.5):

$$p = KGE_k^* \cdot PBIAS_k^* \quad (8.4)$$

where p is the combined performance measure for the parameter set, the * signifies scaled values.

The evaluation period was chosen considering the overlap between all datasets. Thus, the model was evaluated for the period between 2001 and 2017.

Comparison of model scenarios

In order to evaluate the uncertainty of model results to precipitation and model parameters, two main scenarios with four outcomes in total were defined (see Fig.8.4).

The first scenario considers the calibration under two different precipitation forcing datasets (i.e. IMERG and MSWEP). This scenario was designed to provide insights about the model parameterisation and how well the different model components can characterise the main mechanisms of water partitioning for each precipitation dataset. This scenario also provides information about the impact of the spatial distribution of precipitation on the model parameters needed for good performance. It is assumed that each dataset characterises precipitation events differently in terms of spatial and temporal scales. Hence, each calibrated model will potentially have the ability to better represent specific characteristics of the streamflow signal (e.g. low or high events).

The second scenario evaluates the impact of uncertainty in the spatial and temporal distribution of input (forcing) precipitation on the water balance partitioning. This scenario uses the best performing set of parameters estimated in the first case scenario for each precipitation dataset in turn, and then forces this parameter set using the other of the precipitation dataset. For example, the scenario named IMERG-MSWEP is calibrated on the IMERG data and then re-run with the best parameter set but using the MSWEP data to force the model.

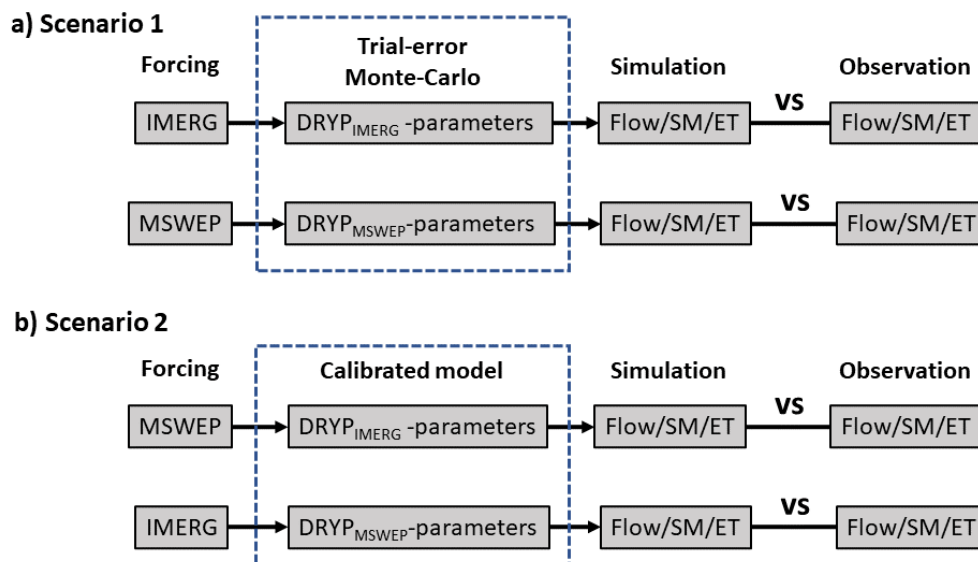


Figure 8.4: Scenarios specified for evaluation of the uncertainty of precipitation and model parameters: a) evaluates the uncertainty of model parameters in water partitioning, and b) evaluates the sensitivity of water partitioning to the spatial and temporal characteristic of precipitation.

8.3 Results

8.3.1 Uncertainty of precipitation datasets

There are substantial spatial differences between the MSWEP and IMERG precipitation datasets that are reflected in the contrasting distributions for different climatic regions over the basin (Fig. 8.5). Dry-humid regions, which shows the greatest differences between datasets, cover an area of $\approx 10\%$ and $\approx 18\%$ for MSWEP and IMERG, respectively. A large difference is also observed in humid regions, where MSWEP precipitation covers a larger area ($\approx 10\%$) in comparison to IMERG ($\approx 3\%$). However, despite markedly different spatial distributions, the extent of semi-arid regions for both MSWEP and IMERG dataset is similar ($\approx 79\%$).

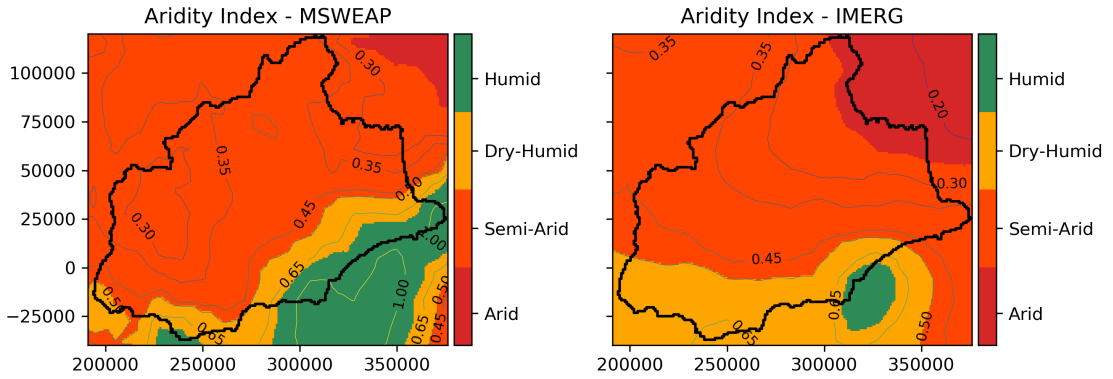


Figure 8.5: Climatic zones in the Upper Ewaso Ng'iro basin estimated using MSWEP and IMERG precipitation datasets and hPET dataset for potential evapotranspiration. Climatic zones are based on the Aridity Index (AI) (see Sect. 2.2)

Mean annual precipitation averaged over the basin is very similar for the two datasets, 794 and 800 mm yr^{-1} for MSWEP and IMERG, respectively. However, mean annual precipitation is higher in semi-arid and dry-humid areas for the IMERG dataset, while in humid areas the values are more similar. The highest values of mean annual precipitation (1800 mm yr^{-1}) are observed in the MSWEP dataset, whereas IMERG's maximum values are lower at ≈ 1600 mm yr^{-1} . Since AI is linearly proportional to mean precipitation, the distribution of aridity index also varies over the basin as a result of the difference between the two precipitation data sets (top panel of Fig. 8.6b).

Precipitation varies strongly with elevation (see Fig. 8.6c), which is expected as orographic characteristics exert great control on precipitation at higher elevations, particularly in areas close to Mount Kenya. Topographically, there are two major areas: Laikipia plateau above 1500 m and Isiolo below 1500 m, with the Mount Kenya representing only a small part of the basin (see elevation distribution in Fig. 8.6c top panel). However, the area corresponding to the Mount Kenya receives more precipitation than the rest of the basin (Fig. 8.6c). IMERG data show a linear relation with surface elevation, whereas MSWEP shows a highly non-linear behaviour, particularly at elevations between 1200 and 2500 m (Fig. 8.6c), although MSWEP precipitation becomes more linear in areas located at elevations above 2500 m. IMERG precipitation is also regularly distributed over the basin, as can be seen on the right bottom panel of figure 8.6c and figure 8.6e. Conversely, MSWEP shows a narrower distribution than IMERG with most precipitation concentrated around 700 mm yr⁻¹ (Fig. 8.6c left bottom panel and Fig. 8.6d).

8.3.2 Model calibration

Results of the calibration resulted in 94 valid models for MSWEP forcing and 92 valid model for IMERG forcing. The best models, considering evaluation at only the streamflow station located at the catchment outlet, resulted in values of *KGE* and *PBIAS* of 0.70 and 3.5%, respectively, for the MSWEP precipitation dataset, whereas the IMERG dataset resulted in 0.66 and 12% for *KGE* and *PBIAS*, respectively. Given the topographic and geologic complexity of the basin and the large-scale gridded datasets used to drive the model, these can be interpreted as excellent model results in representing the Ewaso water balance, particularly for the MSWEP-forced model.

In general terms, the model also well captures the monthly fluctuations in AET, soil moisture, streamflow, and TWSA for the whole basin (see Fig. 8.7), when compared to MOD16, ESA soil moisture, observed streamflow, and GRACE-TWSA, respectively.

For AET, a high correlation between model simulations and MOD16A has been obtained (see Fig. 8.8a), although model fluctuations show higher variations in comparison to MOD16A. The main differences are observed in peak values where model estimations are up to 50% higher than MOD16A (see Fig. 8.7b). This is consistent with previous studies where MOD16A has been shown to underestimate AET in arid and semiarid regions (Aguilar et al., 2018; Jahangir and Arast, 2020; Miralles et al., 2011; Trambauer et al., 2014; Velpuri et al., 2013; Weerasinghe et al., 2020).

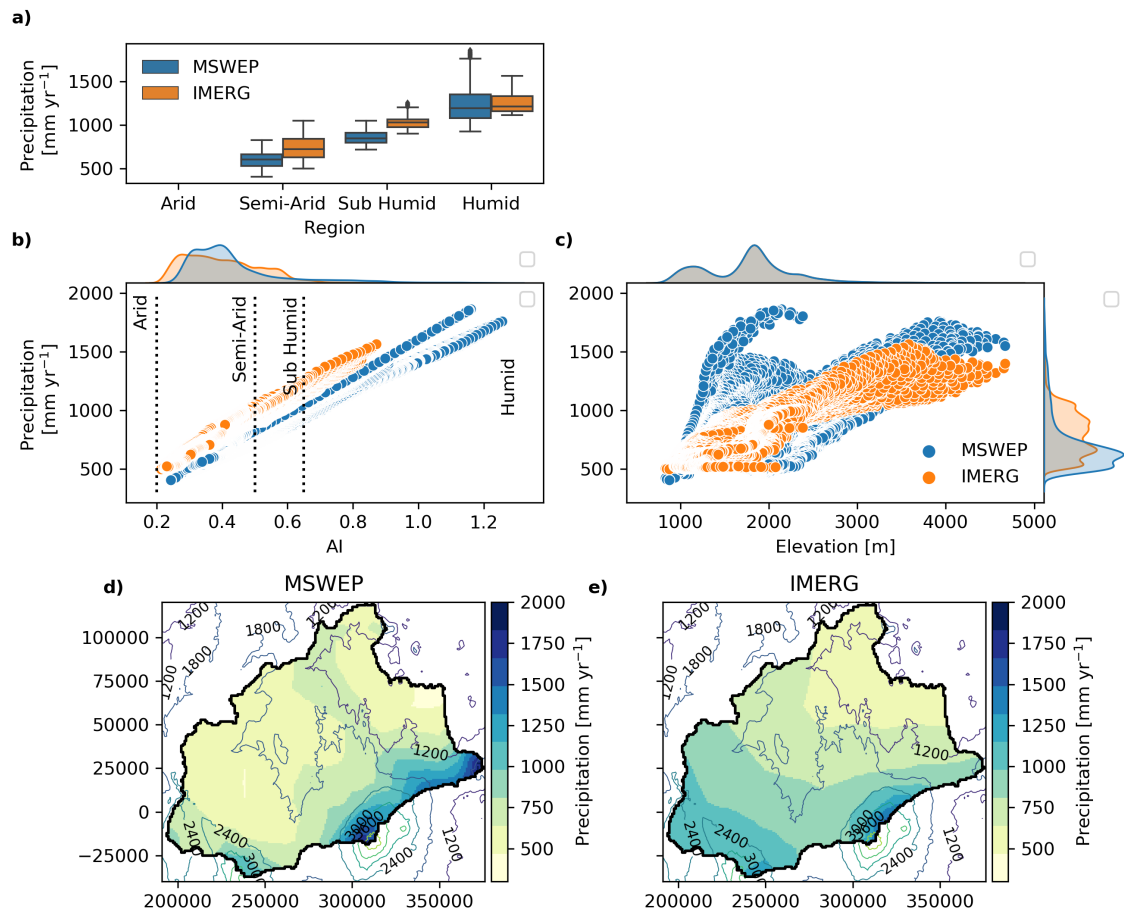


Figure 8.6: Variation of MSWEP and IMERG precipitation datasets for the Upper Ewaso Ng'iro basin : a) mean annual precipitation totals by climatic region; b) distribution of AI over the basin (top) and mean annual precipitation according to AI (bottom); c) distribution of surface elevation (top), mean annual precipitation totals according to the surface elevation (bottom right), and distribution of mean annual precipitation rates over the basin (right); d) MSWEP, mean annual precipitation; and e) IMERG, mean annual precipitation. Vertical and horizontal axes of panels d) and e) are in meters.

In relation to soil moisture, temporal fluctuations are also well captured by the model compared to the ESA-SM combined product (Fig. 8.7d). Figure 8.7d has been plotted on a log-scale in order to observe the skill of the model in representing low values. A high correlation is also obtained between the model and ESA, when normalised values are compared (see Fig. 8.7b). The log-scale and normalisation enable a better comparison since the ESA product represents soil moisture for only the upper 5 cm of the soil.

Fluctuations in streamflow are well captured by the model (Fig. 8.7e), wherein larger flow events are mainly attributed to large precipitation events. High correlations are also observed for both datasets (MSWEP, $R^2=0.62$, and IMERG, $R^2=0.59$) (see Fig. 8.8c), although the model does underestimate peak monthly values. Overall, the model seems to capture the production of runoff despite its parsimoniousness and simplicity and the uncertainty in forcing precipitation and PET datasets.

Model simulations are also able to capture the temporal variation in TWSA compared to GRACE despite the size of the basin ($\approx 15,700$ km²) (Fig. 8.7f). A high correlation is obtained for both datasets (MSWEP, $R^2 = 0.69$, and IMERG, $R^2=0.75$). This is mainly attributed to the high dependence of TWSA on precipitation anomalies over the basin (Fig. 8.7f).

However, the modelled TWSA for both datasets show larger fluctuations with a wide range of variation (-50 to 210 mm) in comparison to GRACE (-70 to 90 mm) for the simulated period (Fig. 8.7f). These larger fluctuations in the model outputs, which also result in a wider uncertainty band, are expected due to the size and heterogeneous nature of the basin. This is because GRACE data only captures the raw TWSA signal at scales larger than 200,000 km². Therefore, an attenuation of the TWS anomalies can be expected producing higher fluctuations of model results that cannot be resolved within a 3° GRACE cell.

The best models showed a good spatial correlation of actual evapotranspiration in relation to MOD16A dataset (Fig. 8.9). Larger areas with high correlation values (≈ 0.75) are observed for MSWEP-forced models. Both models show similar performance in northeast areas, where aridity is higher (see Fig. 8.5 and lower correlations (≈ 0.45) around Mount Kenya.

An overall positive but weak spatial correlation is also observed in modelled soil moisture in relation to the ESA dataset (see Fig. 8.10 and Fig. 8.8). Note, both datasets, MSWEP and IMERG, have been spatially aggregated to the 0.25 degree resolution of ESA to allow this comparison.

Uncertainty of model parameters

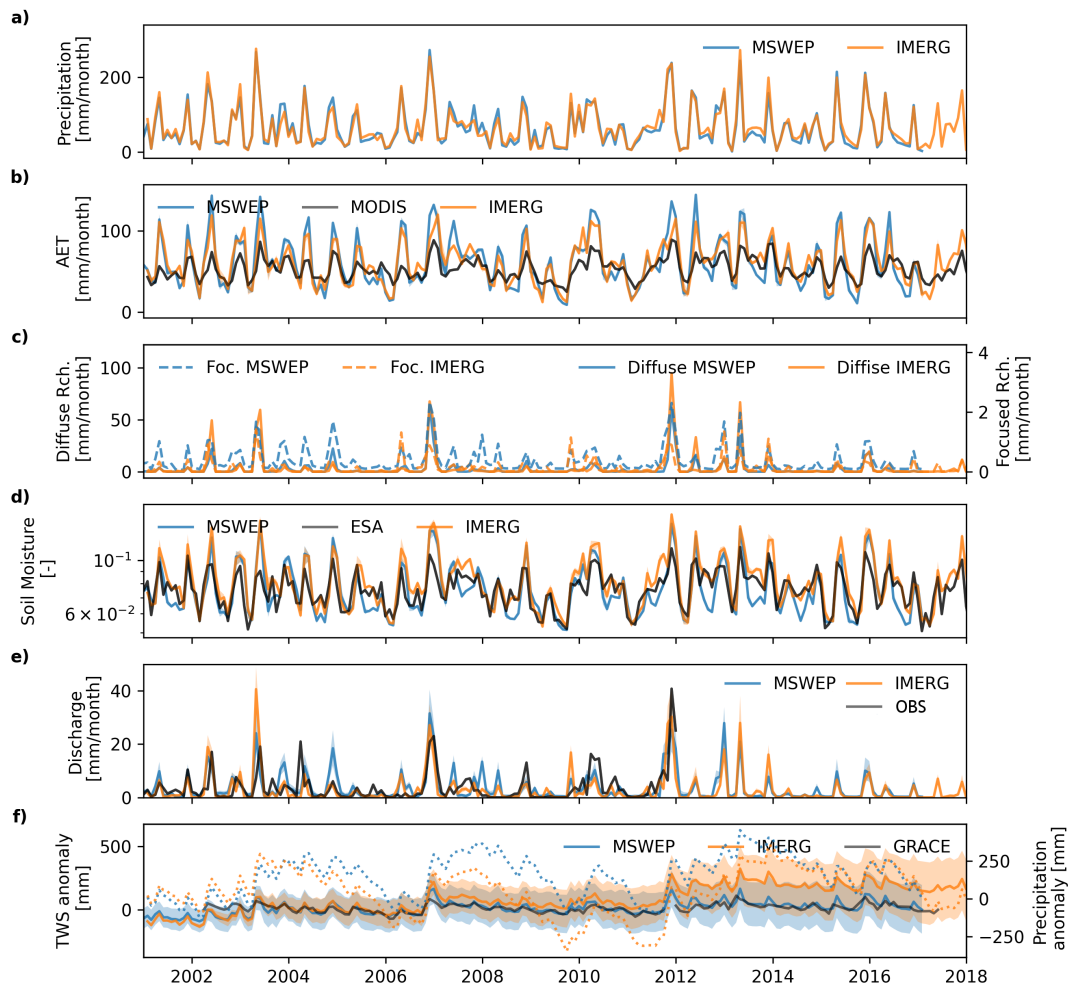


Figure 8.7: Monthly temporal variation over the whole basin for MSWEP and IMERG datasets of: a) precipitation, b) simulated actual evapotranspiration, c) simulated soil moisture, plotted at log scale in order to compare with ESA product, d) simulated diffuse and focused recharge, e) simulated and observed discharge at the catchment outlet (Archer's Post, see Fig. 8.1), and f) change in total water storage anomalies for model output and the GRACE dataset (solid lines), and monthly precipitation anomalies estimated relative to the mean value over the evaluation period (dashed lines).

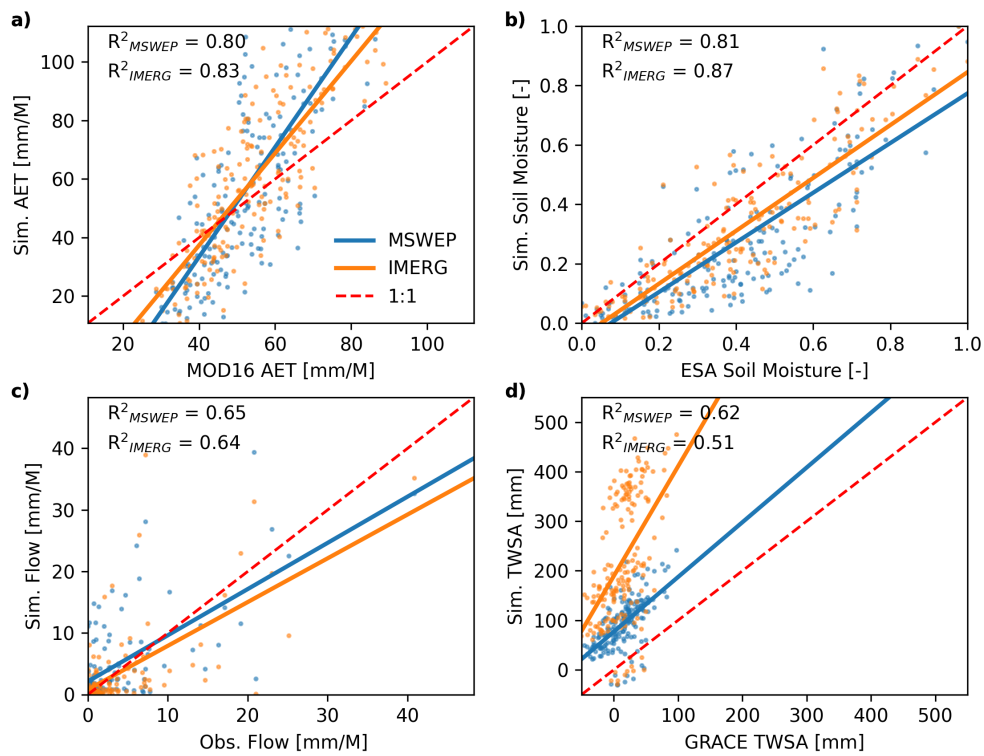


Figure 8.8: Scatter plot between: a) simulated actual evapotranspiration and the MOD16A dataset, b) scaled soil moisture of simulated values and the ESA-CCI-SM dataset, and c) simulated change in total water storage anomalies and the GRACE dataset. Simulated values correspond to MSWEP and IMERG precipitation datasets. Comparison is performed at monthly time steps. The best simulation was considered for comparison.

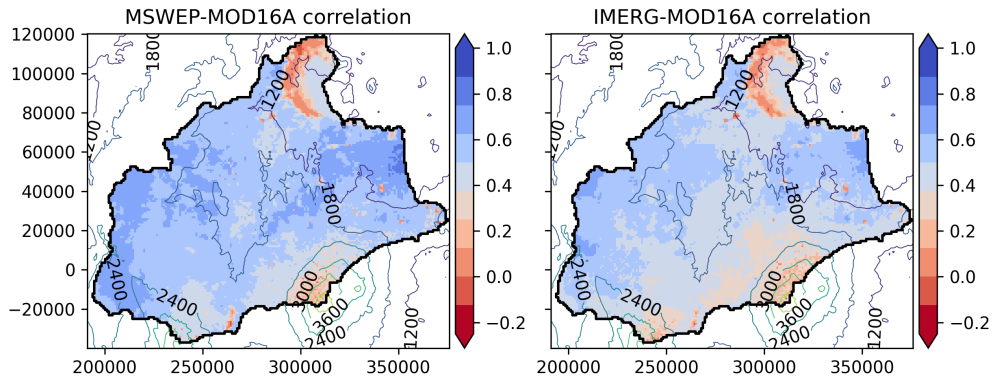


Figure 8.9: Correlation between simulated actual evapotranspiration and MOD16A datasets for both MSWEP and IMERG forcing precipitation datasets, and for the best performing parameter sets. Contour lines represent surface elevation in meters above sea level. Vertical and horizontal axes are in meters.

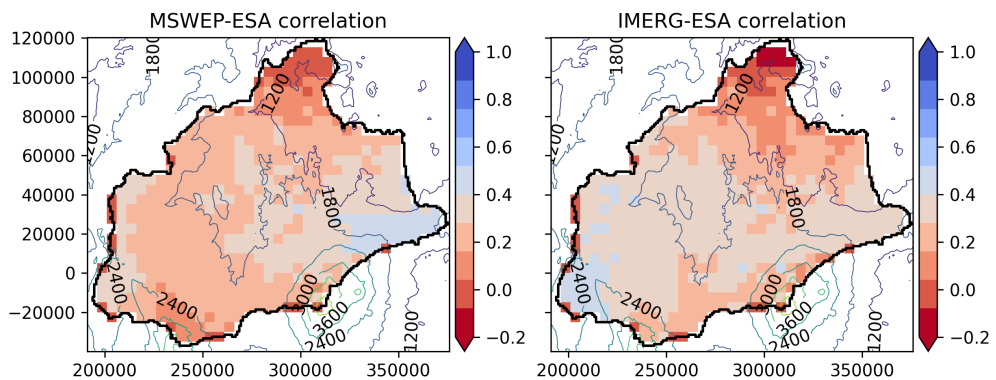


Figure 8.10: Correlation between simulated soil moisture and the ESA combined (active-passive) product for both MSWEP and IMERG precipitation datasets, and for the best performing parameter sets. Contour lines represent surface elevation in meters above sea level. Vertical and horizontal axes are in meters.

Table 8.2: Model parameter factors of the best performing model after calibration for IMERG and MSWEP precipitation forced models

Model	Parameters					
	kD_{root}	kK_{sat}	kK_{ch}	kT	kK_{aq}	kS_y
MSWEP	0.75	0.13	0.75	0.30	5.50	0.87
IMERG	0.77	0.16	0.82	0.20	9.07	1.02

The best sets of parameter values (factors) obtained from the calibrations for each forcing precipitation dataset are shown in Table 8.3. Overall, the analysis shows that D_{root} , K_{sat} , and K_{ch} had to be reduced from their assigned parameter values based on gridded inputs, in order to capture the spatio-temporal characteristics of streamflow at the outlet of the basin. This is consistent with the temporal (and spatial) resolution of the model and results obtained in Chapter 6. Similarly to that analysis, parameters controlling the production of runoff had to be reduced in order to capture the attenuation effect of the increase in the temporal and spatial scale of the model inputs as well as the time step of the model (3-hour).

The results for recession time for channel streamflow, kT , suggest that differences in this parameter for the two forcing datasets means that flow in channels is moving faster for higher precipitation, i.e. within the MSWEP dataset. This is understandable, as there are great differences in the spatial distribution of precipitation between forcing datasets that influence the amount of water that would be present as streamflow at the basin output, the evaluation point. In the case of MSWEP, precipitation is high in the upper parts of the basin, Mount Kenya. Therefore, water is quickly moved to the lower parts of the basin. A more detailed description of the spatial distribution of runoff is presented in the following sections.

There was also substantial differences in kK_{aq} and kS_y between the two forcing datasets. This is mainly attributed to the spatial distribution of precipitation and their impact on recharge, which impacts the temporal availability of water stored in the aquifer. IMERG forcing data generates more recharge in DRYP, which has to flow quickly downstream in order to prevent unrealistic accumulation of water in the channel. Therefore, a higher kK_{aq} is required. Recharge is further analysed in the following sections.

Figure 8.11 shows the distribution of model parameters (bars) for each dataset regardless of the performance and the p-value (eq. 8.4) for the behavioural models. For both datasets, parameters show almost the same distribution with only slight variations. This means that both models show similar behaviours for representing water partitioning, which is in turn translated in the production of runoff over the

basin. Since model parameters were sampled using a uniform distribution, all sets of parameters have the same probability. Therefore, model outputs are sensitive to parameters that exhibit high frequencies. For both models, given the small size of parameter samples (200 simulation) as well as the short range of variation (see Table 8.1), it is not clear which parameters play a key role in affecting the performance of the model. However, based on p-values (dots), it is clear that the parameter kD_{root} has a major impact on the performance of the model.

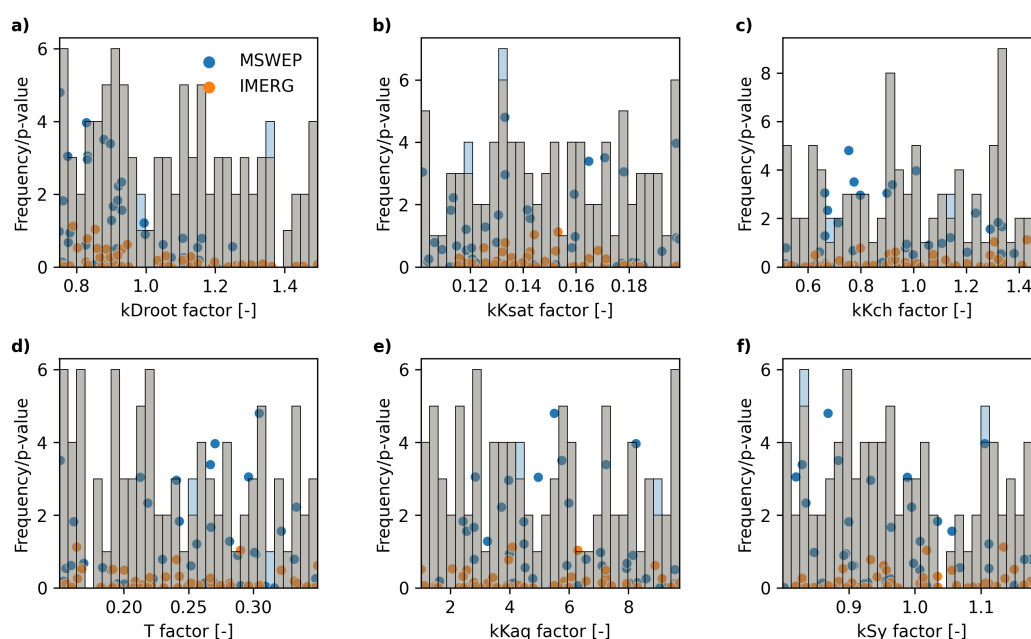


Figure 8.11: Distribution of parameters of valid simulations (bars), and p-values (eq. 8.4) estimated for valid simulations (dots) for both models, MSWEP and IMERG. Grey bars indicate that IMERG model results are similar than MSWEP.

8.3.3 Uncertainty of water partitioning

All behavioural models were used to assess the uncertainty in the modelled water balance partitioning. To have a better appreciation of the overall spatial variations in terms of magnitudes between climatic regions, scatterplots and bar plots presented in the following sections show the results of a spatial aggregation of all model outputs. Thus, the 1-km grid size was aggregated into 5-km grid size by averaging cells.

Actual evapotranspiration

Mean annual values of simulated actual evapotranspiration were 702 and 690 mm yr^{-1} , for MSWEP and IMERG forcing, respectively. Modelled values for both

datasets also showed a similar range of variation between 250 and 1500 mm yr⁻¹. In general, AET increases as AI increases, which is expected since more water is available for direct evaporation and plant transpiration as the precipitation increases. Both datasets resulted in evapotranspiration rates varying linearly with AI (Fig. 8.12a), but there were systematically higher values estimated by MSWEP (Fig. 8.12a). In every climatic region, as defined by the UNEP AI classes (UNEP, 1992), mean values of AET estimated using MSWEP are higher than those obtained from IMERG forcing (Fig. 8.12b). This result is consistent with the generally higher precipitation in each region of the basin for the MSWEP dataset. However, since the spatial distribution of aridity varies over the basin (Fig. 8.12a top panel), mean values distributed over the basin are similar.

Both forcing datasets result in higher modelled values compared to MOD16A. In each AI region, MOD16A underestimates AET, and discrepancies increase with aridity. Mean values of AET in humid areas are closer to modelled AET, which is expected since MOD16A has shown a better performance in areas where evapotranspiration losses occur under energy-limited conditions (Cleugh et al., 2007; Miralles et al., 2016) (Fig. 8.12b and c).

The spatial variation of actual evapotranspiration generally follows the spatial distribution of the precipitation (see Fig. 8.13a and b). In general, the uncertainty of AET increases as precipitation increases, particularly at precipitation totals above 1000 mm yr⁻¹ (see Fig. 8.13c and d, AET and Fig. 8.6d and e for precipitation). IMERG-forced models show more uncertainty in areas at elevations higher than 1800 m (Fig. 8.13c), whereas MSWEP-forced models show a higher uncertainty in areas close to Mount Kenya (Fig. 8.13d).

Lorem ipsum dolor sit amet, consectetur adipiscing elit. Ut purus elit, vestibulum ut, placerat ac, adipiscing vitae, felis. Curabitur dictum gravida mauris. Nam arcu libero, nonummy eget, consectetur id, vulputate a, magna. Donec vehicula augue eu neque. Pellentesque habitant morbi tristique senectus et netus et malesuada fames ac turpis egestas. Mauris ut leo. Cras viverra metus rhoncus sem. Nulla et lectus vestibulum urna fringilla ultrices. Phasellus eu tellus sit amet tortor gravida placerat. Integer sapien est, iaculis in, pretium quis, viverra ac, nunc. Praesent eget sem vel leo ultrices bibendum. Aenean faucibus. Morbi dolor nulla, malesuada eu, pulvinar at, mollis ac, nulla. Curabitur auctor semper nulla. Donec varius orci eget risus. Duis nibh mi, congue eu, accumsan eleifend, sagittis quis, diam. Duis eget orci sit amet orci dignissim rutrum.

Soil moisture

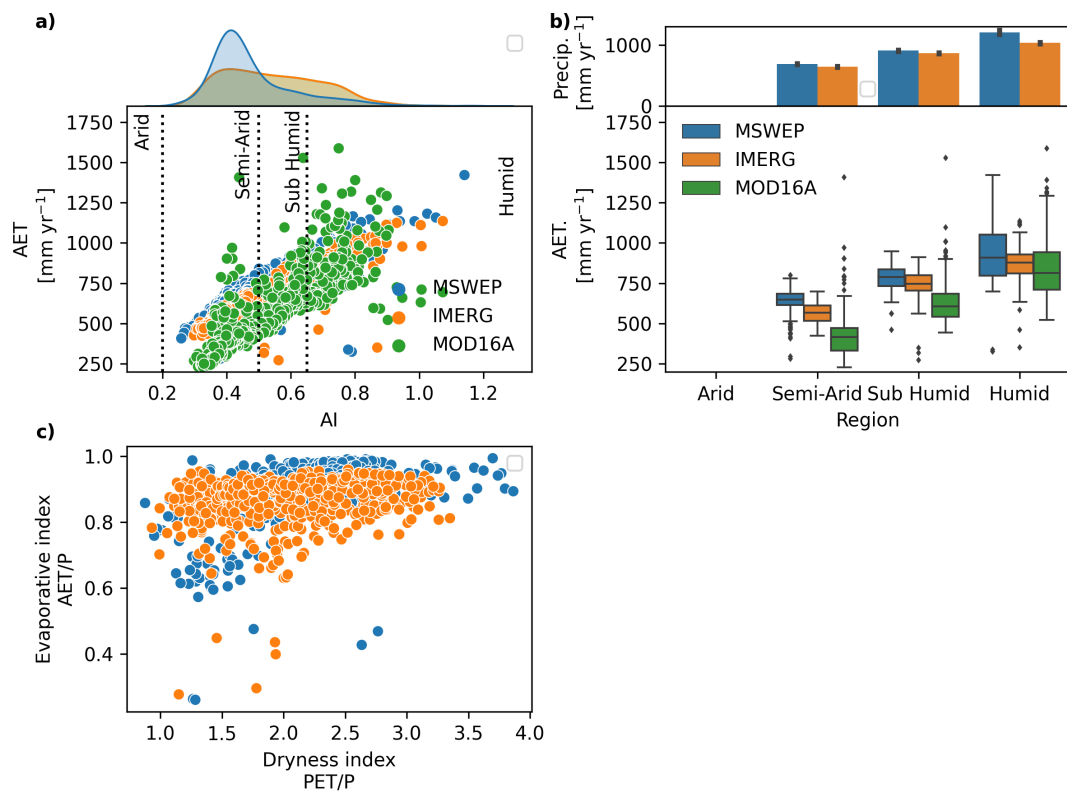


Figure 8.12: Variation of actual evapotranspiration for the Upper Ewaso Ng'iro basin estimated using MSWEP and IMERG precipitation datasets: a) distribution of AI over the basin (top) and mean annual actual evapotranspiration according to AI (bottom); b) annual precipitation rate according to climatic region (top) and mean annual actual evapotranspiration according to AI (bottom); and c) evaporation index (AET/P) against dryness index (PET/P), Budyko aridity index (Budyko, 1961)

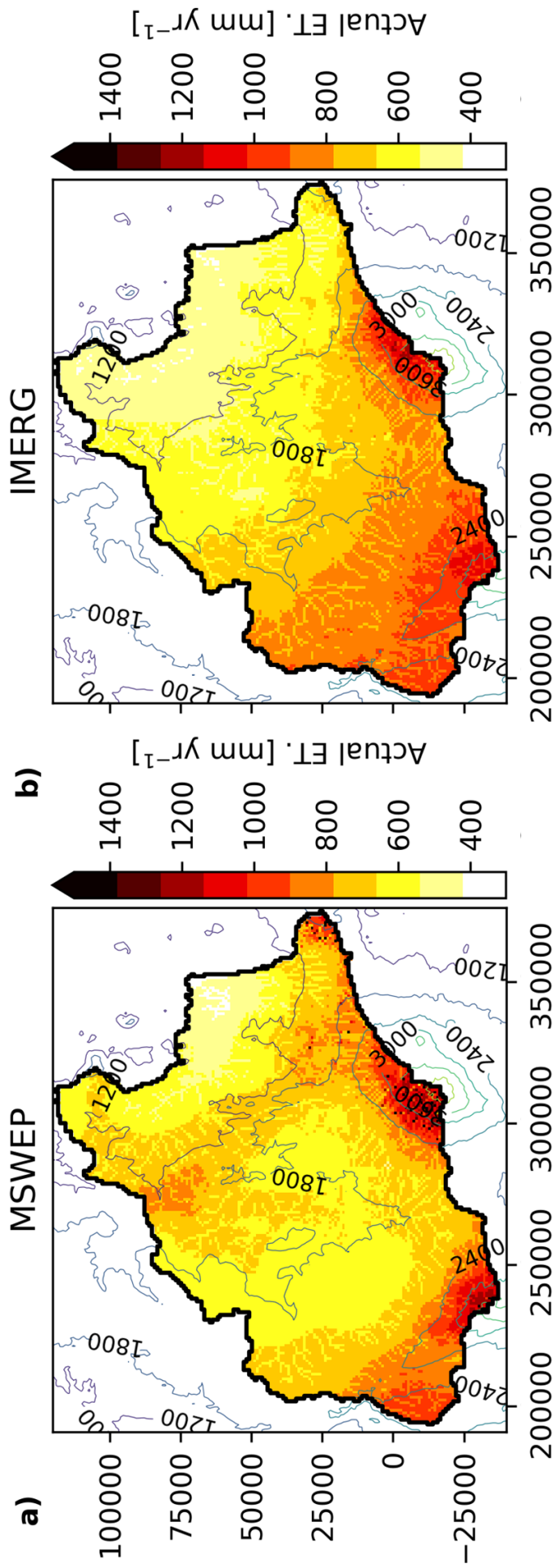


Figure 8.13: Mean annual actual evapotranspiration and standard deviation estimated from the ensemble of valid simulation using both IMERG and MSWEP precipitation datasets for the Upper Ewaso Ng'iro basin. Contour lines represent surface elevation in meters above sea level. Vertical and horizontal axes are in meters.

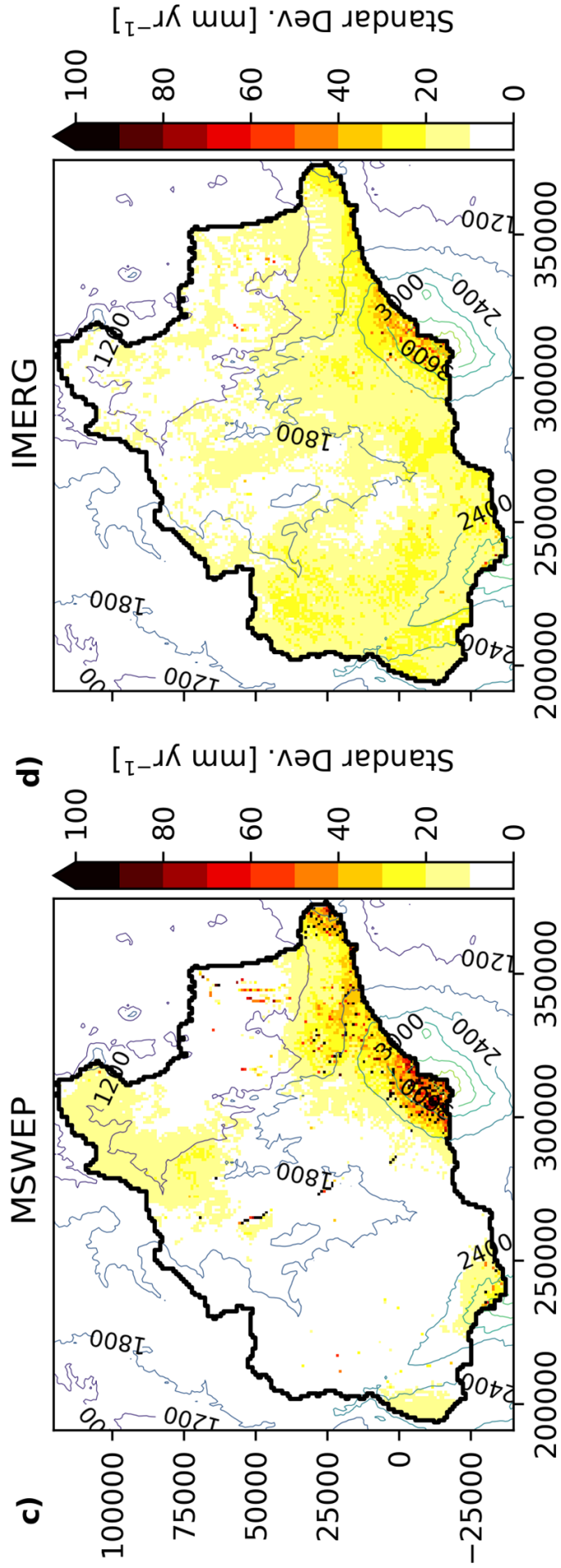


Figure 8.13: Mean annual actual evapotranspiration and standard deviation estimated from the ensemble of valid simulation using both IMERG and MSWEP precipitation datasets for the Upper Ewaso Ng'iro basin. Contour lines represent surface elevation in meters above sea level. Vertical and horizontal axes are in meters (cont.).

Figure 8.14 shows the spatial variation of relative water content for both MSWEP and IMERG forced models. In general, soil hydraulic properties and precipitation control the spatial distribution of soil water content. As expected, areas receiving more precipitation at higher elevations have higher soil water contents, whereas lower soil water contents are predominant in the lower parts of basin. IMERG-forced models have larger areas of higher soil moisture in comparison to MSWEP-forced models.

Uncertainty in modelled soil water content is relatively low (see Fig. 8.14 bottom panels) due to the similar characteristics of the unsaturated zone parameters used by both models, as indicated by similar values of rooting depth and soil saturated hydraulic conductivity factors (Table 8.2). These parameters control the amount of water entering and leaving the soil as evapotranspiration or percolation.

Lorem ipsum dolor sit amet, consectetur adipiscing elit. Ut purus elit, vestibulum ut, placerat ac, adipiscing vitae, felis. Curabitur dictum gravida mauris. Nam arcu libero, nonummy eget, consectetur id, vulputate a, magna. Donec vehicula augue eu neque. Pellentesque habitant morbi tristique senectus et netus et malesuada fames ac turpis egestas. Mauris ut leo. Cras viverra metus rhoncus sem. Nulla et lectus vestibulum urna fringilla ultrices. Phasellus eu tellus sit amet tortor gravida placerat. Integer sapien est, iaculis in, pretium quis, viverra ac, nunc. Praesent eget sem vel leo ultrices bibendum. Aenean faucibus. Morbi dolor nulla, malesuada eu, pulvinar at, mollis ac, nulla. Curabitur auctor semper nulla. Donec varius orci eget risus. Duis nibh mi, congue eu, accumsan eleifend, sagittis quis, diam. Duis eget orci sit amet orci dignissim rutrum.

Recharge: Diffuse and Focused

Mean annual total groundwater recharge (diffuse and focused) varies between ≈ 42 and 53 mm yr^{-1} for MSWEP and IMERG, respectively. The simulations also show that high monthly precipitation ($>100 \text{ mm month}^{-1}$) delivered over the basin result in large values of diffuse recharge (Fig. 8.15 left). Despite exceeding only 20% of the time, those months with high precipitation are responsible for up to $\approx 80\%$ of the total amount of total groundwater recharge occurring during the simulated period. Thus, groundwater recharge in the Upper Ewaso Ng'iro basin mostly depends on large precipitation events.

Diffuse recharge represents the main source of aquifer recharge for the Upper Ewaso Ng'iro basin. Mean annual groundwater diffuse recharge for the whole basin estimated from all valid simulations sums to ≈ 36 and $\approx 51 \text{ mm yr}^{-1}$ for MSWEP and IMERG, respectively. Average focused recharge from all valid simulations using MSWEP is $\approx 5.8 \text{ mm yr}^{-1}$, which accounts for 13% of the total annual recharge.

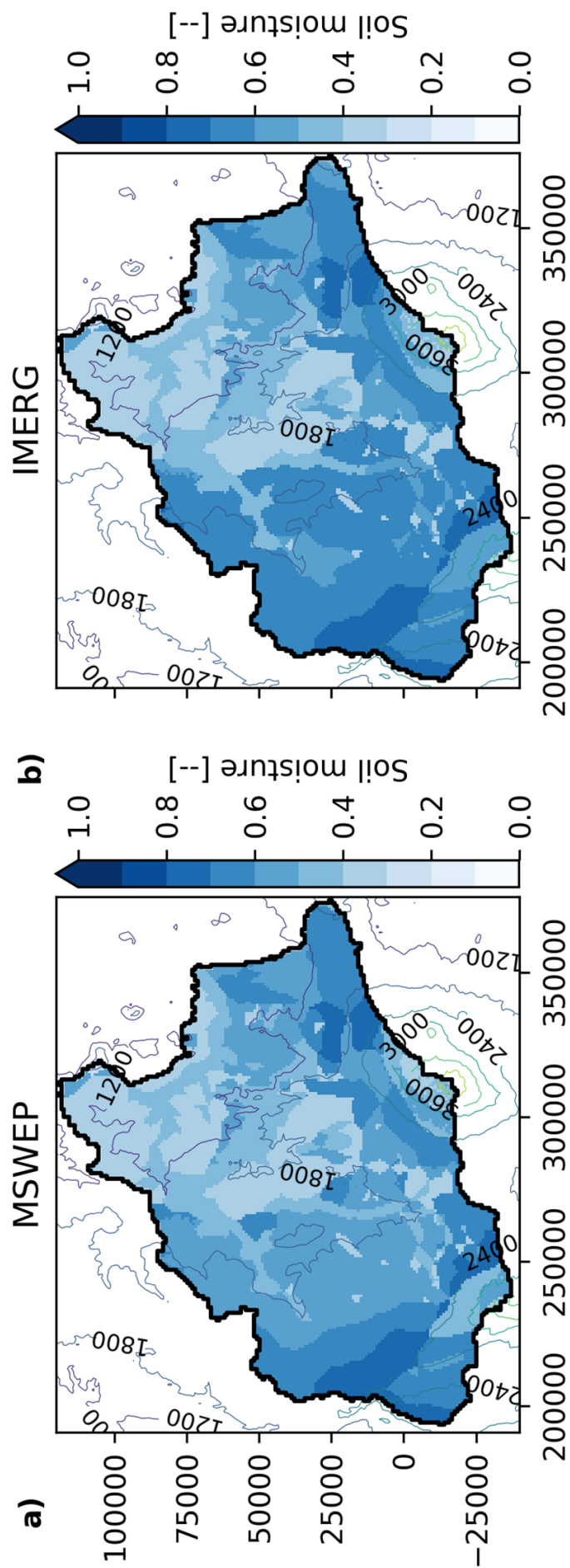


Figure 8.14: Mean annual relative soil moisture and standard deviation estimated from the ensemble of valid simulation using both IMERG and MSWEP precipitation datasets for the Upper Ewaso Ng'iro basin. Contour lines represent surface elevation in meters above sea level. Vertical and horizontal axes are in meters.

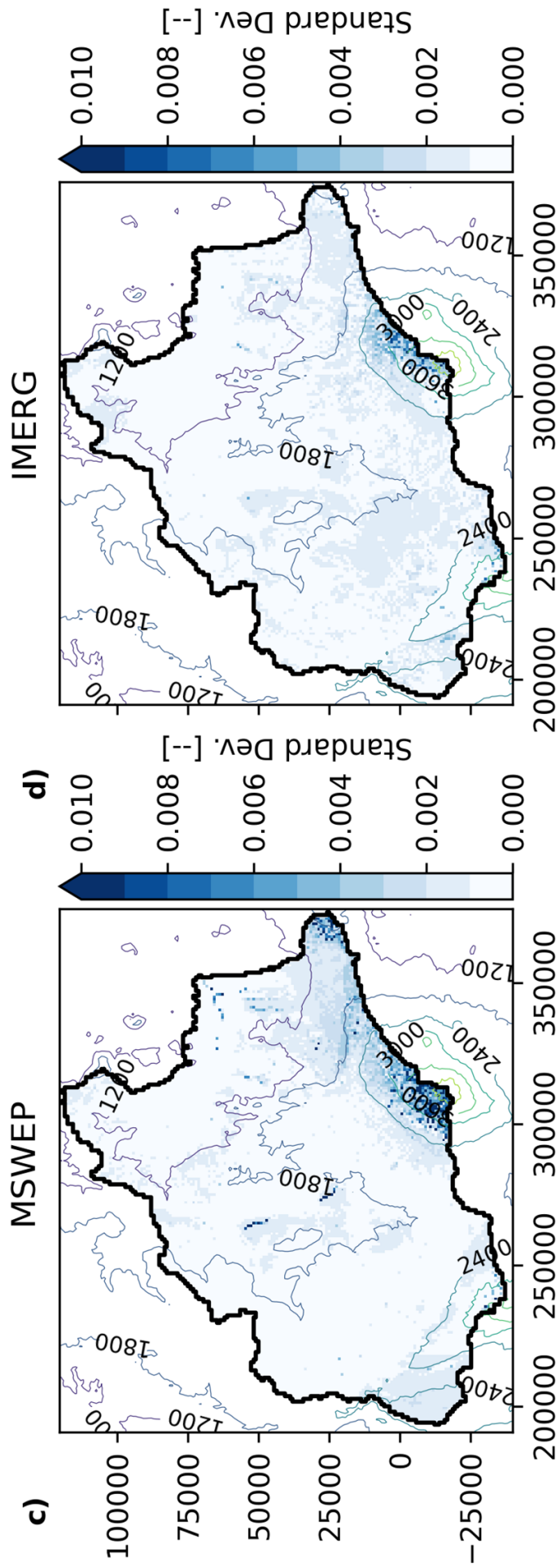


Figure 8.14: Mean annual relative soil moisture and standard deviation estimated from the ensemble of valid simulation using both IMERG and MSWEP precipitation datasets for the Upper Ewaso Ng'iro basin. Contour lines represent surface elevation in meters above sea level. Vertical and horizontal axes are in meters (cont.).

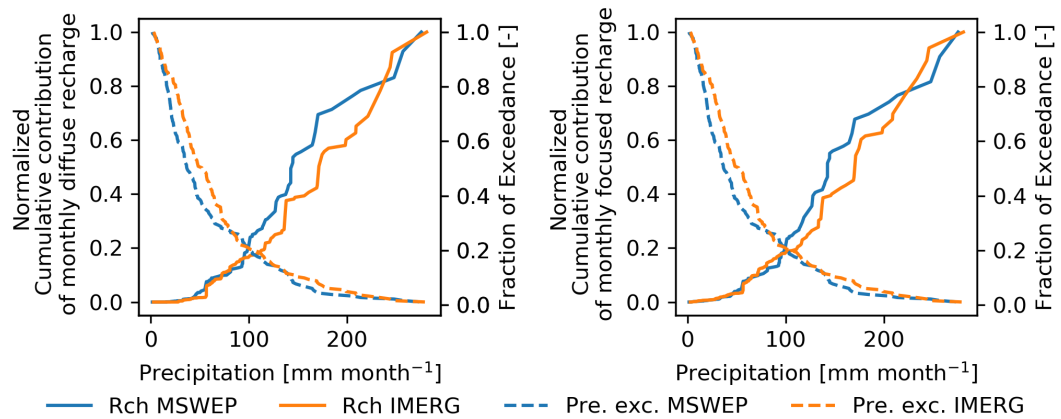


Figure 8.15: Normalised cumulative diffuse (left) and focused (right) recharge in relation to precipitation (solid-lines), and probability of exceedance probability of monthly precipitation events (dashed-lines)

Simulation using IMERG resulted in mean focused recharge of 1.58 mm yr^{-1} , which represents only 3% of the total groundwater recharge.

Regarding the spatial distribution, diffuse recharge follows a similar distribution to precipitation (Fig. 8.16). However, higher uncertainty in recharge rates is also associated with higher recharge rates and consequently higher precipitation rates (Fig. 8.16 bottom panels). For MSWEP-forcing, there are areas where diffuse recharge is negligible, particularly in the Laikipia plateau and lower part of the basin (see Fig. 8.16 left upper panel). For IMERG-forced models, recharge occurs almost everywhere in the basin, although the uncertainty in diffuse recharge estimations using this dataset is higher than when using MSWEP (Fig. 8.16 left bottom panel).

Lorem ipsum dolor sit amet, consectetur adipiscing elit. Ut purus elit, vestibulum ut, placerat ac, adipiscing vitae, felis. Curabitur dictum gravida mauris. Nam arcu libero, nonummy eget, consectetur id, vulputate a, magna. Donec vehicula augue eu neque. Pellentesque habitant morbi tristique senectus et netus et malesuada fames ac turpis egestas. Mauris ut leo. Cras viverra metus rhoncus sem. Nulla et lectus vestibulum urna fringilla ultrices. Phasellus eu tellus sit amet tortor gravida placerat. Integer sapien est, iaculis in, pretium quis, viverra ac, nunc. Praesent eget sem vel leo ultrices bibendum. Aenean faucibus. Morbi dolor nulla, malesuada eu, pulvinar at, mollis ac, nulla. Curabitur auctor semper nulla. Donec varius orci eget risus. Duis nibh mi, congue eu, accumsan eleifend, sagittis quis, diam. Duis eget orci sit amet orci dignissim rutrum. Focused recharge also depends on the spatial and temporal distribution of precipitation, mainly occurring in lower elevation areas where the precipitation is lower and the water table is below the streambed elevation. MSWEP

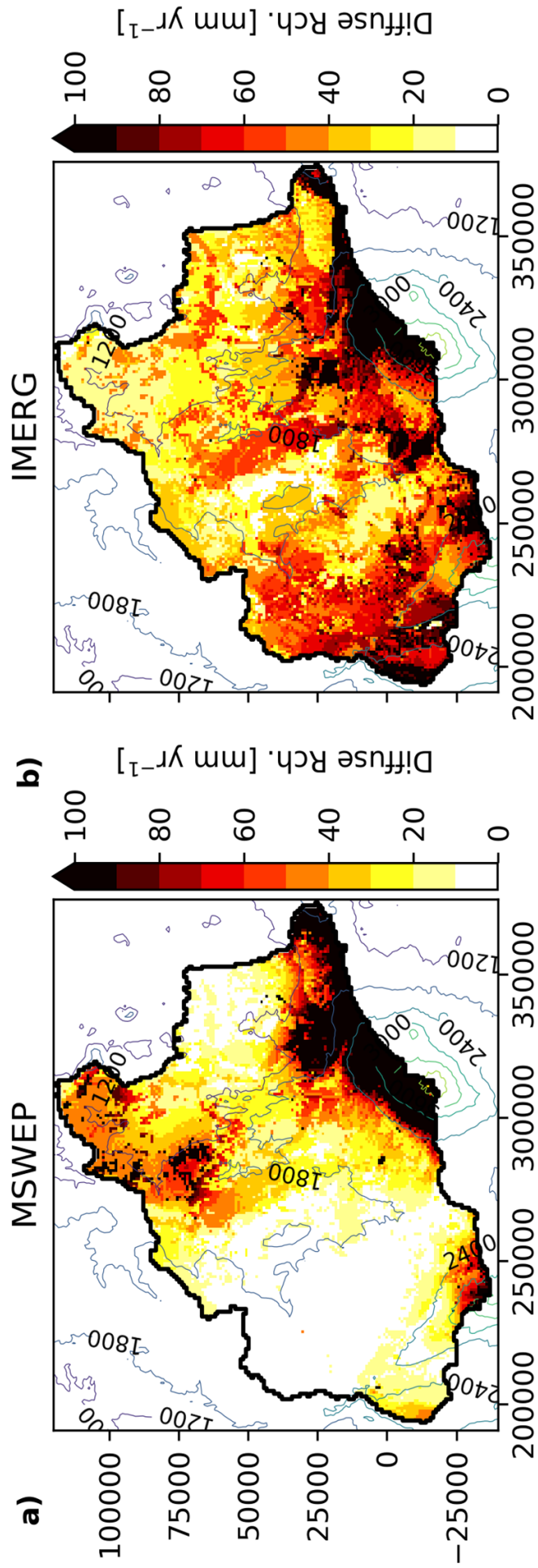


Figure 8.16: Mean annual diffuse recharge and standard deviation estimated from the ensemble of valid simulation using both IMERG and MSWEP precipitation datasets for the Upper Ewaso Ng'iro basin. Contour lines represent surface elevation in meters above sea level. Vertical and horizontal axes are in meters.

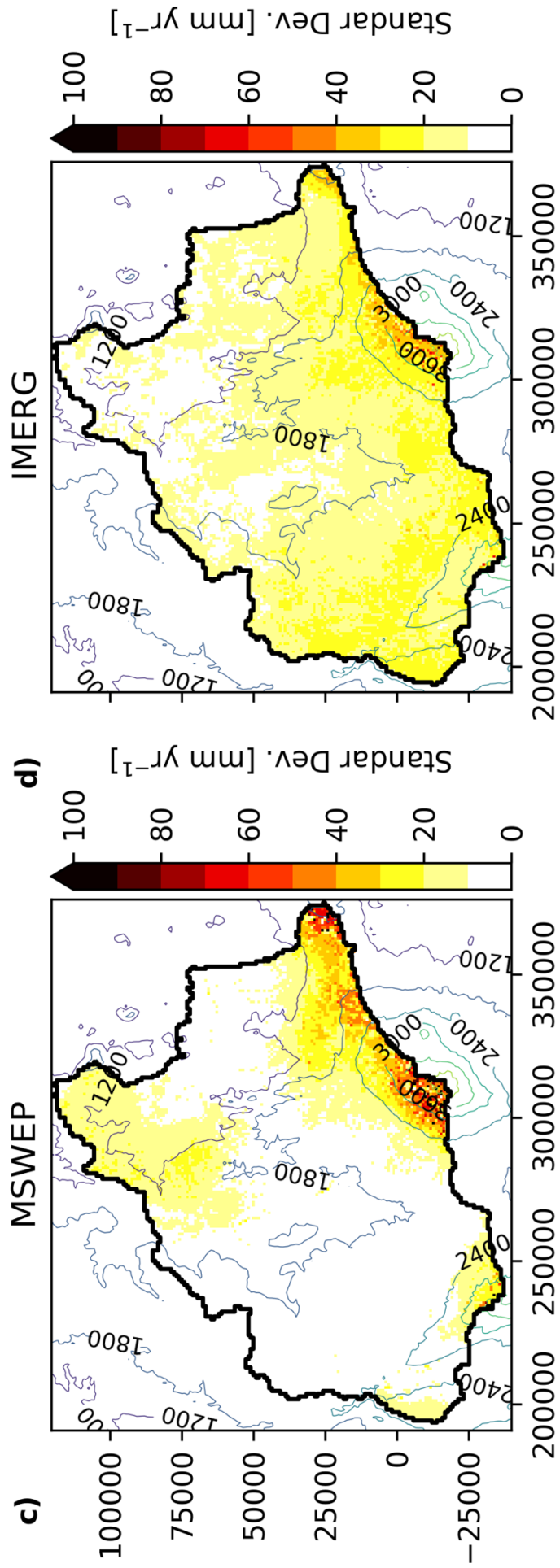


Figure 8.16: Mean annual diffuse recharge and standard deviation estimated from the ensemble of valid simulation using both IMERG and MSWEP precipitation datasets for the Upper Ewaso Ng'iro basin. Contour lines represent surface elevation in meters above sea level. Vertical and horizontal axes are in meters (cont.).

precipitation produces more focused recharge than IMERG (Fig. 8.17a and b) due to the presence of larger areas with water table levels falling below the channel bed. IMERG-forcing, with larger areas of higher rates of annual precipitation, particularly at mid elevations, results in more diffuse recharge and consequently water tables more commonly above the channel stream stage, potentially supporting perennial channels.

The uncertainty of focused recharge varies for both datasets (Fig. 8.17 bottom panels). Since the extent of the area where focused recharge is produced for IMERG dataset is greater than for MSWEP (Fig. 8.17a and b), there is also a higher uncertainty in estimated focused recharge in relation to MSWEP dataset (Fig. 8.17c and d). This higher uncertainty can be mainly attributed to the interaction of the water table with the stream, which is more frequent in IMERG dataset as diffuse recharge greatly contributes to changes in water table depths over larger areas (Fig. 8.16a and b).

Lorem ipsum dolor sit amet, consectetur adipiscing elit. Ut purus elit, vestibulum ut, placerat ac, adipiscing vitae, felis. Curabitur dictum gravida mauris. Nam arcu libero, nonummy eget, consectetur id, vulputate a, magna. Donec vehicula augue eu neque. Pellentesque habitant morbi tristique senectus et netus et malesuada fames ac turpis egestas. Mauris ut leo. Cras viverra metus rhoncus sem. Nulla et lectus vestibulum urna fringilla ultrices. Phasellus eu tellus sit amet tortor gravida placerat. Integer sapien est, iaculis in, pretium quis, viverra ac, nunc. Praesent eget sem vel leo ultrices bibendum. Aenean faucibus. Morbi dolor nulla, malesuada eu, pulvinar at, mollis ac, nulla. Curabitur auctor semper nulla. Donec varius orci eget risus. Duis nibh mi, congue eu, accumsan eleifend, sagittis quis, diam. Duis eget orci sit amet orci dignissim rutrum.

MSWEP and IMERG forcings both show increases in diffuse recharge as AI and precipitation increase (see Fig. 8.18b and d). MSWEP precipitation results in lower mean values for semi-arid and sub-humid areas in comparison to IMERG. This is mainly attributed to the spatial distribution of precipitation and its influence on aridity over the basin, which results in a broader distribution of climatic regions for the IMERG forcing (Fig. 8.19b, top panel).

For MSWEP, focused recharge mainly occurs in semi-arid regions, where less precipitation occurs and where ephemeral streams are developed (Fig. 8.18a). However, most of the water that becomes focused recharge in the semi-arid area of the basin comes as runoff from areas located at higher elevations where large amounts of precipitation falls during the rainy season. IMERG-forced models produce similar re-

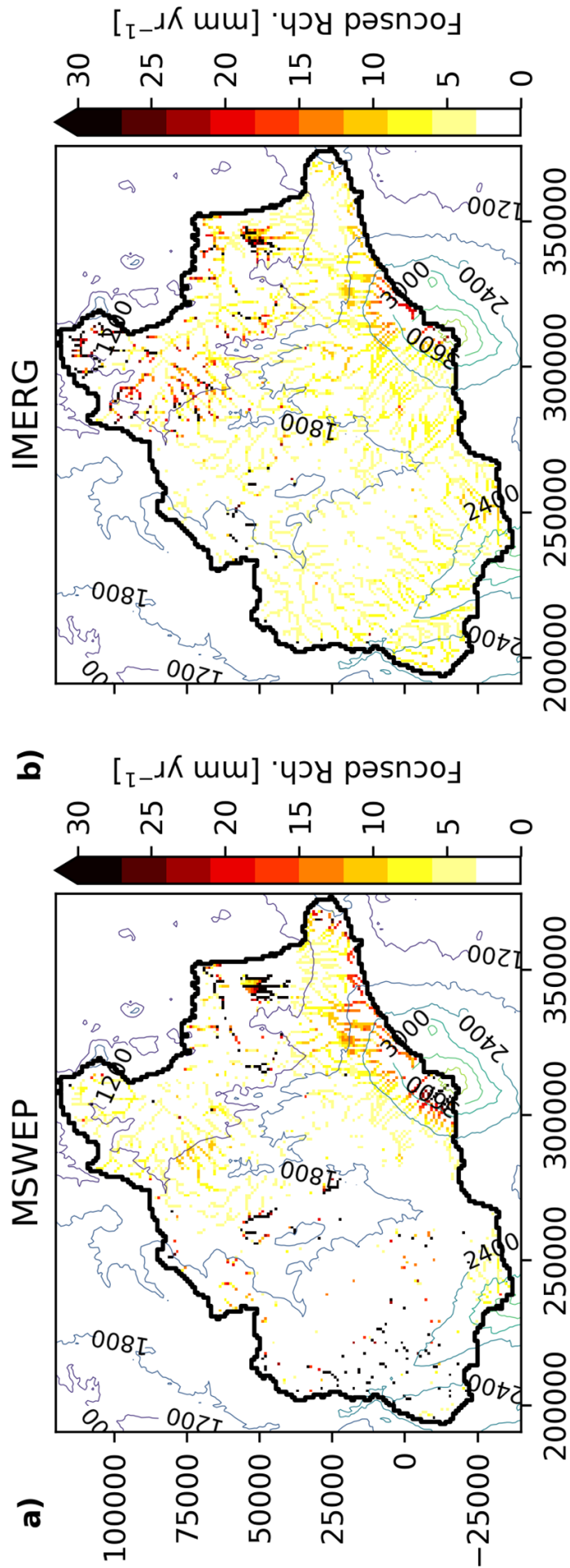


Figure 8.17: Mean annual focused recharge and standard deviation estimated from the ensemble of valid simulation using both IMERG and MSWEP precipitation datasets for the Upper Ewaso Ng'iro basin. Vertical and horizontal axes are in meters.

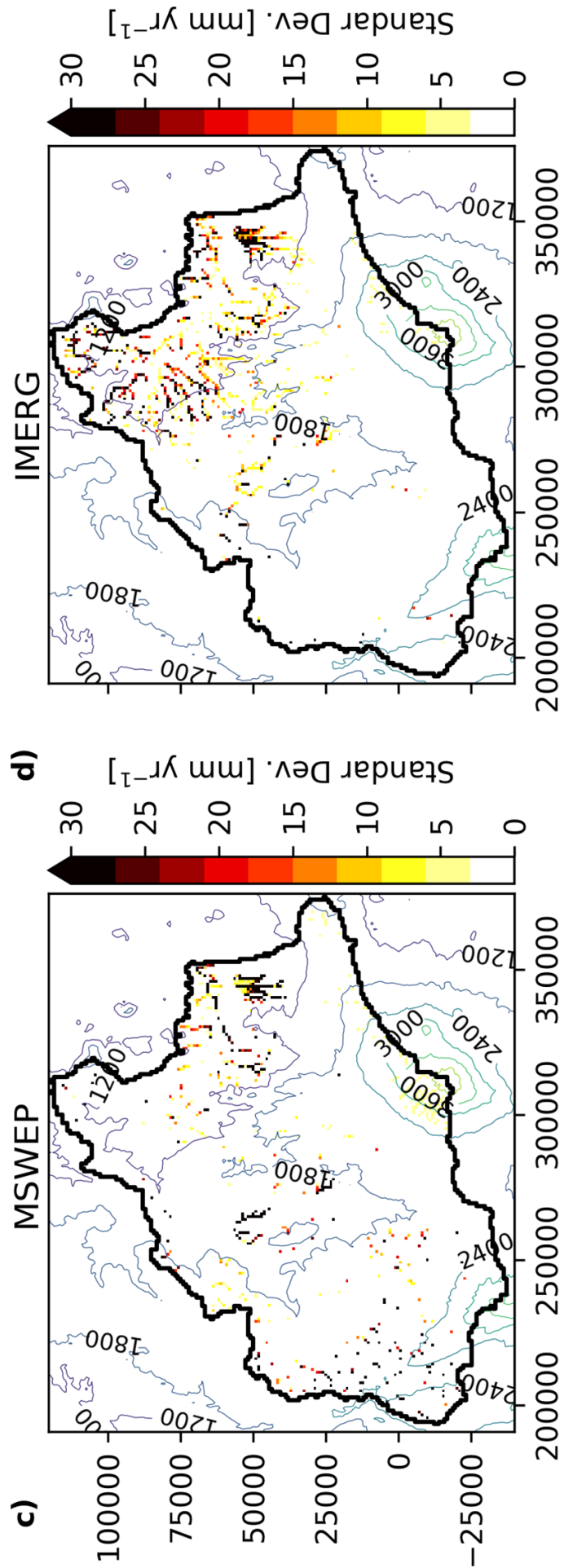


Figure 8.17: Mean annual focused recharge and standard deviation estimated from the ensemble of valid simulation using both IMERG and MSWEP precipitation datasets for the Upper Ewaso Ng'iro basin. Vertical and horizontal axes are in meters (cont.).

sults, with focused recharge mainly occurring in semi-arid areas, yet values of focused recharge are lower than for MSWEP (Fig. 8.18a).

For MSWEP forcing, there is a precipitation threshold at which diffuse recharge becomes dominant of $\approx 600 \text{ mm yr}^{-1}$ or AI greater than 0.35 for both dataset, as can be seen in figure 8.19. This does not occur with IMERG forcing precipitation, where diffuse recharge is the dominant process over the whole basin.

Runoff and channel flow

As expected, the model simulations show that the spatial distribution of precipitation and soil hydraulic properties exert a great control on the distribution of runoff over the basin. Runoff, and consequently streamflow, is mainly generated in the upper parts of the basin where larger amounts of precipitation are delivered (Fig. 8.20). However, part of the runoff produced in the upper part the basin is the result of groundwater discharge as baseflow, where perennial conditions develop (Fig. 8.21). As water flows downstream to the lower parts of the basin, transmission losses reduce the streamflow (see Fig. 8.21), which can eventually result in the development of ephemeral streams when all the flow is consumed by transmission losses.

Overall, DRYP results show that water leaving the basin as runoff represents around 5.1% (40.7 mm yr^{-1}) and 4.8 % (38.1 mm yr^{-1}) for MSWEP and IMERG forced models, respectively. Streamflow for both models is extremely sensitive to extreme precipitation events, which are responsible for high flow conditions (Fig. 8.7e). However, estimated fluxes are sensitive to model parameters, as can be seen in the high uncertainty expressed by the standard deviation of all valid simulations (see bottom panels of Fig. 8.21 and Fig. 8.20).

Lorem ipsum dolor sit amet, consectetur adipiscing elit. Ut purus elit, vestibulum ut, placerat ac, adipiscing vitae, felis. Curabitur dictum gravida mauris. Nam arcu libero, nonummy eget, consectetur id, vulputate a, magna. Donec vehicula augue eu neque. Pellentesque habitant morbi tristique senectus et netus et malesuada fames ac turpis egestas. Mauris ut leo. Cras viverra metus rhoncus sem. Nulla et lectus vestibulum urna fringilla ultrices. Phasellus eu tellus sit amet tortor gravida placerat. Integer sapien est, iaculis in, pretium quis, viverra ac, nunc. Praesent eget sem vel leo ultrices bibendum. Aenean faucibus. Morbi dolor nulla, malesuada eu, pulvinar at, mollis ac, nulla. Curabitur auctor semper nulla. Donec varius orci eget risus. Duis nibh mi, congue eu, accumsan eleifend, sagittis quis, diam. Duis eget orci sit amet orci dignissim rutrum.

Lorem ipsum dolor sit amet, consectetur adipiscing elit. Ut purus elit, vestibulum ut, placerat ac, adipiscing vitae, felis. Curabitur dictum gravida mauris. Nam arcu

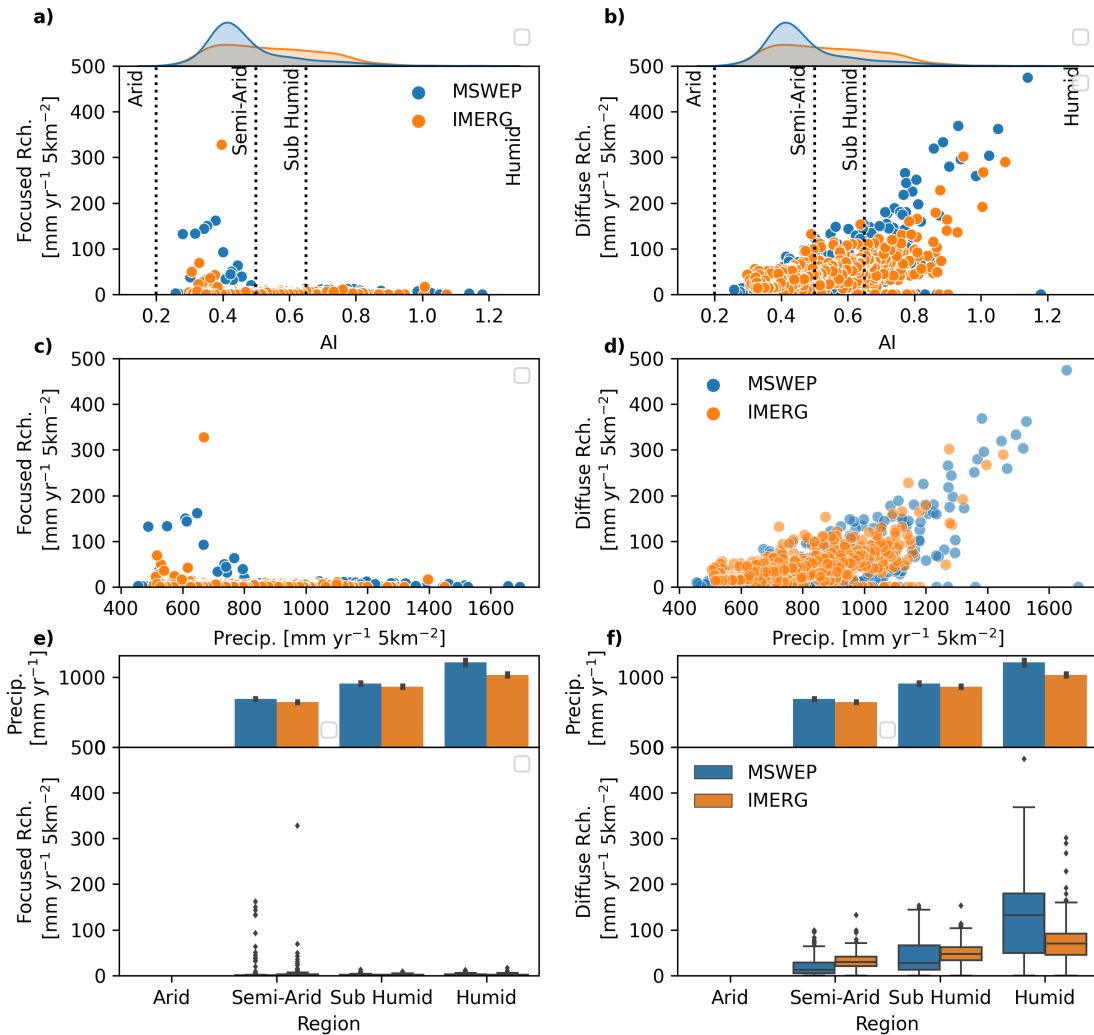


Figure 8.18: Variation of focused and diffuse recharge for the Upper Ewaso Ng'iro basin estimated using MSWEP and IMERG precipitation datasets: a) distribution of AI over the basin (top) and mean annual focused recharge according to AI (bottom); b) distribution of AI over the basin (top) and mean annual diffuse recharge according to AI (bottom); c) focused recharge against surface elevation, d) diffuse recharge against surface elevation, e) annual precipitation according to climatic region (top) and mean annual focused recharge according to AI (bottom); and f) annual precipitation according to climatic region (top) and mean yearly diffuse recharge according to AI (bottom)

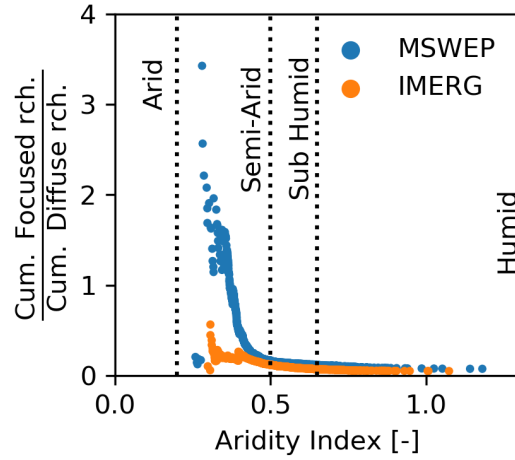


Figure 8.19: Ratio of cumulative focused recharge to cumulative diffuse recharge against aridity index

libero, nonummy eget, consectetur id, vulputate a, magna. Donec vehicula augue eu neque. Pellentesque habitant morbi tristique senectus et netus et malesuada fames ac turpis egestas. Mauris ut leo. Cras viverra metus rhoncus sem. Nulla et lectus vestibulum urna fringilla ultrices. Phasellus eu tellus sit amet tortor gravida placerat. Integer sapien est, iaculis in, pretium quis, viverra ac, nunc. Praesent eget sem vel leo ultrices bibendum. Aenean faucibus. Morbi dolor nulla, malesuada eu, pulvinar at, mollis ac, nulla. Curabitur auctor semper nulla. Donec varius orci eget risus. Duis nibh mi, congue eu, accumsan eleifend, sagittis quis, diam. Duis eget orci sit amet orci dignissim rutrum.

8.3.4 Sensitivity to spatial and temporal distribution of precipitation

Sensitivity of model fluxes to the spatial and temporal variation of precipitation reveals that model uncertainty generally increases with variation in precipitation (see Fig. 8.22). A summary of model performance and water partitioning is shown in Table 8.3. The model calibrated with MSWEP dataset but run with IMERG as forcing dataset, MSWEP_{IMERG}, results demonstrate an increase of the uncertainty in infiltration, runoff, and groundwater recharge (Fig. 8.22) in relation to the MSWEP forcing model. Since higher rates of precipitation are restricted to smaller areas at the top of the basin, lower values of soil hydraulic conductivity are required to produce enough runoff to capture the observed streamflow signature at Archer's Post. This results in lower infiltration rates and consequently lower rates of evapotranspiration.

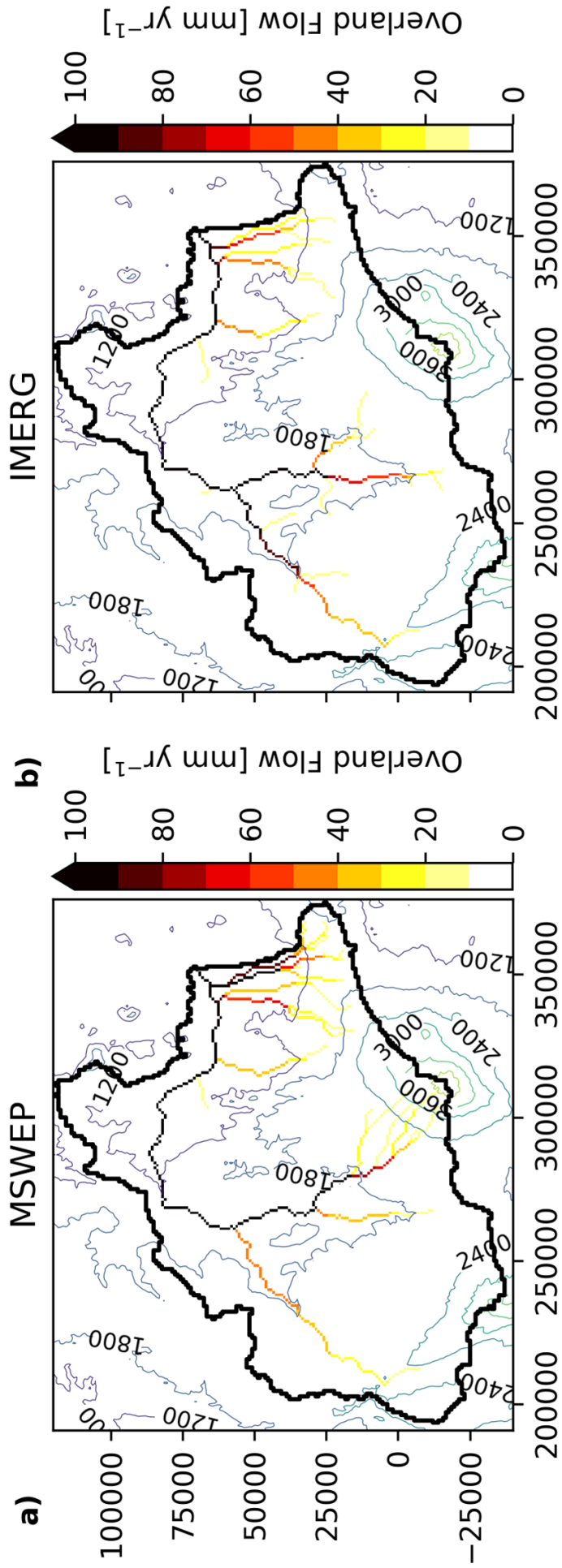


Figure 8.20: Mean annual runoff and standard deviation estimated from the ensemble of valid simulation using both IMERG and MSWEP precipitation datasets for the Upper Ewaso Ng'iro basin. Contour lines represent surface elevation in meters above sea level. Vertical and horizontal axes are in meters.

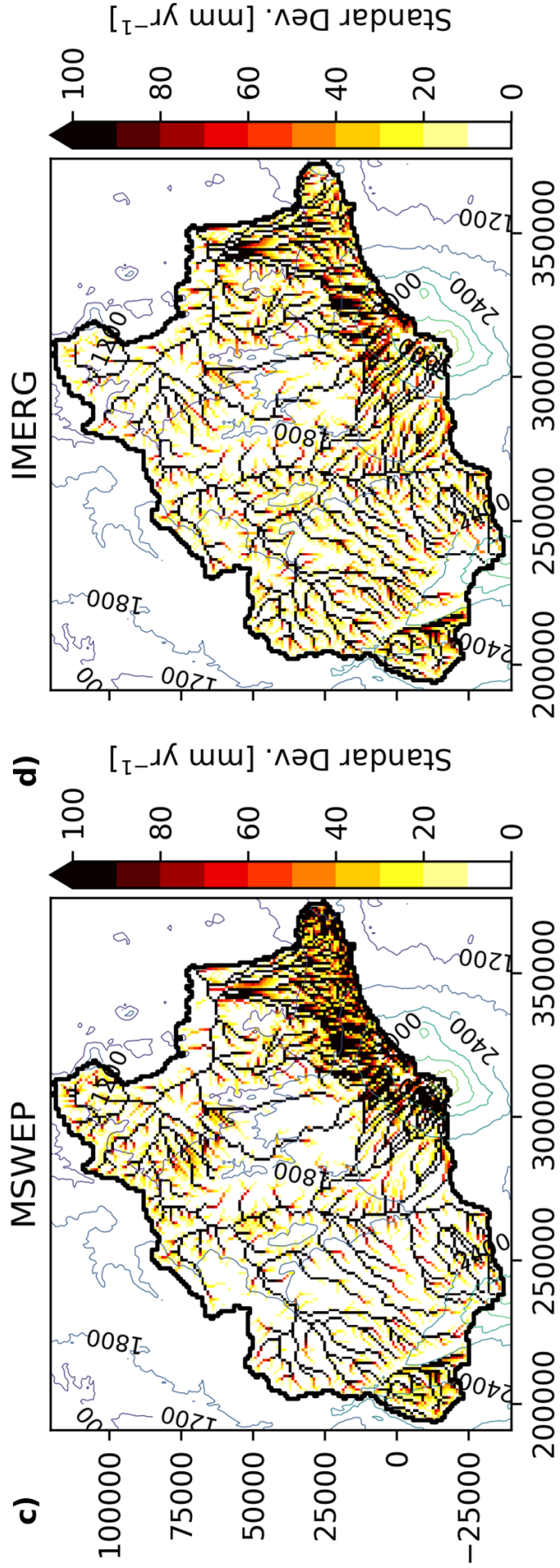


Figure 8.20: Mean annual runoff and standard deviation estimated from the ensemble of valid simulation using both IMERG and MSWEP precipitation datasets for the Upper Ewaso Ng'iro basin. Contour lines represent surface elevation in meters above sea level. Vertical and horizontal axes are in meters (cont.).

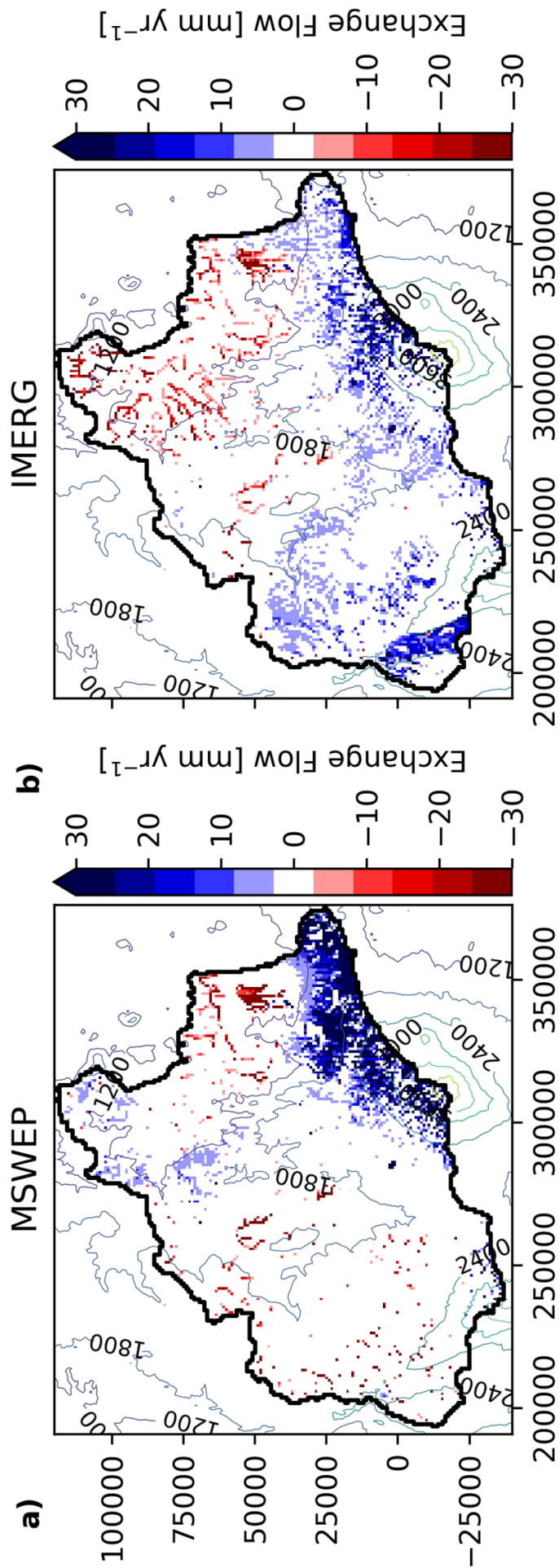


Figure 8.21: Mean annual exchange surface-groundwater fluxes and its standard deviation estimated from the ensemble of valid simulation using both IMERG and MSWEP precipitation datasets for the Upper Ewaso Ng'iro basin. Positive fluxes indicates groundwater discharging into the stream and negative fluxes indicate transmission losses. Contour lines represent surface elevation in meters above sea level.

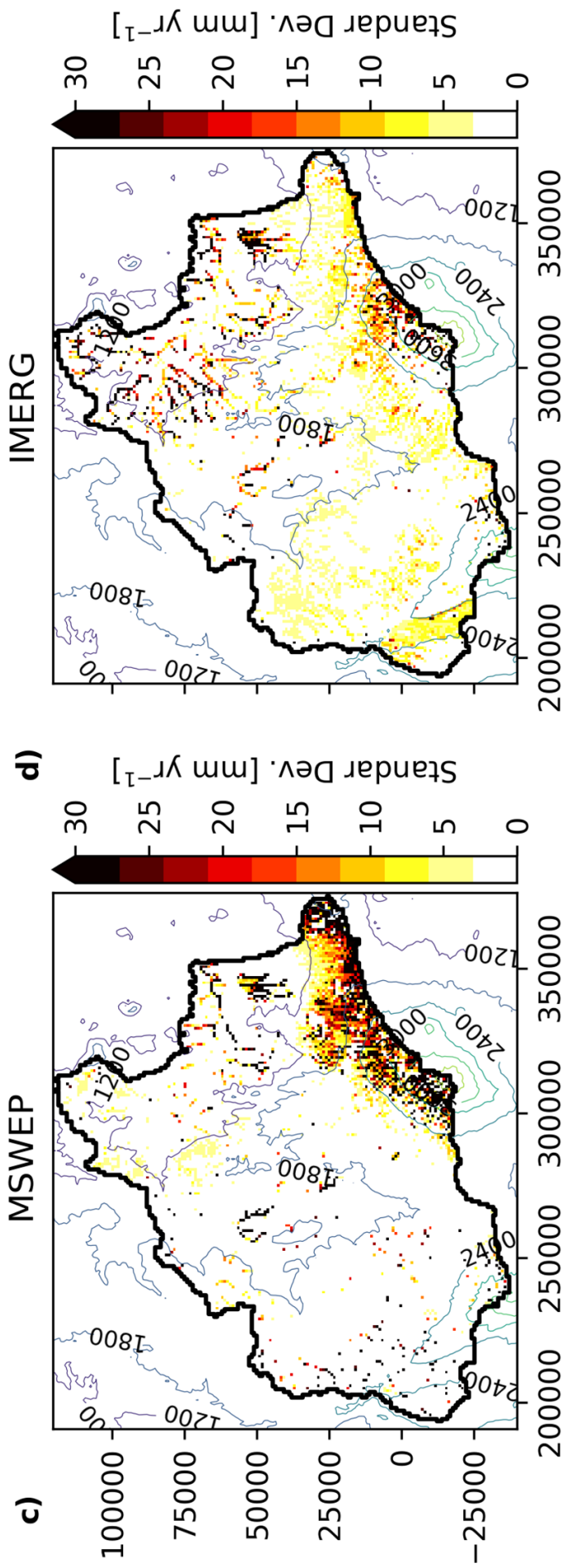


Figure 8.21: Mean annual exchange surface-groundwater fluxes and its standard deviation estimated from the ensemble of valid simulation using both IMERG and MSWEP precipitation datasets for the Upper Ewaso Ng'iro basin. Positive fluxes indicates groundwater discharging into the stream and negative fluxes indicate transmission losses. Contour lines represent surface elevation in meters above sea level (cont.).

Table 8.3: Model performance and water partitioning estimated using both MSWEP and IMERG precipitation datasets for the best models. Parameters for the best models were obtained after calibration using each dataset. Values in brackets represent percentage in relation to precipitation

Calibration forcing	MSWEP		IMERG	
Sensitivity forcing	MSWEP	IMERG	MSWEP	IMERG
Performance				
KGE- runoff [-]	0.70	0.52	0.59	0.66
PBIAS-runoff [%]	3.45	-4.18	-14.49	12.01
Water partitioning [mm yr ⁻¹]				
Precipitation	794.0 (100%)	799.2 (100%)	794.0 (100%)	799.2 (100%)
Infiltration	756.7 (95%)	755.5 (95%)	761.0 (96%)	763.5 (96%)
Actual Evapotranspiration	712.7 (90%)	684.0 (86%)	718.2 (90%)	690.7 (86%)
Total Recharge	62.3 (8%)	73.3 (9%)	60.8 (8%)	77.5 (10%)
Diffuse Recharge	57.8 (7%)	71.4 (9%)	59.4 (7%)	75.1 (9%)
Focused Recharge	4.5 (1%)	1.8 (0.2%)	1.5 (0.2%)	2.3 (0.3%)
Overland Flow	37.2 (5%)	43.8 (5%)	33.0 (4%)	35.8 (4%)
Transmission Losses	9.9 (1%)	0.3 (0.0%)	0.3 (0%)	0.8 (0.1%)
Riparian Evapotranspiration	16.4 (2%)	15.9 (2%)	16.5 (2%)	16.1 (2%)
Runoff	44.2 (6%)	47.7 (6%)	52.4 (7%)	40.3 (5%)

It is also worth noting that transmission losses show lower values than evapotranspiration from the riparian zone. This is because the riparian zone receives water from precipitation in addition to the transmission losses (see Section 5.2.2.2 in Chapter 5). However, there is a difference of $\approx 10\%$ between the MSWEP and IMERG models, with the higher values corresponding to the MSWEP model. It is attributed to the spatial distribution of precipitation which results in a wider area of transmission losses occurring for the MSWEP model, which contrast with groundwater discharge areas occurring in IMERG models (see Fig. 8.21).

It can also be seen in figure 8.22 that similar ranges of evapotranspiration for $MSWEP_{IMERG}$ are observed in IMERG-driven model runs, with mean values $\approx 86\%$ for both $MSWEP_{IMERG}$ and IMERG (Table 8.3). This indicates that the relation between the total actual evapotranspiration and precipitation cannot be attributed to the forcing precipitation datasets, but must be ascribed to the parameters that control water partitioning. Similar results were obtained for diffuse and focused recharge. However, this was not the case for runoff and discharge, which had to increase in order to evacuate all excess water that resulted from low infiltration rates.

Using the IMERG-forced, best model parameters, the uncertainty of MSWEP forcing results in slight variation in distributions of water partitioning for infiltration, evapotranspiration, and groundwater recharge. A narrower distribution was obtained

for overland flow, whereas runoff at the catchment outlet shows a wider distribution when both are compared to those estimated with the IMERG dataset. This can be attributed to higher rates of precipitation infiltrating into the soil, which reduces runoff and consequently discharge at the catchment outlet.

For both models, the use of MSWEP versus IMERG precipitation did not have a great impact on transmission losses, riparian evapotranspiration, or focused recharge. This is because the hydraulic conductivity of the streambed controls the amount of water entering the riparian zone, this resulted in less variability in the amount of water available for evapotranspiration and consequently focused recharge.

8.3.5 Water balance of the Upper Ewaso Ng'iro basin

A summary of the estimated water balance partitioning for the basin is shown in figure 8.22. Considering the lowest and highest values of the 95% confidence interval from all scenarios, approximately 93-97 % of the total precipitation infiltrated into the soil. However, most of this water returned to the atmosphere by evapotranspiration, representing between 83–91 % of the input precipitation. Infiltrated water that percolates to the groundwater compartment producing diffused recharge accounted for 4-10 % of the precipitation. Transmission losses from the stream represent only 0-3 % of the input precipitation. Water contributing to the riparian area as baseflow and transmission losses is partitioned into evapotranspiration, representing ≈ 2 % (± 0.1), and focused recharge, representing 0-1 %. Finally, water leaving the basin as runoff represented 3-7% of the input precipitation.

8.4 Conclusion

Water partitioning of the Upper Ewaso Ng'iro basin has been estimated using the hydrological model, DRYP, calibrated using streamflow observations at the catchment outlet. The model was also evaluated by comparing model results with the remote sensing products: MODIS for evapotranspiration, ESA-SM for soil moisture, and GRACE for total water storage anomalies. The influence of the uncertainty of precipitation on water balance partitioning was evaluated by considering two global-scale datasets, MSWEP and IMERG, whereas uncertainty of model structure was evaluated by performing a Monte Carlo analysis of model parameters. Although the number of simulations for the analysis was restricted to 200, nevertheless, it gives insight of water partitioning of the study area. Thus, the following general conclusions can be drawn from the analysis:

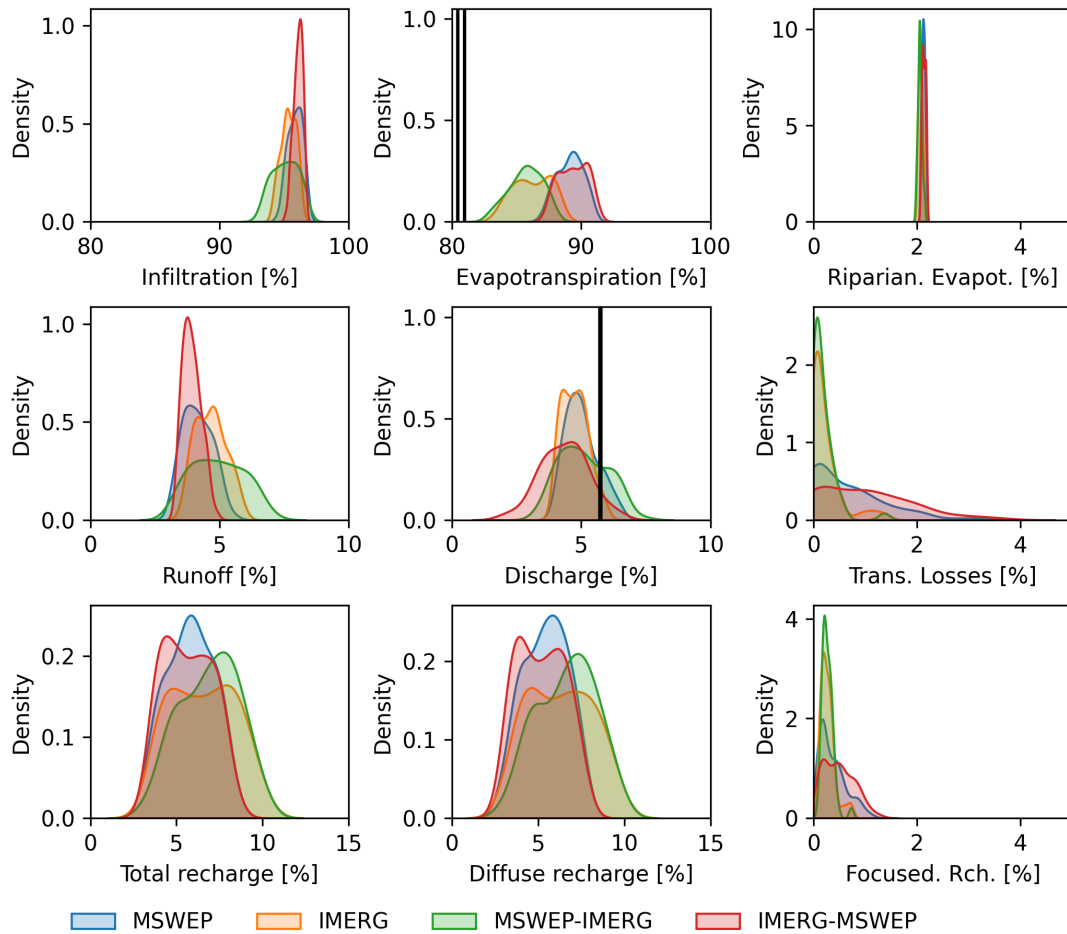


Figure 8.22: Distribution of percentages of main fluxes of the water balance in relation to the input precipitation for the Upper Ewaso Ng'iro basin. Estimated values correspond to valid models for the scenarios specified in Section 8.2.11 (Fig. 8.4) using MSWEP and IMERG datasets. Black lines in evapotranspiration and discharge corresponds to MOD16A AET validation dataset and observed streamflow at Archer's Post station (see Fig. 8.1), respectively.

- DRYP can provide reliable estimations of key components of the water balance in dryland regions, even in climatically, topographically and geologically diverse, data-sparse environments, using only readily available regional-global datasets for parameterisation and forcing.
- owing to the parsimonious structure and low computational demand, the uncertainty of DRYP water balance estimates can be evaluated by performing a Monte Carlo analysis. This is of key importance to constrain and understand the key factors controlling the water partitioning in dryland regions.

Regarding the study site, the following specific conclusions can be drawn from the analysis:

- available large-scale precipitation datasets show contrasting spatial variability over the basin, despite having a small variation in annual average values (less than 10 mm yr^{-1}). MSWEP has higher annual precipitation than IMERG, which translates to marked differences in the modelled water balance of the Upper Ewaso Ng'iro basin. MSWEP concentrates high precipitation in the Mt. Kenya and Nyanbene Hill Peak (East of Mount Kenya), whereas IMERG has a highly linear relation with the topography, which translates in less spatial variability over the basin with high annual precipitation located at Mt. Kenya and the Aberdare Range (southwest of the basin).
- the spatial variability of precipitation greatly impacts modelled infiltration, evapotranspiration, and recharge. Actual evapotranspiration is high, representing more than 90 % of the precipitation. However, it varies spatially following the spatial distribution of precipitation with rates decreasing as elevation decreases.
- groundwater recharge in the basin is dominated by diffuse recharge mechanisms. However, the spatial distribution of recharge depends on the distribution of precipitation. Thus, high rates of diffuse recharge occur in humid areas where yearly precipitation rates are high. In contrast, focused recharge dominates in lower semi-arid areas where diffuse recharge becomes almost negligible. For MSWEP, precipitation $< 600 \text{ mm yr}^{-1}$ ($\text{AI} < 0.37$) represents the threshold below which focused recharge become the dominant process. These results highlight the importance of focused recharge processes as an important source of recharge in dryland regions.

- availability of groundwater in the lower, semi-arid parts of the basin depends on local focused recharge associated with transmission losses from streamflow coming from high elevations where runoff is high. It also depends on groundwater flow from upper parts of the basin where groundwater is diffusively recharged.
- The magnitude and frequency of extreme precipitation events controls the amount of groundwater recharge produced over the basin. High monthly precipitation events, with 20% exceedance (i.e. $>100 \text{ mm yr}^{-1}$), are responsible for up to 80 % of groundwater recharge.

In this context, modelling results from DRYP not only provide an enhanced understanding of water partitioning in the Upper Ewaso Ng'iro basin, but also provide some insights into the transferability of parameters and model processes to other regions, thus:

- based on DRYP simulations, the MSWEP precipitation dataset shows a better representation of the spatial and temporal variability of the precipitation, resulting in improved skill in DRYP to represent evapotranspiration, soil moisture, streamflow, and total water storage over the basin. Therefore, the use of MSWEP data should be considered for quantifying water partitioning in similar dryland regions.
- global datasets of soil and aquifer properties, although having great uncertainty and coarse resolution, seem to capture useful spatial information that allows for good characterisation of hydrological processes in drylands, regions typically characterised by limited data availability.

Finally, the present analysis shows an improved representation and description of key processes in dryland regions that should be included in large-scale models. This is the first step to reduce the currently high uncertainty of the impact of future climate change in dryland groundwater resources. Including processes such as transmission losses and focused recharge in dryland regional models will aid understanding of the spatial and temporal availability of surface and groundwater resources, as well as the potential impacts of anthropogenic activities on water resources.

Chapter 9

Conclusions & Outlook

This thesis aimed to enhance understanding and quantification of water partitioning and flow pathways in dryland regions. To this end, a series of numerical simulations were performed in order to address the main objectives defined at the beginning of the thesis (Chapter 1). First, a characterisation of the potential groundwater - surface water interactions in ephemeral streams in 2D and 3D in dryland regions was presented (Chapters 3 and 4, respectively). Then a new parsimonious model, DRYP, was developed in order to quantify water partitioning at the catchment scale within dryland regions (Chapter 5). The ability of DRYP to accurately represent the water partitioning and the water balance at different spatial and temporal scales (Chapter 6 and 7) was then evaluated for the data-rich Walnut Gulch Experimental Watershed in Arizona, USA. Finally, DRYP was applied to the semi-arid Upper Ewaso Ng'iro basin in Kenya to address the challenges of estimating water partitioning in data-scarce dryland regions (Chapter 8). Based on the main objectives presented in Chapter 1, the main conclusions are presented below.

9.1 Conclusions

Objective 1: Enhancing understanding of groundwater - surface water interactions in ephemeral streams

Understanding the main factors that control water partitioning in ephemeral streams allows for the characterisation and parameterisation of transmission losses and focused recharge (Chapter 3 and 4). The spatial and temporal variability of transmission losses controls the availability of water below the channel and consequently focused recharge. This variability needs to be included in hydrological models in order to

capture the critical contribution of these processes to the water balance of a dryland basin.

This work challenges the use of the terms *connected* and *disconnected* to characterise groundwater - surface water interactions in ephemeral streams because they are inherently misleading regarding the interpretation of groundwater - surface water (SW-GW) interactions in ephemeral streams. Specifically, the use of the term 'disconnected streams' neglects the potential feedback of groundwater changes on infiltration rates from streams. Therefore, it is recommended the use of the terms bi-directional and unidirectional SW-GW interactions, which acknowledges the hydraulic interactions and feedbacks between the water table position and stream losses.

This aspect is of particular interest in the context of the impact of climate change and anthropogenic activities on the availability and sustainability of water resources. Natural or human-induced changes in water table depth are likely to influence the infiltration rates within ephemeral streams, and would in turn affect the availability of water in streams as well as recharge of aquifers. Positive feedbacks on infiltration rates are expected when water table depth is high whereas negative feedbacks will be expected when the water table is low. These new insights are important for robust future water resource decision making in dryland regions.

Climate variability, expressed in the spatial and temporal variation of precipitation, is likely to affect the distribution of surface water and consequently groundwater. Short and high-intensity precipitation events will impact the production of runoff and consequently, streamflow in channels. Given that infiltration through the streambed controls the availability of water along the channel, short but high streamflow events will result in more water available at downstream locations, whereas long but low magnitude streamflow events will result in less water available downstream due to more water being infiltrated at upstream locations (Chapter 4). Such spatial discontinuities between water production in the landscape and subsequent water availability to plants and society are particularly acute in drylands.

Objective 2: Development of a parsimonious model to quantify water partitioning in dryland regions

To quantify the contribution to water partitioning and flow pathways of transmission losses and focused recharge in combination with hydrological processes and their spatial and temporal variability, the parsimonious DRYland water Partitioning model, DRYP, was developed (Chapter 5). DRYP is a spatially distributed model that

represents variability in climatic forcing and its impact on the overall catchment water balance. It includes a component to estimate transmission losses and focused recharge from ephemeral streams, a key process of the water balance in dryland regions.

DRYP provides an improved representation of hydrological processes that will support better understanding of surface and groundwater processes, as well as quantification of water balance fluxes and stores. Given that DRYP explicitly integrates hydrological processes at the surface, subsurface and groundwater components, it enables the evaluation of the hydrological behaviour of dryland environments based on well understood conceptual models. Based on rigorous evaluation, DRYP can be considered as an efficient model to investigate and anticipate the impact of climate variability on dryland groundwater resources.

Objective 3: Assessing the sensitivity of water partitioning to the spatial and temporal scale of process description

In general, the high spatial and temporal variability of hydrological processes in dryland regions is well represented by DRYP. The model shows a good skill in representing water partitioning at and near the land surface. At WGEW, the estimation of the main components of the water balance by DRYP agrees well with the set observations available for the basin (Chapter 6). Thus, despite its simplicity and parsimonious structure, model simulations result in an accurate representation of groundwater - surface water interactions. The model captures well the development of ephemeral streams and the production of focused recharge and its contribution to the groundwater aquifer in the basin. It is shown that transmission losses represent around 7% of the yearly total precipitation, which considerably reduces the flow in channels, thus increasing the amount of water in the subsurface riparian zone. Water entering the riparian area is considerably reduced by high evapotranspiration, at rates near or at the full potential based on evaporative demand in the atmosphere, representing around half the transmission losses. Water that is not stored in the riparian zone, percolates to the aquifer and produces focused recharge. Diffuse recharge in the basin is very low (<0.03 %), which makes focused recharge the dominant mechanism of groundwater recharge in the basin, consistent with my perceptual understand of dryland catchments, and highlighting the potential importance of DRYP.

A multi-scale analysis of the performance of DRYP in the WGEW shows that variations in scale (both spatial and temporal) greatly impact water balance components and fluxes (Chapter 6). High spatial and temporal resolution (≤ 1 km and < 1 day)

improve the performance of the model for representing the magnitude and number of streamflow events, evapotranspiration, recharge, and soil moisture. In contrast, lower spatial and temporal resolutions result in lower performance and the misrepresentation of the water balance, i.e. diffuse recharge increases and focused recharge decreases as the spatial and temporal resolution decreases; although soil moisture and actual evapotranspiration are less sensitive to temporal and spatial resolution. The analysis also revealed that decreasing the temporal resolution of the climatic forcing data, from sub-hourly to weekly, results in the underestimation of streamflow, suggesting the importance of capturing short-term precipitation regimes. Overall, the spatial resolution of the model affects the spatial and temporal distribution of water along the stream, particularly as contributing areas of sub-basins change at different spatial resolutions.

It is therefore of key importance for accurately representing the water partitioning in drylands to choose an appropriate scale of the model for any basin. It is even more important in the context of climate change, where the spatial and temporal variability of precipitation events will result in variations of runoff production and consequently groundwater recharge. Short and high magnitude streamflow events will result in focused recharge being distributed over long distances along the channel, which will impact the availability of groundwater, increasing groundwater in downstream areas. This may result in areas prone to flooding conditions for shallow water tables, and less groundwater available at upstream locations. How it will affect the overall availability of groundwater at basin scale is still unknown and more research is needed to understand and predict the impacts of climate change on water distribution through dryland catchments. DRYP is the ideal tool for such future work.

Objective 4: Gaining insights into the best way to approach estimating water balance partitioning in dryland basins with limited data

The model was applied at a larger scale ($\approx 15,000 \text{ km}^2$), at the Upper Ewaso Ng'iro basin, Kenya, in which DRYP demonstrated skill at capturing the water partitioning in the basin, despite the coarse data available in the area (Chapter 8). The analysis further highlighted the importance of focused recharge in dryland regions, a recharge mechanism that eventually becomes dominant in relation to diffuse recharge as the degree of dryness increases into the semi-arid to arid transition. The analysis also highlighted the boundary condition effect of humid regions in basins that span a variety of climatic conditions. In the Upper Ewaso Ng'iro basin, the humid area

located at the highest elevations supplies water to the lower arid and semi-arid areas of the basin, so boundary condition specification is critical in such cases. Results were in agreement with the current understanding of the controls of groundwater recharge, particularly for dryland regions (Cuthbert et al. (2019b)), suggesting (again) that DRYP may be a valuable tool for improving the quantification of water partitioning in dryland regions, even where data is scarce. Thus, DRYP can be used to assist decision makers to better evaluate the availability of water resources in dryland regions by providing an improved representation and quantification of the main components of the water balance. DRYP can also be used to evaluate the impact of climate change on groundwater resources in arid and semi-arid environments where focused recharge is the main source of groundwater recharge.

These results also highlight the use of readily available regional and global data of soil and aquifer properties. Despite high uncertainty and coarse resolution, these datasets capture useful spatial information that allows a better characterization of hydrological processes in drylands simulated by DRYP. Therefore, these datasets are a viable alternative to high resolution in situ data for parameterising large scale models, which in combination with DRYP can provide reliable estimations of the water partitioning in dryland regions.

Objective 5: Assessing the sensitivity of water partitioning to the forcing climatic conditions

Although the uncertainty of global datasets of climatological variables of precipitation and potential evapotranspiration is still high, my results show that the MSWEP V2 Global 3-Hourly 0.1° dataset has a more accurate representation of the spatial and temporal variability of the precipitation in relation to IMERG, particularly in areas with orographic precipitation, in the semi-arid Upper Ewaso Ng'iro basin, Kenya (Chapter 8). This basin is characterised by a variety of climatic conditions that makes it difficult to describe the hydrological behaviour without the use of a high-resolution precipitation dataset. Thus, using MSWEP and hPET as forcing data into DRYP resulted in a good representation of various water balance components including evapotranspiration, soil moisture, streamflow, and total water storage over the basin. Therefore, MSWEP may be a useful forcing dataset to characterise water partitioning in similar dryland regions.

9.1.1 Summary of the main outputs

A summary of the key conclusions of the thesis is presented below:

- In an ephemeral streams, for a given streamflow event, the initial saturation conditions, the hydraulic conductivity of the sediments, and the water table depth all provide strong controls on the infiltration rates lost from the stream.
- Deeper water tables combined with longer dry periods and higher hydraulic conductivity increase the amount of infiltrated water; the opposite occurs when these parameters decrease.
- Infiltration rates vary non-linearly with water table depth, although they become constant, dependent on the local conditions, when a threshold in the water table depth is reached.
- Longer streamflow events, characterised by longer residence times, in combination with deep water tables, can more quickly reduce the streamflow along the channel, resulting in complete loss of inflows and dry channels over shorter distances from the source point. For a homogeneous aquifer with hydraulic properties corresponding to a sandy loam material, the threshold for a 7-day streamflow event (with a 1 day peak) is reached for water table depths greater than approximately 10 meters.
- The contribution of early infiltration during the onset of a streamflow event (rising limb) can reach up to 25 % of the total infiltration. However, this contribution is reduced to 6 % for longer residence times ($T = 9$ d). Hence, for working at larger scales, in many instances, it may be reasonable to simplify the infiltration rate to a steady rate during an event.
- Groundwater – surface water interactions should be referred to as hydraulically unidirectional or bi-directional, instead of “connected” or ‘disconnected’, depending on the relative extent of hydraulic feedback given by groundwater to stream losses.
- Global comparisons of water depth and ephemeral stream networks (although rather uncertain) show that potential losses from a large percentage of dryland streams may be sensitive to changes in water table depths. Feedbacks between rates of recharge and changes in water table depths due to, for example, climate

change or pumping may have important implications for the availability and consequently, management of water resources in dryland regions.

- The parsimonious Dryland water partitioning model, DRYP, has shown good skill for producing behavioural simulations that match observed phenomena. Thus, DRYP is demonstrably effective and allows the characterisation of the spatio-temporal variation in the main components of the dryland water balance. DRYP also showed a good performance under different climatic, topographical and geological conditions.
- At a catchment scale, in the Walnut Gulch Experimental Watershed, evapotranspiration is the dominant process comprising ≈ 90 % of water leaving the catchment. It was found that focused recharge is the major contributor to groundwater recharge with ≈ 2.5 % the total amount of rainfall whereas diffuse recharge is below 0.03 %. The analysis also showed that evapotranspiration from riparian areas may considerably reduce (up to 60 %) the amount of water entering the riparian zone as transmission losses.
- A multi-scale analysis showed that estimates of actual evapotranspiration and soil moisture are better simulated by a larger range of models than streamflow discharge.
- Owing to the trade-offs between runoff generation and transmission losses leading to equifinality in simulating flow at a particular flow gauge, estimates of transmission losses are highly uncertain without additional observational constraints from multiple flow gauges.
- The water partitioning is highly sensitive to the spatial and temporal scales. In general, in order to capture the main characteristics of the streamflow and focused recharge components of the water balance, a high temporal resolution (<1 day) of rainfall forcing is required for model simulations. In contrast, soil moisture and AET are much less sensitive to larger aggregations of rainfall forcing above 1 day.
- DRYP can provide reliable estimations of key components of the water balance in dryland regions, even in climatically, topographically and geologically diverse, data-sparse environments, using only readily available regional-global datasets for parameterisation and forcing.

- For the Upper Ewaso Ng'iro basin, a comparison of the model performance using two global datasets of precipitation, MSWEP and IMERG, showed that the spatial and temporal distribution of precipitation greatly impact the variability of surface and groundwater processes, despite having a small variation in annual average values (less than 10 mm yr^{-1}).
- Also for the Ewaso Ng'iro basin, high rates of diffuse recharge occur in humid areas where yearly precipitation rates are high. In contrast, focused recharge dominates in lower semi-arid areas where diffuse recharge becomes almost negligible. A precipitation of $>600 \text{ mm yr}^{-1}$ ($AI < 0.37$) represents the threshold below which focused recharge become the dominant process.
- The availability of groundwater in the lower, semi-arid parts of the Ewaso Ng'iro basin depends on local focused recharge associated with transmission losses from streamflow coming from high elevations where runoff is high. It also depends on groundwater flow from upper parts of the basin where groundwater is diffusively recharged.
- The magnitude and frequency of extreme precipitation events control the amount of groundwater recharge produced over the basin. High monthly precipitation events, with 20 % exceedance (i.e. $\approx 100 \text{ mm yr}^{-1}$), are responsible for up to 80 % of groundwater recharge.

9.2 Directions for future work

Enhancing understanding and quantification of water partitioning in dry-land regions

The potential degree of groundwater - surface water interactions along streams may have a great impact on water partitioning at regional and global scales. Estimated water table depths at global scales, although highly uncertain, show that losing streams with shallow water table depths are widely distributed over the globe (Fan et al., 2013). Recharge from these streams is sensitive to changes in water table depths, but has not yet been evaluated. In this context, given that DRYP considers groundwater - surface water interactions, the potential effect on groundwater due to focused and diffuse recharge can be evaluated by the model. However, the degree of groundwater - surface water interaction depends on various factors including the geometry of the channel. Information about channel geometry at regional or global scale is

only available for large river networks. Therefore, in order to better describe the impact of water partitioning in ephemeral streams, information about geometrical characteristics of the channel needs to be included as these data become available.

The use of remote sensing as well as data assimilation techniques may also improve the characterization of groundwater - surface water interactions. Data assimilation techniques have already been successfully used for improving the performance of hydrological models, and their implementation into DRYP could potentially increase the performance of the model. Additionally, although it has not been yet developed at large scales (Walker et al., 2019), using remotely sensed data, such as Sentinel-2 at the spatial resolution of 10m, to identify open water features such as large ephemeral streams, could greatly enhance the ability of DRYP to characterise groundwater - surface water interactions.

The dynamic behaviour of vegetation in dryland regions may have a great impact on water partitioning. Thus natural and/or induced changes in vegetation and land cover may also influence the availability of water resources in dryland regions. This is even more important when the demand for direct or indirect water-related resources increases as a result of the increasing population. This will put more pressure on the already stressed ecosystems and will threaten the sustainability of water resources. Therefore, in order to enhance the understanding of water partitioning in drylands, the dynamic behaviour of vegetation needs to be included, especially in riparian zones.

Using DRYP to reduce the uncertainty of climate change

There is an urgent need for improving the quantification of the availability of water resources, particularly in dryland parts of Africa, where the lack of reliable information has restricted their quantitative assessment. In particular, enhancing understanding of water partitioning by evaluating the role of processes such as transmission losses and focused recharge is of key importance, particularly for managing groundwater resources which are the main source of fresh water in dryland regions.

Although results in the Upper Ewaso Ng'iro basin are promising, there is still a lot of uncertainty in the parameterisation of the model, particularly of the saturated zone, which currently prevents a better evaluation of the availability of the water partitioning. This is important given the increasing demand for fresh water and the lack of surface water, which will likely result in more groundwater being depleted. Therefore, a better representation of these critical parameters will allow the evaluation

of the sustainability of surface and groundwater resources. It will also allow a better understanding of groundwater-related problems such as subsidence, groundwater contamination and salinisation, and impacts to groundwater dependent ecosystems. Ultimately, shallow and deep aquifers both need to be represented in the model, in addition to a better characterisation of the aquifer hydraulic behaviour.

References

- Abbot, M. (1979). Computational Hydraulics: Elements of the theory of free surface flows. *Pitman, London*.
- Abdulrazzak, M. J. (1995). Losses of flood water from alluvial channels. *Arid Soil Research and Rehabilitation*, 9(1):15–24.
- Abdulrazzak, M. J. and Morel-Seytoux, H. J. (1983). Recharge from an ephemeral stream following wetting front arrival to water table. *Water Resources Research*, 19(1):194–200.
- Acworth, R. I., Rau, G. C., Cuthbert, M. O., Leggett, K., and Andersen, M. S. (2021). Runoff and focused groundwater-recharge response to flooding rains in the arid zone of Australia. *Hydrogeology Journal*, 29(2):737–764.
- Aeschbacher, J., Liniger, H., and Weingartner, R. (2005). River Water Shortage in a Highland–Lowland System. *Mountain Research and Development*, 25(2):155–162. Publisher: International Mountain Society.
- Aguilar, A. L., Flores, H., Crespo, G., Marín, M. I., Campos, I., and Calera, A. (2018). Performance Assessment of MOD16 in Evapotranspiration Evaluation in Northwestern Mexico. *Water*, 10(7):901. Number: 7 Publisher: Multidisciplinary Digital Publishing Institute.
- Ajami, H., Evans, J. P., McCabe, M. F., and Stisen, S. (2014). Technical Note: Reducing the spin-up time of integrated surface water–groundwater models. *Hydrology and Earth System Sciences*, 18(12):5169–5179. Publisher: Copernicus GmbH.
- Albergel, C., Dutra, E., Munier, S., Calvet, J.-C., Munoz-Sabater, J., de Rosnay, P., and Balsamo, G. (2018). ERA-5 and ERA-Interim driven ISBA land surface model simulations: which one performs better? *Hydrology and Earth System Sciences*, 22(6):3515–3532. Publisher: Copernicus GmbH.
- Albergel, C., Rüdiger, C., Pellarin, T., Calvet, J.-C., Fritz, N., Froissard, F., Suquia, D., Petitpa, A., Pignatelli, B., and Martin, E. (2008). From near-surface to root-zone soil moisture using an exponential filter: an assessment of the method based on in-situ observations and model simulations. *Hydrology and Earth System Sciences*, 12(6):1323–1337. Publisher: Copernicus GmbH.
- Alfieri, L., Lorini, V., Hirpa, F. A., Harrigan, S., Zsoter, E., Prudhomme, C., and Salamon, P. (2020). A global streamflow reanalysis for 1980–2018. *Journal of Hydrology X*, 6:100049.

- Allen, R. G., Pereira, L. S., Raes, D., and Smith, M. (1998). Crop evapotranspiration. Guidelines for computing crop water requirements. *FAO Irrigation and Drainage Paper (FAO)*. ISBN: 9789251042199 Publisher: FAO.
- Alley, W. M. (2007). Another Water Budget Myth: The Significance of Recoverable Ground Water in Storage. *Ground Water*, 45(3):251–251.
- Alley, W. M. and Leake, S. A. (2004). The Journey from Safe Yield to Sustainability. *Ground Water*, 42(1):12–16.
- Altchenko, Y. and Villholth, K. G. (2015). Mapping irrigation potential from renewable groundwater in Africa – a quantitative hydrological approach. *Hydrology and Earth System Sciences*, 19(2):1055–1067. Publisher: Copernicus GmbH.
- Anderson, M. P., Woessner, W. W., and Hunt, R. J. (2015). *Applied Groundwater Modeling: Simulation of Flow and Advective Transport*. Academic Press. Google-Books-ID: jcOcBAAAQBAJ.
- Aryal, S. K., Silberstein, R. P., Fu, G., Hodgson, G., Charles, S. P., and McFarlane, D. (2020). Understanding spatio-temporal rainfall-runoff changes in a semi-arid region. *Hydrological Processes*, 34(11):2510–2530. _eprint: <https://onlinelibrary.wiley.com/doi/pdf/10.1002/hyp.13744>.
- Assouline, S. (2013). Infiltration into soils: Conceptual approaches and solutions. *Water Resources Research*, 49(4):1755–1772. _eprint: <https://agupubs.onlinelibrary.wiley.com/doi/pdf/10.1002/wrcr.20155>.
- Baker, B. H. (1967). GEOLOGY OF THE MOUNT KENYA AREA. 79, MINISTRY OF NATURAL RESOURCES GEOLOGICAL SURVEY OF KENYA, Kenya.
- Bakker, M., Post, V., Langevin, C. D., Hughes, J. D., White, J., Starn, J., and Fienen, M. N. (2016a). FloPy: Python package for creating, running, and post-processing MODFLOW-based models. Technical report, U.S. Geological Survey.
- Bakker, M., Post, V., Langevin, C. D., Hughes, J. D., White, J. T., Starn, J. J., and Fienen, M. N. (2016b). Scripting MODFLOW Model Development Using Python and FloPy. *Groundwater*, 54(5):733–739. _eprint: <https://ngwa.onlinelibrary.wiley.com/doi/pdf/10.1111/gwat.12413>.
- Barnhart, K. R., Hutton, E. W. H., Tucker, G. E., Gasparini, N. M., Istanbuloglu, E., Hobbey, D. E. J., Lyons, N. J., Mouchene, M., Nudurupati, S. S., Adams, J. M., and Bandaragoda, C. (2020). Short communication: Landlab v2.0: a software package for Earth surface dynamics. *Earth Surface Dynamics*, 8(2):379–397. Publisher: Copernicus GmbH.
- Barthel, R. and Banzhaf, S. (2016). Groundwater and Surface Water Interaction at the Regional-scale – A Review with Focus on Regional Integrated Models. *Water Resources Management*, 30(1):1–32.
- Batelaan, O. and Smedt, F. D. (2004). SEEPAGE, a New MODFLOW DRAIN Package. *Groundwater*, 42(4):576–588. _eprint: <https://ngwa.onlinelibrary.wiley.com/doi/pdf/10.1111/j.1745-6584.2004.tb02626.x>.

- Batelis, S.-C., Rahman, M., Kollet, S., Woods, R., and Rosolem, R. (2020). Towards the representation of groundwater in the Joint UK Land Environment Simulator. *Hydrological Processes*, 34(13):2843–2863. _eprint: <https://onlinelibrary.wiley.com/doi/pdf/10.1002/hyp.13767>.
- Beck, H. E., Wood, E. F., Pan, M., Fisher, C. K., Miralles, D. G., Dijk, A. I. J. M. v., McVicar, T. R., and Adler, R. F. (2019). MSWEP V2 Global 3-Hourly 0.1° Precipitation: Methodology and Quantitative Assessment. *Bulletin of the American Meteorological Society*, 100(3):473–500. Publisher: American Meteorological Society Section: Bulletin of the American Meteorological Society.
- Becker, R., Gebremichael, M., and Märker, M. (2018). Impact of soil surface and sub-surface properties on soil saturated hydraulic conductivity in the semi-arid Walnut Gulch Experimental Watershed, Arizona, USA. *Geoderma*, 322:112–120.
- Belnap, J., Welter, J. R., Grimm, N. B., Barger, N., and Ludwig, J. A. (2005). Linkages Between Microbial and Hydrologic Processes in Arid and Semiarid Watersheds. *Ecology*, 86(2):298–307.
- Beven, K. (1989). Changing ideas in hydrology — The case of physically-based models. *Journal of Hydrology*, 105(1):157–172.
- Beven, K. (1991). Scale Considerations. In Bowles, D. S. and O’Connell, P. E., editors, *Recent Advances in the Modeling of Hydrologic Systems*, NATO ASI Series, pages 357–371. Springer Netherlands, Dordrecht.
- Beven, K. (1995). Linking parameters across scales: Subgrid parameterizations and scale dependent hydrological models. *Hydrological Processes*, 9(5-6):507–525.
- Beven, K. (2001). How far can we go in distributed hydrological modelling? *Hydrol. Earth Syst. Sci.*, 5(1):1–12.
- Beven, K. (2002). Towards an alternative blueprint for a physically based digitally simulated hydrologic response modelling system. *Hydrological Processes*, 16(2):189–206.
- Beven, K. and Binley, A. (1992). The future of distributed models: model calibration and uncertainty prediction. *Hydrological processes*, 6(3):279–298.
- Beven, K. J. (2004). *Rainfall - Runoff Modelling: The Primer*. Wiley.
- Bianchi, M., MacDonald, A. M., Macdonald, D. M. J., and Asare, E. B. (2020). Investigating the Productivity and Sustainability of Weathered Basement Aquifers in Tropical Africa Using Numerical Simulation and Global Sensitivity Analysis. *Water Resources Research*, 56(9):e2020WR027746. _eprint: <https://agupubs.onlinelibrary.wiley.com/doi/pdf/10.1029/2020WR027746>.
- Birkinshaw, S. J., James, P., and Ewen, J. (2010). Graphical user interface for rapid set-up of SHETRAN physically-based river catchment model. *Environmental Modelling & Software*, 25(4):609–610.
- Blöschl, G., Grayson, R. B., and Sivapalan, M. (1995). On the representative elementary area (REA) concept and its utility for distributed rainfall-runoff modelling. *Hydrological Processes*, 9(3-4):313–330.

- Blöschl, G. and Sivapalan, M. (1995a). Scale issues in hydrological modelling: A review. *Hydrological Processes*, 9(3-4):251–290.
- Blöschl, G. and Sivapalan, M. (1995b). Scale issues in hydrological modelling: A review. *Hydrological Processes*, 9(3-4):251–290.
- Bonsor, H. C., MacDonald, A. M., and Davies, J. (2014). Evidence for extreme variations in the permeability of laterite from a detailed analysis of well behaviour in Nigeria. *Hydrological Processes*, 28(10):3563–3573. eprint: <https://onlinelibrary.wiley.com/doi/pdf/10.1002/hyp.9871>.
- Bonsor, H. C., Shamsudduha, M., Marchant, B. P., MacDonald, A. M., and Taylor, R. G. (2018). Seasonal and Decadal Groundwater Changes in African Sedimentary Aquifers Estimated Using GRACE Products and LSMs. *Remote Sensing*, 10(6):904. Number: 6 Publisher: Multidisciplinary Digital Publishing Institute.
- Braun, J. and Willett, S. D. (2013). A very efficient $O(n)$, implicit and parallel method to solve the stream power equation governing fluvial incision and landscape evolution. *Geomorphology*, 180-181:170–179.
- Bredehoeft, J. (1997). Safe yield and the water budget myth. *Ground Water*, 35(6):929–930.
- Bredehoeft, J., Papadopoulos, S., and Cooper, H. (1982). The water budget myth (scientific basis of water management). *Studies in Geophysics, National Academy of Sciences*, pages 51–57.
- Bredehoeft, J. D. (2002). The Water Budget Myth Revisited: Why Hydrogeologists Model. *Ground Water*, 40(4):340–345.
- Brocca, L., Ciabatta, L., Massari, C., Camici, S., and Tarpanelli, A. (2017). Soil Moisture for Hydrological Applications: Open Questions and New Opportunities. *Water*, 9(2):140. Number: 2 Publisher: Multidisciplinary Digital Publishing Institute.
- Brooks, R. H. and Corey, A. T. (1964). *Hydraulic Properties of Porous Media*. Hydrology Paper No. 3. Colorado State University, Fort Collins. Google-Books-ID: F_1HOgAACAAJ.
- Brunner, P., Cook, P. G., and Simmons, C. T. (2009a). Hydrogeologic controls on disconnection between surface water and groundwater. *Water Resources Research*, 45(1):W01422.
- Brunner, P., Cook, P. G., and Simmons, C. T. (2011). Disconnected Surface Water and Groundwater: From Theory to Practice. *Ground Water*, 49(4):460–467.
- Brunner, P., Simmons, C. T., and Cook, P. G. (2009b). Spatial and temporal aspects of the transition from connection to disconnection between rivers, lakes and groundwater. *Journal of Hydrology*, 376(1):159–169.
- Brunner, P., Therrien, R., Renard, P., Simmons, C. T., and Franssen, H.-J. H. (2017). Advances in understanding river-groundwater interactions. *Reviews of Geophysics*, 55(3):2017RG000556.

- Budyko, M. I. (1961). The Heat Balance of the Earth's Surface. *Soviet Geography*, 2(4):3–13. Publisher: Routledge. eprint: <https://doi.org/10.1080/00385417.1961.10770761>.
- Carrier, M.-A., Boyaud, C., Lefebvre, R., Asare, E., INRS-ETE, SNC-Lavalin, Canadian Executing Agency, and Water Resource Commission of Ghana (2011). Hydrogeological Assessment Project of the Northern Regions of Ghana (HAP) FINAL TECHNICAL REPORT. Technical report, Canadian International Development Agency (CIDA) by SNCLavalin/INRS joint venture, Québec. OCLC: 861258488.
- Carsel, R. F. and Parrish, R. S. (1988). Developing joint probability distributions of soil water retention characteristics. *Water Resources Research*, 24(5):755–769.
- Cataldo, J., Behr, C., and Montalto, F. (2005). An Analysis of Transmission Losses in Ephemeral Streams, A Case Study in Walnut Gulch Experimental Watershed. *National Center for Housing and Environment, Tombstone, AZ*, pages 1–35.
- Cataldo, J., Behr, C., Montalto, F., and Pierce, R. J. (2004). A summary of published reports of transmission losses in ephemeral streams in the US. *National Center for Housing and the Environment*, pages 28–29.
- Cataldo, J. C., Behr, C., Montalto, F. A., and Pierce, R. J. (2010). Prediction of Transmission Losses in Ephemeral Streams, Western U.S.A. *The Open Hydrology Journal*, 4(1).
- CGIAR-CSI (2009). Global Aridity and PET Database.
- Chen, F. and Dudhia, J. (2001). Coupling an Advanced Land Surface–Hydrology Model with the Penn State–NCAR MM5 Modeling System. Part I: Model Implementation and Sensitivity. *Monthly Weather Review*, 129(4):569–585. Publisher: American Meteorological Society.
- Chen, S.-A., Michaelides, K., Grieve, S. W. D., and Singer, M. B. (2019). Aridity is expressed in river topography globally. *Nature*, 573(7775):573–577. Number: 7775. Publisher: Nature Publishing Group.
- Chen, X. and Sivapalan, M. (2020). Hydrological Basis of the Budyko Curve: Data-Guided Exploration of the Mediating Role of Soil Moisture. *Water Resources Research*, 56(10):e2020WR028221. eprint: <https://agupubs.onlinelibrary.wiley.com/doi/pdf/10.1029/2020WR028221>.
- Cherlet, M., Hutchinson, C., Reynolds, J., Hill, J., Sommer, S., and von Maltitz, G. (2018). *World atlas of desertification*. Luxembourg: Publication Office of the European Union. Luxembourg, 3rd edition.
- Chilton, P. J. and Foster, S. S. D. (1995). Hydrogeological Characterisation And Water-Supply Potential Of Basement Aquifers In Tropical Africa. *Hydrogeology Journal*, 3(1):36–49.
- Chow, V. T., Maidment, D. R., and Mays, L. W. (1988). *Applied Hydrology*. McGraw Hill, Singapore.

- Chui, T. F. M. and Freyberg, D. L. (2009). Implementing Hydrologic Boundary Conditions in a Multiphysics Model. *Journal of Hydrologic Engineering*, 14(12):1374–1377.
- Chui, T. F. M., Low, S. Y., and Liong, S.-Y. (2011). An ecohydrological model for studying groundwater–vegetation interactions in wetlands. *Journal of Hydrology*, 409(1):291–304.
- Clapp, R. B. and Hornberger, G. M. (1978). Empirical equations for some soil hydraulic properties. *Water Resources Research*, 14(4):601–604. _eprint: <https://agupubs.onlinelibrary.wiley.com/doi/pdf/10.1029/WR014i004p00601>.
- Clark, M. P., Fan, Y., Lawrence, D. M., Adam, J. C., Bolster, D., Gochis, D. J., Hooper, R. P., Kumar, M., Leung, L. R., Mackay, D. S., Maxwell, R. M., Shen, C., Swenson, S. C., and Zeng, X. (2015). Improving the representation of hydrologic processes in Earth System Models. *Water Resources Research*, 51(8):5929–5956. _eprint: <https://agupubs.onlinelibrary.wiley.com/doi/pdf/10.1002/2015WR017096>.
- Cleugh, H. A., Leuning, R., Mu, Q., and Running, S. W. (2007). Regional evaporation estimates from flux tower and MODIS satellite data. *Remote Sensing of Environment*, 106(3):285–304.
- Coelho, V. H. R., Montenegro, S., Almeida, C. N., Silva, B. B., Oliveira, L. M., Gusmão, A. C. V., Freitas, E. S., and Montenegro, A. A. A. (2017). Alluvial groundwater recharge estimation in semi-arid environment using remotely sensed data. *Journal of Hydrology*, 548(Supplement C):1–15.
- Constantz, J. and Thomas, C. L. (1997). Stream bed temperature profiles as indicators of percolation characteristics beneath arroyos in the Middle Rio Grande Basin, USA. *Hydrological Processes*, 11(12):1621–1634.
- Cook, P. G., Walker, G. R., and Jolly, I. D. (1989). Spatial variability of groundwater recharge in a semiarid region. *Journal of Hydrology*, 111(1):195–212.
- Cosgrove, B. A., Lohmann, D., Mitchell, K. E., Houser, P. R., Wood, E. F., Schaake, J. C., Robock, A., Sheffield, J., Duan, Q., Luo, L., Higgins, R. W., Pinker, R. T., and Tarpley, J. D. (2003). Land surface model spin-up behavior in the North American Land Data Assimilation System (NL-DAS). *Journal of Geophysical Research: Atmospheres*, 108(D22). _eprint: <https://agupubs.onlinelibrary.wiley.com/doi/pdf/10.1029/2002JD003316>.
- Costa, A. C., Bronstert, A., and de Araújo, J. C. (2012). A channel transmission losses model for different dryland rivers. *Hydrol. Earth Syst. Sci.*, 16(4):1111–1135.
- Costigan, K. H., Kennard, M. J., Leigh, C., Sauquet, E., Datry, T., and Boulton, A. J. (2017). Chapter 2.2 - Flow Regimes in Intermittent Rivers and Ephemeral Streams. In *Intermittent Rivers and Ephemeral Streams*, pages 51–78. Academic Press.
- Courtois, N., Lachassagne, P., Wyns, R., Blanchin, R., Bougairé, F. D., Somé, S., and Tapsoba, A. (2010). Large-Scale Mapping of Hard-Rock Aquifer

- Properties Applied to Burkina Faso. *Groundwater*, 48(2):269–283. [_eprint: https://ngwa.onlinelibrary.wiley.com/doi/pdf/10.1111/j.1745-6584.2009.00620.x](https://ngwa.onlinelibrary.wiley.com/doi/pdf/10.1111/j.1745-6584.2009.00620.x).
- Craig, J. R., Liu, G., and Soulis, E. D. (2010). Runoff–infiltration partitioning using an upscaled Green–Ampt solution. *Hydrological Processes*, 24(16):2328–2334. [_eprint: https://onlinelibrary.wiley.com/doi/pdf/10.1002/hyp.7601](https://onlinelibrary.wiley.com/doi/pdf/10.1002/hyp.7601).
- Cui, T., Raiber, M., Pagendam, D., Gilfedder, M., and Rassam, D. (2017). Response of groundwater level and surface-water/groundwater interaction to climate variability: Clarence-Moreton Basin, Australia. *Hydrogeology Journal*, pages 1–22.
- Custodio, E. (1989). Groundwater characteristics and problems in volcanic rock terrains. In *Isotope techniques in the study of the hydrology of fractured and fissured rocks*, pages 87–137, International Atomic Energy Agency (IAEA), Vienna, Austria. IAEA. INIS Reference Number: 20063467.
- Cuthbert, M. O. (2010). An improved time series approach for estimating groundwater recharge from groundwater level fluctuations. *Water Resources Research*, 46(9):W09515.
- Cuthbert, M. O. (2014). Straight thinking about groundwater recession. *Water Resources Research*, 50(3):2407–2424.
- Cuthbert, M. O., Acworth, R. I., Andersen, M. S., Larsen, J. R., McCallum, A. M., Rau, G. C., and Tellam, J. H. (2016). Understanding and quantifying focused, indirect groundwater recharge from ephemeral streams using water table fluctuations. *Water Resources Research*, 52(2):827–840.
- Cuthbert, M. O., Gleeson, T., Moosdorf, N., Befus, K. M., Schneider, A., Hartmann, J., and Lehner, B. (2019a). Global patterns and dynamics of climate–groundwater interactions. *Nature Climate Change*, 9(2):137–141. Number: 2 Publisher: Nature Publishing Group.
- Cuthbert, M. O., Gleeson, T., Reynolds, S. C., Bennett, M. R., Newton, A. C., McCormack, C. J., and Ashley, G. M. (2017). Modelling the role of groundwater hydro-refugia in East African hominin evolution and dispersal. *Nature Communications*, 8(1):15696. Bandiera_abtest: a Cc_license_type: cc.by Cg_type: Nature Research Journals Number: 1 Primary_atype: Research Publisher: Nature Publishing Group Subject_term: Archaeology;Hydrology;Palaeoecology Subject_term.id: archaeology;hydrology;palaeoecology.
- Cuthbert, M. O., Taylor, R. G., Favreau, G., Todd, M. C., Shamsudduha, M., Villholth, K. G., MacDonald, A. M., Scanlon, B. R., Kotchoni, D. O. V., Vouillamoz, J.-M., Lawson, F. M. A., Adjomayi, P. A., Kashaigili, J., Seddon, D., Sorensen, J. P. R., Ebrahim, G. Y., Owor, M., Nyenje, P. M., Nazoumou, Y., Goni, I., Ousmane, B. I., Sibanda, T., Ascott, M. J., Macdonald, D. M. J., Agyekum, W., Koussoubé, Y., Wanke, H., Kim, H., Wada, Y., Lo, M.-H., Oki, T., and Kukuric, N. (2019b). Observed controls on resilience of groundwater to climate variability in sub-Saharan Africa. *Nature*, 572(7768):230–234.
- Daesslé, L. W., van Geldern, R., Orozco-Durán, A., and Barth, J. A. C. (2016). The 2014 water release into the arid Colorado River delta and associated water losses by evaporation. *Science of The Total Environment*, 542:586–590.

- Dahan, O., Tatarsky, B., Enzel, Y., Kulls, C., Seely, M., and Benito, G. (2008). Dynamics of Flood Water Infiltration and Ground Water Recharge in Hyperarid Desert. *Ground Water*, 46(3):450–461.
- Dai, A. (2011). Drought under global warming: a review. *WIREs Climate Change*, 2(1):45–65. _eprint: <https://onlinelibrary.wiley.com/doi/pdf/10.1002/wcc.81>.
- Dai, A. (2012). Increasing drought under global warming in observations and models. *Nature Climate Change*, 3(1):nclimate1633.
- Dai, Y., Shanguan, W., Wei, N., Xin, Q., Yuan, H., Zhang, S., Liu, S., Lu, X., Wang, D., and Yan, F. (2019a). A review of the global soil property maps for Earth system models. *SOIL*, 5(2):137–158.
- Dai, Y., Xin, Q., Wei, N., Zhang, Y., Shanguan, W., Yuan, H., Zhang, S., Liu, S., and Lu, X. (2019b). A Global High-Resolution Data Set of Soil Hydraulic and Thermal Properties for Land Surface Modeling. *Journal of Advances in Modeling Earth Systems*, 11(9):2996–3023. _eprint: <https://agupubs.onlinelibrary.wiley.com/doi/pdf/10.1029/2019MS001784>.
- Datry, T., Bonada, N., and Boulton, A., editors (2017). *Intermittent Rivers and Ephemeral Streams, Ecology and Management*. Academic Press, Netherlands.
- de Saint-Venant B. (1871). Théorie du mouvement non permanent des eaux, avec application aux crues des rivières et à l'introduction des marées dans leurs lits. *Comptes Rendus des séances de l'Académie des Sciences*, 73:237–240.
- Deblauwe, V., Barbier, N., Couteron, P., Lejeune, O., and Bogaert, J. (2008). The global biogeography of semi-arid periodic vegetation patterns. *Global Ecology and Biogeography*, 17(6):715–723.
- Decurtins, S. (1992). *Hydrogeographical investigations in the Mount Kenya subcatchment of the Ewaso Ngiro River*. PhD thesis, University of Berne, Institute of Geography, Berne, Switzerland. ISBN: 9783906290775 OCLC: 30377526.
- Desilets, D. and Zreda, M. (2013). Footprint diameter for a cosmic-ray soil moisture probe: Theory and Monte Carlo simulations. *Water Resources Research*, 49(6):3566–3575. _eprint: <https://agupubs.onlinelibrary.wiley.com/doi/pdf/10.1002/wrcr.20187>.
- Desilets, D., Zreda, M., and Ferré, T. P. A. (2010). Nature's neutron probe: Land surface hydrology at an elusive scale with cosmic rays. *Water Resources Research*, 46(11):W11505. _eprint: <https://agupubs.onlinelibrary.wiley.com/doi/pdf/10.1029/2009WR008726>.
- Devlin, J. F. and Sophocleous, M. (2005). The persistence of the water budget myth and its relationship to sustainability. *Hydrogeology Journal*, 13(4):549–554.
- Dharani, N. (2009). *Field Guide to Acacias of East Africa*. Struik Publishers, Cape Town.
- Dillon, P. J. and Liggett, J. A. (1983). An ephemeral stream-aquifer interaction model. *Water Resources Research*, 19(3):621–626.

- D'Odorico, P. and Porporato, A. (2006). *Dryland Ecohydrology*. Springer Science & Business Media.
- Dorigo, W., Wagner, W., Albergel, C., Albrecht, F., Balsamo, G., Brocca, L., Chung, D., Ertl, M., Forkel, M., Gruber, A., Haas, E., Hamer, P. D., Hirschi, M., Ikonen, J., de Jeu, R., Kidd, R., Lahoz, W., Liu, Y. Y., Miralles, D., Mistelbauer, T., Nicolai-Shaw, N., Parinussa, R., Pratola, C., Reimer, C., van der Schalie, R., Seneviratne, S. I., Smolander, T., and Lecomte, P. (2017). ESA CCI Soil Moisture for improved Earth system understanding: State-of-the art and future directions. *Remote Sensing of Environment*, 203:185–215.
- Dunkerley, D. and Brown, K. (1999). Flow behaviour, suspended sediment transport and transmission losses in a small (sub-bank-full) flow event in an Australian desert stream. *Hydrological Processes*, 13(11):1577–1588.
- Dunkerley, D. L. (1992). Channel geometry, bed material, and inferred flow conditions in ephemeral stream systems, barrier range, western N.S.W. Australia. *Hydrological Processes*, 6(4):417–433.
- Dunkerley, D. L. (2002). Infiltration rates and soil moisture in a groved mulga community near Alice Springs, arid central Australia: evidence for complex internal rainwater redistribution in a runoff–runon landscape. *Journal of Arid Environments*, 51(2):199–219.
- Dunkerley, D. L. (2008). Bank permeability in an Australian ephemeral dry-land stream: variation with stage resulting from mud deposition and sediment clogging. *Earth Surface Processes and Landforms*, 33(2):226–243.
- Döll, P., Hoffmann-Dobrev, H., Portmann, F. T., Siebert, S., Eicker, A., Rodell, M., Strassberg, G., and Scanlon, B. R. (2012). Impact of water withdrawals from groundwater and surface water on continental water storage variations. *Journal of Geodynamics*, 59–60:143–156.
- Döll, P., Müller Schmied, H., Schuh, C., Portmann, F. T., and Eicker, A. (2014). Global-scale assessment of groundwater depletion and related groundwater abstractions: Combining hydrological modeling with information from well observations and GRACE satellites. *Water Resources Research*, 50(7):5698–5720.
- El-Kafagee, M. and Rahman, A. (2011). A study on initial and continuing losses for design flood estimation in New South Wales. *19th International Congress on Modelling and Simulation, Perth, Australia, 12–16 December 2011*, page 6.
- El Khalki, E. M., Tramblay, Y., Massari, C., Brocca, L., Simonneaux, V., Gascoin, S., and Saidi, M. E. M. (2020). Challenges in flood modeling over data-scarce regions: how to exploit globally available soil moisture products to estimate antecedent soil wetness conditions in Morocco. *Natural Hazards and Earth System Sciences*, 20(10):2591–2607. Publisher: Copernicus GmbH.
- Emmerich, W. E. and Verdugo, C. L. (2008). Long-term carbon dioxide and water flux database, Walnut Gulch Experimental Watershed, Arizona, United States. *Water Resources Research*, 44:W05S09.
- Ewen, J. (2001). *SHETRAN User Manual*. WRSRL.

- Ewen, J., Parkin, G., and O'Connell, P. E. (2000). SHETRAN: Distributed River Basin Flow and Transport Modeling System. *Journal of Hydrologic Engineering*, 5(3):250–258.
- Fan, Y., Li, H., and Miguez-Macho, G. (2013). Global Patterns of Groundwater Table Depth. *Science*, 339(6122):940–943.
- Farthing, M. W. and Ogden, F. L. (2017). Numerical Solution of Richards' Equation: A Review of Advances and Challenges. *Soil Science Society of America Journal*, 81(6):1257–1269.
- Faurès, J.-M., Goodrich, D. C., Woolhiser, D. A., and Sorooshian, S. (1995). Impact of small-scale spatial rainfall variability on runoff modeling. *Journal of Hydrology*, 173(1):309–326.
- Favreau, G., Cappelaere, B., Massuel, S., Leblanc, M., Boucher, M., Boulain, N., and Leduc, C. (2009). Land clearing, climate variability, and water resources increase in semiarid southwest Niger: A review. *Water Resources Research*, 45(7):W00A16.
- Feng, S. and Fu, Q. (2013). Expansion of global drylands under a warming climate. *Atmos. Chem. Phys.*, 13(19):10081–10094.
- Fenicia, F., Savenije, H. H. G., Matgen, P., and Pfister, L. (2008). Understanding catchment behavior through stepwise model concept improvement. *Water Resources Research*, 44(1). [_eprint: https://onlinelibrary.wiley.com/doi/pdf/10.1029/2006WR005563](https://onlinelibrary.wiley.com/doi/pdf/10.1029/2006WR005563).
- Ferguson, G., Cuthbert, M. O., Befus, K., Gleeson, T., and McIntosh, J. C. (2020). Rethinking groundwater age. *Nature Geoscience*, 13(9):592–594. Bandiera_abtest: a Cg.type: Nature Research Journals Number: 9 Primary_atype: Comments & Opinion Publisher: Nature Publishing Group Subject_term: Hydrology;Sustainability;Water resources Subject_term.id: hydrology;sustainability;water-resources.
- Flug, M., Abi-Ghanem, G. V., and Duckstein, L. (1980). An event-based model of recharge from an ephemeral stream. *Water Resources Research*, 16(4):685–690.
- Foley, J. A., Ramankutty, N., Brauman, K. A., Cassidy, E. S., Gerber, J. S., Johnston, M., Mueller, N. D., O'Connell, C., Ray, D. K., West, P. C., Balzer, C., Bennett, E. M., Carpenter, S. R., Hill, J., Monfreda, C., Polasky, S., Rockström, J., Sheehan, J., Siebert, S., Tilman, D., and Zaks, D. P. M. (2011). Solutions for a cultivated planet. *Nature*, 478(7369):nature10452.
- Fox, G. A. and Durnford, D. S. (2003). Unsaturated hyporheic zone flow in stream/aquifer conjunctive systems. *Advances in Water Resources*, 26(9):989–1000.
- Franz, T. E., Caylor, K. K., King, E. G., Nordbotten, J. M., Celia, M. A., and Rodríguez-Iturbe, I. (2012). An ecohydrological approach to predicting hillslope-scale vegetation patterns in dryland ecosystems. *Water Resources Research*, 48(1). [_eprint: https://agupubs.onlinelibrary.wiley.com/doi/pdf/10.1029/2011WR010524](https://agupubs.onlinelibrary.wiley.com/doi/pdf/10.1029/2011WR010524).

- Franz, T. E., Caylor, K. K., Nordbotten, J. M., Rodríguez-Iturbe, I., and Celia, M. A. (2010). An ecohydrological approach to predicting regional woody species distribution patterns in dryland ecosystems. *Advances in Water Resources*, 33(2):215–230.
- Franz, T. E., Zreda, M., Rosolem, R., and Ferre, T. P. A. (2013). A universal calibration function for determination of soil moisture with cosmic-ray neutrons. *Hydrology and Earth System Sciences*, 17(2):453–460. Publisher: Copernicus GmbH.
- Gichuki, F. N. (2002). Water scarcity and conflicts: A case study of the Upper Ewaso Ng'iro North Basin. *The changing face of irrigation in Kenya: Opportunities for anticipating change in eastern and southern Africa*, pages 113–134. Publisher: Citeseer.
- Gichuki, F. N. (2004). Managing the externalities of declining dry season river flow: A case study from the Ewaso Ng'iro North River Basin, Kenya. *Water Resources Research*, 40(8). _eprint: <https://agupubs.onlinelibrary.wiley.com/doi/pdf/10.1029/2004WR003106>.
- Giordano, M. (2009). Global Groundwater? Issues and Solutions. *Annual Review of Environment and Resources*, 34(1):153–178.
- Gleeson, T., Moosdorf, N., Hartmann, J., and van Beek, L. P. H. (2014). A glimpse beneath earth's surface: GLobal HYdrogeology MaPS (GLHYMPS) of permeability and porosity. *Geophysical Research Letters*, 41(11):3891–3898.
- Gleeson, T., Wada, Y., Bierkens, M. F. P., and Beek, L. P. H. v. (2012). Water balance of global aquifers revealed by groundwater footprint. *Nature*, 488(7410):nature11295.
- Glenn, E. P., Scott, R. L., Nguyen, U., and Nagler, P. L. (2015). Wide-area ratios of evapotranspiration to precipitation in monsoon-dependent semiarid vegetation communities. *Journal of Arid Environments*, 117:84–95.
- Goodrich, D. C., Keefer, T. O., Unkrich, C. L., Nichols, M. H., Osborn, H. B., Stone, J. J., and Smith, J. R. (2008). Long-term precipitation database, Walnut Gulch Experimental Watershed, Arizona, United States. *Water Resources Research*, 44(5):W05S04.
- Goodrich, D. C., Kepner, W. G., Levick, L. R., and Wigington, P. J. (2018). Southwestern Intermittent and Ephemeral Stream Connectivity. *JAWRA Journal of the American Water Resources Association*, 54(2):400–422.
- Goodrich, D. C., Lane, L. J., Shillito, R. M., Miller, S. N., Syed, K. H., and Woolhiser, D. A. (1997). Linearity of basin response as a function of scale in a semiarid watershed. *Water Resources Research*, 33(12):2951–2965.
- Goodrich, D. C., Schmugge, T. J., Jackson, T. J., Unkrich, C. L., Keefer, T. O., Parry, R., Bach, L. B., and Amer, S. A. (1994). Runoff simulation sensitivity to remotely sensed initial soil water content. *Water Resources Research*, 30(5):1393–1405. _eprint: <https://agupubs.onlinelibrary.wiley.com/doi/pdf/10.1029/93WR03083>.

- Goodrich, D. C., Williams, D. G., Unkrich, C. L., Hogan, J. F., Scott, R. L., Hultine, K. R., Pool, D., Goes, A. L., and Miller, S. (2013). Comparison of Methods to Estimate Ephemeral Channel Recharge, Walnut Gulch, San Pedro River Basin, Arizona. In *Groundwater Recharge in a Desert Environment: The Southwestern United States*, pages 77–99. American Geophysical Union (AGU).
- Gorelick, S. M. and Zheng, C. (2015). Global change and the groundwater management challenge. *Water Resources Research*, 51(5):3031–3051.
- Green, T. R., Taniguchi, M., Kooi, H., Gurdak, J. J., Allen, D. M., Hiscock, K. M., Treidel, H., and Aureli, A. (2011). Beneath the surface of global change: Impacts of climate change on groundwater. *Journal of Hydrology*, 405(3):532–560.
- Green, W. H. and Ampt, G. A. (1911). Studies on Soil Physics. 1, The flow of air and water through soils. *The Journal of Agricultural Science*, 4(1):1–24.
- Gregory, J. W. (1900). Contributions to the Geology of British East Africa.—Part II. The Geology of Mount Kenya. *Quarterly Journal of the Geological Society*, 56(1-4):205–222. Publisher: Geological Society of London.
- Guardiola-Albert, C. and Christopher, R. J. c. (2011). Potential Impacts of Climate Change on Groundwater Supplies to the Doñana Wetland, Spain. *Wetlands*, 31(5):907–920.
- Gupta, H. V., Kling, H., Yilmaz, K. K., and Martinez, G. F. (2009). Decomposition of the mean squared error and NSE performance criteria: Implications for improving hydrological modelling. *Journal of Hydrology*, 377(1):80–91.
- Hackman, B. D. (1988). Geology of the Baringo—Laikipia area. Technical Report 104, MINISTRY OF ENVIRONMENT AND NATURAL RESOURCES, Nairobi, Kenya.
- Harbaugh, A. (2005). MODFLOW-2005, The U.S. Geological Survey Modular Ground-Water Model—the Ground-Water Flow Process. Technical report, U.S. Geological Survey Techniques and Methods 6- A16.
- Harbaugh, A. W., Banta, E. R., Hill, M. C., and McDonald, M. G. (2000). MODFLOW-2000, The U.S. Geological Survey Modular Ground-Water Model - User Guide to Modularization Concepts and the Ground-Water Flow Process. Report 2000-92, Geological Survey (U.S.), Denver, CO.
- Healy, R. W. and Scanlon, B. R. (2010). *Estimating Groundwater Recharge*. Cambridge University Press, Cambridge ; New York.
- Heilman, P., Nichols, M. H., Goodrich, D. C., Miller, S. N., and Guertin, D. P. (2008). Geographic information systems database, Walnut Gulch Experimental Watershed, Arizona, United States. *Water Resources Research*, 44(5):W05S11.
- Henderson (1966). *Open Channel Flow*. Macmillan Series in Civil Engi, Berkeley, edición: facsimile edition.

- Hersbach, H., Bell, B., Berrisford, P., Hirahara, S., Horányi, A., Muñoz-Sabater, J., Nicolas, J., Peubey, C., Radu, R., Schepers, D., Simmons, A., Soci, C., Abdalla, S., Abellan, X., Balsamo, G., Bechtold, P., Biavati, G., Bidlot, J., Bonavita, M., Chiara, G. D., Dahlgren, P., Dee, D., Diamantakis, M., Dragani, R., Flemming, J., Forbes, R., Fuentes, M., Geer, A., Haimberger, L., Healy, S., Hogan, R. J., Hólm, E., Janisková, M., Keeley, S., Laloyaux, P., Lopez, P., Lupu, C., Radnoti, G., Rosnay, P. d., Rozum, I., Vamborg, F., Villaume, S., and Thépaut, J.-N. (2020). The ERA5 global reanalysis. *Quarterly Journal of the Royal Meteorological Society*, 146:1999–2049. eprint: <https://rmets.onlinelibrary.wiley.com/doi/pdf/10.1002/qj.3803>.
- Hill, P. (1996). *Empirical analysis of data to derive losses for design flood estimation in South-Eastern Australia*. Number Accessed from <https://nla.gov.au/nla.cat-vn279080> in Report (Cooperative Research Centre for Catchment Hydrology) ; 96/5. Cooperative Research Centre for Catchment Hydrology, [Clayton, Vic.].
- Hobley, D. E. J., Adams, J. M., Siddhartha Nudurupati, S., Hutton, E. W. H., Gasparini, N. M., Istanbuluoglu, E., and Tucker, G. E. (2017). Creative computing with Landlab: an open-source toolkit for building, coupling, and exploring two-dimensional numerical models of Earth-surface dynamics. *Earth Surface Dynamics*, 5:21–46. Publisher: European Geosciences Union (EGU) / Copernicus Publications.
- Holland, M. (2012). Evaluation of factors influencing transmissivity in fractured hard-rock aquifers of the Limpopo Province. *Water SA*, 38(3):379–390. Number: 3.
- Holtan, H. N. (1945). Time-condensation in hydrograph-analysis. *Eos, Transactions American Geophysical Union*, 26(3):407–413. eprint: <https://agupubs.onlinelibrary.wiley.com/doi/pdf/10.1029/TR026i003p00407>.
- Houston, J. (2002). Groundwater recharge through an alluvial fan in the Atacama Desert, northern Chile: mechanisms, magnitudes and causes. *Hydrological Processes*, 16(15):3019–3035.
- Huang, J., Li, Y., Fu, C., Chen, F., Fu, Q., Dai, A., Shinoda, M., Ma, Z., Guo, W., Li, Z., Zhang, L., Liu, Y., Yu, H., He, Y., Xie, Y., Guan, X., Ji, M., Lin, L., Wang, S., Yan, H., and Wang, G. (2017). Dryland climate change: Recent progress and challenges. *Reviews of Geophysics*, 55(3):719–778. eprint: <https://agupubs.onlinelibrary.wiley.com/doi/pdf/10.1002/2016RG000550>.
- Huang, J., Yu, H., Guan, X., Wang, G., and Guo, R. (2015). Accelerated dryland expansion under climate change. *Nature Climate Change*, 6(2):nclimate2837.
- Huffman, G. J., Adler, R. F., Arkin, P., Chang, A., Ferraro, R., Gruber, A., Janowiak, J., McNab, A., Rudolf, B., and Schneider, U. (1997). The Global Precipitation Climatology Project (GPCP) Combined Precipitation Dataset. *Bulletin of the American Meteorological Society*, 78(1):5–20. Publisher: American Meteorological Society Section: Bulletin of the American Meteorological Society.
- Huffman, G. J., Bolvin, D. T., Braithwaite, D., Hsu, K., Joyce, R., Xie, P., and Yoo, S.-H. (2015). NASA global precipitation measurement (GPM) integrated

- multi-satellite retrievals for GPM (IMERG). *Algorithm Theoretical Basis Document (ATBD) Version*, 4:26.
- Hughes, A., Mansour, M., Robins, N., and Peach, D. (2006). Numerical Modelling of Run-off Recharge in a Catchment in the West Bank. *MODFLOW and More 2006: Managing Ground-Water Systems, Conference Proceedings*, 1:385–389.
- Hughes, A. G., Mansour, M. M., and Robins, N. S. (2008). Evaluation of distributed recharge in an upland semi-arid karst system: the West Bank Mountain Aquifer, Middle East. *Hydrogeology Journal*, 16(5):845–854.
- Hughes, D. A. (2019). A simple approach to estimating channel transmission losses in large South African river basins. *Journal of Hydrology: Regional Studies*, 25:100619.
- Hughes, D. A., Hannart, P., and Watkins, D. (2004). Continuous baseflow separation from time series of daily and monthly streamflow data. *Water SA*, 29(1):43–48.
- Hughes, D. A. and Sami, K. (1992). Transmission losses to alluvium and associated moisture dynamics in a semiarid ephemeral channel system in Southern Africa. *Hydrological Processes*, 6(1):45–53. eprint: <https://onlinelibrary.wiley.com/doi/pdf/10.1002/hyp.3360060105>.
- Hulme, M., Marsh, R., and Jones, P. D. (1992). Global changes in a humidity index between 1931–60 and 1961–90. *Climate Research*, 2(1):1–22. Publisher: Inter-Research Science Center.
- Huxman, T. E., Wilcox, B. P., Breshears, D. D., Scott, R. L., Snyder, K. A., Small, E. E., Hultine, K., Pockman, W. T., and Jackson, R. B. (2005). Ecohydrological Implications of Woody Plant Encroachment. *Ecology*, 86(2):308–319.
- IAEA (2017). *Cosmic Ray Neutron Sensing: Use, Calibration and Validation for Soil Moisture Estimation*. Number 1809 in TECDOC Series. INTERNATIONAL ATOMIC ENERGY AGENCY, Vienna.
- IPCC (2012). *Managing the risks of extreme events and disasters to advance climate change adaptation: special report of the Intergovernmental Panel on Climate Change*. Cambridge University Press, New York, NY. OCLC: ocn796030880.
- IPCC (2013). *Climate change 2013: the physical science basis: Working Group I contribution to the Fifth assessment report of the Intergovernmental Panel on Climate Change*. Cambridge University Press, New York.
- IPCC6 (2021). *Climate Change 2021: The Physical Science Basis. Contribution of Working Group I to the Sixth Assessment Report of the Intergovernmental Panel on Climate Change*. Cambridge University Press, in press edition.
- Ivanov, V. Y., Vivoni, E. R., Bras, R. L., and Entekhabi, D. (2004). Catchment hydrologic response with a fully distributed triangulated irregular network model. *Water Resources Research*, 40(11):W11102.
- Izbicki, J. A., Radyk, J., and Michel, R. L. (2000). Water movement through a thick unsaturated zone underlying an intermittent stream in the western Mojave Desert, southern California, USA. *Journal of Hydrology*, 238(3):194–217.

- Jaeger, K. L., Sutfin, N. A., Tooth, S., Michaelides, K., and Singer, M. (2017). Chapter 2.1 - Geomorphology and Sediment Regimes of Intermittent Rivers and Ephemeral Streams. In Datry, T., Bonada, N., and Boulton, A., editors, *Intermittent Rivers and Ephemeral Streams*, pages 21–49. Academic Press.
- Jahangir, M. H. and Arast, M. (2020). Remote sensing products for predicting actual evapotranspiration and water stress footprints under different land cover. *Journal of Cleaner Production*, 266:121818.
- Jarihani, A. A., Larsen, J. R., Callow, J. N., McVicar, T. R., and Johansen, K. (2015). Where does all the water go? Partitioning water transmission losses in a data-sparse, multi-channel and low-gradient dryland river system using modelling and remote sensing. *Journal of Hydrology*, 529:1511–1529.
- Jasechko, S., Perrone, D., Befus, K. M., Bayani Cardenas, M., Ferguson, G., Gleeson, T., Luijendijk, E., McDonnell, J. J., Taylor, R. G., Wada, Y., and Kirchner, J. W. (2017). Global aquifers dominated by fossil groundwaters but wells vulnerable to modern contamination. *Nature Geoscience*, 10(6):425–429. Number: 6 Publisher: Nature Publishing Group.
- Jazayeri, A. and Werner, A. D. (2019). Boundary Condition Nomenclature Confusion in Groundwater Flow Modeling. *Groundwater*, 57(5):664–668. _eprint: <https://ngwa.onlinelibrary.wiley.com/doi/pdf/10.1111/gwat.12893>.
- Kalf, F. R. P. and Woolley, D. R. (2005). Applicability and methodology of determining sustainable yield in groundwater systems. *Hydrogeology Journal*, 13(1):295–312.
- Kampf, S. K. and Burges, S. J. (2007). A framework for classifying and comparing distributed hillslope and catchment hydrologic models. *Water Resources Research*, 43(5):W05423. _eprint: <https://agupubs.onlinelibrary.wiley.com/doi/pdf/10.1029/2006WR005370>.
- Keefer, T. O., Moran, M. S., and Paige, G. B. (2008). Long-term meteorological and soil hydrology database, Walnut Gulch Experimental Watershed, Arizona, United States. *Water Resources Research*, 44(5):W05S07.
- Keppel, R. V. and Renard, K. G. (1962). Transmission Losses in Ephemeral Stream Beds. *Journal of the Hydraulics Division*, 88(3):59–68.
- Kernodle, M. (1999). Overview of the Hydrogeology and Geohydrology of the Northern Rio Grande Basin - Colorado, New Mexico, and Texas. page 24.
- Kipkemoi, I., Michaelides, K., Rosolem, R., and Singer, M. B. (2021). Climatic expression of rainfall on soil moisture dynamics in drylands. *Hydrology and Earth System Sciences Discussions*, pages 1–24. Publisher: Copernicus GmbH.
- Kiteme, B. P. and Gikonyo, J. (2002). Preventing and Resolving Water Use Conflicts in the Mount Kenya Highland–Lowland System through Water Users’ Associations. *Mountain Research and Development*, 22(4):332–337. Publisher: International Mountain Society.
- Knighton, A. D. and Nanson, G. C. (1994). Flow transmission along an arid zone anastomosing river, cooper creek, australia. *Hydrological Processes*, 8(2):137–154.

- Knighton, A. D. and Nanson, G. C. (2001). An event-based approach to the hydrology of arid zone rivers in the Channel Country of Australia. *Journal of Hydrology*, 254(1–4):102–123.
- Koech, G., Makokha, G. O., and Mundia, C. N. (2020). Climate change vulnerability assessment using a GIS modelling approach in ASAL ecosystem: a case study of Upper Ewaso Nyiro basin, Kenya. *Modeling Earth Systems and Environment*, 6(1):479–498.
- Krause, P., Boyle, D. P., and Bäse, F. (2005). Comparison of different efficiency criteria for hydrological model assessment. *Advances in Geosciences*, 5:89–97.
- Kurc, S. A. and Small, E. E. (2004). Dynamics of evapotranspiration in semiarid grassland and shrubland ecosystems during the summer monsoon season, central New Mexico. *Water Resources Research*, 40(9):W09305.
- Lahmers, T. M., Gupta, H., Castro, C. L., Gochis, D. J., Yates, D., Dugger, A., Goodrich, D., and Hazenberg, P. (2019). Enhancing the Structure of the WRF-Hydro Hydrologic Model for Semiarid Environments. *Journal of Hydrometeorology*, 20(4):691–714. Publisher: American Meteorological Society.
- Landerer, F. W. and Swenson, S. C. (2012). Accuracy of scaled GRACE terrestrial water storage estimates. *Water Resources Research*, 48(4). _eprint: <https://agupubs.onlinelibrary.wiley.com/doi/pdf/10.1029/2011WR011453>.
- Lange, J. (2005). Dynamics of transmission losses in a large arid stream channel. *Journal of Hydrology*, 306(1-4):112–126.
- Leenaars, J. G. B., Claessens, L., Heuvelink, G. B. M., Hengl, T., Ruiperez González, M., van Bussel, L. G. J., Guilpart, N., Yang, H., and Cassman, K. G. (2018). Mapping rootable depth and root zone plant-available water holding capacity of the soil of sub-Saharan Africa. *Geoderma*, 324:18–36.
- Lehner, B. and Grill, G. (2013). Global river hydrography and network routing: baseline data and new approaches to study the world’s large river systems. *Hydrological Processes*, 27(15):2171–2186. _eprint: <https://onlinelibrary.wiley.com/doi/pdf/10.1002/hyp.9740>.
- Lehner, B., Verdin, K., and Jarvis, A. (2008). New Global Hydrography Derived From Spaceborne Elevation Data. *Eos, Transactions American Geophysical Union*, 89(10):93.
- Lerner, D., Issar, A., and Simmers, I. (1990). *Groundwater Recharge: A Guide to Understanding and Estimating Natural Recharge*. Heise.
- Lesschen, J. P., Stoorvogel, J. J., and Smaling, E. M. A. (2004). *Scaling soil nutrient balances. Enabling mesolevel applications for African realities*. Food and Agriculture Organization of the United Nations.
- Lettenmaier, D. P., Alsdorf, D., Dozier, J., Huffman, G. J., Pan, M., and Wood, E. F. (2015). Inroads of remote sensing into hydrologic science during the WRR era. *Water Resources Research*, 51(9):7309–7342. _eprint: <https://agupubs.onlinelibrary.wiley.com/doi/pdf/10.1002/2015WR017616>.

- Levis, S., Coe, M. T., and Foley, J. A. (1996). Hydrologic budget of a land surface model: A global application. *Journal of Geophysical Research: Atmospheres*, 101(D12):16921–16930. [_eprint: https://agupubs.onlinelibrary.wiley.com/doi/pdf/10.1029/96JD01164](https://agupubs.onlinelibrary.wiley.com/doi/pdf/10.1029/96JD01164).
- Liniger, H., Gichuki, F. N., Kironchi, G., and Njeru, L. (1998). Pressure on land: the search for sustainable use in a highly diverse environment. Resources, actors and policies-towards sustainable regional development in the highland-lowland system of Mount Kenya.
- Liniger, H., Gikonyo, J., Kiteme, B., and Wiesmann, U. (2005). Assessing and Managing Scarce Tropical Mountain Water Resources. *Mountain Research and Development*, 25(2):163–173. Publisher: International Mountain Society.
- Liniger, H., Mbuvi, J. P., and Kironchi, G. (1992). *Soil type and landuse effects on infiltration in Sirima and Mukogodo catchments, Laikipia District*. Laikipia Research Programme, Universities of Nairobi and Bern (Nanyuki, Kenya. Accepted: 2013-06-17T06:59:23Z.
- Linke, S., Lehner, B., Ouellet Dallaire, C., Ariwi, J., Grill, G., Anand, M., Beames, P., Burchard-Levine, V., Maxwell, S., Moidu, H., Tan, F., and Thieme, M. (2019). Global hydro-environmental sub-basin and river reach characteristics at high spatial resolution. *Scientific Data*, 6(1):283. Bandiera_abtest: a Cc_license_type: cc_publicdomain Cg_type: Nature Research Journals Number: 1 Primary_atype: Research Publisher: Nature Publishing Group Subject_term: Freshwater ecology;Hydrology Subject_term_id: freshwater-ecology;hydrology.
- Liu, B., Phillips, F., Hoines, S., Campbell, A. R., and Sharma, P. (1995). Water movement in desert soil traced by hydrogen and oxygen isotopes, chloride, and chlorine-36, southern Arizona. *Journal of Hydrology*, 168(1):91–110.
- Liu, Y. Y., Parinussa, R. M., Dorigo, W. A., De Jeu, R. a. M., Wagner, W., van Dijk, A. I. J. M., McCabe, M. F., and Evans, J. P. (2011). Developing an improved soil moisture dataset by blending passive and active microwave satellite-based retrievals. *Hydrology and Earth System Sciences*, 15(2):425–436. Publisher: Copernicus GmbH.
- Liu Guoxiang, Craig James R., and Soulis Eric D. (2011). Applicability of the Green-Ampt Infiltration Model with Shallow Boundary Conditions. *Journal of Hydrologic Engineering*, 16(3):266–273. Publisher: American Society of Civil Engineers.
- Longuevergne, L., Scanlon, B. R., and Wilson, C. R. (2010). GRACE Hydrological estimates for small basins: Evaluating processing approaches on the High Plains Aquifer, USA. *Water Resources Research*, 46(11). [_eprint: https://agupubs.onlinelibrary.wiley.com/doi/pdf/10.1029/2009WR008564](https://agupubs.onlinelibrary.wiley.com/doi/pdf/10.1029/2009WR008564).
- Lopes, V. L. (1996). On the effect of uncertainty in spatial distribution of rainfall on catchment modelling. *CATENA*, 28(1):107–119.
- Loáiciga, H. A. (2017). The Safe Yield and Climatic Variability: Implications for Groundwater Management. *Groundwater*, 55(3):334–345.

- Ludwig, F., Dawson, T. E., de Kroon, H., Berendse, F., and Prins, H. H. T. (2003). Hydraulic lift in *Acacia tortilis* trees on an East African savanna. *Oecologia*, 134(3):293–300.
- MacDonald, A. M., Bonsor, H. C., Dochartaigh, B. , and Taylor, R. G. (2012). Quantitative maps of groundwater resources in Africa. *Environmental Research Letters*, 7(2):024009. Publisher: IOP Publishing.
- Maidment, D. R. (1993). *Handbook of Hydrology*. McGraw-Hill Education, New York, 1 edition edition.
- Maimone, M. (2004). Defining and Managing Sustainable Yield. *Ground Water*, 42(6):809–814.
- Mainga, P. and Mbuvi, J. (1994). *Preliminary soil conditions of Embori, Kalalu, and Mukogodo sites*. Nanyuki.
- Malmon, D. V., Reneau, S. L., and Dunne, T. (2004). Sediment sorting and transport by flash floods. *Journal of Geophysical Research: Earth Surface*, 109(F2).
- Mansour, M., Peach, D., Robins, N., and Hughes, A. (2019). Using a Distributed Recharge Model to Quantify Recharge Processes in a Semi-Arid Karst Catchment: An Example from Wadi Natuf, West Bank. *Water*, 11(2):276. Number: 2 Publisher: Multidisciplinary Digital Publishing Institute.
- Mansour, M. M., Peach, D. W., Hughes, A. G., and Robins, N. S. (2012). Tension over equitable allocation of water: estimating renewable groundwater resources beneath the West Bank and Israel. *Geological Society, London, Special Publications*, 362(1):355–361. Publisher: Geological Society of London Section: Articles.
- Markstrom, S. L., Niswonger, R. G., Regan, R. S., Prudic, D. E., and Barlow, P. M. (2008). GSFLOW-Coupled Ground-water and Surface-water FLOW model based on the integration of the Precipitation-Runoff Modeling System (PRMS) and the Modular Ground-Water Flow Model (MODFLOW-2005). Technical report, Geological Survey (US).
- Marçais, J., de Dreuzy, J. R., and Erhel, J. (2017). Dynamic coupling of subsurface and seepage flows solved within a regularized partition formulation. *Advances in Water Resources*, 109:94–105.
- Maréchal, D. (2004). *A soil-based approach to rainfall-runoff modelling in ungauged catchments for England and Wales*. PhD thesis, Cranfield University at Silsoe Institute of Water and Environment.
- Massuel, S., Cappelaere, B., Favreau, G., Leduc, C., Lebel, T., and Vischel, T. (2011). Integrated surface water–groundwater modelling in the context of increasing water reserves of a regional Sahelian aquifer. *Hydrological Sciences Journal*, 56(7):1242–1264.
- Massuel, S., Favreau, G., Descloitres, M., Le Troquer, Y., Albouy, Y., and Cappelaere, B. (2006). Deep infiltration through a sandy alluvial fan in semiarid Niger inferred from electrical conductivity survey, vadose zone chemistry and hydrological modelling. *CATENA*, 67(2):105–118.

- Mati, B. M., Muchiri, J. M., Njenga, K., Vries, F. P. d., and Merrey, D. J. (2006). *Assessing water availability under pastoral livestock systems in drought-prone Isiolo District, Kenya*. IWMI. Google-Books-ID: c9UYBQAAQBAJ.
- Mayes, M., Caylor, K. K., Singer, M. B., Stella, J. C., Roberts, D., and Nagler, P. (2020). Climate sensitivity of water use by riparian woodlands at landscape scales. *Hydrological Processes*, 34(25):4884–4903. _eprint: <https://onlinelibrary.wiley.com/doi/pdf/10.1002/hyp.13942>.
- Mbuvi, J. P. and Kironchi, G. (1994). *Explanations and Profile Description to Reconnaissance Soil Survey of the Upper Ewaso Ng'iro Basin (Laikipia East and Slopes West to North of Mount)*. Laikipia Research Programme, Natural Resource Monitoring, Modelling, and Management (Nanyuki, Kenya. Accepted: 2013-06-30T10:44:44Z.
- McCallum, A. M., Andersen, M. S., and Acworth, R. I. (2014a). A New Method for Estimating Recharge to Unconfined Aquifers Using Differential River Gauging: Ground Water xx, no. xx: xx-xx. *Groundwater*, 52(2):291–297.
- McCallum, A. M., Andersen, M. S., Giambastiani, B. M. S., Kelly, B. F. J., and Ian Acworth, R. (2013). River-aquifer interactions in a semi-arid environment stressed by groundwater abstraction: River-aquifer interactions in a semi-arid environment. *Hydrological Processes*, 27(7):1072–1085.
- McCallum, A. M., Andersen, M. S., Rau, G. C., Larsen, J. R., and Acworth, R. I. (2014b). River-aquifer interactions in a semi-arid environment investigated using point and reach measurements. *Water Resources Research*, 50(4):2815–2829. _eprint: <https://agupubs.onlinelibrary.wiley.com/doi/pdf/10.1002/2012WR012922>.
- McKee, T. B., Doesken, N. J., and Kleist, J. (1993). THE RELATIONSHIP OF DROUGHT FREQUENCY AND DURATION TO TIME SCALES. page 6, Anaheim.
- McNally, A., Shukla, S., Arsenault, K. R., Wang, S., Peters-Lidard, C. D., and Verdin, J. P. (2016). Evaluating ESA CCI soil moisture in East Africa. *International Journal of Applied Earth Observation and Geoinformation*, 48:96–109.
- Mein, R. G. and Larson, C. L. (1973). Modeling infiltration during a steady rain. *Water Resources Research*, 9(2):384–394. _eprint: <https://agupubs.onlinelibrary.wiley.com/doi/pdf/10.1029/WR009i002p00384>.
- Meixner, T., Huth, A. K., Brooks, P. D., Conklin, M. H., Grimm, N. B., Bales, R. C., Haas, P. A., and Petti, J. R. (2007). Influence of shifting flow paths on nitrogen concentrations during monsoon floods, San Pedro River, Arizona. *Journal of Geophysical Research: Biogeosciences*, 112(G3).
- Mekonnen, M. M. and Hoekstra, A. Y. (2012). A Global Assessment of the Water Footprint of Farm Animal Products. *Ecosystems*, 15(3):401–415.
- Merz, R., Parajka, J., and Blöschl, G. (2009). Scale effects in conceptual hydrological modeling. *Water Resources Research*, 45(9). _eprint: <https://onlinelibrary.wiley.com/doi/pdf/10.1029/2009WR007872>.

- Michaelides, K., Hollings, R., Singer, M. B., Nichols, M. H., and Nearing, M. A. (2018). Spatial and temporal analysis of hillslope–channel coupling and implications for the longitudinal profile in a dryland basin. *Earth Surface Processes and Landforms*, 43(8):1608–1621.
- Michaelides, K. and Wainwright, J. (2002). Modelling the effects of hillslope–channel coupling on catchment hydrological response. *Earth Surface Processes and Landforms*, 27(13):1441–1457. eprint: <https://onlinelibrary.wiley.com/doi/pdf/10.1002/esp.440>.
- Michaelides, K. and Wilson, M. D. (2007). Uncertainty in predicted runoff due to patterns of spatially variable infiltration. *Water Resources Research*, 43(2):W02415.
- Miguez-Macho, G., Fan, Y., Weaver, C. P., Walko, R., and Robock, A. (2007). Incorporating water table dynamics in climate modeling: 2. Formulation, validation, and soil moisture simulation: SOIL MOISTURE SIMULATION WITH WATER TABLE. *Journal of Geophysical Research: Atmospheres*, 112(D13):n/a–n/a.
- Miller, S. N., Youberg, A., Guertin, D. P., and Goodrich, D. C. (2000). Channel morphology investigations using Geographic Information Systems and field research. In *Land Stewardship in the 21st Century: The Contributions of Watershed Management, 13–16 March 2000*, volume 13, pages 415–419, Tucson, Arizona. US Department of Agriculture, Forest Service, Rocky Mountain Research Station.
- Miralles, D. G., Holmes, T. R. H., Jeu, R. A. M. D., Gash, J. H., Meesters, A. G. C. A., and Dolman, A. J. (2011). Global land-surface evaporation estimated from satellite-based observations. *Hydrology and Earth System Sciences*, 15(2):453–469. Publisher: Copernicus GmbH.
- Miralles, D. G., Jiménez, C., Jung, M., Michel, D., Ershadi, A., McCabe, M. F., Hirschi, M., Martens, B., Dolman, A. J., Fisher, J. B., Mu, Q., Seneviratne, S. I., Wood, E. F., and Fernández-Prieto, D. (2016). The WACMOS-ET project – Part 2: Evaluation of global terrestrial evaporation data sets. *Hydrology and Earth System Sciences*, 20(2):823–842. Publisher: Copernicus GmbH.
- Morin, E., Grodek, T., Dahan, O., Benito, G., Kulls, C., Jacoby, Y., Langenhove, G. V., Seely, M., and Enzel, Y. (2009). Flood routing and alluvial aquifer recharge along the ephemeral arid Kuiseb River, Namibia. *Journal of Hydrology*, 368(1):262–275.
- Morin, J. and Benyamini, Y. (1977). Rainfall infiltration into bare soils. *Water Resources Research*, 13(5):813–817.
- Mortimore, M. (2009). *Dryland Opportunities: A New Paradigm for People, Ecosystems and Development*. IUCN. Google-Books-ID: ji5FAQAAIAAJ.
- Mu, Q., Heinsch, F. A., Zhao, M., and Running, S. W. (2007). Development of a global evapotranspiration algorithm based on MODIS and global meteorology data. *Remote Sensing of Environment*, 111(4):519–536.
- Mudd, S. M. (2006). Investigation of the hydrodynamics of flash floods in ephemeral channels: Scaling analysis and simulation using a shock-capturing flow model incorporating the effects of transmission losses. *Journal of Hydrology*, 324(1):65–79.

- Muriithi, F. K. (2016). Land use and land cover (LULC) changes in semi-arid sub-watersheds of Laikipia and Athi River basins, Kenya, as influenced by expanding intensive commercial horticulture. *Remote Sensing Applications: Society and Environment*, 3:73–88.
- Mutiga, J. K., Mavengano, S. T., Zhongbo, S., Woldai, T., and Becht, R. (2010a). Water Allocation as a Planning Tool to Minimise Water Use Conflicts in the Upper Ewaso Ng'iro North Basin, Kenya. *Water Resources Management*, 24(14):3939–3959.
- Mutiga, J. K., Su, Z., and Woldai, T. (2010b). Using satellite remote sensing to assess evapotranspiration: Case study of the upper Ewaso Ng'iro North Basin, Kenya. *International Journal of Applied Earth Observation and Geoinformation*, 12:S100–S108.
- Nash, I. E. and Sutcliffe, I. V. (1970). River flow forecasting through conceptual models. *Journal of Hydrology*, 10:282–290.
- Ngigi, S. N., Savenije, H. H. G., and Gichuki, F. N. (2007). Land use changes and hydrological impacts related to up-scaling of rainwater harvesting and management in upper Ewaso Ng'iro river basin, Kenya. *Land Use Policy*, 24(1):129–140.
- Nijdam, D., Rood, T., and Westhoek, H. (2012). The price of protein: Review of land use and carbon footprints from life cycle assessments of animal food products and their substitutes. *Food Policy*, 37(6):760–770.
- Niswonger, R. G., Prudic, D. E., Fogg, G. E., Stonestrom, D. A., and Buckland, E. M. (2008). Method for estimating spatially variable seepage loss and hydraulic conductivity in intermittent and ephemeral streams. *Water Resources Research*, 44(5):W05418.
- Noorduijn, S. L., Harrington, G. A., and Cook, P. G. (2014a). The representative stream length for estimating surface water–groundwater exchange using Darcy's Law. *Journal of Hydrology*, 513(Supplement C):353–361.
- Noorduijn, S. L., Shanafield, M., Trigg, M. A., Harrington, G. A., Cook, P. G., and Peeters, L. (2014b). Estimating seepage flux from ephemeral stream channels using surface water and groundwater level data. *Water Resources Research*, 50(2):1474–1489.
- Notter, B., MacMillan, L., Viviroli, D., Weingartner, R., and Liniger, H.-P. (2007). Impacts of environmental change on water resources in the Mt. Kenya region. *Journal of Hydrology*, 343(3):266–278.
- Ojwang', G. O. (2010). *Analysis of climate change and variability risks in the small-holder sector : case studies of the Laikipia and Narok districts representing major agro-ecological zones in Kenya*. Environment and natural resources management series ; no. 41. Rome: Department of Resource Surveys and Remote Sensing (DRSRS) in collaboration with the Food and Agriculture Organization of the United Nations.
- Osborn, H. B., Renard, K. G., and Simanton, J. R. (1979). Dense networks to measure convective rainfall in the southwestern United

- States. *Water Resources Research*, 15(6):1701–1711. [_eprint: https://agupubs.onlinelibrary.wiley.com/doi/pdf/10.1029/WR015i006p01701](https://agupubs.onlinelibrary.wiley.com/doi/pdf/10.1029/WR015i006p01701).
- Osterkamp, W. R. (2008). Geology, Soils, and Geomorphology of the Walnut Gulch Experimental Watershed, Tombstone, Arizona. *Journal of the Arizona-Nevada Academy of Science*, 40(2):136–154. Publisher: The Arizona-Nevada Academy of Science.
- Pacheco-Guerrero, A., Goodrich, D. C., González-Trinidad, J., Júnez-Ferreira, H. E., and Bautista-Capetillo, C. F. (2017). Flooding in ephemeral streams: incorporating transmission losses. *Journal of Maps*, 13(2):350–357.
- Padrón, R. S., Gudmundsson, L., Decharme, B., Ducharne, A., Lawrence, D. M., Mao, J., Peano, D., Krinner, G., Kim, H., and Seneviratne, S. I. (2020). Observed changes in dry-season water availability attributed to human-induced climate change. *Nature Geoscience*, 13(7):477–481. Bandiera_abtest: a Cg_type: Nature Research Journals Number: 7 Primary_atype: Research Publisher: Nature Publishing Group Subject_term: Attribution;Hydrology;Water resources Subject_term_id: attribution;hydrology;water-resources.
- Palmer, W. C. (1965). *Meteorological Drought*. U.S. Department of Commerce, Weather Bureau.
- Paniconi, C. and Putti, M. (2015). Physically based modeling in catchment hydrology at 50: Survey and outlook. *Water Resources Research*, 51(9):7090–7129. [_eprint: https://agupubs.onlinelibrary.wiley.com/doi/pdf/10.1002/2015WR017780](https://agupubs.onlinelibrary.wiley.com/doi/pdf/10.1002/2015WR017780).
- Parissopoulos, G. A. and Wheeler, H. S. (1992). Experimental and numerical infiltration studies in a wadi stream bed. *Hydrological Sciences Journal*, 37(1):27–37.
- Pelletier, J. D., Broxton, P. D., Hazenberg, P., Zeng, X., Troch, P. A., Niu, G.-Y., Williams, Z., Brunke, M. A., and Gochis, D. (2016). A gridded global data set of soil, intact regolith, and sedimentary deposit thicknesses for regional and global land surface modeling. *Journal of Advances in Modeling Earth Systems*, 8(1):41–65. [_eprint: https://agupubs.onlinelibrary.wiley.com/doi/pdf/10.1002/2015MS000526](https://agupubs.onlinelibrary.wiley.com/doi/pdf/10.1002/2015MS000526).
- Peterson, D. M. and Wilson, J. L. (1988). Variably saturated flow between streams and aquifers.
- Philip, J. R. (1957). Theory of Infiltration: The infiltration equation and its solutions. *Soil Science*, 171(6):S34–S46.
- Phillips, J. V. and Tadayan, S. (2006). Selection of Manning’s Roughness Coefficient for Natural and Constructed Vegetated and Non-Vegetated Channels, and Vegetation Maintenance Plan Guidelines for Vegetated Channels in Central Arizona. : *U.S. Geological Survey Scientific Investigations Report 2006–5108*, page 41. Number: 2006-5108.
- Pilgrim, D. H., Chapman, T. G., and Doran, D. G. (1988). Problems of rainfall-runoff modelling in arid and semiarid regions. *Hydrological Sciences Journal*, 33(4):379–400.

- Pool, D. R. (2005). Variations in climate and ephemeral channel recharge in southeastern Arizona, United States. *Water Resources Research*, 41(11):W11403.
- Pool, D. R. and Schmidt, W. (1997). *Measurement of Ground-water Storage Change and Specific Yield Using the Temporal-gravity Method Near Rillito Creek, Tucson, Arizona*. U.S. Department of the Interior, U.S. Geological Survey. Google-Books-ID: U2vuAAAAMAAJ.
- Power, D., Rico-Ramirez, M., Desilets, S., Desilets, D., and Rosolem, R. (2021). Cosmic-Ray neutron Sensor PYthon tool (crspy): An open-source tool for the processing of cosmic-ray neutron and soil moisture data. *Geoscientific Model Development*.
- Prancevic, J. P. and Kirchner, J. W. (2019). Topographic Controls on the Extension and Retraction of Flowing Streams. *Geophysical Research Letters*, 46(4):2084–2092. eprint: <https://onlinelibrary.wiley.com/doi/pdf/10.1029/2018GL081799>.
- Preimesberger, W., Scanlon, T., Su, C.-H., Gruber, A., and Dorigo, W. (2021). Homogenization of Structural Breaks in the Global ESA CCI Soil Moisture Multisatellite Climate Data Record. *IEEE Transactions on Geoscience and Remote Sensing*, 59(4):2845–2862. Conference Name: IEEE Transactions on Geoscience and Remote Sensing.
- Qin, D., Zhao, Z., Han, L., Qian, Y., Ou, L., Wu, Z., and Wang, M. (2012). Determination of groundwater recharge regime and flowpath in the Lower Heihe River basin in an arid area of Northwest China by using environmental tracers: Implications for vegetation degradation in the Ejina Oasis. *Applied Geochemistry*, 27(6):1133–1145.
- Quichimbo, E. A. (2016). Understanding the sensitivity of focused, indirect groundwater recharge to climate change. Master’s thesis, University of Birmingham, United Kingdom.
- Rahman, M., Rosolem, R., Kollet, S. J., and Wagener, T. (2019). Towards a computationally efficient free-surface groundwater flow boundary condition for large-scale hydrological modelling. *Advances in Water Resources*, 123:225–233.
- Rassam, D. W., Peeters, L., Pickett, T., Jolly, I., and Holz, L. (2013). Accounting for surface-groundwater interactions and their uncertainty in river and groundwater models: A case study in the Namoi River, Australia. *Environmental Modelling & Software*, 50(Supplement C):108–119.
- Rau, G. C., Halloran, L. J. S., Cuthbert, M. O., Andersen, M. S., Acworth, R. I., and Tellam, J. H. (2017). Characterising the dynamics of surface water-groundwater interactions in intermittent and ephemeral streams using streambed thermal signatures. *Advances in Water Resources*, 107(Supplement C):354–369.
- Rawls, W. J., Brakensiek, D. L., and Saxton, K. E. (1982). Estimation of Soil Water Properties. *Transactions of the ASAE*, 25(5):1316–1320.
- Reinecke, R., Foglia, L., Mehl, S., Trautmann, T., Cáceres, D., and Döll, P. (2019). Challenges in developing a global gradient-based groundwater model (G³M v1.0) for the integration into a global hydrological model. *Geoscientific Model Development*, 12(6):2401–2418. Publisher: Copernicus GmbH.

- Renard, K. G. (1970). The Hydrology of Semiarid Rangeland Watersheds. Technical Report ARS-41-162, Agricultural Research Service, United States Department of Agriculture, Washington, D. C. Google-Books-ID: YOKrFBNTYrsC.
- Renard, K. G., Hickey, J. J., Wallace, D. E., and Bounoary, S. (1964). Performance of Local Aquifers as Influenced by Stream Transmission Losses and Riparian Vegetation. *Transactions of the American Society of Agricultural Engineers*, 7(4):471–474.
- Renard, K. G. and Keppel, R. V. (1966). Hydrographs of Ephemeral Streams in the Southwest. *Journal of the Hydraulics Division*, 92(2):33–52.
- Renard, K. G., Nichols, M. H., Woolhiser, D. A., and Osborn, H. B. (2008). A brief background on the U.S. Department of Agriculture Agricultural Research Service Walnut Gulch Experimental Watershed. *Water Resources Research*, 44(5):W05S02. eprint: <https://agupubs.onlinelibrary.wiley.com/doi/pdf/10.1029/2006WR005691>.
- Reynolds, J. F., Maestre, F. T., Kemp, P. R., Stafford-Smith, D. M., and Lambin, E. (2007a). Natural and Human Dimensions of Land Degradation in Drylands: Causes and Consequences. In Canadell, J. G., Pataki, D. E., and Pitelka, L. F., editors, *Terrestrial Ecosystems in a Changing World*, Global Change — The IGBP Series, pages 247–257. Springer, Berlin, Heidelberg.
- Reynolds, J. F., Smith, D. M. S., Lambin, E. F., Turner, B. L., Mortimore, M., Batterbury, S. P. J., Downing, T. E., Dowlatabadi, H., Fernández, R. J., Herrick, J. E., Huber-Sannwald, E., Jiang, H., Leemans, R., Lynam, T., Maestre, F. T., Ayarza, M., and Walker, B. (2007b). Global Desertification: Building a Science for Dryland Development. *Science*, 316(5826):847–851.
- Richards, L. A. (1931). Capillary conduction of liquids through porous mediums. *Physics*, 1(5):318–333.
- Richardson, A. D., Hollinger, D. Y., Burba, G. G., Davis, K. J., Flanagan, L. B., Katul, G. G., William Munger, J., Ricciuto, D. M., Stoy, P. C., Suyker, A. E., Verma, S. B., and Wofsy, S. C. (2006). A multi-site analysis of random error in tower-based measurements of carbon and energy fluxes. *Agricultural and Forest Meteorology*, 136(1):1–18.
- Rodell, M., Houser, P. R., Berg, A. A., and Famiglietti, J. S. (2005). Evaluation of 10 Methods for Initializing a Land Surface Model. *Journal of Hydrometeorology*, 6(2):146–155. Publisher: American Meteorological Society Section: Journal of Hydrometeorology.
- Rodell, M., Houser, P. R., Jambor, U., Gottschalck, J., Mitchell, K., Meng, C.-J., Arsenault, K., Cosgrove, B., Radakovich, J., Bosilovich, M., Entin, J. K., Walker, J. P., Lohmann, D., and Toll, D. (2004). The Global Land Data Assimilation System. *Bulletin of the American Meteorological Society*, 85(3):381–394. Publisher: American Meteorological Society Section: Bulletin of the American Meteorological Society.

- Rosolem, R., Shuttleworth, W. J., Zreda, M., Franz, T. E., Zeng, X., and Kurc, S. A. (2013). The Effect of Atmospheric Water Vapor on Neutron Count in the Cosmic-Ray Soil Moisture Observing System. *Journal of Hydrometeorology*, 14(5):1659–1671. Publisher: American Meteorological Society.
- Rowlands, D. D., Luthcke, S. B., Klosko, S. M., Lemoine, F. G. R., Chinn, D. S., McCarthy, J. J., Cox, C. M., and Anderson, O. B. (2005). Resolving mass flux at high spatial and temporal resolution using GRACE intersatellite measurements. *Geophysical Research Letters*, 32(4). _eprint: <https://agupubs.onlinelibrary.wiley.com/doi/pdf/10.1029/2004GL021908>.
- Rulli, M. C., Savioli, A., and D’Odorico, P. (2013). Global land and water grabbing. *Proceedings of the National Academy of Sciences*, 110(3):892–897.
- Running, S., Qiaozhen, M., and Maosheng, Z. (2017). MOD16A2 MODIS/Terra Net Evapotranspiration 8-Day L4 Global 500m SIN Grid V006. Type: dataset.
- Sabathier, R., Singer, M. B., Stella, J. C., Roberts, D. A., and Caylor, K. K. (2021). Vegetation responses to climatic and geologic controls on water availability in south-eastern Arizona. *Environmental Research Letters*, 16(6):064029. Publisher: IOP Publishing.
- Sanford, W. E., Plummer, L. N., McAda, D. P., Bexfield, L. M., and Anderholm, S. K. (2004). Hydrochemical tracers in the middle Rio Grande Basin, USA: 2. Calibration of a groundwater-flow model. *Hydrogeology Journal*, 12(4):389–407.
- Sargeant, C. I. and Singer, M. B. (2016). Sub-annual variability in historical water source use by Mediterranean riparian trees. *Ecohydrology*, 9(7):1328–1345.
- Save, H., Bettadpur, S., and Tapley, B. D. (2016). High-resolution CSR GRACE RL05 mascons. *Journal of Geophysical Research: Solid Earth*, 121(10):7547–7569. _eprint: <https://agupubs.onlinelibrary.wiley.com/doi/pdf/10.1002/2016JB013007>.
- Scanlon, B. R., Faunt, C. C., Longuevergne, L., Reedy, R. C., Alley, W. M., McGuire, V. L., and McMahon, P. B. (2012). Groundwater depletion and sustainability of irrigation in the US High Plains and Central Valley. *Proceedings of the National Academy of Sciences*, 109(24):9320–9325. Publisher: National Academy of Sciences Section: Physical Sciences.
- Scanlon, B. R., Keese, K. E., Flint, A. L., Flint, L. E., Gaye, C. B., Edmunds, W. M., and Simmers, I. (2006). Global synthesis of groundwater recharge in semiarid and arid regions. *Hydrological Processes*, 20(15):3335–3370.
- Schaake, J. C., Koren, V. I., Duan, Q.-Y., Mitchell, K., and Chen, F. (1996). Simple water balance model for estimating runoff at different spatial and temporal scales. *Journal of Geophysical Research: Atmospheres*, 101(D3):7461–7475. _eprint: <https://agupubs.onlinelibrary.wiley.com/doi/pdf/10.1029/95JD02892>.
- Scheidegger, J. M., Jackson, C. R., Muddu, S., Tomer, S. K., and Filgueira, R. (2021). Integration of 2D Lateral Groundwater Flow into the Variable Infiltration Capacity (VIC) Model and Effects on Simulated Fluxes for Different Grid Resolutions and Aquifer Diffusivities. *Water*, 13(5):663. Number: 5 Publisher: Multidisciplinary Digital Publishing Institute.

- Schenk, H. J. and Jackson, R. B. (2002). The Global Biogeography of Roots. *Ecological Monographs*, 72(3):311–328.
- Schlaepfer, D. R., Bradford, J. B., Lauenroth, W. K., Munson, S. M., Tietjen, B., Hall, S. A., Wilson, S. D., Duniway, M. C., Jia, G., Pyke, D. A., Lkhagva, A., and Jamiyansharav, K. (2017). Climate change reduces extent of temperate drylands and intensifies drought in deep soils. *Nature Communications*, 8:ncomms14196.
- Schmidt, A., Hanson, C., Chan, W. S., and Law, B. E. (2012). Empirical assessment of uncertainties of meteorological parameters and turbulent fluxes in the Ameri-Flux network. *Journal of Geophysical Research: Biogeosciences*, 117(G4):G04014. eprint: <https://agupubs.onlinelibrary.wiley.com/doi/pdf/10.1029/2012JG002100>.
- Schoener, G. (2017). Quantifying Transmission Losses in a New Mexico Ephemeral Stream: A Losing Proposition. *Journal of Hydrologic Engineering*, 22(3):05016038. Publisher: American Society of Civil Engineers.
- Schreiner-McGraw, A., Ajami, H., and Vivoni, E. R. (2019). Extreme weather events and transmission losses in arid streams. *Environmental Research Letters*, 14(8):084002.
- Schreiner-McGraw, A. P. and Ajami, H. (2021). Delayed response of groundwater to multi-year meteorological droughts in the absence of anthropogenic management. *Journal of Hydrology*, page 126917.
- Schreiner-McGraw, A. P. and Vivoni, E. R. (2017). Percolation observations in an arid piedmont watershed and linkages to historical conditions in the Chihuahuan Desert. *Ecosphere*, 8(11).
- Schreiner-McGraw, A. P. and Vivoni, E. R. (2018). On the Sensitivity of Hillslope Runoff and Channel Transmission Losses in Arid Piedmont Slopes. *Water Resources Research*, 54(7):4498–4518.
- Scoging, H. M. and Thornes, J. B. (1979). Infiltration characteristics in a semiarid environment. In *The Hydrology of areas of low precipitation*, volume 128, pages 159–168. IAHS Publication. Publisher: Paris, International Association of Hydrological Sciences.
- Scott, R. L. (2010). Using watershed water balance to evaluate the accuracy of eddy covariance evaporation measurements for three semiarid ecosystems. *Agricultural and Forest Meteorology*, 150(2):219–225.
- Scott, R. L., Biederman, J. A., Hamerlynck, E. P., and Barron-Gafford, G. A. (2015). The carbon balance pivot point of southwestern U.S. semiarid ecosystems: Insights from the 21st century drought. *Journal of Geophysical Research: Biogeosciences*, 120(12):2612–2624.
- SERI (2013). LAND FOOTPRINT SCENARIOS A discussion paper including a literature review and scenario analysis on the land use related to changes in Europe’s consumption patterns Report for Friends of the Earth Europe. Technical report, Sustainable Europe Research Institute, Vienna.

- Shanafield, M., Bourke, S. A., Zimmer, M. A., and Costigan, K. H. (2021). An overview of the hydrology of non-perennial rivers and streams. *WIREs Water*, 8(2):e1504. `_eprint:` <https://onlinelibrary.wiley.com/doi/pdf/10.1002/wat2.1504>.
- Shanafield, M. and Cook, P. G. (2014). Transmission losses, infiltration and groundwater recharge through ephemeral and intermittent streambeds: A review of applied methods. *Journal of Hydrology*, 511:518–529.
- Shanafield, M., Cook, P. G., Brunner, P., McCallum, J., and Simmons, C. T. (2012). Aquifer response to surface water transience in disconnected streams. *Water Resources Research*, 48(11):W11510.
- Shanafield, M., Niswonger, R. G., Prudic, D. E., Pohll, G., Susfalk, R., and Panday, S. (2014). A method for estimating spatially variable seepage and hydraulic conductivity in channels with very mild slopes. *Hydrological Processes*, 28(1):51–61.
- Sharma, K. D. and Murthy, J. S. R. (1995). Hydrologic Routing of Flow in Arid Ephemeral Channels. *Journal of Hydraulic Engineering*, 121(6):466–471. Publisher: American Society of Civil Engineers.
- Shentsis, I., Meirovich, L., Ben-Zvi, A., and Rosenthal, E. (1999). Assessment of transmission losses and groundwater recharge from runoff events in a wadi under shortage of data on lateral inflow, Negev, Israel. *Hydrological Processes*, 13(11):1649–1663.
- Shentsis, I. and Rosenthal, E. (2003). Recharge of aquifers by flood events in an arid region. *Hydrological Processes*, 17(4):695–712.
- Sherman, L. K. (1943). Comparison f-curves derived by the methods of sharp and Holtan and of Sherman and Mayer. *Eos, Transactions American Geophysical Union*, 24(2):465–467. `_eprint:` <https://agupubs.onlinelibrary.wiley.com/doi/pdf/10.1029/TR024i002p00465>.
- Shrestha, R. and Houser, P. (2010). A heterogeneous land surface model initialization study. *Journal of Geophysical Research: Atmospheres*, 115(D19). `_eprint:` <https://agupubs.onlinelibrary.wiley.com/doi/pdf/10.1029/2009JD013252>.
- Siebert, S., Burke, J., Faures, J. M., Frenken, K., Hoogeveen, J., Döll, P., and Portmann, F. T. (2010). Groundwater use for irrigation – a global inventory. *Hydrology and Earth System Sciences*, 14(10):1863–1880.
- Simmers, I., editor (1997). *Recharge of phreatic aquifers in (semi-) arid areas*. Number 19 in International Association of Hydrogeologists. Balkema, Rotterdam ; Brookfield, VT, USA. OCLC: ocm39233191.
- Simmers, I. (2003). *Understanding water in a dry environment: hydrological processes in arid and semi-arid zones*. Balkema, Lisse; Exton, Pa. OCLC: 61363565.
- Singer, M. B., Asfaw, D. T., Rosolem, R., Cuthbert, M. O., Miralles, D. G., MacLeod, D., Quichimbo, E. A., and Michaelides, K. (2021). Hourly potential evapotranspiration at 0.1° resolution for the global land surface from 1981-present. *Scientific Data*, 8(1):224. `Bandiera_abtest:` a `Cc_license_type:` cc_publicdomain `Cg_type:` Nature Research Journals Number: 1 `Primary_atype:` Research Publisher: Nature Publishing Group `Subject_term:` Hydrology `Subject_term_id:` hydrology.

- Singer, M. B., Harrison, L. R., Donovan, P. M., Blum, J. D., and Marvin-DiPasquale, M. (2016). Hydrologic indicators of hot spots and hot moments of mercury methylation potential along river corridors. *Science of The Total Environment*, 568:697–711.
- Singer, M. B. and Michaelides, K. (2014). How is topographic simplicity maintained in ephemeral dryland channels? *Geology*, 42(12):1091–1094.
- Singer, M. B. and Michaelides, K. (2017). Deciphering the expression of climate change within the Lower Colorado River basin by stochastic simulation of convective rainfall. *Environmental Research Letters*, 12(10):104011.
- Sivapalan, M. and Milly, P. C. D. (1989). On the relationship between the time condensation approximation and the flux concentration relation. *Journal of Hydrology*, 105(3):357–367.
- Skirvin, S., Kidwell, M., Biedenbender, S., Henley, J. P., King, D., Collins, C. H., Moran, S., and Weltz, M. (2008). Vegetation data, Walnut Gulch Experimental Watershed, Arizona, United States. *Water Resources Research*, 44(5).
- Small, E. E. (2005). Climatic controls on diffuse groundwater recharge in semi-arid environments of the southwestern United States. *Water Resources Research*, 41(4):W04012.
- Snyder, K. A. and Williams, D. G. (2000). Water sources used by riparian trees varies among stream types on the San Pedro River, Arizona. *Agricultural and Forest Meteorology*, 105(1):227–240.
- Sophocleous, M. (1997). Managing Water Resources Systems: Why “Safe Yield” Is Not Sustainable. *Ground Water*, 35(4):561–561.
- Sophocleous, M. and Devlin, J. (2004). “The Water Budget Myth Revisited: Why Hydrogeologists Model,” by John D. Bredehoeft, July–August 2002 issue, v. 40, no. 4: 340–345. *Ground Water*, 42(4):618–618.
- Sophocleous, M., Koussis, A., Martin, J. L., and Perkins, S. P. (1995). Evaluation of Simplified Stream-Aquifer Depletion Models for Water Rights Administration. *Ground Water*, 33(4):579–588.
- Sorman, A. and Abdulrazzak, M. J. (1993). Infiltration-recharge through wadi beds in arid regions. *Hydrological Sciences Journal*, 38(3):173–186.
- Sorman, A. U., Abdulrazzak, M. J., and Morel-Seytoux, H. J. (1997). Groundwater recharge estimation from ephemeral streams. Case study: Wadi Tabalah, Saudi Arabia. *Hydrological Processes*, 11(12):1607–1619.
- Spinoni, J., Vogt, J., Naumann, G., Carrao, H., and Barbosa, P. (2015). Towards identifying areas at climatological risk of desertification using the Köppen–Geiger classification and FAO aridity index. *International Journal of Climatology*, 35(9):2210–2222.
- Stadler, S. J. (1987). ARIDITY INDEXES Aridity indexes. In *Climatology*, pages 102–107. Springer US, Boston, MA.

- Stone, J. J., Nichols, M. H., Goodrich, D. C., and Buono, J. (2008). Long-term runoff database, Walnut Gulch Experimental Watershed, Arizona, United States. *Water Resources Research*, 44(5):W05S05.
- Sutfin, N. A., Shaw, J. R., Wohl, E. E., and Cooper, D. J. (2014). A geomorphic classification of ephemeral channels in a mountainous, arid region, southwestern Arizona, USA. *Geomorphology*, 221:164–175.
- Tarek, M., Brissette, F. P., and Arsenault, R. (2020). Evaluation of the ERA5 reanalysis as a potential reference dataset for hydrological modelling over North America. *Hydrology and Earth System Sciences*, 24(5):2527–2544. Publisher: Copernicus GmbH.
- Taylor, R. and Howard, K. (2000). A tectono-geomorphic model of the hydrogeology of deeply weathered crystalline rock: Evidence from Uganda. *Hydrogeology Journal*, 8(3):279–294.
- Taylor, R., Tindimugaya, C., Barker, J., Macdonald, D., and Kula-bako, R. (2010). Convergent Radial Tracing of Viral and Solute Transport in Gneiss Saprolite. *Groundwater*, 48(2):284–294. eprint: <https://ngwa.onlinelibrary.wiley.com/doi/pdf/10.1111/j.1745-6584.2008.00547.x>.
- Taylor, R. G., Scanlon, B., Döll, P., Rodell, M., Beek, R. v., Wada, Y., Longuevergne, L., Leblanc, M., Famiglietti, J. S., Edmunds, M., Konikow, L., Green, T. R., Chen, J., Taniguchi, M., Bierkens, M. F. P., MacDonald, A., Fan, Y., Maxwell, R. M., Yechieli, Y., Gurdak, J. J., Allen, D. M., Shamsudduha, M., Hiscock, K., Yeh, P. J.-F., Holman, I., and Treidel, H. (2012). Ground water and climate change. *Nature Climate Change*, 3(4):nclimate1744.
- Taylor, R. G., Todd, M. C., Kongola, L., Maurice, L., Nahozya, E., Sanga, H., and MacDonald, A. M. (2013). Evidence of the dependence of groundwater resources on extreme rainfall in East Africa. *Nature Climate Change*, 3(4):374–378. Number: 4 Publisher: Nature Publishing Group.
- Theis, C. V. (1940). The source of water derived from wells. *Civil Engineering*, 10(5):277–280.
- Thomas, C. L., Stewart, A. E., and Constantz, J. E. (2000). Determination of infiltration and percolation rates along a reach of the Santa Fe River near La Bajada, New Mexico. USGS Numbered Series 2000-4141, U.S. Geological Survey. Code Number: 2000-4141 Code: Determination of infiltration and percolation rates along a reach of the Santa Fe River near La Bajada, New Mexico Publication Title: Determination of infiltration and percolation rates along a reach of the Santa Fe River near La Bajada, New Mexico Reporter: Determination of infiltration and percolation rates along a reach of the Santa Fe River near La Bajada, New Mexico Series: Water-Resources Investigations Report.
- Trabucco, A. and Zomer, R. J. (2009). Global aridity index (global-aridity) and global potential evapo-transpiration (global-PET) geospatial database. *CGIAR Consortium for Spatial Information*.

- Trambauer, P., Dutra, E., Maskey, S., Werner, M., Pappenberger, F., van Beek, L. P. H., and Uhlenbrook, S. (2014). Comparison of different evaporation estimates over the African continent. *Hydrology and Earth System Sciences*, 18(1):193–212. Publisher: Copernicus GmbH.
- Trenberth, K. E., Dai, A., Schrier, G. v. d., Jones, P. D., Barichivich, J., Briffa, K. R., and Sheffield, J. (2013). Global warming and changes in drought. *Nature Climate Change*, 4(1):nclimate2067.
- Turner, R. J., Mansour, M. M., Dearden, R., Ó Dochartaigh, B. , and Hughes, A. G. (2015). Improved understanding of groundwater flow in complex superficial deposits using three-dimensional geological-framework and groundwater models: an example from Glasgow, Scotland (UK). *Hydrogeology Journal*, 23(3):493–506.
- Twine, T. E., Kustas, W. P., Norman, J. M., Cook, D. R., Houser, P. R., Meyers, T. P., Prueger, J. H., Starks, P. J., and Wesely, M. L. (2000). Correcting eddy-covariance flux underestimates over a grassland. *Agricultural and Forest Meteorology*, 103(3):279–300.
- UNEP (1992). *World atlas of desertification. United Nations Environment Programme*. Edward Arnold, London ; Baltimore, second edition.
- UNEP and of Economic and Social Affairs, D. (2017). World Population Prospects: The 2017 Revision, Key Findings and Advance Tables. United Nations Environment Programme. Working Paper ESA/P/WP/248.
- USBR (1977). *Central Arizona Project, Geology and Ground-water Resources Report, Maricopa and Pinal Counties, Arizona, October 1977*. Bureau of Reclamation, Lower Colorado Region. Google-Books-ID: Awi5oDhGtbcC.
- Valett, H. M., Fisher, S. G., and Stanley, E. H. (1990). Physical and Chemical Characteristics of the Hyporheic Zone of a Sonoran Desert Stream. *Journal of the North American Benthological Society*, 9(3):201–215.
- van Genuchten, M. T. (1980). A Closed-form Equation for Predicting the Hydraulic Conductivity of Unsaturated Soils¹. *Soil Science Society of America Journal*, 44(5):892.
- Velpuri, N. M., Senay, G. B., Singh, R. K., Bohms, S., and Verdin, J. P. (2013). A comprehensive evaluation of two MODIS evapotranspiration products over the conterminous United States: Using point and gridded FLUXNET and water balance ET. *Remote Sensing of Environment*, 139:35–49.
- Vicente-Serrano, S. M., Beguería, S., López-Moreno, J. I., Angulo, M., and Kenawy, A. E. (2010). A New Global 0.5° Gridded Dataset (1901–2006) of a Multiscalar Drought Index: Comparison with Current Drought Index Datasets Based on the Palmer Drought Severity Index. *Journal of Hydrometeorology*, 11(4):1033–1043. Publisher: American Meteorological Society Section: Journal of Hydrometeorology.
- Villeneuve, S., Cook, P. G., Shanafield, M., Wood, C., and White, N. (2015). Groundwater recharge via infiltration through an ephemeral riverbed, central Australia. *Journal of Arid Environments*, 117(Supplement C):47–58.

- Wada, Y., van Beek, L. P. H., van Kempen, C. M., Reckman, J. W. T. M., Vasak, S., and Bierkens, M. F. P. (2010). Global depletion of groundwater resources. *Geophysical Research Letters*, 37(20):L20402.
- Wagner, W., Lemoine, G., and Rott, H. (1999). A Method for Estimating Soil Moisture from ERS Scatterometer and Soil Data. *Remote Sensing of Environment*, 70(2):191–207.
- Walker, D., Smigaj, M., and Jovanovic, N. (2019). Ephemeral sand river flow detection using satellite optical remote sensing. *Journal of Arid Environments*, 168:17–25.
- Walker, W. R. (1989). Guidelines for designing and evaluating surface irrigation systems. Technical Report FAO Irrigation and Drainage Paper 45, Food and Agriculture Organization of the United Nations, Rome. ISBN: 9789251028797 Publisher: FAO.
- Wallace, D. E. and Renard, K. G. (1967). Contribution to Regional Water Table from Transmission Losses of Ephemeral Streambeds. *Transactions of the ASAE*, 10(6):0786–0789.
- Walters, M. O. (1990). Transmission Losses in Arid Region. *Journal of Hydraulic Engineering*, 116(1):129–138.
- Wang, H. F. and Anderson, M. P. (1982). *Introduction to Groundwater Modeling: Finite Difference and Finite Element Methods*. W.H.Freeman & Co Ltd, San Francisco.
- Wang, L., Chen, W., Huang, G., and Zeng, G. (2017a). Changes of the transitional climate zone in East Asia: past and future. *Climate Dynamics*, 49(4):1463–1477.
- Wang, T., Franz, T. E., You, J., Shulski, M. D., and Ray, C. (2017b). Evaluating controls of soil properties and climatic conditions on the use of an exponential filter for converting near surface to root zone soil moisture contents. *Journal of Hydrology*, 548:683–696.
- Wang, W., Dai, Z., Zhao, Y., Li, J., Duan, L., Wang, Z., and Zhu, L. (2016). A quantitative analysis of hydraulic interaction processes in stream-aquifer systems. *Scientific Reports*, 6:srep19876.
- Wang, W., Li, J., Wang, W., Chen, X., Cheng, D., and Jia, J. (2014). Estimating streambed parameters for a disconnected river. *Hydrological Processes*, 28(10):3627–3641.
- Warter, M. M., Singer, M. B., Cuthbert, M. O., Roberts, D., Caylor, K. K., Sabathier, R., and Stella, J. (2020). Onset and propagation of drought into soil moisture and vegetation responses during the 2012–2019 drought in Southern California. *Hydrology and Earth System Sciences Discussions*, pages 1–35. Publisher: Copernicus GmbH.
- Watkins, M. M., Wiese, D. N., Yuan, D.-N., Boening, C., and Landerer, F. W. (2015). Improved methods for observing Earth’s time variable mass distribution with GRACE using spherical cap mascons. *Journal of Geophysical Research: Solid Earth*, 120(4):2648–2671. eprint: <https://agupubs.onlinelibrary.wiley.com/doi/pdf/10.1002/2014JB011547>.

- Weerasinghe, I., Bastiaanssen, W., Mul, M., Jia, L., and van Griensven, A. (2020). Can we trust remote sensing evapotranspiration products over Africa? *Hydrology and Earth System Sciences*, 24(3):1565–1586. Publisher: Copernicus GmbH.
- Wekesa, S. S., Stigter, T. Y., Olang, L. O., Oloo, F., Fouchy, K., and McClain, M. E. (2020). Water Flow Behavior and Storage Potential of the Semi-Arid Ephemeral River System in the Mara Basin of Kenya. *Frontiers in Environmental Science*, 8. Publisher: Frontiers.
- Wheater, H., Sorooshian, S., and Sharma, I. K. D. (2008). *Hydrological Modelling in Arid and Semi-Arid Areas*. Cambridge University Press.
- Wheater, H., Sorooshian, S., and Sharma, K. D., editors (2007). *Hydrological Modelling in Arid and Semi-Arid Areas*. Cambridge University Press, Cambridge ; New York, 1 edition edition.
- Wheater, H. S., Butler, A. P., Stewart, E. J., and Hamilton, G. S. (1991). A multivariate spatial-temporal model of rainfall in southwest Saudi Arabia. I. Spatial rainfall characteristics and model formulation. *Journal of Hydrology*, 125(3):175–199.
- Wheater, H. S., Mathias, S. A., and Li, X. (2010). *Groundwater Modelling in Arid and Semi-Arid Areas*. Cambridge University Press.
- White, R. P. and Nackoney, J. (2003). Drylands, People, and Ecosystem Goods and Services. Technical report, World Resources Institute, Washington, D. C.
- Wiese, D. N., Landerer, F. W., and Watkins, M. M. (2016). Quantifying and reducing leakage errors in the JPL RL05M GRACE mascon solution. *Water Resources Research*, 52(9):7490–7502. eprint: <https://agupubs.onlinelibrary.wiley.com/doi/pdf/10.1002/2016WR019344>.
- Wiesmann, U., Gichuki, F. N., Kiteme, B. P., and Liniger, H. (2000). Mitigating Conflicts Over Scarce Water Resources in the Highland-Lowland System of Mount Kenya. *Mountain Research and Development*, 20(1):10–15. Publisher: International Mountain Society.
- Winter, T. C., Harvey, J. W., Franke, O. L., and Alley, W. M. (1998). Ground water and surface water; a single resource. USGS Numbered Series 1139, U.S. Geological Survey.
- Wood, E. F., Lettenmaier, D. P., Liang, X., Lohmann, D., Boone, A., Chang, S., Chen, F., Dai, Y., Dickinson, R. E., Duan, Q., Ek, M., Gusev, Y. M., Habets, F., Irannejad, P., Koster, R., Mitchel, K. E., Nasonova, O. N., Noilhan, J., Schaake, J., Schlosser, A., Shao, Y., Shmakin, A. B., Verseghy, D., Warrach, K., Wetzel, P., Xue, Y., Yang, Z. L., and Zeng, Q. C. (1998). The project for intercomparison of land-surface parameterization schemes (PILPS) phase 2(c) Red-Arkansas River basin experiment: 1. Experiment description and summary intercomparisons. *Global and Planetary Change*, 19(1-4):115–135.
- Woodward, C. S. and Dawson, C. N. (2000). Analysis of Expanded Mixed Finite Element Methods for a Nonlinear Parabolic Equation Modeling Flow into Variably Saturated Porous Media. *SIAM Journal on Numerical Analysis; Philadelphia*, 37(3):701–724.

- Woolhiser, D. A. (1989). KINEROS, A Kinematic Runoff and Erosion Model. *Documentation and Use Manual*. Publisher: U.S. Department of Agriculture.
- WRAP (1987). Water Resources Assessment Study in Laikipia. Technical report, Ministry of Water Development Report, Nairobi, Kenya.
- Xian, Y., Jin, M., Liu, Y., and Si, A. (2017). Impact of lateral flow on the transition from connected to disconnected stream-aquifer systems. *Journal of Hydrology*, 548(Supplement C):353–367.
- Xie, Y., Cook, P. G., Brunner, P., Irvine, D. J., and Simmons, C. T. (2014). When Can Inverted Water Tables Occur Beneath Streams? *Groundwater*, 52(5):769–774.
- Yatheendradas, S., Wagener, T., Gupta, H., Unkrich, C., Goodrich, D., Schaffner, M., and Stewart, A. (2008). Understanding uncertainty in distributed flash flood forecasting for semiarid regions. *Water Resources Research*, 44(5). eprint: <https://agupubs.onlinelibrary.wiley.com/doi/pdf/10.1029/2007WR005940>.
- Zarate, E., Hogley, D., MacDonald, A. M., Swift, R. T., Chambers, J., Kashaigili, J. J., Mutayoba, E., Taylor, R. G., and Cuthbert, M. O. (2021). The role of superficial geology in controlling groundwater recharge in the weathered crystalline basement of semi-arid Tanzania. *Journal of Hydrology: Regional Studies*, 36:100833.
- Zimmer, M. A., Kaiser, K. E., Blaszcak, J. R., Zipper, S. C., Hammond, J. C., Fritz, K. M., Costigan, K. H., Hosen, J., Godsey, S. E., Allen, G. H., Kampf, S., Burrows, R. M., Krabbenhoft, C. A., Dodds, W., Hale, R., Olden, J. D., Shanafield, M., DelVecchia, A. G., Ward, A. S., Mims, M. C., Datry, T., Bogan, M. T., Boersma, K. S., Busch, M. H., Jones, C. N., Burgin, A. J., and Allen, D. C. (2020). Zero or not? Causes and consequences of zero-flow stream gage readings. *WIREs Water*, 7(3):e1436. eprint: <https://onlinelibrary.wiley.com/doi/pdf/10.1002/wat2.1436>.
- Zocatelli, D., Marra, F., Armon, M., Rinat, Y., Smith, J. A., and Morin, E. (2019). Contrasting rainfall-runoff characteristics of floods in desert and Mediterranean basins. *Hydrology and Earth System Sciences*, 23(6):2665–2678. Publisher: Copernicus GmbH.
- Zocatelli, D., Marra, F., Smith, J., Goodrich, D., Unkrich, C., Rosensaft, M., and Morin, E. (2020). Hydrological modelling in desert areas of the eastern Mediterranean. *Journal of Hydrology*, 587:124879.
- Zomer, R. J., Bossio, D. A., Trabucco, A., Yuanjie, L., Gupta, D. C., and Singh, V. P. (2007). *Trees and water: smallholder agroforestry on irrigated lands in Northern India*, volume 122. IWMI.
- Zreda, M., Shuttleworth, W. J., Zeng, X., Zweck, C., Desilets, D., Franz, T., and Rosolem, R. (2012). COSMOS: the COsmic-ray Soil Moisture Observing System. *Hydrology and Earth System Sciences*, 16(11):4079–4099. Publisher: Copernicus GmbH.
- Ó Dochartaigh, B. E., MacDonald, A. M., Darling, W. G., Hughes, A. G., Li, J. X., and Shi, L. A. (2010). Determining groundwater degradation from irrigation in desert-marginal northern China. *Hydrogeology Journal*, 18(8):1939–1952.

Šimůnek, J., Van Genuchten, M. T., and Šejna, M. (2006). The HYDRUS software package for simulating two-and three-dimensional movement of water, heat, and multiple solutes in variably-saturated media. *Technical manual, version*, 1:241.

Appendix A

Governing equations

In the basin, water can flow over the surface or it can flow through a porous media such as soils or aquifers. These two types of flow allow for the characterisation of three main components of hydrological cycle: (i) surface flow, representing overland flow and channel flow, (ii) subsurface, representing the variably saturated flow through the soil, and (iii) groundwater flow, representing the saturated flow in the aquifer.

A.1 Overland and channel flow

Surface flow can be described by the Saint-Venant equation (de Saint-Venant B., 1871) which is a simplification of the Navier-Stokes equation for shallow water flow. However, for practical uses, further simplification such as diffusive-wave and kinematic-wave approximation are considered enough to represent surface flow (Paniconi and Putti, 2015). The kinematic-wave approximation for the 2-D Saint-Venant equation for wide channel is presented as:

$$\frac{\partial h}{\partial t} = -\frac{\partial v_x h}{\partial x} - \frac{\partial v_y h}{\partial y} + q_e + q_r \quad (\text{A.1})$$

where: h is the depth of water above the surface [L], t is time [T], q_e represents the exchange of water between the surface and subsurface zone [L T⁻¹], q_r represent any other water source of sink, and v_x and v_y represent flow velocity at x and y directions, respectively. v_x and v_y can also be simplified by assuming the Manning equation as the relation between discharge and flow depth based on boundary roughness (Henderson, 1966):

$$v_x = \frac{S_x^{1/2}}{n} h^{2/3} \quad v_y = \frac{S_y^{1/2}}{n} h^{2/3} \quad (\text{A.2})$$

where: S_x and S_y are the channel slope [-].

The kinematic-wave approximation works adequately in high slope surfaces where backward effect are negligible. However, negative topographic gradient and shallow water levels will limit their application (Maidment, 1993), in such cases, diffuse-wave approximations are more suitable.

A.2 Variable saturated flow

In the case of flow through soil, the physical processes under unsaturated conditions can be described by Richard ´s equation (Richards, 1931):

$$\eta \frac{\partial \psi}{\partial t} = \frac{\partial}{\partial x} \left[K_x k_r \frac{\partial \psi}{\partial x} \right] + \frac{\partial}{\partial y} \left[K_y k_r \frac{\partial \psi}{\partial y} \right] + \frac{\partial}{\partial z} \left[K_z k_r \frac{\partial \psi}{\partial z} \right] - q \quad (\text{A.3})$$

where ϕ represents the pressure potential [L], that can vary in time and space; K_x , K_y , and K_z , with dimension [L T⁻¹], represent the saturated hydraulic conductivity in the directions x , y , and z , respectively; k_r is the relative hydraulic conductivity, dimensionless [-]; η represents the storage coefficient defined as:

$$\eta = \frac{\theta \cdot S_s}{n} + \frac{d\theta}{d\psi} \quad (\text{A.4})$$

where S_s is the specific storativity [L⁻¹], θ is volumetric soil water content [-]; n is the porosity of the medium [-], and q is the specific volumetric flow rate out of the medium [L T⁻¹], which can represent any source or sink term such as evapotranspiration.

Under unsaturated conditions the relation between ϕ and θ can be specified by the soil water-retention and the hydraulic conductivity curves. Empirical equations for representing these curves based on soil properties are suggested by van Genuchten (1980), and Brooks and Corey (1964).

Numerical solution of Richards' equation is computationally intensive. In order to reduce the computational cost, simplifications, for example the use of only the vertical components or the kinematic-wave approximation (Markstrom et al., 2008) are often used. However, the Philip's equation (Philip, 1957) and the Green-Ampt equation (Green and Ampt, 1911) can be used as simplifications for describing the movement of water through porous media (Dillon and Liggett, 1983; Niswonger et al., 2008; Noorduijn et al., 2014a,b; Shanafield et al., 2014). The main characteristics of the Philip's equation are the ability to represent the higher rates of infiltration due to capillarity at the initial wetting stage of the streambed and the posterior decay of that rate, reaching steady-state, when the capillarity pressure decreases.

A.3 Saturated flow

When saturated conditions develop, the change in water content with respect to time becomes zero and the saturated conductivity becomes a constant under the assumption that viscosity and density of the fluid are constants. Richards' equation under saturated conditions can be expressed as:

$$S_s \frac{\partial \psi}{\partial t} = \frac{\partial}{\partial x} \left[K_{xx} \frac{\partial \psi}{\partial x} \right] + \frac{\partial}{\partial y} \left[K_{yy} \frac{\partial \psi}{\partial y} \right] + \frac{\partial}{\partial z} \left[K_{zz} \frac{\partial \psi}{\partial z} \right] - q \quad (\text{A.5})$$

Despite the ability of Richards' equation to represent flow through a porous media, the use of this equation is compromised when preferential flow develops in the unsaturated zone. Although some approaches have been proposed to address this, they are still inapplicable due to the complexity in the measurement/estimation of the variables/states involved in the system (Beven, 2002; Beven and Binley, 1992; Beven, 2004; ?).

Appendix B

DRYP User Guide

B.1 Introduction

B.1.1 Running DRYP

DRYP v1.0 has been tested in Python 3.7.4. and runs in windows and Linux.

The following python packages must be installed in order to use DRYP:

Landlab 2.0. (see <https://landlab.readthedocs.io/en/master/index.html>)

Numpy 1.16.4

Pandas 0.25.1

DRYP can run in previous versions of python that are compatible with packages listed above.

DRYP comes with an example (GW_1D) in addition to the following python scripts:

DRYP_Gen_Func.py

DRYP_groundwater_EFD.py

DRYP_infiltration.py

DRYP_io.py

DRYP_model_list.txt

DRYP_Modflow.py

DRYP_rainfall.py

DRYP_routing.py

DRYP_soil_layer.py

run_DRYP_v1_0.py

run_model.py

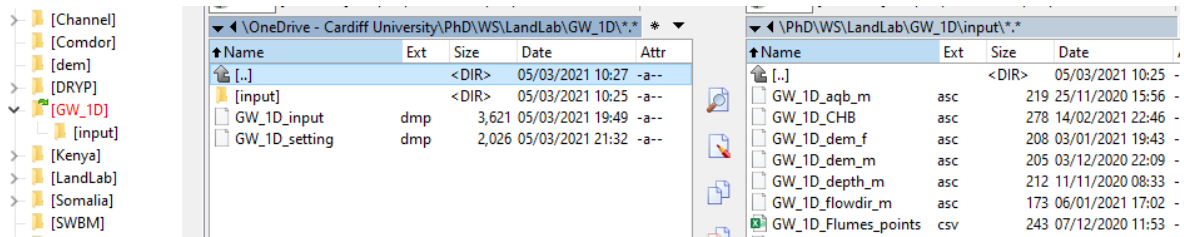


Figure B.1: Location of the GW_1D example

test_dryp.py

The folder GW_1D contains all files required to run a simple integrated 1D model. Inside this folder a folder called 'input' as well as two files 'input.dmp' and 'settings.dmp' required to run the model are provided. All files provided in this folder can be read/modified using a notepad or any other text editors.

For running DRYP, follow the steps below:

1. Copy and paste the folder DRYP in a convenient location in your PC.
2. Open the file 'run_model.py' and change the name of the input file of the function 'run_DRYP(model_input_filename)'. This function will call DRYP and its components.
3. Open the command line or any IDLE available in your PC and run the file previously edited ('run_model.py')

Details about the input files, model parameter files as well as simulation setting are specified in the following sections.

For running the example copy and paste the folder GW_1D into the same directory of DRYP folder (see figure B.1).

For testing the installation, run `pytest` command providing the location of the DRYP folder. A simple test file ('test_dryp.py') is provided in order to check the installation.

For running the lossy flow accumulator using the 'cython' transmission losses function, `TransLoss` function must be installed. The `TransLoss` function should be installed using the "setup.py" file. This file is located in the folder components. For running, it has to be installed into same directory.

The installation can be done by using the python terminal using the following command:

```
python setup.py build_ext --inplace
```

B.2 Model parameter files

B.2.1 Forcing Data

The main driven variables of the model are the precipitation and evapotranspiration. Time variable parameters can be provided as gridded data in netcdf format or they can be provided as time series in '.csv' format. When provided as time series, the precipitation/evapotranspiration will be uniform for the entire model domain for each time step.

The model will not interpolate/aggregate spatially or temporally any variable. Therefore, all input, variables and parameters, must have the same spatial resolution when gridded data is used. Model grid size will depend entirely on datasets/maps provided as input files. The time step of precipitation/evapotranspiration has to be according to the time step specified in the model setting parameters.

For netcdf datasets, a variable representing time has to be specified with name 'time'. Time has to be defined as numeric values but it should include a time units and the calendar. Names of variables must be specified as 'pre' for precipitation and 'pet' for evapotranspiration. The model will not recognise any other name specified for these variables.

Forcing data can be pre-processed or created by using xarray or the netCDF4 API for python. An example of variable creation using the netCDF4 API is shown below:

```
dataset = Dataset(fname_out, 'w', format='NETCDF4_CLASSIC')
dataset.createDimension('time', None)
dataset.createDimension('lon', columns)
dataset.createDimension('lat', rows)
dataset.createDimension('grid', grid size)
lat = dataset.createVariable('lat', np.float64, ('lat',))
lon = dataset.createVariable('lon', np.float64, ('lon',))
time = dataset.createVariable('time', np.float64, ('time',))
pre = dataset.createVariable('pre', np.float32, ('time', 'grid'))
time.units = 'hours since 1980-01-01 00:00:00'
time.calendar = 'gregorian'
```

For dataset provided as time series in csv files, columns must be label as 'Date' for time and 'pre' and 'ETo' for precipitation and evapotranspiration, respectively. An example is provided bellow:

```
Date,pre,ETo
01/01/2000 00:00,0,0
01/01/2000 01:00,0,0
01/01/2000 02:00,0,0
01/01/2000 03:00,0,0
```

Model parameters can be provided as numerical values or as maps. When maps are provided, they must be raster files. Raster files are easily read by the Landlab package of python. An example of the raster format for a 3×3 grid size map is shown below.

```
ncols      3
nrows      3
xllcorner  574361
yllcorner  3502989
cellsize   1000
NODATA_value -9999
825.233 860.3439 864.650
825.233 860.3439 864.650
825.233 860.3439 -99999
```

In the case of boundary conditions, raster files must have a value -9999 as nodata when a cell does not a specific boundary condition, any other value will be assumed as boundary conditions. Boundary conditions should also follow the

B.2.2 Model Parameters

A list of parameters required for each component is presented below:

Surface component:

- Digital elevation model (DEM), required
- River network (values greater than zero are considered as river), if not available all cells are considered rivers
- Flow direction in landlab format (ID of receiving node following landlab indexing), if no available, Landlab will automatically find the direction of flow based on the DEM.
- Drainage area, it can specified as the model domain for the catchment. Default value is 1.0.

Subsurface component:

- Rooting depth in mm, default value 1000mm
- Wilting Point (θ_{wp}), default value 0.1
- field capacity (θ_{fc}), default value 0.15
- Porosity, n_e , default value 0.35
- Standard deviation of the saturated hydraulic conductivity, σ
- Infiltration at saturated conditions, (K_{sat}) in mm/h
- Water content at residual capacity, θ_r
- Exponent of the water retention function, b default value 2.
- Suction head, ψ , default value 300mm

Groundwater component

- Aquifer saturated hydraulic conductivity, Ks_{GW} , default value 1 [m/h]
- Aquifer specific yield, Ks_{GW} , default value 0.01 [-]
- Groundwater model domain, optional, in case that groundwater catchment is different than surface catchment.
- Initial water table, default value is specified at 1 meter below the rooting depth.
- Head boundary conditions
- Flux boundary conditions
- Bottom stream bed elevation, default value: $z - 5m$

Main Input file

All input file name's must be listed in model parameters file, which is further explained explained below, However, if a filename is not provided, default values will be considered.

The input file must be a plain text file. This file must start with 'drylandmodel' in the first line (see example below), omitting the first line will stop the simulation.

Filenames provided in the input file must be written in each line specified in the example, changes will result in simulation errors or wrong variables being read (e.g. if the file 'GW_1D_dem_m.asc' is written in line 5, python will raise an exception error).

```

input_file
1 drylandmodel
2 Model name -----(3):
3 test
4 ===== TERRAIN COMPONENTS =====
5 Topography (DEM)(m)----- (4):
6 test/input/test_dem_m.asc
7 Cell area factor (-)----- (6):
8 test/input/test_area_m.asc
9 Flow Direction (fd)(-)----- (8):
10 test/input/test_flowdir_m.asc
11 Boundary conditions (check CHB) (-)----- (10):
12 test/input/test_chb.asc
13 Basin Mask (catchment) (-)----- (12):
14 test/input/test_mask_m.asc
15 River length (m)----- (14):
16 test/input/test_riv_m.asc
17 River width (m)----- (16):
18 none
19 River bottom elevation (m)----- (18):
20 none
21 ===== SURFACE COMPONENTS =====
22 Vegetation type Kc (-)----- (21):
23 none
24 Soil land use (-)----- (23):
25 none
26 Other (-)----- (25):
27 none
28 ===== SOIL AND SUBSURFACE PARAMETERS =====
29 Soil porosity: porosity (-)----- (28):
30 test/input/test_rawls_ne.txt
31 Theta residual (-)----- (30):
32 test/input/test_rawls_theta_r.txt
33 Available Water content (AWC) (-)----- (32):
34 test/input/test_rawls_aws.txt
35 Wilting Point (wp) (-)----- (34):
36 test/input/test_rawls_wp.txt
37 Soil Depth (D) (m)----- (36):
38 test/input/test_depth_m.asc
39 Soil particle distribution parameter (b) (-)----- (38):
40 test/input/test_rawls_n.txt
41 Soil suction head (psi)(m)----- (40):
42 test/input/test_rawls_phi.txt
43 Saturated hydraulic conductivity (mm_h)----- (42):
44 test/input/test_rawls_ks.txt
45 sigma_Ksat (mm_h)----- (44):
46 test/input/test_rawls_sigma_ks.txt
47 Initial soil water content (-)----- (46):

```

```

48 none
49 Other -----(48):
50 none
51 === GROUNDWATER PARAMETER AND BOUNDARY CONDITIONS ===
52 Groundwater Boundary condition (domain) -----(53):
53 test/input/test_mask_m.asc
54 Aquifer Sat. Hydraulic Conductivity (Ksat_aq) (m_h)-(55):
55 test/input/test_rawls_ks1.txt
56 Specific Yield (-)-----(57):
57 none
58 Initial Conditions Water table elevation (m)----- (59):
59 test/input/test_wte_ini.asc
60 Flux Boundary Conditions (m_h)----- (61):
61 None
62 Head Boundary Conditions (m)----- (63):
63 test/input/test_CHB1.asc
64 Other----- (65):
65 none
66 ===== METEOROLOGICAL DATA =====
67 Precipitation (mm_h)----- (68):
68 test/input/Pre_60m_00_05_10_sin.csv
69 Potential Evapotranspiration (mm_h)----- (70):
70 test/input/Pre_60m_p00_e00.csv
71 Water abstractions file (mm_h)----- (72):
72 none
73 Other ----- (74):
74 none
75 ===== RESULTS AND OUTPUT DIRECTORIES =====
76 Discharge point results ----- (77):
77 test/input/test_Flumes_points.csv
78 Soil point results output ----- (79):
79 test/input/test_SM_points.csv
80 Groundwater point results ----- (81):
81 test/input/test_well_point_m.csv
82 Folder location results ----- (83):
83 test/output
84 Other ----- (85):
85 none
86 Other ----- (87):
87 none
88 MODEL PARAMETER SETTINGS FILE ----- (89):
89 test/setting_test.dmp

```

If abstractions and irrigation are available, it must be provided in line 72. Information can be provided in netCDF format in order to take into account the spatial variability, if a ".csv" file is provided a uniform rate will be applied over the entire

model domain (not common). Additionally, name's variables must be specified with the following codes:

Table B.1: Code and Name of variables for input datasets of anthropogenic fluxes

code	variable
ASW	Surface component: River abstractions
AUZ	Unsaturated component: Irrigation
ASZ	Saturated component: Groundwater abstractions

For the groundwater component, boundary conditions can be specified as head and flux boundary conditions on lines 61 and 63, respectively. A raster file of head/flux must be provided if boundary conditions are considered in the model. The raster file must have as non boundary condition values of -9999, otherwise it will be assumed as head/flux condition. If boundary file are not provided, zero flux boundary conditions will be assumed.

Simulation parameter file

Information about simulation parameters such as period or time step must also be provided in a plain text file. This file should contain parameters that control the simulations such as simulation period, format of input files as well as the activation of model components such as groundwater flow.

Simulation settings file has to include in the first line the following text 'DWAPM.SET', as it is shown in the example below, omitting the first line will stop the simulation. Lines with numerical values are allowed to change, but they can not be displaced by adding a new line. The change of position of lines will result in errors or will stop the simulation.

```

_____ simulation_setting_file _____
1 DWAPM_SET
2 ===== SIMULATION PERIOD AND TIME STEP =====
3 Initial date for simulation (YYYY MM DD) .....(4)
4 2000 1 1
5 Initial date for simulation (YYYY MM DD) .....(6)
6 2004 1 3
7 OF Time step - dt_Pre (min) - (1440 for daily)...(8)
8 60
9 UZ Time step - dt_Pre (min) - (1440 for daily)..(10)
10 60
11 SZ Time step - dt_Pre (min) - (1440 for daily)..(12)
12 60
13 ===== MODEL READING OPTIONS =====
14 Read Precipitation from NETCF file.....(15)

```

```

15 0 60
16 Read Evapotranspiration from NETCF file.....(17)
17 0 60
18 Read Abstractions from NETCF file .....(19)
19 0
20 ===== MODEL COMPONENTS =====
21 Inf.- 0: Scheeke 1: Philips 2: Up_GA 3: Mod_GA....(22)
22 1
23 Run surface routing -----..(24)
24 0
25 Run Groundwater-Enable Type: 0-Unc 1-func 2-Con-..(26)
26 1 1
27 Run OF linear reservoir: 1 active 0 disable.....(28)
28 0
29 Run UZ linear reservoir: 1 active 0 disable.....(30)
30 0
31 ===== OUTPUT OPTIONS =====
32 Show simulation times 1 active 0 disable .....(33)
33 0
34 Save state rasults in netcf files.....(35)
35 1
36 Temporal aggregation results (eg. 3M Y H).....(37)
37 6M
38 Plot maps and the end of the period.....(39)
39 0
40 Save maps as raster at the end of the period.....(41)
41 0
42 Print daily maps.....(43)
43 0
44 Print simulation time.....(45)
45 0
46 ===== MODEL PARAMETERS FACTORS =====
47 Runoff partition parameter factor (kdt-Sheeke)....(48)
48 1.0
49 Soil Depth factor - kDroot .....(50)
50 1.0
51 Available Water Content factor - kAWC .....(52)
52 1.0
53 Infiltration rate factor - kKsat .....(54)
54 0.004
55 Heterogeneity factor - k_sigma - (Upscaled GA)....(56)
56 1.0
57 Transmission losses factor - kKch.....(58)
58 10.52967
59 Discharge decay factor - kT .....(60)
60 0.1512967
61 Channel width parameter (pe-not activated).....(62)

```

```

62 1
63 Aquifer sat. hydraulic conductivity factor (kKaq).(64)
64 1.250
65 Aquifer specific yield factor (kSy).....(66)
66 1.00

```

Information related to simulation period should be specified as the initial and final date of the simulation and must be specified in lines 4 and 6. Date must be specified as integers separated by spaces (e.g. 2001 1 9), zero on the left side is not allowed and will stop the simulation (e.g 2001 01 19, will raise an error).

Simulation time step of the surface component must be specified in line 10. Time has to be specified in minutes, with a maximum time step of one day. Time step must be an integer, and values must be rational fraction of the hour (e.g 20 min is allowed but 25 will stop the simulation) when sub-hourly time step is set. In case of hourly time steps, it must be a rational fraction of the day (e.g. 180 min (3h) is allowed but 300 min (5h) will result in errors).

For the groundwater component, the simulation time step must be specified on line 12. Time step has to be an integer value, and should be specified in hours.

The format of precipitation, evapotranspiration and water abstraction files must be specified in lines 15, 17 and 19, respectively. The time frequency of the of model input files should be specified along with the file format parameter. For the format, a value of 1 represent grids in netcdf format, whereas a value of zero represent comma-separated formats (".csv"). Time frequency should be specified in minutes (see example below). If frequency is not provided, DRYP will assume a default value of 60 min.

```

13 ===== MODEL READING OPTIONS =====
14 Read Precipitation from NETCF file (format time-scale) .....(15)
15 0 60
16 Read Evapotranspiration from NETCF file (format time-scale)..(17)
17 0 720
18 Read water abstractions (format time-scale) .....(19)
19 0 60

```

DRYP has four types of infiltration methods implemented which can be selected by a specific code on line 22. The following codes can be chosen depending on the infiltration approach adopted:

- 0: Schaake model,
- 1: Philip's equation,
- 2: Upscaled Green and Ampt,
- 3: Modified Green and Ampt method.

For the groundwater component, three different approaches for groundwater flow conditions are available:

- 0: Variable transmissivity, fully unconfined conditions,
- 1: Constant transmissivity,
- 2: Transmissivity function,

The groundwater components can be activated or disabled in line 26, a value of 1 enable the groundwater component whereas a value of 0 disables it. The groundwater approach is specified along with the activation code of the groundwater component as shown in the example below:

```

25 Run Groundwater-Enable Type: 0-Unc 1-func 2-Con-(26)
26 1 1

```

in case that the approach is not specified, the "variable transmissivity", option 0, is used as default approach.

Line 27 is currently disabled.

To save model results as netCDF files, lines 33 and 35 of the setting parameters file need to be modified. A value of 1 in line 33 will activate the option save, whereas line 35 is used to specify the aggregation frequency. Frequency should be specified as integer and a string character. Accepted character are D for days, M for months and Y for years, an example is specified below:

```

32 Save state rasults in netcf files.....(33)
33 1
34 Temporal aggregation results (eg. 3M Y H).....(35)
35 6M

```

A set of parameters that globally modify the model parameters are also specified in the simulation settings file. Values are scale factors of the following parameters, this values are unitless:

line 48: kdt, for water partitioning of the Shaake infiltration approach,
line 50: kDroot, for rooting depth,
line 52: kAWC, for available water content,
line 54: kKsat for the saturated hydraulic conductivity of the soil,
line 56: kSigma, for the standard deviation of the saturated hydraulic conductivity of the Modified Green and Ampt approach,
line 58: kKch, for infiltration rates in the channel,
line 60: kT for decay parameter of discharge,
line 62: kKaq for aquifer saturated hydraulic conductivity,
line 64: kSy for aquifer specific yield factor,

B.3 Model results

Output variables for each model component are summarised below:

Surface component

- Runoff
- Infiltration rate
- Flow accumulation
- Transmission losses

Subsurface component:

- Water content (θ)
- Actual evapotranspiration (AET)
- Percolation

Groundwater component:

- Recharge (percolation + transmission losses)
- Water table elevation

Table B.2: Suffix of model result files stored by DRYP

Code	Variable
avg:	average results over the active model domain
THT:	Soil moisture [-]
PET:	Potential evapotranspiration [L T ⁻¹]
AETr:	Actual evapotranspiration from riparian area [L T ⁻¹]
AET:	Actual evapotranspiration [L T ⁻¹]
INF:	Infiltration rate [L T ⁻¹]
EXS:	Infiltration excess [L T ⁻¹]
RCH:	Recharge [L T ⁻¹]
Dis:	Discharge [L T ⁻¹]
BFL:	Baseflow [L T ⁻¹]
QFL:	Baseflow [L ³ T ⁻¹]
wte:	Water table elevation [L]

By default, DRYP saves all results in the directory specified in the line 83 of the input parameter file (see Sect. B.2). Output file name's start with the name of the model (line 2, in input files, Sect. B.2), followed by the following codes:

Result at different locations of each model component can be obtained by providing a file containing a list of coordinates. This should be specified in a comma separated format (e.g. .csv) with column heads specified as **Nort** and **East** for the y and x, respectively. If a coordinate is not located inside the model domain, the simulation will stop. Note that at least one point coordinate should be specified, otherwise, an error will be produced.

Coordinate files must be specified in the following lines of the main input file:

- line 77: File of coordinates for surface component,
- line 79: File of coordinates for unsaturated zone,
- line 81: File of coordinates for saturated zone,

Point result file are named with the model name (line 3, see B.2.2) as prefix followed by the codes specified in table B.2. Point result files store a number of variables depending on the component, with one file for each model variable. A list of model variables for each component is specified below:

Point result files are time series with the first column specified as time with head 'Date'. The number of columns of result files depend on the number of points specified in the coordinate files defined above. Columns are label depending on the component and variable (see B.3) followed by number starting by zero (e.g. for discharge, the file

Table B.3: Model variable name's and codes stored for point result files, for filename see table B.2

code	variable
Surface component	
OF	Discharge
TL	Transmission losses
EXS	infiltration excess
Unsaturated zone	
SM	soil moisture
AET	actual evapotranspiration
RCH	recharge, diffuse and foccused recharge
Saturated zone	
WT	water table elevation

model_name.Dis.txt will contain the following columns, 'Date' for time and 'OF_0', 'OF_1', .. etc. for discharge values)

DRYP automatically save spatially averaged fluxes and water content of model compartments. The name of the this result file has the suffix **avg** and the end. Results are saved at time steps specified for the surface component.

Average results are saved in a comma separated file that can be opened in microsoft excel or any text editor. The document contains the following information which is specified by codes for each variable in the first line:

- pre: precipitation,
- rch: recharge,
- dis: discharge,
- aet: actual evapotranspiration,
- usz: soil water content,
- gws: groundwater storage,

Discharge stored in the 'avg' file corresponds to the first row of the coordinate file. Therefore, in order to close the mass balance of the catchment, the first row of the coordinate file must be the coordinate of the catchment output.

Appendix C

Python Code - DRYP

Model scripts and example files are publicly available at the following location:

<https://github.com/AndresQuichimbo/DRYP>